# Adiabatic Cooling for Rovibrational Spectroscopy of Molecular Ions

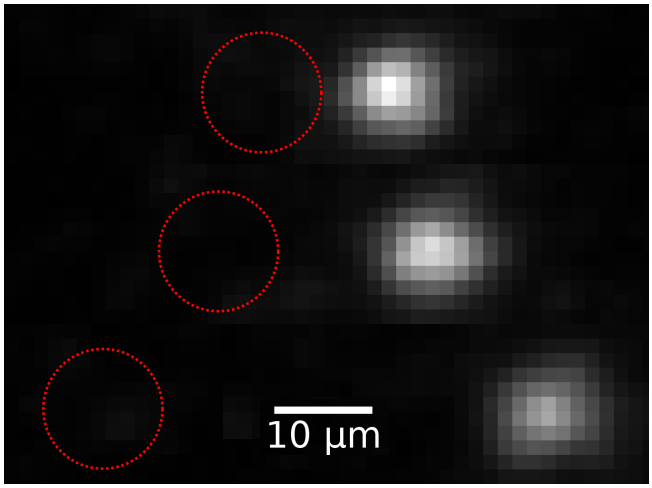


Karin Fisher

PhD Thesis

Department of Physics and Astronomy
Aarhus University

July 2017

This thesis is submitted to the Faculty of Science at Aarhus University, Denmark, in order to fulfill the requirements for obtaining the PhD degree in Physics.
The studies have been carried out under the supervision of Prof. Michael Drewsen in the Ion Trap Group at the Department of Physics and Astronomy at Aarhus University from March 2014 to July 2017.



karin.fisher@phys.au.dk

*To my grandfather Arnold L. Bloom*

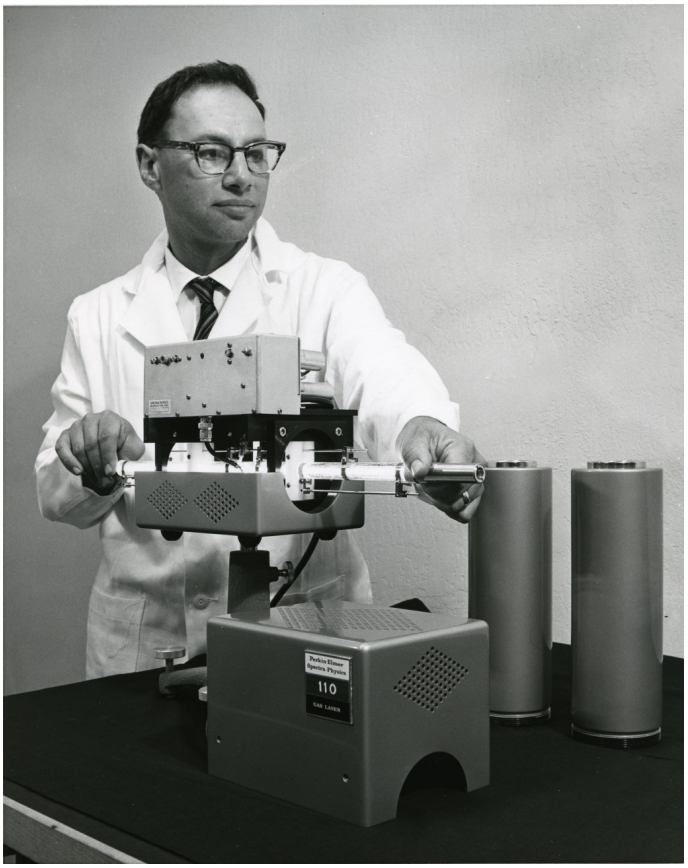


Though you may not know it, you are my inspiration. Your house is filled with little treasures, from old textbooks and conference proceedings to Helium Neon lasers hidden in the bathroom closet, and I'm certain you can claim the discovery of cats' fascination with lasers.

# Abstract (English)

The field of cold molecular ions is a fast growing one, with applications in high resolution spectroscopy and metrology, the search for time variations of fundamental constants, cold chemistry and collisions, and quantum information processing, to name a few. The study of single molecular ions is attractive as it enables one to push the limits of spectroscopic accuracy. Non-destructive spectroscopic detection of molecular ions can be achieved by co-trapping with an easier to detect atomic ion. The ion chain has coupled motion, and transitions which change both the internal and motional states of the molecule can be detected on the atomic ion as a change its motion. Scattered photons of the mid-IR rovibrational transitions in molecular ions are less energetic than those of the optical transitions in atomic ions, and are thus less likely to change the motional state of the ion crystal. This thesis proposes to adiabatically relax the trapping potential, called adiabatic cooling, when performing rovibrational excitations of the molecular ion to reduce the energy spacing of the harmonic motional levels, thus increasing the likelihood of a motional transition.

The work presented in this thesis covers the implementation of adiabatic cooling for the application of rovibrational spectroscopy on single molecular ions. This entailed constructing and testing a new DC supply capable of employing adiabatic ramps of the ion's axial frequency on the 100's of µs timescale. The DC supply went through several iterations to reduce the voltage noise output, which translates into unwanted motional excitation (heating) of the ions in the trap. Non-destructive detection relies on motional excitation coming only from optical excitation, thus it was necessary to characterize how the DC supply noise contributed to unwanted heating. Characterization of four different supply iterations was carried out for axial trap frequencies of a single $^{40}Ca^{+}$ ranging from 68 kHz to 509 kHz, and reduction of the heating rates was observed for each successive improvement of the DC supply. The supply's output noise spectrum has been directly connected to the measured heating rates, almost perfectly fitting existing heating rate theory. Further, the same model successfully predicted the heating rates of the in-phase mode of a two-ion crystal, indicating that we can use it to predict the heating rates in experiments on molecule-atom chains.

Adiabatic cooling experiments with total ramp times of 290 µs, 20-times faster than previous experiments, have been subsequently carried out, and show that heating due to technical noise is the main limitation in how low we can cool the ions. Results with the out-of-phase mode of a two-ion crystal demonstrate cooling with an axial frequency reduction of a factor of 12, with a mode temperature reduction of at least a factor 7. This results in a mode temperature of about 800 nK at the bottom of the ramp. Lastly, by reducing DC supply noise, I show reduction of the axial frequency below 50 kHz with nearly no motional gain is possible with some optimization.

Rovibrational transitions in $^{24}MgH^{+}$ are only known to the 1.5 GHz level compared to their Hz-linewidths. Simulations for broadband spectroscopy aimed reducing this uncertainty are presented for a rovibrational transition in $^{24}MgH^{+}$. This technique allows for illumination times much less than the lifetime of the state. Adiabatic cooling is shown to decrease illumination time further by an order of magnitude for attainable trap parameters. Finally, further applications to adiabatic cooling for cold chemistry, collisions, and vibration-sensing are presented.

# Resumé (Dansk)

Forskningsfeltet kolde molekulære ioner er under kraftig udvikling og medfører anvendelsesmuligheder, såsom højopløsnings spektroskopi og metrologi, eftersøgning af variationer i de fundamentelle fysiske konstanter, kold kemi og kollisioner, kvanteinformationsmetoder og mange andre. Undersøgelsen af enkle molekulære ioner er interessant da den fører til at grænsen for spektroskopisk præcision flyttes. Ikke-destruktiv spektroskopisk detektion af overgange i enkle molekylære ioner kan blive opnået ved hjælp af en ko-indfangning af en atomisk ion der er lettere at måle. Kæden af ioner har en sammenkoblet bevægelse, og overgange der ændrer både indre og bevægelsesmæssige tilstande for molekylet kan blive målt på den atomiske ion som en ændring af dens bevægelse. Spredte fotoner fra de mellem-IR rovibrationelle overgange i molekylære ioner har mindre energi end dem der skyldes optiske overgange i atomisker ioner, og det er derfor mindre sandsynligt at disse vil ændre bevægelsestilstanden for den ioniske krystal. I denne tese foreslår jeg at adiabatisk afslappe potentialet for ion-fælden, imens rovibrationelle eksitationer af den molekylære ion foretages, så energiafstanden mellem de harmoniske bevægelsesniveauer fører til en større sandsynlighed for en bevægelsesmæssig overgang. Denne adiabatiske åbning af potentialet for ion-fælden kaldes adiabatisk køling.

Denne tese omhandler udviklingen af adiabatisk køling for at foretage direkte rovibrationel spektroskopi på enkle molekulære ioner. Dette indebar konstruktion og afprøvning af en ny DC strømforsyning der kan understøtte adiabatiske ramper for ionens aksiale frekvens over 100'eder af µs. Strømforsyningen gik igennem flere udviklinger for at reducere støjen i den genererede spænding, der fører til uønskede eksitationer (opvarmning) af ionen i fælden. Ikke-destruktiv detektion er afhængig af den bevægelsesmæssige eksitation kun skyldes det optiske felt, og det var derfor nødvendigt at karakterisere hvordan strømforsyningen førte til den uønskede opvarmning. Fire udgaver af strømforsyningen var karakteriseret for aksiale fælde frekvenser for enkelt $^{40}Ca^{+}$ i området fra 68 kHz til 509 kHz, og opvarmningensraterne blev reduceret for hver forbedrede version. Strømforsyningens udgangsstøjspektrum er blevet direkte forbundet til den målte opvarmningsrate, hvilket næsten passer perfekt med den eksisterende teori for disse opvarmingsrater. Den samme model forudsagde også opvarmningsraterne for i-fase tilstanen af to-ion krystaller, hvilket indikerer at vi kan bruge denne model til at forudsige opvarmningsrater i eksperimenter med molekyle-atom kæder.

Eksperimenter med adiabatisk køling over 290 µs — 20 gange hurtigere end tidligere eksperimenter – er yderligere blevet udført. Dette viser at den tekniske støj er den største begrænsning i hvor kraftigt vi kan køle ionerne. I forsøg med ude-af-fase tilstande for to-ion krystaller lykkedes det at demonstere køling med en reduktion i aksial frekvens med en faktor 12 med en reduktion i tilstandstemperatur på mindst faktor 7. Dette resulterer i en tilstandstemperatur på omkring 800 nK på bunden af rampen. Endeligt viser jeg en reduktion i aksial frekvens mindre end 50 kHz er mulig ved at reducere støjen af DC strømforsyningen, næsten uden at tilføre bevægelsesmæssig energi.

Rovibrationelle overgange i $^{24}MgH^{+}$ er kun bestemt med en præcision på 1.5 GHz i forhold til deres enkelt-Hz liniebredde. Jeg viser simulationer af bredbåndsspektroskopi udviklet til at reducere denne usikkerhed for rovibrationelle overgange i $^{24}MgH^{+}$. Denne teknik tillader illumination i meget kortere tid end tilstandens levetid. Adiabatisk køling fører yderligere til at illuminationen kan gøres en størrelsesorden kortere for mulige ion-fælde parametre. Endeligt beskrives yderligere anvendelser for adiabatisk køling for kold kemi, kollisioner og vibrationsmålinger.

# Acknowledgements

Thank you first and foremost, to my supervisor Michael Drewsen, for giving me the opportunity to complete this PhD, and for his support along the way.

Likewise, thanks to all members of the Ion Trap Group and Optomechanics lab, past and present. Thanks especially to Steffen Meyer and Cyrille Solaro, who have proofread this thesis, as well as worked with me on the same trap. To Mike DePalatis and Gregers Poulsen, both former postdocs with whom I also worked on the same trap. Mike, thank you for your solidarity in what constitutes a real taco. To Julian for your endless supply of chocolate, and Jacob for the many interesting and difficult questions you asked. To Bhagya, for being my bestie, and distracting me when I needed it. Thank you to Andreas, who provided me with a Danish translation of my abstract. And of course to everyone else, Hans, Thomas, Olivier, Katérina, Aurelien, and Sepideh who have constantly given me support, made me laugh at lunch, and with whom I have shared many a coffee throughout the years.

Likewise, thank you to the Marie-Curie Initial Training Network COMIQ (Cold Molecular Ions at the Quantum Limit) who provided the funding for my project. Through this network I was brought together with 12 other young researchers, with whom I shared discussions of physics and many laughs. I hope to see you all again soon at a reunion!

Another group that requires special mention is the Electronics department here at the Physics department. All members of the electronics group have supported me throughout my PhD, but special mention must go to Martin Stougaard with whom I collaborated on the DC supplies presented in this thesis.

To my pole vault family here in Denmark, especially Ole Kvist, Iben Høgh-Pedersen, Michael Christiansen, and Merilin Iital who kept me sane these past three years, as well as the other members of the athletics clubs (Aarhus 1900 and Randers Freja) here for training with me and always asking how it's going, especially Bea and Mathilde. Thank you to Lauren Kuntz who, despite the distance, reminds me every day that I can do it. And thank you to the rest of my friends here in Denmark, in Zürich, and in the US. I know it's been a while since we've talked... this is what I've been doing.

And my family... my parents, who raised me just as I am. My mom for letting me live at the Exploratorium as a child, and my dad for always asking and answering questions, and building crazy things with me. My brother for... well, being my brother. My grandmothers Saloma and Barbara, who have encouraged me never to make compromises as a result of my gender. I certainly come from a long line of strong, intelligent, independent women. To my grandpa Bob, who always ensured that I would have access to the education that I wanted. And to my grandpa Arnold, who ignited the physics bug in me.

And of course, to Ben, who has been brave enough to marry me. Also he helped proofread and turn some hand-drawn figures into Inkscape creations. Thank you!

# Contents

# Chapter 1

# Introduction

When quantum mechanics was first developed, its founders could hardly imagine experimenting on single quantum systems. In 1952, Schrödinger himself wrote,

> *"We never experiment with just one electron or atom or (small) molecule. In thought experiments we sometimes assume that we do; this invariably entails ridiculous consequences...it is fair to state that we are not experimenting with single particles, any more than we can raise Ichthyosauria in the zoo." [1]*

But perhaps it is exactly these 'ridiculous' consequences that make the field of ion trapping such a rich one. Not long after Schrödinger wrote this, the first ion traps were built: a Paul trap in 1954 by Wolfgang Paul [2] and a Penning trap in 1959 by Hans Dehmelt[1] [3]. Both Dehmelt and Wolfgang Paul would go on to share the Nobel prize in 1989 "for the development of the ion trap technique [4]."

With the development of Doppler laser cooling [5] in 1975, it became possible to localize and image trapped ions, and the first single ion, $Ba^+$, was imaged in 1980 in the group of Peter Toschek [6]. The existence of quantum jumps, of which Schrödinger was debating the existence when he penned his infamous quote, was still debated by 1985 [7]; however, the debate ended when they were observed in Dehmelt's group, followed closely by Wineland's group and Toschek's group, all in 1986[2] [8–10]. Wineland would go on to share the Nobel prize in 2012 "for groundbreaking experimental methods that enable measuring and manipulation of individual quantum systems [11]."

Quantum jumps are a hallmark of single quantum systems, where the state of the system 'jumps' between two eigenstates. In trapped ions they can be observed when a typically fluorescing ion decays into a metastable state. The ion is dark until decaying and fluorescing again. The resulting fluorescence signal has discrete steps, random in time. This was challenging to accept initially since quantum optics theory was continuous in time. However, the existence of quantum jumps are also what make detection in single-ion systems so efficient—the absorption of a single photon on a narrow transition can be detected by purposely 'shelving' the ion in the metastable state [13]. By not scattering any photons once shelved, the single photon absorption event is amplified into a macroscopic signal. As such, there is no loss in spectroscopic precision as the result of detection.

This is not the only aspect of laser-cooled ions that make them attractive candidates for spectroscopy. As spectroscopic systems, the sub-millikelvin laser-cooled ions nearly reach the ideal

[1] This was in fact used to trap electrons, initially.

[2] Actually, quantum jumps were observed earlier, but not recognized for what they were [7].

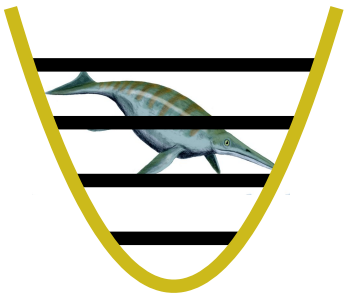

Little known fact: Ichthyosauria can also be found lurking in quantum harmonic wells. Ichthyosaur image credit: [12]

of a single atom at rest in free space [14], as at the center of the trap, the trapping fields vanish. Further, when the ion is cooled into the Lamb Dicke regime, or in other words, cooled into the regime where the wavelength of the exciting field is much larger than the extent of the wavefunction of the ion, first order Doppler broadening vanishes. These properties, along with the ability to employ long integration times due to long storage times[3] and their relative isolation from their environments, make ions ideal tools for high precision spectroscopy. The attainability of high precision[4] combined with the ability to observe quantum interference effects lead to the development of the first optical atomic clock, created at NIST from a single $^{199}Hg^{+}$ ion, with fractional frequency instability of $7 \times 10^{-15}$, significantly lower than microwave atomic clocks [15]. This clock has been surpassed by newer ion trap clocks, which now reach uncertainties of order $10^{-18}$ [16, 17].

The cooling of ions to their ground state of motion by means of sideband cooling was proposed by Wineland and Dehmelt in 1975 and demonstrated first by Diedrich, *et al.* in 1989 [18]. Ground-state-cooled ions opened the door to the fully coherent control of single and few ions' internal and motional states. The coherent control of these transitions, coupled with long lifetime states, has made ions a choice also for quantum information. In addition, ground state cooling reduces the second order Doppler shift, and can be used to reduce the uncertainty due to this shift in atomic clocks by a factor of 50 [19].

These experiments, however, could only be undertaken for a small subset of atomic ions, due to available optical transitions suitable for Doppler cooling. This left out studies of many atomic and practically all molecular ions[5]. This problem is solved by sympathetically cooling [21] inaccessible species by cooling a co-trapped accessible species. This works because co-trapped ions share motional modes due to the Coulomb interaction pushing them apart combined with the harmonic trapping potential pushing them together. In 1995, the first sympathetically cooled molecular ions were reported by T. Baba and I. Waki [22], and in 2000, the first Coulomb crystals of sympathetically-cooled molecular ions were reported by Mølhave and Drewsen [23].

With cold molecular ions, an expanded realm of physics can be studied. For example, high resolution spectroscopy [24, 25] of molecular ions sheds insight on molecular structure, and enables theorists to evaluate their models. High resolution spectroscopy can also be used for searching for the time variation of fundamental constants, for which molecular ions are often better choices than atomic ions [26, 27]. For experiments cold chemistry, reactions with laser-cooled molecular ions can shed light on the role of quantum mechanics in reaction dynamics, as at temperatures un-

[3] The same single ion can be used for years.

[4] Coupled with the development of optical frequency combs [5]

[5] Though a few schemes to exist for the direct laser cooling of molecular ions [20], they are generally either complex or require a low starting temperature.

der 1 K, quantum effects begin to play a major role [28, 29]. Further, the study of cold chemistry with molecular ions helps evaluate models for ion-neutral reactions, which play an important role in astrochemistry [30, 31]. For quantum computation, molecular ions hold interest due to the possibility of magnetic-field insensitive transitions and large state space with many long-lived states [32–35]. For the same reason, molecules may also be good candidates for metrology [36].

Molecular ions have, for the most part, been studied in mixed-species Coulomb crystals thus far. These crystals suffer from a few limitations. One is that in a Coulomb crystal, the outer ions experience more micromotion, and the crystal temperatures reached are higher than those achievable with single ions, limiting the precision of spectroscopy. Further, in these experiments, measurement often takes place destructively, for example by photo-dissociation [37, 38], reaction [23], or ion ejection [39]. This means that for each measurement, the ion trap must be reloaded with new ions—very different from keeping the same ion for a year. Lastly, the large state space of a molecular ion has, in a room-temperature trap, a population distributed throughout the rotational levels, and, in heavier molecules, the vibrational levels as well. While a number of techniques have been developed to prepare a Coulomb crystal in a specific state, including laser-induced rotational cooling [40–42] and buffer gas cooling [43], these methods do not prepare any state with 100 % efficiency.

Going to a ground-state cooled single molecular provides a number of advantages. Firstly, the ultimate spectroscopic resolution comes with a ground-state cooled single molecular ion. We can sympathetically sideband cool the molecular ion with the atomic ion, as has been demonstrated by [44–47]. This also allows us to implement a detection scheme called quantum logic spectroscopy [48], where the state of the molecular ion can be mapped onto the shared motion between the atomic ion and molecular ion. By performing motional state dependent detection on the atomic ion, the state of the molecular ion can be inferred, thereby enabling non-destructive detection. This technique has been implemented in two molecular ion experiments: one which performed electronic spectroscopy of $^{24}MgH^+$ [49], and one which performed Zeeman spectroscopy in $CaH^+$ [47]. This technique can be further used to implement state preparation with near-unity preparation [50, 51], and was demonstrated for Zeeman state-preparation in $CaH^+$ [47]. State preparation enables more efficient spectroscopy, state-prepared chemistry [28], and possibly quantum logic [34].

Our goal is to use this technique to perform direct rovibrational spectroscopy of $^{24}MgH^+$. In $^{24}MgH^+$, the lowest-lying rovibrational transitions have wavelengths in the mid-infrared, on the order of 6 µm. In contrast, the ion which we use for sympathetic cooling and readout is $^{40}Ca^+$. Its sideband cooling and shelving transition has a wavelength of 729 nm. These two wavelengths are an order of magnitude different.

This is important because to perform quantum logic spectroscopy, it is necessary to change the motional state of the two-ion chain by at least one motional quanta—once with the molecular ion, and once with the atomic ion. Because it carries a larger momentum, a scattered photon at 729 nm is much more likely to kick the state one rung up the harmonic oscillator than a scattered photon at 6 µm is. This likelihood of a scattering event providing a sufficient kick is described by the square of the Lamb Dicke parameter

$$\eta^2 \propto \left(\frac{2\pi}{\lambda}\right)^2 \frac{\hbar}{2m\omega_z}$$

where $\lambda$ is the wavelength of the light and $\omega_z$ is the trap's harmonic frequency. Thus, we see that, given all else is the same, the $^{24}MgH^+$ ion is 100 times less likely to scatter with a momentum change than $^{40}Ca^+$ is. This reduced probability to scatter on $^{24}MgH^+$ slows the total measurement down. To speed up the measurement, we can increase $\eta$ for $^{24}MgH^+$.

We can do this by decreasing $\omega_z$. By reducing the trap confinement, we increase the Lamb Dicke parameter. However, it is advantageous to cool and to measure $^{40}Ca^+$ at high $\omega_z$, so we need to change $\omega_z$ in between cooling on $^{40}Ca^+$, measuring on $^{24}MgH^+$, and measuring on $^{40}Ca^+$. This process is called adiabatic cooling because if we adiabatically expand the potential, the motional state population does not change but the kinetic energy and thus the temperature are reduced.

While adiabatic cooling experiments on single $^{40}Ca^+$ ions had been previously carried out in our group prior to the start of my PhD [52], these experiments were limited by the very slow ramp speeds for $\omega_z$, where the entire process, down and up, took 12 ms. In the work presented in this thesis, I describe the implementation of adiabatic cooling for a timescale 100-times faster than previously achieved. This involved building, characterizing, and improving a new DC supply capable of changing the axial potential on these timescales. Further, with the new electronic supplies, I characterized the ion heating rates, which must be minimized for quantum logic spectroscopy, and matched the measured heating rates directly to the output noise of the supply, thus enabling targeted improvement. In addition, I have performed calculations showing the effect of adiabatic cooling on broadband rovibrational spectroscopy in $^{24}MgH^+$.

### Outline of the thesis

This thesis is split into five parts. Part I, titled **Physics of Ion Trapping**, contains three chapters: Chapter 2, *Ion trapping*, covers the physics behind confining a single ion in a trap, Chapter 3, *Light-matter interactions*, describes how light fields interact with one and two trapped two-level ions, and Chapter 4, *Cooling*, describes the theory of cooling and heating in two-level trapped ion systems.

Part II, **Ions in Aarhus**, consists of two chapters. Chapter 5, *Cooling and detection of $^{40}Ca^+$*, discusses how the cooling methods presented in the previous part are implemented in our experiment for $^{40}Ca^+$, and how detection is carried out. In Chapter 6, *Cooling and detection of $^{24}MgH^+$*, I discuss methods to cool the internal and external degrees of freedom of a $^{24}MgH^+$ ion. I also discuss the challenge of detection of molecular ions, introducing quantum logic spectroscopy paired with adiabatic cooling as a method to directly probe rovibrational transitions.

In Part III, **Experimental Setup**, I describe various aspects of the setup, describing the trap, chamber, imaging, and related aspects in Chapter 7, *Trap setup*, and the lasers and their stabilization in Chapter 8, *Laser systems*. In Chapter 9, *Trap electronics*, I discuss the electronics system, including the DC supply which I built, programmed, and characterized, and I explain the subsequent DC supply iterations. Lastly, in Chapter 10, *Sequence automation*, I briefly discuss the experimental control system.

In Part IV, **Experiments with $^{40}Ca^+$**, has two chapters in which I discuss the experiments that I have undertaken using one or two $^{40}Ca^+$ or $^{42}Ca^+$ ions. In Chapter 11, *Heating rates*, I show the characterization of the heating rate for different DC supply iterations for varying axial frequencies. I show that using the heating rate expressions given in the theory section, I can model the heating rate based on the noise measured out of the DC supply. In Chapter 12, *Adiabatic cooling*, I present adiabatic cooling experiments for three different situations: single ions, two ions, and a single ion using another DC supply iteration, showing promising results for adiabatic cooling applied to spectroscopy.

Part V, **Future Experiments with $^{24}MgH^+$**, consists of two chapters. In Chapter 13, *Narrow spectroscopy*, I discuss the future implementation of high resolution rovibrational spectroscopy in $^{24}MgH^+$ using quantum logic. However, because the rovibrational transition frequencies are only known to the GHz level, we will first want to perform spectroscopy in a broad regime. Chapter 14, *Broadband spectroscopy*, covers the simulations I carried out to model rovibrational spectroscopy

in $^{24}MgH^+$ with a broadband light source using adiabatic cooling. I demonstrate that the application of adiabatic cooling is expected to decrease the amount of time needed to excite detectable motional transitions in $^{24}MgH^+$ by one order of magnitude for typical experimental conditions.

Lastly, I end the thesis in Chapter 15 with a *Conclusion and outlook*, where I summarize the thesis and next steps, as well as present other applications for adiabatic cooling.

# Part I

# Physics of Ion Trapping

# Chapter 2

# Ion trapping

There are several methods for trapping particles. For neutral atoms, traps rely on creating confinement via magnetic and/or optical interaction with the atoms [53]. These traps are inherently limited as the forces are dependent on the atom's structure and internal state. Ions have an advantage in that their charge strongly interacts with electromagnetic fields independent of their internal states. However, Earnshaw's theorem [54] states that one cannot stably confine a charged particle by electrostatic interaction alone, which stems from the fact that the Laplace equation for electrostatic forces must be satisfied

$$\nabla^2 \phi = 0 \tag{2.1}$$

where $\phi$ is the electric potential.

There are two major classes of ion traps: Penning traps [55] and Paul traps [56]. Penning traps use a strong magnetic field in conjunction with a quadrupole electric field to trap ions in an orbit [57], thereby circumventing the issue with Earnshaw's theorem. Paul traps, on the other hand, use a fast oscillating electric field in conjunction with a static electric field to provide confinement. Most Paul traps are designed with the goal of an approximately quadrupolar potential such that the motion of the ion in the trap is harmonic. The type of the Paul trap used in the experiments covered in this thesis is called a linear Paul trap [58]. This chapter will cover the physics of trapping ions in a linear Paul trap.

## 2.1 Linear Paul trap

The trap consists of four rods, where each of the four rods is split into three separate electrodes. Figure 2.1 shows a schematic of the trap. Due to the semi-cylindrical symmetry, the z-direction is referred to as the trap axis, and the x- and y-directions are both referred to as radial directions.

We can confine an ion in the axial ($z$) direction by applying a static positive voltage to the 8 electrodes at the ends of the rods (electrodes 1, 4, 7, 10 and 3, 6, 9, 12 in Figure 2.1, called endcap electrodes) relative to the 4 center electrodes. A positively[1] charged ion will see a potential minimum along the axis at the center of the trap. The electric potential near the center due to the voltages on the endcap electrodes is given by

$$\phi_z = \frac{\kappa}{z_0^2} \left( V_{end} \right) z^2 \tag{2.2}$$

[1] Ion trapping generally deals with positively instead of negatively charged ions. While there have been a few experiments trapping negatively charged ions in traps, [59–62] for example, the lack of bound excited states in most negatively charged atomic ions make them poor candidates for laser cooling [63, 64].

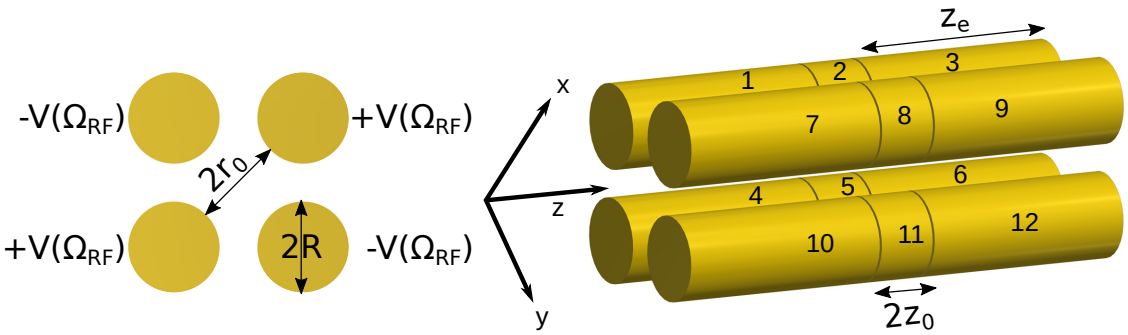


Figure 2.1: Schematic of the linear Paul trap.

where the scaling factor $\kappa$ is geometrically determined, $z_0$ is half the length of the center electrodes (see Figure 2.1), and $V_{end}$ is the voltage applied to the eight endcaps. The equation of motion of the ion in the axial direction is therefore given by

$$\frac{d^2z}{dt^2} = -\frac{2Q\kappa}{mz_0^2}\left(V_{end}\right)z \tag{2.3}$$

where $m$ is the mass and Q is the charge of the ion. This is the equation of motion for a harmonic oscillator with a frequency of

$$\omega_z = \sqrt{\frac{2Q\kappa}{mz_0^2}V_{end}} \tag{2.4}$$

With just these DC potentials, the ion is not, however, confined in the radial ($x$-$y$) direction. Radial confinement is achieved by applying an alternating (radio frequency, RF) voltage with the same phase to diagonal rods while applying an RF voltage of frequency with a 180° phase difference to adjacent rods

$$V\left(\Omega_{RF}\right) = \pm\frac{V_{RF}}{2}\cos(\Omega_{RF}t) \tag{2.5}$$

where the RF voltage's peak-to-peak voltage is $V_{RF}$, and its frequency is $\Omega_{RF}/2\pi$.

To gain an intuitive understanding of how this traps the ion, we can imagine a ball sitting on a "flapping" saddle potential, as shown in Figure 2.2. If the saddle potential is static, the ball will roll down the slope and be lost. If it "flaps" at a slow rate, more slowly than the ball moves, the ball will roll down the slope more quickly than the potential can change and be lost. But if the potential flaps more quickly than the ball moves, then when the ball starts rolling away from the center, the potential will flip directions and push it back towards the center. Of course it will then roll in the other direction, and the potential will flip back to push it back towards the center.

The electrostatic potential in the radial direction is given by the superposition of the potentials resulting from both the DC and the RF voltages. For an appropriately-chosen geometry (see f.ex [65]), the field near the trap axis is approximately quadrupolar, and can be expressed as

$$\phi_{x,y} = -\frac{\kappa V_{end}}{2z_0^2}(x^2+y^2) - \frac{V_{RF}}{2r_o^2}(x^2-y^2)\cos(\Omega_{RF}t) \tag{2.6}$$

where $2r_o$ is the radial distance between two diagonal rods, as seen in Figure 2.1.

The equation of motion of a single ion in the radial direction takes the form of the Mathieu equation, and can be written as [66]

$$\frac{d^2u}{d\tau^2} + [a_r - 2q_u\cos(2\tau)]u = 0 \qquad \text{with} \qquad u = x, y \tag{2.7}$$

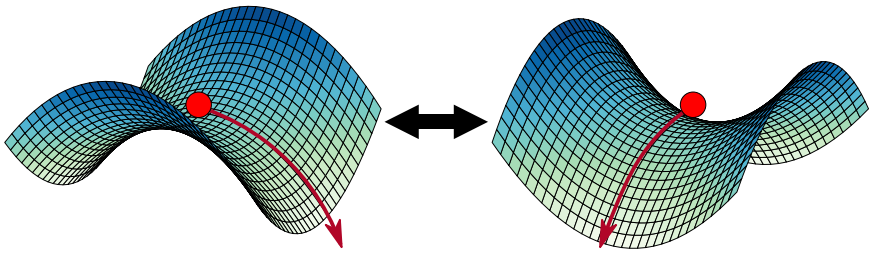

Figure 2.2: The ball, representing the ion, can be held on top of the saddle if the saddle inverts fast enough. On the left, we see that the ball wants to fall off the saddle, but to the right, the saddle has flipped, and the ball no longer will roll in that direction. Instead, it wants to roll perpendicularly. The ball is kept on the saddle when the saddle flips back to the initial state.

where the dimensionless constants are given by

$$\tau = \frac{\Omega_{RF} t}{2}, \qquad a_r = -\frac{4Q\kappa V_{end}}{m z_0^2 \Omega_{RF}^2}, \qquad \text{and} \qquad q_r = q_x = -q_y = 2\frac{QV_{RF}}{m r_0^2 \Omega_{RF}^2} \tag{2.8}$$

where $2r_0$ (see Figure 2.1) is the shortest distance between diagonally opposite rods.

The non-diverging solutions to the Mathieu equation give the stable trajectories for the ions. The shaded regions in Figure 2.3 show which $a_r$ and $q_{x,y}$ parameters give table trajectories. This stability diagram is further modified when considering axial confinement. For a positively charged ion ($Q > 0$), $V_{end}$ must be positive for axial confinement, which means that $a < 0$. The new stability diagram is shown in Figure 2.4.

When $|a_r|, |q_{x,y}| \ll 1$, the trajectory can be approximated as [67]

$$u(t) = u_0 \left[1 - \frac{q_u}{2}\cos(\Omega_{RF} t)\right] \cos(\omega_r t) \tag{2.9}$$

where $\omega_r$ is given by

$$\omega_r = \frac{\Omega_{RF}}{2}\sqrt{\frac{q_r^2}{2} + a_r} \tag{2.10}$$

Figure 2.5 shows the ion motion described in Equation 2.9.

The motion of the ion in the trap can be separated into two timescales. In this limit, oscillations at the frequency $\omega_/2\pi$ are called secular motion and are slower and have a larger amplitude than oscillations at $\Omega_{RF}$, called the micromotion. Because of its small amplitude and fast oscillations, we can average over the micromotion and describe the radial trapping potential as harmonic

$$\phi_r = \frac{1}{2} m \omega_r^2 r^2 \tag{2.11}$$

Along the trap axis, the RF field cancels, so there is no micromotion. Its amplitude grows with the distance from the RF null line, as is shown in Figure 2.6. If off-axis, the ion will always experience some micromotion in addition to the secular motion. Excess micromotion can occur, however, if the ion is pushed off-axis by external fields, imbalances in electrode voltages, or stray fields due to defects in the trap design. Axial micromotion can also occur due to imbalances in the RF phases or amplitudes on individual electrodes. This excess micromotion can be compensated for, as described in Chapter 9.

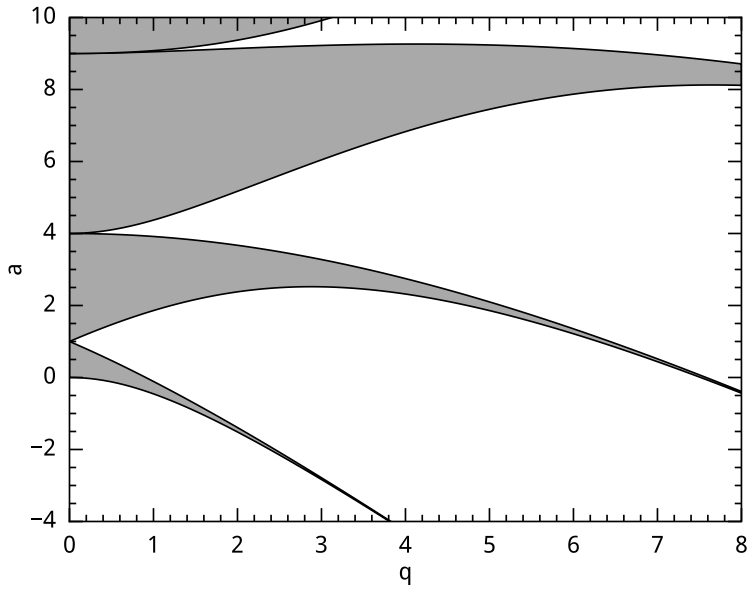


Figure 2.3: The shaded areas show the stable solutions for $a$ and $q$ in the radial direction.

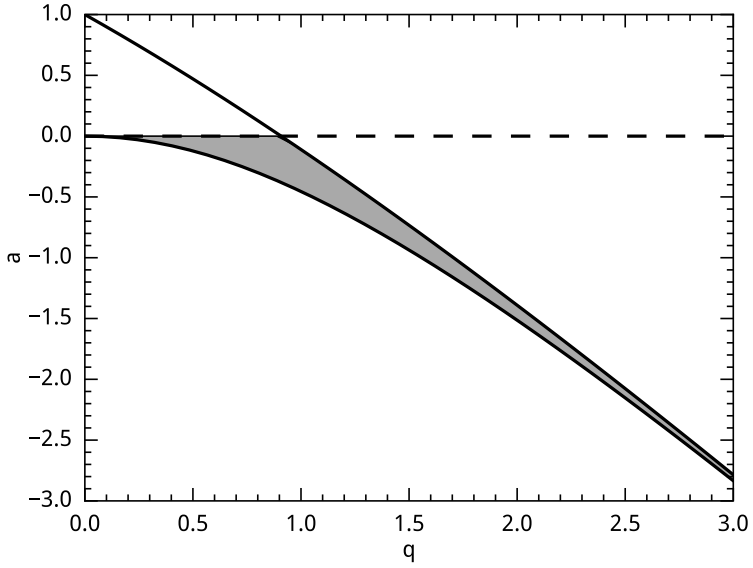


Figure 2.4: Stable $a$ and $q$ parameters for the linear Paul trap.

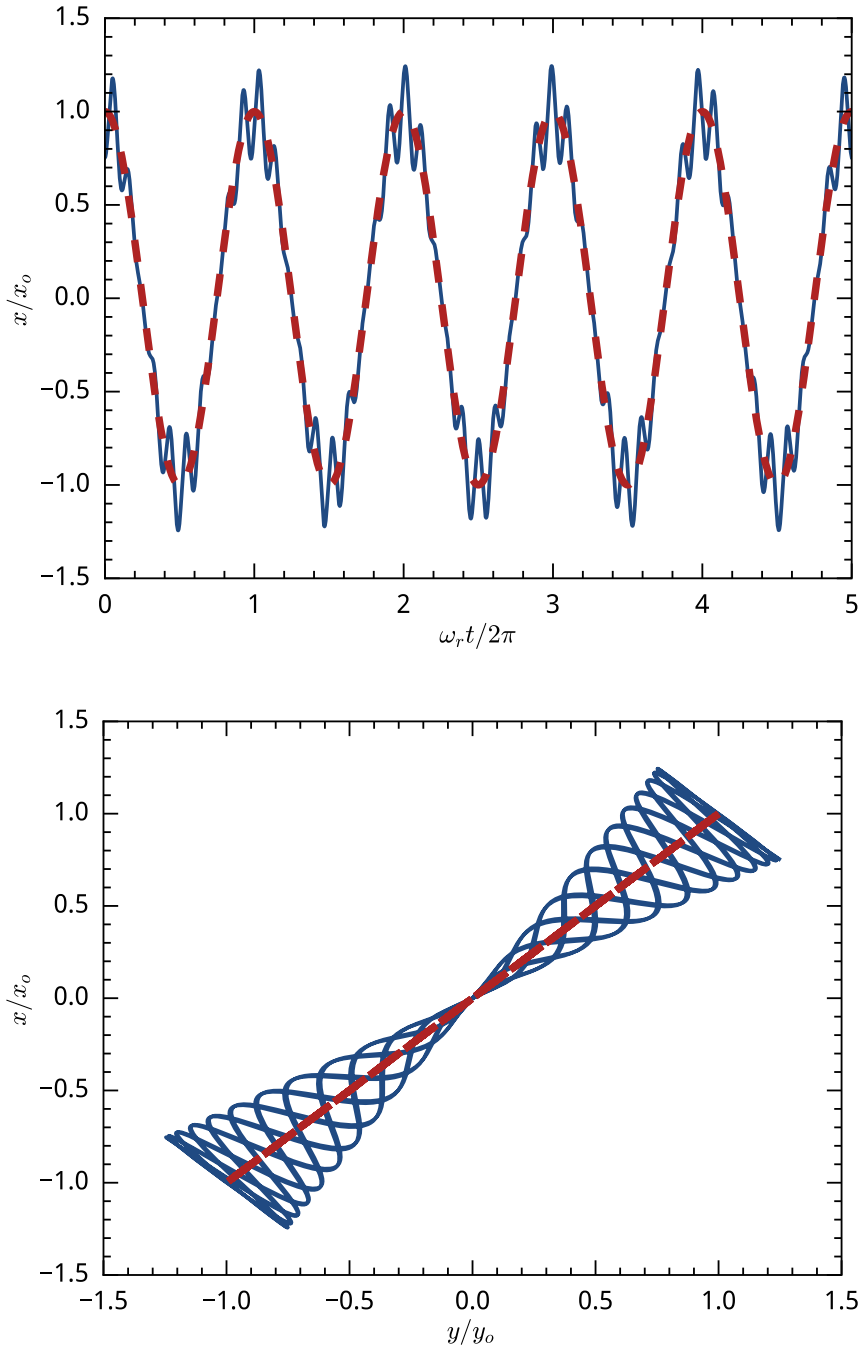


Figure 2.5: Blue: normalized motion with $q = .49$ and $a = -.023$. While $q \ll 1$ does not hold, these are typical trap parameters for single ion experiments. Red: purely secular motion. **Top:** x motion as a function of time. **Bottom:** x and y motions over the same time period.

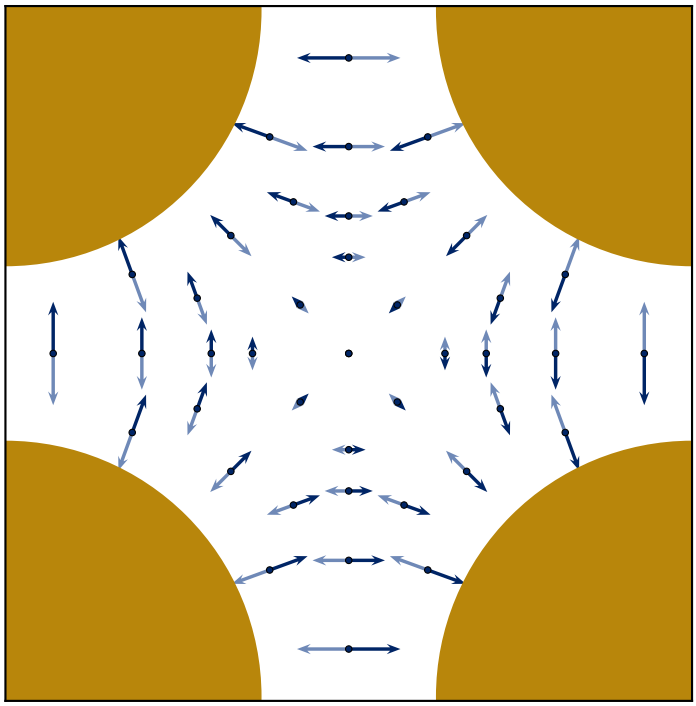

Figure 2.6: Looking along the trap axis, we see how micromotion increases as the ion moves away from the axis. Figure courtesy of Hans Harhoff Andersen [68].

## 2.2 Two-ion chains

So far we have only discussed a single ion in a trap, but we wish to trap two ions of different species at the same time, crystallized along the trap axis. Both the Coulomb potential between and the differing mass of the two ions add to the complexity of the system, resulting in 6 modes of motion, two axially and 4 radially, in contrast to the three from the single ion case. These motional modes are shown schematically in Figure 2.7.

### 2.2.1 Axial modes

The potential along the z-axis for a two singly-charged ion string in a harmonic trap is given by the sum of the harmonic potential and the Coulomb potential, producing [69]

$$V = \frac{1}{2}u_0(z_1^2 + z_2^2) + \frac{Q^2/4\pi\epsilon_0}{|z_2 - z_1|} \tag{2.12}$$

where $u_0 = \frac{2Q\kappa}{z_0^2}V_{end}$, and $z_1$ and $z_2$ are the ion positions along the axis.

By setting $\frac{\partial V}{\partial z_i}|_{z_i^{(0)}} = 0$, we can find the mass-independent equilibrium positions, given by [70]

$$-z_1^{(0)} = z_2^{(0)} = \left(\frac{Q^2/4\pi\epsilon_0}{4u_0}\right)^{\frac{1}{3}} \tag{2.13}$$

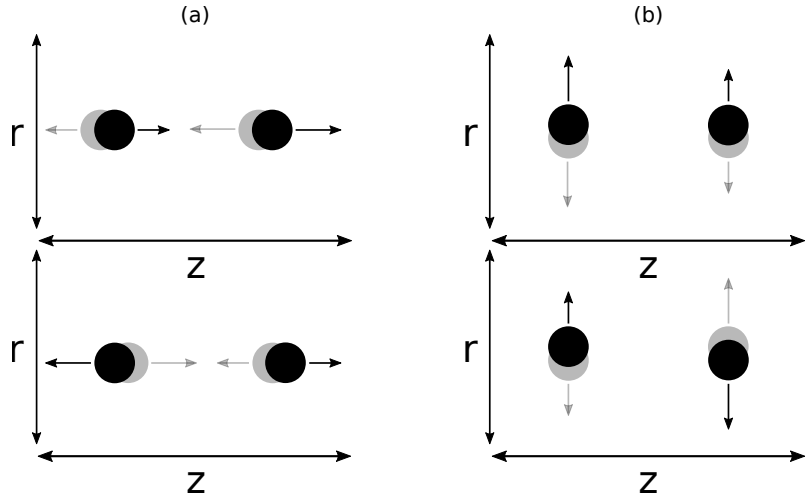


Figure 2.7: Motional modes of a two ion crystal, showing the axial modes in **(a)** and the radial modes in **(b)**. In both, the top figure shows the in-phase motion, and the bottom shows the out-of-phase motion.

which results in an equilibrium distance

$$z_{eq} = z_2^{(0)} - z_1^{(0)} = \left( \frac{2Q^2/4\pi\epsilon_0}{u_0} \right)^{\frac{1}{3}} \tag{2.14}$$

We are interested in small displacements of the ions from their equilibrium positions, so we Taylor-expand the Coulomb potential around them to second order. Defining the displacement from equilibrium $q_i = z_i - z_i^{(0)}$, the Lagrangian is given by

$$L = \frac{1}{2} \left[ \sum_{i=1}^{2} m_i \dot{q}_i^2 - \sum_{i,j=1}^{2} V_{ij} q_i q_j \right] \tag{2.15}$$

where $V_{ij}$ is the Taylor-expanded potential given by

$$V_{ij} = \frac{\partial^2}{\partial z_i \partial z_j} V(z_1, z_2)|_{\{z_i^{(0)}\}} \tag{2.16}$$

By changing into mass-weighted coordinates $q_i' = \sqrt{m_i} q_i$, we remove the mass-dependence of the kinetic energy. The potential energy can be rewritten as $V_{ij}' = \frac{V_{ij}}{\sqrt{m_i m_j}}$, and the equations of motion can be solved to find

$$\sum_{j=1}^{2} V_{ij}' \beta_j^{\alpha\prime} = \omega_\alpha^2 \beta_i^{\alpha\prime} \tag{2.17}$$

This describes two independent harmonic oscillator modes denoted by $\alpha$, whose oscillation frequencies are given by $\omega_\alpha$, and whose eigenvectors are given by $\beta^{\alpha\prime}$. We can calculate the oscillation frequencies to be

$$\omega_\pm^2 = \frac{u_0}{m_1} \left( 1 + \frac{1}{\mu} \mp \sqrt{1 + \frac{1}{\mu^2} - \frac{1}{\mu}} \right) \tag{2.18}$$

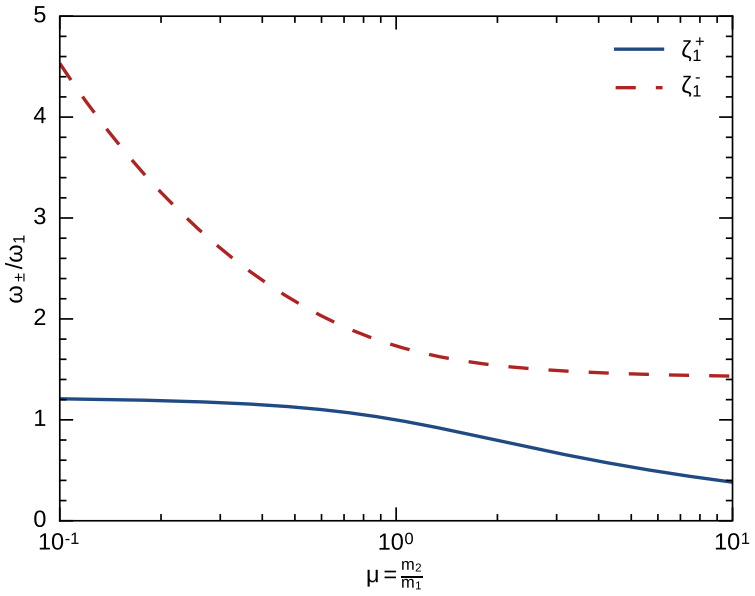


Figure 2.8: Frequencies of the in-phase and out-of-phase axial modes of a two ion crystal as a function of mass ratio, normalized to the axial frequency of a single ion of mass $m_1$.

where $\mu = \frac{m_2}{m_1}$. For ions of the same mass, $\omega_+$ describes the center-of-mass mode, and $\omega_-$ describes the breathing mode. In the general case, they describe the in-phase and out-of-phase modes, respectively.

Their eigenvectors are then found to be

$$\beta^{\pm\prime} = \frac{1}{\sqrt{1+r_\pm^2}}(r_\pm, 1) \tag{2.19}$$

where

$$r_\pm = \frac{-\mu + 1 \pm \sqrt{\mu^2 - \mu + 1}}{\sqrt{\mu}}$$

We can also define a normalized frequency,

$$\zeta_i^\pm = \frac{\omega_\pm}{\omega_i}$$

where $\omega_i = \sqrt{\frac{u_0}{m_i}}$ is the single ion axial frequency for ion of mass $m_i$ given by Equation 2.4, yielding the equations

$$\begin{aligned} \zeta_1^\pm &= \left(1 + \frac{1}{\mu} \mp \sqrt{1 + \frac{1}{\mu^2} - \frac{1}{\mu}}\right)^{\frac{1}{2}} \\ \zeta_2^\pm &= \sqrt{\mu}\zeta_1^\pm \end{aligned} \tag{2.20}$$

Figure 2.8 shows how the in- and out-of-phase normalized mode frequencies vary as a function $\mu$.

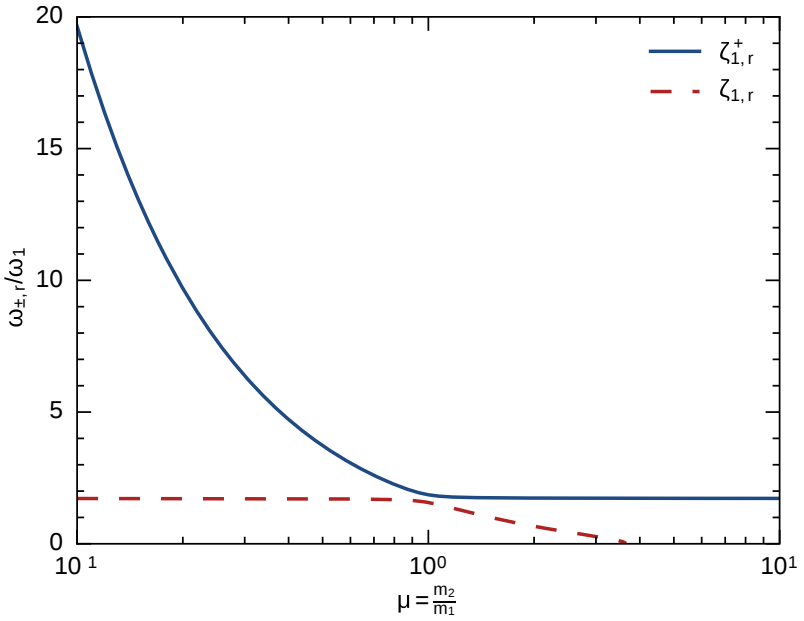


Figure 2.9: Frequency normalized to the single $m_1$ ion axial frequency, for the radial in- and out-of-phase modes with $\epsilon = 2$.

For ions of the same mass, the in-phase mode has eigenvectors of equal amplitude, and the out-of-phase mode has eigenvectors of opposite amplitude. These correspond to the center-of-mass (COM) and breathing modes, respectively. The COM mode frequency is equal to the single ion frequency, and the breathing mode frequency is given by $\omega_- = \sqrt{3}\omega_+$.

### 2.2.2 Radial modes

As with the axial modes, we find in- and out-of-phase modes in the radial direction as well. They can be calculated in a similar manner, where we find [71]

$$\omega^2_{r,\pm} = -\frac{(\mu + \mu^2 - \epsilon^2(1+\mu^2) \mp s)}{2\mu^2}\omega_1^2 \tag{2.21}$$

where $\omega_1$ is the axial frequency of ion 1, as before, where

$$s = \sqrt{\epsilon^4(\mu^2-1)^2 - 2\epsilon^2(1-\mu)^2\mu(1+\mu) + \mu^2(1+(\mu-1)\mu)} \tag{2.22}$$

and where $\epsilon^2 = -q_r^2/4a_r$

The eigenmodes are given by

$$\beta^{r,\pm\prime} = N\begin{pmatrix} 2\sqrt{\mu}\left(\omega_{r,\pm^2} - \frac{\epsilon^2}{\mu^2}\right) \\ 1 \end{pmatrix} \tag{2.23}$$

where $N$ is a normalization factor, such that norm of the vector is 1.

# Chapter 3

# Light-matter interactions

In our experiments, we use light fields in the form of lasers to address transitions between energy states in atomic and molecular ions, as well as couple these internal states to the external motional modes. The following section describes the basic physics behind these light-matter interactions for an ideal two-level atom in free space, a trapped two-level ion, and two trapped two-level ions.

## 3.1 Two-level atom in free space

The simplest picture of light interacting with an atom comes when we simplify our system to two levels split by energy $\hbar\omega_a$. We can label these two levels as the lower-energy ground state $|g\rangle$, and as the higher-energy excited state $|e\rangle$. The atomic Hamiltonian is thus written as

$$\begin{aligned} H_a &= \hbar\frac{\omega_a}{2}(|e\rangle\langle e| - |g\rangle\langle g|) \\ &= \hbar\frac{\omega_a}{2}\hat{\sigma}_z \end{aligned} \tag{3.1}$$

where $\hat{\sigma}_z = |e\rangle\langle e| - |g\rangle\langle g|$[1].

To understand the interaction between the light field and the atom, we must construct the Hamiltonian $H_i$ describing this interaction. It is simplest to first consider a monochromatic plane wave, defined as

$$E(z,t) = \frac{E_0}{2}\hat{\epsilon}[e^{-i(kz-\omega_L t+\phi)} + e^{i(kz-\omega_L t+\phi)}] \tag{3.2}$$

interacting with the atom. Here $E_0$ is the amplitude of the electric field, $\hat{\epsilon}$ is the polarization, $\omega_L$ is the frequency of the wave, $k = \omega_L/c$ is the wavenumber of the light, and $\phi$ is the phase of the light. Note that $|E_o|^2 = 2I/(\epsilon_o c)$ where $I$ is the intensity of the plane wave [72].

For a dipole transition, the coupling can be described by a simple dipole interaction:

$$H_i = -e\hat{z}\cdot E(z,t) \tag{3.3}$$

[1] I define my basis vectors as $|g\rangle = \begin{pmatrix}1\\0\end{pmatrix}$ and $|e\rangle = \begin{pmatrix}0\\1\end{pmatrix}$. That actually makes this the negative z-Pauli matrix, compared to the typical representation of the z-Pauli matrix. It does not change the physics, and is just a matter of notation. If I had defined my basis vectors the other way around, it would match the conventional z-Pauli matrix.

This Hamiltonian can be re-expressed in terms of the Pauli operators as

$$\begin{aligned} H_i &= \frac{\hbar}{2}\Omega_0 \left(|e\rangle\langle g| + |g\rangle\langle e|\right)\left[e^{-i(kz-\omega_L t+\phi)} + e^{i(kz-\omega_L t+\phi)}\right] \\ &= \frac{\hbar}{2}\Omega_0 \left(\hat{\sigma}_+ + \hat{\sigma}_-\right)\left[e^{-i(kz-\omega_L t+\phi)} + e^{i(kz-\omega_L t+\phi)}\right] \end{aligned} \tag{3.4}$$

where the vacuum Rabi frequency $\Omega_0$ is given by [73]

$$\Omega_0 = \frac{eE_0}{\hbar}\langle g|\hat{\epsilon}\cdot\hat{z}|e\rangle \tag{3.5}$$

for dipole allowed transitions. Note that we have made the dipole approximation by assuming that the electric field amplitude is constant over the extent of the electron wavefunction. For dipole-forbidden quadrupole transitions, $\Omega_0$ is approximately [74]

$$\Omega_0 = \frac{eE_0}{2\hbar}\langle g|(\hat{\epsilon}\cdot\hat{z})(\vec{k}\cdot\hat{z})|e\rangle \tag{3.6}$$

The total Hamiltonian for the system is given by

$$H = H_a + H_i \tag{3.7}$$

Since the atom is at rest, we can neglect $kz$ in $H_i$ as a complex phase. We can now transform into the interaction picture, in which $H_i$ transforms into

$$H_{i,I} = \frac{\hbar}{2}\Omega_0\left(\hat{\sigma}_+ e^{i\omega_a t} + \hat{\sigma}_- e^{-i\omega_a t}\right)\left[e^{i(\omega_L t+\phi)} + e^{-i(\omega_L t+\phi)}\right] \tag{3.8}$$

As long as the detuning of the light field $\delta = \omega_L - \omega_a$ is small compared to $\omega_L + \omega_a$, and $\Omega_0$ is small compared to $\omega_a$, we can neglect the fast rotating terms, in other words, make the rotating wave approximation, and simplify $H_I$ to

$$H_{i,I} = \frac{\hbar}{2}\Omega_0\left(\hat{\sigma}_+ e^{-i(\delta t+\phi)} + \hat{\sigma}_- e^{i(\delta t+\phi)}\right) \tag{3.9}$$

We can switch into a frame rotating with the detuning by making the unitary transformation $H' = UH_IU^\dagger - \hat{A}$ with $U = e^{\frac{i\hat{A}t}{\hbar}}$ and $\hat{A} = \frac{\hbar}{2}\delta\sigma_z$, yielding the Hamiltonian

$$H = \frac{\hbar}{2}\begin{pmatrix} \delta & \Omega \\ \Omega^* & -\delta \end{pmatrix} \tag{3.10}$$

where $\Omega = \Omega_0 e^{i\phi}$. We can now solve the Schrödinger equation to find that the population of the excited state as a function of time is given by

$$\rho_{ee}(t) = \frac{\Omega_0^2}{\Omega_0^2+\delta^2}\sin^2\left(\sqrt{\Omega_0^2+\delta^2}\frac{t}{2}\right) \tag{3.11}$$

assuming that the atom starts in the ground state. The sinusoidal behavior of the population over time shows how population is coherently transferred to and from the excited state. This is called Rabi flopping. At a time $t = \frac{\pi}{\Omega_0}$, called a $\pi$-pulse, we get full population transfer from the ground to the excited state for $\delta = 0$. After a $2\pi$-pulse, we have transferred population completely back down to the ground state. The time and frequency dependence of Equation 3.11 is depicted graphically in Figure 3.1.

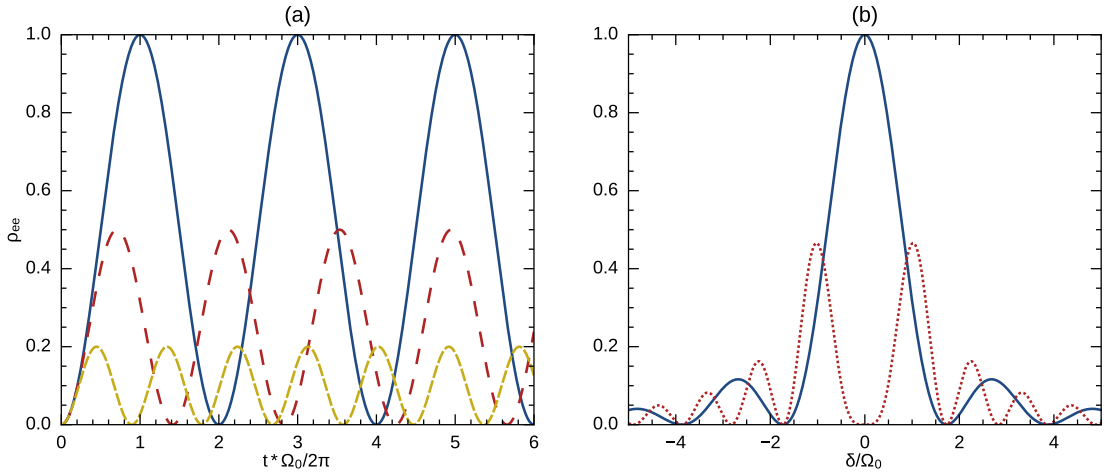


Figure 3.1: Excited state population as a function of **(a)**: time and **(b)**: detuning. In **(a)**, Rabi flopping for $\delta$ =0, $\delta = \Omega$ and $\delta = 2\Omega$. In **(b)**, the Rabi spectrum for a $\pi$-pulse, and for a $2\pi$-pulse.

### 3.1.1 Optical Bloch equations

In the picture discussed in the previous section, a fundamental feature of atomic transitions is missing: spontaneous emission. Spontanteous emisson is notably absent from a semi-classical picture of the interaction of light and atoms. If one quantizes the light field, spontaneous emission appears as the result of the atom interacting with vacuum fluctuations of the light field. For our purposes, however, it is sufficient to add spontaneous emission in a heuristic manner.

Let us start from the Hamiltonian presented in Equation 3.10. We wish to find the time evolution of the system when acted upon by this Hamiltonian (as briefly covered in the previous section). The density matrix describing a two-level atom is

$$\rho = \begin{pmatrix} \rho_{gg} & \rho_{ge} \\ \rho_{eg} & \rho_{ee} \end{pmatrix} \tag{3.12}$$

where the diagonal terms represent the population in the ground and excited states, and the off-diagonal terms are their coherences. The time evolution of this density matrix with the Hamiltonian is governed by the von Neumann equation, and results in

$$\frac{d}{dt}\begin{pmatrix} \rho_{gg} & \tilde{\rho}_{ge} \\ \tilde{\rho}_{eg} & \rho_{ee} \end{pmatrix} = -i\begin{pmatrix} \frac{1}{2}(\Omega\tilde{\rho}_{eg} - \Omega^*\tilde{\rho}_{ge}) & \delta\tilde{\rho}_{ge} + \frac{\Omega}{2}(\rho_{ee} - \rho_{gg}) \\ -\delta\tilde{\rho}_{eg} - \frac{\Omega^*}{2}(\rho_{ee} - \rho_{gg}) & -\frac{1}{2}(\Omega\tilde{\rho}_{eg} - \Omega^*\tilde{\rho}_{ge}) \end{pmatrix} \tag{3.13}$$

where $\tilde{\rho}_{ge} = \rho_{ge}e^{-i\omega_L t}$ and $\tilde{\rho}_{eg} = \rho_{eg}e^{i\omega_L t}$ due to the rotating frame.

We know that an atom undergoes spontaneous emission at a rate $\Gamma_a$. It is logical to insert this decay into the equations as a loss for $\rho_{ee}$ and a gain for $\rho_{gg}$ [72,75,76]

$$\dot{\rho}_{gg} = -\dot{\rho}_{ee} = \Gamma_a\rho_{ee} - \frac{i}{2}(\Omega\tilde{\rho}_{eg} - \Omega^*\tilde{\rho}_{ge}) \tag{3.14}$$

Spontaneous decay also contributes to a loss of coherence, and can be included as

$$\dot{\tilde{\rho}}_{ge} = \dot{\tilde{\rho}}^*_{eg} = (-\frac{\Gamma_a}{2} - \gamma_c - i\delta)\tilde{\rho}_{ge} - i\frac{\Omega}{2}(\rho_{ee} - \rho_{gg}) \tag{3.15}$$

where $\gamma_c$ is a rate associated with other coherence loss processes, for example collisions or fluctuations in $\omega_L$. Henceforth I will refer to $\gamma = \Gamma_a/2 + \gamma_c$. These equations are called the optical Bloch equations.

While Equation 3.11 showed the excited state population oscillating indefinitely, the addition of spontaneous decay and decoherence means that this will no longer be the case. While it is sufficient to use Equation 3.11 when $\Gamma_a \ll \Omega$, the optical Bloch equations become useful when we leave that regime.

If one excites the transition for a long time with a non-zero $\gamma$, $\rho_{ee}$ settles into steady state. Assuming $\gamma_c = 0$ [72,75,76]

$$\rho_{ee,ss} = \frac{\frac{\Omega^2}{4}}{\delta^2 + \frac{\Gamma_a^2}{4} + \frac{\Omega^2}{2}} \tag{3.16}$$

Defining the saturation parameter, $s$

$$s = \frac{I}{I_{sat}} = \frac{2\Omega^2}{\Gamma_a^2} \tag{3.17}$$

where $I_{sat} = I_{sat} = \frac{\pi}{3}\frac{hc}{\lambda^3}\Gamma_a$ is the saturation intensity, $\rho_{ee,ss}$ becomes

$$\rho_{ee,ss} = \frac{\frac{s}{2}}{1 + s + \left(\frac{2\delta}{\Gamma_a}\right)^2} \tag{3.18}$$

At zero detuning, in the limit that $s$ is large, increasing the intensity has no effect on the steady state population of $1/2$. This also gives rise to power broadening of the absorption, as the detuning must be larger and larger with increasing $s$ to have an impact on the steady state population.

When $\gamma_c \neq 0$.

$$\rho_{ee,ss} = \frac{\frac{\gamma}{2\Gamma_a}\Omega^2}{\delta^2 + \gamma^2 + \frac{\gamma}{\Gamma_a}\Omega^2} \tag{3.19}$$

### 3.1.2 Einstein A and B coefficients

In the case that an atom is driven by broadband radiation, $\Gamma_L >> \Gamma_a$ where $\Gamma_L$ is the width of the radiation, the time evolution of the states can be modeled by rate equations. The A coefficient provides the rate of spontaneous decay, and is equivalent to the linewidth of the transition. From the B coefficient one can calculate the rates of the absorption and stimulated emission as $R_{ge} = B_{ge}\rho(\omega)$, where $\rho(\omega)$ is the spectral energy density of the radiation. The Einstein B coefficients are given by

$$\begin{aligned} B_{eg} &= \frac{\pi^2 c^3}{\hbar \omega_{ge}^3} A_{eg} \\ B_{ge} &= \frac{g_e}{g_g} B_{eg} \end{aligned} \tag{3.20}$$

where $g_{g,e}$ are the degeneracies of the ground and excited states, and $\omega_{eg}$ is the splitting between the two states.

## 3.2 Trapped ion

The state of a harmonically trapped ion has components that come both from the energy levels intrinsic to the ion as well as from the secular motion[2] of the ion due to the trap. The intrinsic

[2]Because we generally focus only on axial motion, I will neglect micromotion in this section.

levels of the ion are, in the atomic case, the internal electronic states, and, in the molecular case, can be rotational, vibrational, or electronic energy levels. Whether working with an atomic or molecular ion, one often works in a regime where the transition can be considered as that of a two-level system as described in the preceding section. This two-level model is a good description in the limit where off-resonant coupling of the light field to other transitions is negligible, and the ion has a stable ground state.

The motion of the ion in the trap is that of a harmonic oscillator for which the oscillation frequency along the trap axis is given by $\omega_z$, as defined in Equation 2.4. The Hamiltonian for the ion is thus given by

$$H_0 = \hbar\omega_z \left(\hat{a}^\dagger \hat{a} + \frac{1}{2}\right) + H_a \tag{3.21}$$

where $\hat{a}$ and $\hat{a}^\dagger$ are the ladder operators associated with the harmonic motion of the ion in the trap. The total Hamiltonian is given by $H = H_0 + H_i$, where $H_i$ is given as before. The big difference is that now when we transform into the interaction picture, we cannot neglect $k\hat{z}$ in the plane wave, as

$$\hat{z} = \sqrt{\frac{\hbar}{2m\omega_z}}(a + a^\dagger) \tag{3.22}$$

where $m$ is the mass of the ion.

After transforming into the interaction picture, the Hamiltonian $H_i$ becomes $H_{i,I}$, given by

$$H_{i,I} = \frac{\hbar}{2}\Omega_0(\hat{\sigma}_+ e^{i\eta(\hat{a}_I + \hat{a}_I^\dagger)} e^{-i\delta t + \phi} + \text{h.c.}) \tag{3.23}$$

where $\eta$ is the Lamb Dicke parameter, $\hat{a}_I = \hat{a}e^{-i\omega_z t}$, and $\phi$ is a phase. Note that in obtaining this expression, the rotating wave approximation was made.

The Lamb Dicke parameter $\eta$ is the ratio of the extent of the ground state wavefunction of the ion in the trap to the wavelength of the incoming light, as well as the ratio of the recoil energy to the separation of the motional states. It describes how easily the absorption or emission of a photon can change the motional state of the ion. The expression for $\eta$ is

$$\eta = \vec{k} \cdot \vec{z}\sqrt{\frac{\hbar}{2m\omega_z}} \tag{3.24}$$

for single ions.

If $\eta^2(2n+1) \ll 1$, we can expand Equation 3.23 as

$$H_I = \frac{\hbar}{2}\Omega_0\hat{\sigma}_+(e^{-i\delta t} + i\eta(\hat{a}e^{-i(\omega_z+\delta)t} + \hat{a}^\dagger e^{i(\omega_z-\delta)t})) + \text{h.c.} \tag{3.25}$$

where we have set $\phi = 0$ for simplicity. This is called the Lamb Dicke regime. Physically, it describes the regime in which the extent of the wavefunction of the ion motion is much smaller than the wavelength of the light.

In this regime, if we adjust the frequency of the light field such that $\delta = 0$ and drop off-resonant terms, Rabi oscillations are driven between the ground and the excited state at the Rabi frequency $\Omega_0$ without change in the motional state. That is, we drive **carrier** transitions between $|g, n\rangle$ and $|e, n\rangle$, where $|n = 0\rangle$ denotes the motional ground state.

If $\delta = -\omega_z$, we drive first **red sideband** transitions between $|g, n\rangle$ and $|e, n-1\rangle$ at an approximate frequency of $\Omega_{n,s=-1} = \eta\sqrt{n}\Omega_0$, where $s = -1$ refers to the sideband order, which will be described shortly.

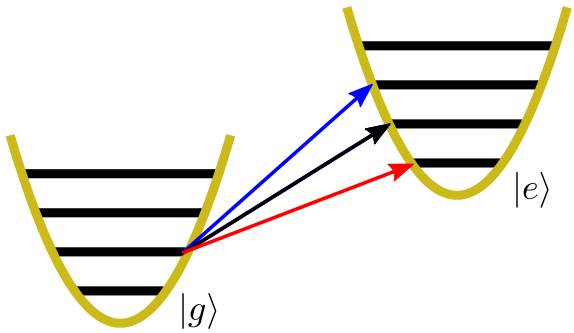


Figure 3.2: Schematic showing carrier (black), blue sideband (blue), and red sideband (red) transitions between the ground and excited state of a trapped two-level atom.

Finally, if we tune the light field to $\delta = \omega_z$, we drive **blue sideband** transitions between $|g,n\rangle$ and $|e,n+1\rangle$ at an approximate frequency of $\Omega_{n,s=1} = \eta\sqrt{n+1}\Omega_0$. These transitions are illustrated in Figure 3.2.

If the exponential were to be expanded to higher orders, we would see that there are higher order sidebands arising, at integer multiples of $\omega_z$. These higher order sidebands, with the $n^{th}$ order being denoted by $s = \pm n$ with a plus for blue and a minus for red, have a coupling strength $\Omega_{n,s}$ that approximately scales as $\eta^{|s|}$. The actual coupling strength is given by the matrix elements [77,78]

$$\Omega_{n,s} = \Omega_0 |\langle n|e^{i\eta(\hat{a}+\hat{a}^\dagger)}|n+s\rangle| \tag{3.26}$$

which results in

$$\Omega_{n,s} = \Omega_0 e^{-\frac{\eta^2}{2}} \eta^{|s|} \sqrt{\frac{n_<!}{n_>!}} L_{n_<}^{|s|}(\eta^2) \tag{3.27}$$

where $n_<$ denotes the lesser of $n$ and $n+s$, and $n_>$ denotes the greater of the two. $L_{n_<}^{|s|}$ is the generalized Laguerre polynomial.

In order to resolve the sidebands, both the natural linewidth $\Gamma$ of the transition and the linewidth $\Gamma_L$ of the light field must be much less than the spacing of the sidebands $\omega_z$. Another condition to resolve the sidebands is that $\Omega_0 \ll \omega_z$. This is to ensure that the transition is not power-broadened to a width comparable to the sideband spacing. Neglecting spontaneous decay, the excited state as a function of time tuned near a resonance (carrier or sideband) will evolve as

$$\rho_{ee}(t) = \frac{\Omega_{n,s}^2}{\Omega_{n,s}^2 + \delta_s^2} \sin^2\left(\sqrt{\Omega_{n,s}^2 + \delta_s^2}\frac{t}{2}\right) \tag{3.28}$$

where $\delta_s$ is the detuning from the resonance being addressed. This is the same Rabi flopping behavior as presented in Equation 3.11.

### 3.2.1 AC Stark shifts

Off-resonant coupling to transitions causes a shift in the levels involved, called AC Stark shifts, or light shifts. These shifts are most important when absorption is negligible. For light with an on-resonance Rabi frequency of $\Omega$, detuned by $\delta$, the shift for each level involved is

$$\Delta\omega = \pm\frac{\Omega^2}{4\delta} \tag{3.29}$$

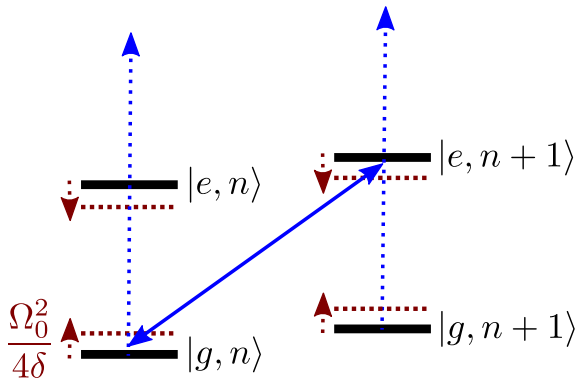


Figure 3.3: Off-resonant coupling on the carrier transition shifts the sideband transition. The solid blue arrow shows coupling on the blue sideband. This off-resonantly couples to the carrier, shown as dotted blue arrows, causing the levels to shift together.

where the plus is for the lower level, and the minus is for the upper level. This means that red-detuned light shifts the levels apart, and blue-detuned light shifts them together. This is important for a trapped ion because off resonant coupling on the carrier transition will shift the sideband transitions together. In this case, $\delta \simeq \omega_z$. The full shift of the transition on sideband $s'$ can be calculated as [79]

$$\Delta\omega = \sum_{s \neq s'} \frac{\Omega_{n,n+s}^2}{2\omega_z(s-s')} \tag{3.30}$$

where the unshifted transition frequency is given by $\omega_0 + s'\omega_z$. Note that these shifts are motional state dependent. It is generally sufficient to consider only the carrier coupling in the shift of first sidebands. This is shown schematically in Figure 3.3.

## 3.3 Two trapped ions

For the most part when we think about light-matter interactions with two trapped ions, we can consider having the same case as the single ion but now with two modes: the in-phase and the out-of-phase modes. We can replace $e^{i\eta(\hat{a}_I + \hat{a}_I^\dagger)}$ in Equation 3.23 by

$$\Pi_\alpha e^{i\eta^\alpha(\hat{a}_{\alpha,I} + \hat{a}_{\alpha,I}^\dagger)} \tag{3.31}$$

where as previously $\alpha$ denotes the modes[3]. In the first order expansion these two modes do not interact with one another so can be considered separately. If we expand to higher orders, we see that extra sidebands form at combinations of in- and out-of-phase modes. As such, we have 'sidebands on the sidebands,' and can have a sideband that excites $\Delta n_+ = 1$, but $\Delta n_- = -1$. Thus, out of the Lamb Dicke regime, the sideband structure becomes quite complex.

The two modes have different Lamb Dicke parameters, given by [69]

$$\eta_i^\pm = k|\beta_i^{\pm\prime}|\sqrt{\frac{\hbar}{2m_i\omega_\pm}} \tag{3.32}$$

[3]This is also how we could include the radial modes, if we so wished.

| | Carrier | Red sideband | Blue Sideband |
|---|---|---|---|
| $P(\downarrow\downarrow)$ | $\rho_{gg}^2$ | $\left(1-\frac{n}{2n-1}\left[1-\cos(g_r\eta_\pm\Omega_0 t)\right]\right)^2$ | $\left(1-\frac{n+1}{2n+3}\left[1-\cos(g_b\eta_\pm\Omega_0 t)\right]\right)^2$ |
| $P(\uparrow\downarrow)$ | $\rho_{ee}\rho_{gg}$ | $\frac{n}{2(2n-1)}\sin^2(g_r\eta_\pm\Omega_0 t)$ | $\frac{n+1}{2(2n+3)}\sin^2(g_b\eta_\pm\Omega_0 t)$ |
| $P(\uparrow\uparrow)$ | $\rho_{ee}^2$ | $\frac{n(n-1)}{(2n-1)^2}\left[1-\cos(g_r\eta_\pm\Omega_0 t)\right]^2$ | $\frac{(n+1)(n+2)}{(2n+3)^2}\left[1-\cos(g_b\eta_\pm\Omega_0 t)\right]^2$ |

Table 3.1: Population of different joint states as a function of time, for the carrier and sidebands [81,82]. Here, $g_b=\sqrt{\frac{2n+3}{2}}$ and $g_r=\sqrt{\frac{2n-1}{2}}$. These equations are valid for small $n$.

where $\beta_i^{\pm\prime}$ is given by Equation 2.19. These Lamb-Dicke parameters are dependent on which ion the transition is being driven.

The full expression for the Rabi frequency when driving a transition on ion $i$ is given by [80]

$$\begin{aligned}\Omega_{n_+,n_-,s_+,s_-}&\\ &=\langle n_+,n_-|\Pi_\alpha e^{i\eta^\alpha(\hat{a}_\alpha+\hat{a}_\alpha^\dagger)}|n_++s+,n_-+s_-\rangle\\ &=\Omega_0\Pi_\alpha e^{-\frac{\eta_i^{\alpha 2}}{2}}\eta_i^{\alpha|s_\alpha|}\sqrt{\frac{n_{\alpha<}!}{n_{\alpha>}!}}L_{n_{\alpha<}}^{|s_\alpha|}\left(\eta_i^{\alpha 2}\right)\end{aligned} \tag{3.33}$$

where $n_\pm$ is the motional occupation in the in- or out-of-phase mode, and $s_\pm$ is the sideband number for the corresponding mode. From this equation, we can see that the motional state of the one mode influences the Rabi frequency of the orthogonal mode, and the motion of both modes influences the carrier Rabi frequency.

A special situation occurs when we have two ions of the same species and isotope, and the light field interacts with both of them. In this special case, in the Lamb Dicke regime and in the interaction picture, the Hamiltonian becomes

$$\begin{aligned}H_I=&\frac{\hbar\Omega_1}{2}e^{i(\delta t-\phi_1)}\sigma_{1-}\left[1-i\eta_+\left(a_+e^{-i\omega_+t}+a_+^\dagger e^{i\omega_+t}\right)+i\eta_-\left(a_-e^{-i\omega_-t}+a_-^\dagger e^{i\omega_-t}\right)\right]\\ &+\frac{\hbar\Omega_2}{2}e^{i(\delta t-\phi_2)}\sigma_{2-}\left[1-i\eta_+\left(a_+e^{-i\omega_+t}+a_+^\dagger e^{i\omega_+t}\right)-i\eta_-\left(a_-e^{-i\omega_-t}+a_-^\dagger e^{i\omega_-t}\right)\right]+c.c.\end{aligned} \tag{3.34}$$

where $\Omega_i$ refers to the Rabi frequency on ion $i$ and $\phi_i$ refers to the phase of the light field on each ion. $\Delta\phi=\phi_2-\phi_1$ is given by the wavelength of the light compared to the separation between the ions. In the case of two ions, for notational reasons, it becomes easier to refer to the ground state as $|\downarrow\rangle$ and the excited state as $|\uparrow\rangle$.

Because the light field now interacts with both ions, there are four states that play a role in blue sideband excitation: $|\downarrow\downarrow,n\rangle$, $|\uparrow\downarrow,n+1\rangle$, $|\downarrow\uparrow,n+1\rangle$, $|\uparrow\uparrow,n+2\rangle$. If both ions have a blue sideband transition, then two quanta of motion will be added to the relevant mode.

Instead of the traditional Rabi formula as in Equation 3.28, we now have a different formulation dependent on which joint state we measure, and these formulas are tabulated in Table 3.1. These formulae take the assumption that $\Omega_1=\Omega_2=\Omega_0$.

# Chapter 4

# Cooling

In an ion trap, there are two regimes in which we cool in order to reach the ground state of motion. The first is the unresolved sideband regime, where $\omega_z \ll \Gamma_a$. In this regime, we employ Doppler cooling, where we take advantage of a high scattering rate to cool the ion from initially hot temperatures down to the Doppler limit. In this regime we can treat the problem in a semi-classical manner.

The second regime is the resolved sideband regime, where $\omega_z \gg \Gamma_a$. In this regime, we must consider the quantum characteristics of the ion motion. It is in this regime that we employ sideband cooling to cool down to the ground state of motion. Because it becomes challenging (and slow) to sideband cool far outside of the Lamb Dicke regime, Doppler cooling is used prior to sideband cooling.

In this chapter, I describe the theory of laser cooling (both Doppler and sideband) of a two-level ion in a trap. In addition, I describe the theory of ion heating due to electric field noise. The chapter ends with a discussion on motional state measurement and the definition of temperature.

## 4.1 Doppler cooling

Doppler cooling was first proposed by Hänsch and Schawlow [5] as well as by Wineland and Dehmelt in 1975 [90] and first implemented in ion traps by Wineland *et al.* [83] and by Neuhauser *et al.* [84], both in 1978. The basic idea of Doppler cooling is to use the Doppler effect to cool the ion(s). If an ion is moving with velocity $v$ toward a light source of frequency $\omega_L$, the atom will see the frequency of the light shifted, with the observed frequency

$$\omega_{obs} = \sqrt{\frac{1+\frac{v}{c}}{1-\frac{v}{c}}}\omega_L \tag{4.1}$$

For non-relativistic velocities, this simplifies to

$$\omega_{obs} \simeq 1 - \vec{k}\cdot\vec{v} \tag{4.2}$$

where $\vec{k}$ is the wavevector of the light. This is shown schematically in Figure 4.1

We take advantage of this effect by tuning the frequency of a monochromatic traveling wave to be red-detuned from an atomic transition of frequency $\omega_a$. When the ion moves towards the field, the field is Doppler shifted towards $\omega_a$, so the ion is more likely to absorb the light. Conversely, when it moves away from the field, the field is Doppler shifted away from $\omega_a$, and the ion is less likely to absorb the light. When the ion absorbs light, it will experience radiation pressure.

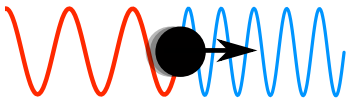

Figure 4.1: As the ion moves towards the cooling beam, it sees the light blue-shifted, and as it moves away, it sees it red-shifted. Thus, if the light is red-detuned from the transition frequency, the ion will be more likely to absorb it while moving towards it than away from it.

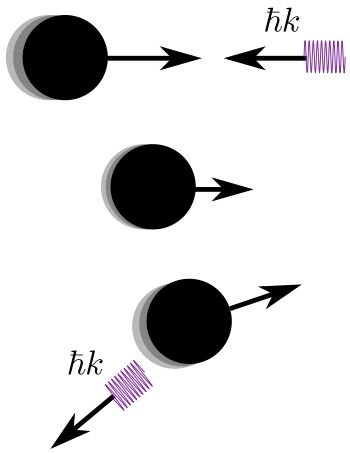


Figure 4.2: The ion moves towards a photon with momentum $\hbar k$. When the ion absorbs the photon, the momentum of the ion decreases by $\hbar k$. When the ion decays, it emits a photon in a random direction, causing the momentum of the ion to change accordingly. Because the emission direction is random but the absorbtion direction is fixed, the ion's momentum on average is changed in the propagation direction of the photon.

Given that absorption will more frequently reduce the velocity than increase it, the ion will be as a whole cooled.

When the ion then decays after absorption, it can emit in any direction. The minimum temperature the ion can reach is therefore limited by this random walk. In this section I will first discuss Doppler cooling in the axial direction, before moving on to more dimensions.

### 4.1.1 Axial cooling

Here I consider a simple picture of Doppler cooling, where there is no micromotion. This picture can be related to cooling along the trap axis, as the ion is confined axially by a static potential, and thus does not experience micromotion in the axial direction. This section is mainly based on the treatment of Doppler cooling in [73] and [85].

To set up the model, consider a two-level atom in the center of a trap being cooled along the axial direction, that is, a plane wave propagates along the trap axis ($z$-direction). When the atom absorbs a photon, it will gain momentum in the propagation direction of the wave

$$\Delta p = \hbar \vec{k} \tag{4.3}$$

This is shown in the first two steps of Figure 4.2.

When the atom then decays, another kick will be given to the atom, as shown in the last step of Figure 4.2. Since the radiation pattern is symmetric, the average change in momentum due

to spontaneous emission will be zero. This emission does contribute to the uncertainty in the velocity distribution of the ion, and I will come back to that fact later.

Because when Doppler cooling $\Gamma_a \gg \omega_z$, each scattering event can be considered as an instantaneous event, so occurring at a static velocity. As a result, the harmonic potential can be neglected in the light-matter interaction, and only considered as a parameter in the scattering probability.

We can thus calculate the average force on the ion as the result of absorption by multiplying the change in momentum $\Delta p$ by the scattering rate $\Gamma_a \rho_{ee}$

$$\frac{dp}{dt} \simeq F = \hbar k \Gamma_a \rho_{ee} \tag{4.4}$$

where $\rho_{ee}$ is the excited state population, given by Equation 3.16. This equation is dependent on the detuning, which for the ion is velocity dependent due to the Doppler effect. The effective detuning that the ion sees is given by

$$\delta_{eff} = \omega_{eff} - \omega_a = \delta - \vec{k} \cdot \vec{v} \tag{4.5}$$

where $\delta = \omega_L - \omega_a$ as previously. This effective detuning replaces the detuning in Equation 3.16, and the full equation for the average force is given by

$$F = \hbar k \Gamma_a \frac{s/2}{1 + s + \left(2(\delta - kv)/\Gamma_a\right)^2} \tag{4.6}$$

To understand what happens towards the end of Doppler cooling, it is helpful to take a first-order Taylor expansion of the force, such that it is linear in velocity. This is a good expression for the force for velocities where the Doppler broadening is small compared to the linewidth of the transition. This yields an equation of the form

$$F \simeq F_0 + \beta v \tag{4.7}$$

where $F_0$ is the constant force

$$F_0 = \hbar k \Gamma_a \frac{s/2}{1 + s + \left(2\delta/\Gamma_a\right)^2} \tag{4.8}$$

and $\beta$ is the frictional coefficient

$$\beta = \frac{8\hbar s k^2 \delta / 2\Gamma_a}{\left[1 + s + \left(2\delta/\Gamma_a\right)^2\right]^2} \tag{4.9}$$

A plot of $\beta$ is shown in Figure 4.3 (a) for two s parameters. We see that it is negative when $\delta$ is negative, and thus acts as viscous drag, damping the motion of the atom.

The cooling rate of the atom is given as the change in the energy in time, $Fv$, averaged over many cooling cycles

$$\dot{E}_c = \langle Fv \rangle = \beta \langle v^2 \rangle \tag{4.10}$$

since $\langle v \rangle = 0$ for harmonic motion.

Though this equation would indicate that there would be no limit to how far one could cool, we still need to consider the random walk in momentum space that the atom experiences as a result of two things: the randomness of the spontaneous emission, and the randomness associated with the absorption time. This random walk can be described with the Focker Planck equation [86], but qualitatively this means that the variance of the momentum is non-zero and is proportional to the number of scattering events.

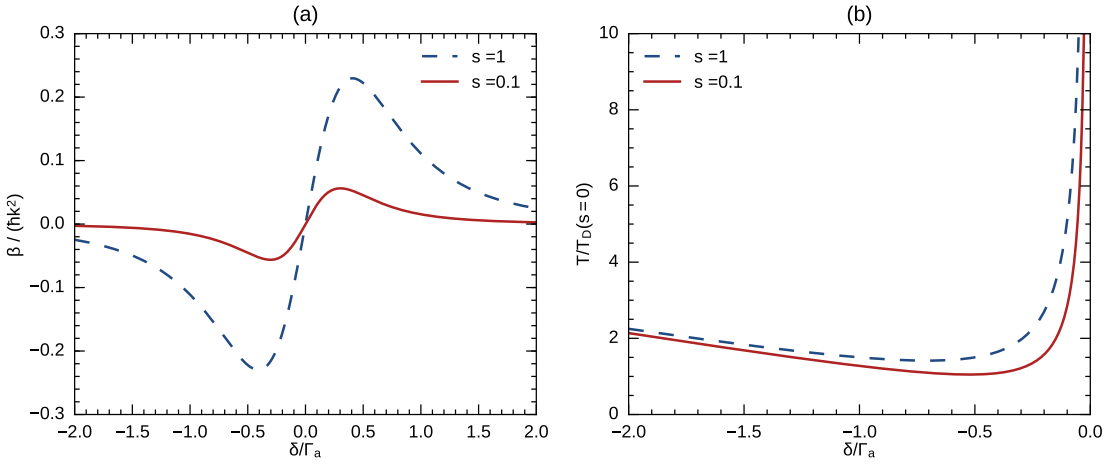


Figure 4.3: A plot of **(a)** $\beta$, defined in Equation 4.9 and **(b)** $T$, defined in Equation 4.13, normalized by $T_D(s=0)$. The drag is stronger for a higher saturation parameter, but the final temperature is likewise higher.

In the limit $s \ll 1$, the absorption and spontaneous emission processes will happen at the same rate, and thus their contribution to the increase in the momentum uncertainty will differ only by a factor dependent on geometry. For dipole transitions, this factor $\alpha = \frac{2}{5}$ and describes, based on the dipole radiation pattern, the likelihood that a kick is along the axis[1] [85].

At low velocities, the heating rate as a result of this random walk is given by

$$\dot{E_h} \simeq \frac{1}{2m}(\hbar k)^2 \Gamma_a (1+\alpha) \frac{s/2}{1+s+\left(2\delta/\Gamma_a\right)^2} \tag{4.11}$$

At equilibrium, $-\dot{E_h} = \dot{E_c}$, yielding

$$\langle v^2 \rangle = -\frac{1}{m}\frac{\hbar\Gamma_a}{8}(1+\alpha)\left((1+s)\frac{\Gamma_a}{2\delta} + \frac{2\delta}{\Gamma_a}\right) \tag{4.12}$$

The kinetic energy is given by $E_{kin} = \frac{1}{2}k_B T = \frac{1}{2}m\langle v^2 \rangle$, yielding an equilibrium temperature of

$$T = -\frac{\hbar\Gamma_a}{8k_B}(1+\alpha)\left((1+s)\frac{\Gamma_a}{2\delta} + \frac{2\delta}{\Gamma_a}\right) \tag{4.13}$$

The temperature is minimized with a detuning $\delta = -\frac{\Gamma_a\sqrt{1+s}}{2}$, yielding

$$T_D = \frac{\hbar\Gamma_a\sqrt{1+s}}{4k_B}(1+\alpha) \tag{4.14}$$

$T_D$ is thus the Doppler limit for the axial direction, cooling axially. For dipolar $\pi$ radiation, this limit reduces to

$$T_D = \frac{7\hbar\Gamma_a\sqrt{1+s}}{20k_B} \tag{4.15}$$

[1] This parameter $\alpha$ is actually only $\frac{2}{5}$ in a two-level system where the only decay path is that of $\Delta m = 0$ transition, in other words, a $\pi$ transition. $\alpha$ has different values for different systems [87]. For isotropic radiation, $\alpha = \frac{1}{3}$.

and for isotropic radiation ($\alpha = \frac{1}{3}$), it reduces to

$$T_D = \frac{\hbar\Gamma_a\sqrt{1+s}}{3k_B} \tag{4.16}$$

Figure 4.3 (b) shows Equation 4.13 plotted for $s = 1$ and $s = 0.1$. Comparing with Figure 4.3 (a), we see that closer to saturation, we get a higher drag, however, the minimum temperature is also higher. It should also be noted that we have not considered correlations between simulated emission and absorption, which become important when we are not much below saturation.

### 4.1.2 Cooling at an angle

To cool a single ion (or an axial chain) in all three directions, we must either use multiple cooling beams or use a single beam which has a projection onto all three oscillation directions. With the latter, in the unsaturated limit, the Doppler temperature in the $u$-direction is given by [87]

$$T_{D,u} = \frac{\hbar\Gamma_a}{4k_B}\left(1 + \frac{\alpha_u}{\hat{k_u}^2}\right) \tag{4.17}$$

where $\alpha_u$ gives the likelihood of momentum change in the $u$ direction, and $\hat{k}_u$ is the projection of the unit $k$-vector onto the $u$-direction. For isotropic radiation propagating 45° to all axes, the total average kinetic energy is minimized, yielding

$$T_{D,u} = \frac{\hbar\Gamma_a}{2k_B} \tag{4.18}$$

One other consideration is that we are no longer cooling in a direction with no micromotion. The presence of intrinsic micromotion causes the Doppler shift to have a time-dependence, and thus the cooling force is also time dependent. The effect of micromotion on Doppler cooling is particularly important for the cooling of Coulomb crystals when cooling in directions with components along the micromotion. In-depth treatments of the effect of micromotion on cooling can be found in [88] and [89].

## 4.2 Sideband cooling

Sideband cooling[2] is a cooling technique that allows the ion to be cooled much below the Doppler limit, to nearly the ground state of motion. It was first proposed by Wineland and Dehmelt in 1975 [90], and first implemented in the cooling of $^{198}Hg^+$ in 1988 [18].

In the regime where $\Gamma_a, \Omega_0 \ll \omega_z$, the motional sidebands of the ion become resolved, as described in section 3.2. By addressing the red sideband of the transition, we couple $|g, n+1\rangle$ to $|e, n\rangle$. From the excited state, the ion can decay either on the carrier or on one of the sidebands. Within the Lamb Dicke regime, a decay on the sidebands is much less likely than a decay on the carrier, as the probability scales with $n\eta^2$. Therefore, if we apply a $\pi$-pulse to the red sideband and then wait for a decay, the motional quantum number will most likely change by one, cooling the ion. One can picture this as falling down the staircase, as presented in Figure 4.4

[2]It should be clarified that when I refer to sideband cooling, I am referring to resolved sideband cooling. In fact Doppler cooling has been termed sideband cooling in the past, but generally these days when an ion trapper refers to sideband cooling, they mean resolved sideband cooling.

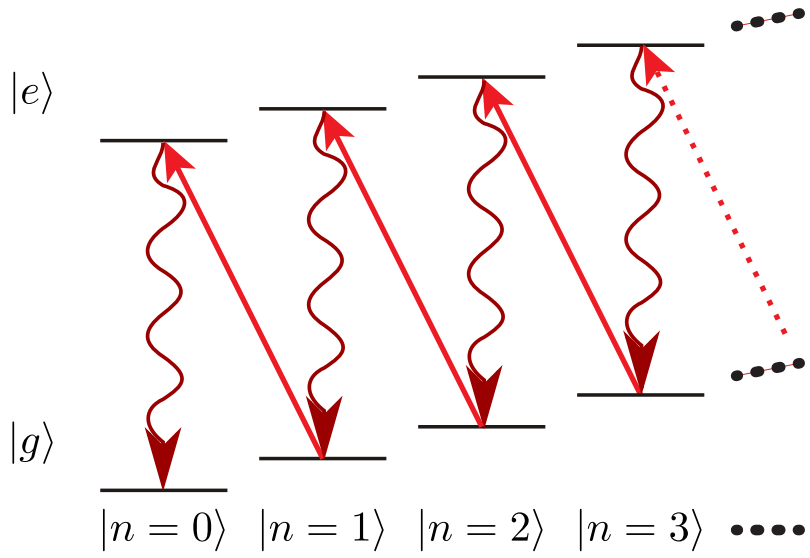


Figure 4.4: The ion is driven from the ground to the excited electronic state on a red sideband, losing a quanta of motion each step. The ion then decays to the ground electronic state, and the process is repeated until the ion sits in the ground state of motion and a sideband can no longer be driven.

It is natural to now ask the question, why not drive down on a blue sideband ($|e,n\rangle \rightarrow |g,n-1\rangle$), and not have to wait for a decay? The ion does not start out in a well defined motional quantum state. Rather, it starts in a thermal superposition with average motional quantum number $\bar{n}$ resulting from the Doppler limit and $\omega_z$ [78, 85]:

$$\bar{n} \simeq \frac{\Gamma}{2\omega_z} \tag{4.19}$$

Because the sideband Rabi frequency is dependent on the motional quantum number (see Equation 3.27), it is not possible to perform a $\pi$-pulse for every occupied state. In fact, you could be driving a $2\pi$-pulse instead. In this extreme case, by trying to 'drive down' on the blue sideband, you would actually increase the motional quantum number. It is necessary to have the spontaneous decay such that all information about the prior state is lost. Only then can we have cooling.

To understand sideband cooling of a two-level system, we consider a light field continuously driving the red sideband transition in the Lamb Dicke regime. Because decay is most likely on the carrier, each spontaneous emission results in a loss of a quanta of motion. This system can be described by rate equations, using the steady state population in conjunction with spontaneous emission to calculate the cooling rate [85]. The rate equations consist of two parts, shown in Figure 4.5: contributions which heat, $A_+$, and contributions which cool, $A_-$, given by

$$A_\pm = \eta^2 \Gamma_a \left(\alpha \rho_{ee}(\omega_z) + \rho_{ee}(\omega_z \mp \omega_z)\right) \tag{4.20}$$

where $\rho_{ee}$ is given by Equation 3.16. The first term in this equation corresponds to driving a carrier transition, and subsequently decaying on one of the sidebands: the red (increasing motional state) for plus terms, and the blue (decreasing the motional state) for minus terms. Because the laser field is resonant with the red sideband, the detuning of $\rho_{ee}$ is $\omega_z$.

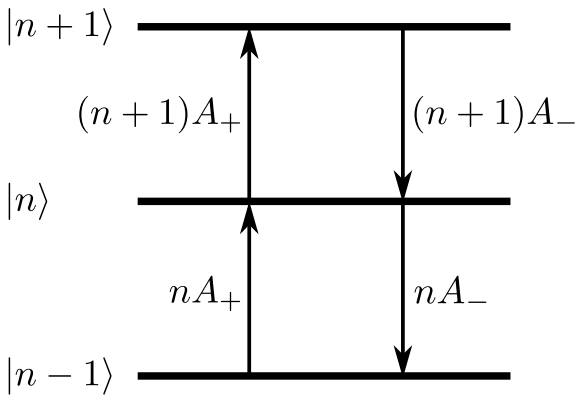


Figure 4.5: First order terms of the rate equation description of sideband cooling. Plus terms contribute to heating, and minus terms contribute to cooling. In the Lamb Dicke regime, the rates are proportional to the motional quantum number of the state. Figure inspired by [85].

The second term corresponds to driving sideband transitions. In the case of the plus term, it is off-resonant excitation on the blue sideband, with a decay on the carrier. For the minus term, it is resonant excitation on the red sideband with a decay on the carrier.

The factors of $n$ and $n+1$ in Figure 4.5 are related to the $n$-dependent Rabi frequency. The rate equations are formulated as [85]

$$\dot{P}(n) = (n+1)A_-P(n+1) - [(n+1)A_+ + nA_-]\,P(n) + nA_-P(n-1) \tag{4.21}$$

The solutions to these rate equations give that the steady state motional population is approximately equal to [85,91]

$$\bar{n}_{SS} = \frac{A_+ + \Gamma_h}{A_- - A_+} \tag{4.22}$$

where $\Gamma_h$ describes a heating rate due to other processes. In the unsaturated limit and assuming $\Gamma_h = 0$, this corresponds to

$$\bar{n} = \left(\frac{\Gamma_a/2}{\omega_z}\right)^2 (1 + \frac{\alpha}{4}) \tag{4.23}$$

which is much smaller than 1. This gives an approximate temperature limit of [85,92]

$$T_s = \frac{\hbar\omega_z}{\ln\left(\left(\frac{\omega_z}{\Gamma_a/2}\right)^2 (1+\frac{\alpha}{4})^{-1}\right)} \tag{4.24}$$

The harmonic oscillator energy is given by

$$E = \hbar\omega_z \left(\left(\frac{\Gamma_a/2}{\omega_z}\right)^2 (1 + \frac{\alpha}{4}) + \frac{1}{2}\right) \tag{4.25}$$

which is composed of the limit of the sideband cooling and the zero-point energy. Since $\Gamma_a \ll \omega_z$, we see that the zero-point energy dominates.

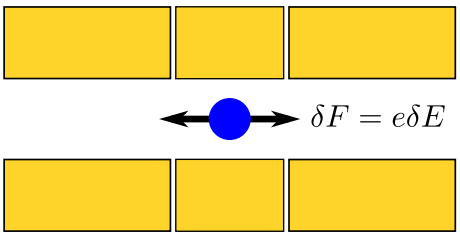


Figure 4.6: A fluctuating electric field exerts a fluctuating force on the ion.

## 4.3 Motional heating

During Doppler cooling, a random walk in phase space is responsible for the lower limit of the temperature. In sideband cooling, off-resonant scattering and unlikely decays on the sidebands are responsible for this lower limit. In Equation 4.22, I also presented an additional heating rate limiting the lower motional bound. This heating rate stems from the fact that any lab environment is non-ideal, and not only puts a lower bound on sideband cooled temperature, but dictates how long the ion stays cold once cooling stops. This dictates how long we can spend probing dynamics relying on well-prepared motional states.

Mode heating can occur as the result of unwanted oscillating electric fields (electric field noise) driving the motion of the ions. This electric field noise can come from a number of sources: technical noise, Johnson noise, fluctuating patch potentials, and more [93]. Regardless of electric field noise source, the physics of heating can be understood with a simple model, which I will cover in this section. In our experiments, we are primarily concerned with motion along the trap axis, and thus I will focus on heating along the trap axis. The first part will deal with heating of a single ion, and the second will deal with heating of two ions.

### 4.3.1 Single ion

The Hamiltonian of the trapped ion in the presence of an oscillating electric field is given by [93,94]

$$\hat{H} = \hat{H}_0 - \hat{H}_E \tag{4.26}$$

where $H_0$ is given in equation 3.21 and

$$\hat{H}_E(t) = e\delta E(t)\hat{z} = e\sqrt{\frac{\hbar}{2m\omega_z}}(\hat{a}^\dagger e^{i\omega_z t} + \hat{a}e^{-i\omega_z t})\delta E(t) \tag{4.27}$$

where $\delta E(t)$ is a fluctuating electric field. One can see how this affects the motional state of the ion, as the fluctuating electric field translates to a fluctuating force on the ion, as shown in Figure 4.6. The spectral density of the electric field (in units $(\mathrm{V/m})^2/\mathrm{Hz}$) is given by

$$S_E(\omega) = 2\int_{-\infty}^{\infty} d\tau \langle \delta E(\tau)\delta E(0)\rangle e^{-i\omega\tau} \tag{4.28}$$

Using first-order perturbation theory, the heating rate can be calculated for the simple case of increasing one quanta from $|n=0\rangle$ to $|n=1\rangle$ [80,95]

$$\begin{aligned}\Gamma_h &\simeq \frac{e^2}{2m\hbar\omega_z}\int_{-\infty}^{\infty}\delta\tau\langle\delta E(\tau)\delta E(0)\rangle e^{-i\omega_z\tau}|\langle 0|\hat{a}^\dagger + \hat{a}|1\rangle|^2 \\ &= \frac{e^2}{4m\hbar\omega_z}S_E(\omega_z)\end{aligned} \tag{4.29}$$

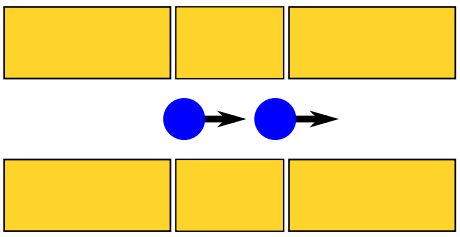

Figure 4.7: If the noise is perfectly spatially correlated, the two ions feel the same force, resulting in heating only of the center of mass.

Close to the ground state, the heating rate $\dot{\bar{n}} \simeq \Gamma_h$ [93, 96].

### 4.3.2 Two ion chains

As explained in section 2.2, chains of ions will have more than one mode of oscillation. The electric field noise will interact with these modes in different ways, depending both on the spatial properties of the noise over the two ions as well as the eigenvectors of the two modes.

The easiest case to think about is the case of two ions of identical mass. In this case, the in-phase mode consists purely of center-of-mass (COM) motion, and the out-of-phase mode has the same but opposite amplitudes, called the breathing mode. If the noise is perfectly spatially correlated, that is, is the same amplitude and phase on both ions, the COM motion will be excited. This is because both ions will be 'pushed' by the electric field in the same way. This is shown schematically in Figure 4.7. The breathing mode will, on the other hand, not be excited at all. If, on the other hand, the noise is perfectly spatially anti-correlated, the two ions will be pushed together and apart from one another, and the breathing mode yet not the COM mode will be excited. The assumption that the noise is spatially correlated is in general a good assumption when the ion-electrode distance is much larger than the ion-ion separation.

As the mass ratio $\mu$ changes from 1, the in-phase and out-of-phase modes become composed of both the COM and breathing modes. This means that both modes are then sensitive to spatially correlated noise. With the assumption that the noise is spatially correlated, we can write down an expression for the heating rate of each mode [97]

$$\dot{\bar{n}}_{\pm} \simeq \frac{e^2 S_E(\zeta_1^{\pm}\omega_1)}{4m_1\hbar\zeta_1^{\pm}\omega_1}\left(\beta_1^{\pm\prime} + \frac{\beta_2^{\pm\prime}}{\sqrt{\mu}}\right)^2 \tag{4.30}$$

where the eigenvectors $\beta'$ and the normalized frequencies $\zeta$ are as defined as in section 2.2.

With the assumption that the noise spectral density is white noise, we can normalize these heating rates to the heating rate of a single ion of mass $m_1$.

$$\frac{\dot{\bar{n}}_{\pm}}{\dot{\bar{n}}_1} = \frac{1}{\zeta_1^{\pm}}\left(\beta_1^{\pm\prime} + \frac{\beta_2^{\pm\prime}}{\sqrt{\mu}}\right)^2 \tag{4.31}$$

The normalized heating rates of the two modes are shown in Figure 4.8. For mass ratios close to one, the heating rate of the out-of-phase mode is much lower than that of the in-phase mode, as expected. As the modes become more and more mixed between COM and breathing motion, the heating rate of the out-of-phase mode increases. The asymmetry of the plot can be understood as a result of being normalized to a specific ion's axial frequency.

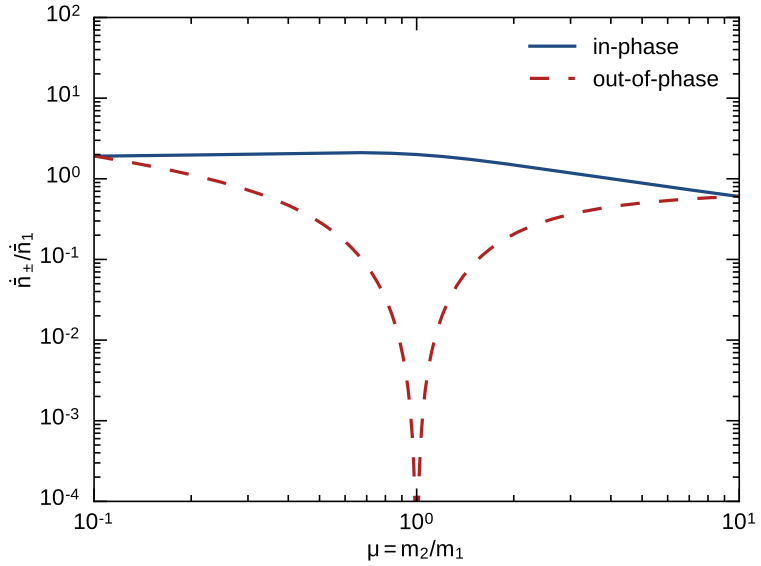


Figure 4.8: The heating rates of in- and out-of-phase modes in a two ion crystal with mass ratio $\mu = \frac{m_2}{m_1}$, normalized to the heating rate of a single ion of mass $m_1$, assuming a spatially-correlated white electric field noise spectral density.

Quantum logic spectroscopy (QLS), which will be covered in subsection 6.4.1, is one experimental procedure that we wish to implement. It is vital in this procedure that the ion stay cold during the course of the procedure. QLS as we intend to implement it will require that only one mode stay very cold during measurements. To demonstrate how much we gain in choosing one mode over the other for these experiments, Figure 4.9 shows the ratio between the out-of-phase and in-phase mode heating rates for a constant endcap voltage.

We can also understand the two-ion heating rate without assuming a white noise spectral density. If we know the heating rate of the single $m_1$ ion as a function of frequency, $\dot{n}_s(\omega)$, we can calculate the heating rates of the in- and out-of-phase modes as

$$\dot{n}_\pm(\omega_\pm) = \dot{n}_s(\omega_\pm)\left(\beta_1^{\pm\prime} + \frac{\beta_2^{\pm\prime}}{\sqrt{\mu}}\right)^2 \tag{4.32}$$

This means that the single ion heating rate at the same frequency is modified only by a scaling dependent on the mass ratio and mode. Figure 4.10 shows $\dot{n}_\pm(\omega_\pm)/\dot{n}_s(\omega_\pm)$ as a function of $\mu$. Note that this is a comparison at the same frequency, and that $\omega_z$, $\omega_+$, and $\omega_-$ do not all have the same frequency at the same trap parameters.

## 4.4 Motional state measurement

It is necessary to have diagnostic tools to be able to quantitatively determine how cold the ion is. The method we most commonly employ to determine the motional state of our ions is the sideband strength comparison method. The basic idea of this method depends on the fact that when the ion sits in the ground state, it cannot couple on the red sideband. Therefore, the only

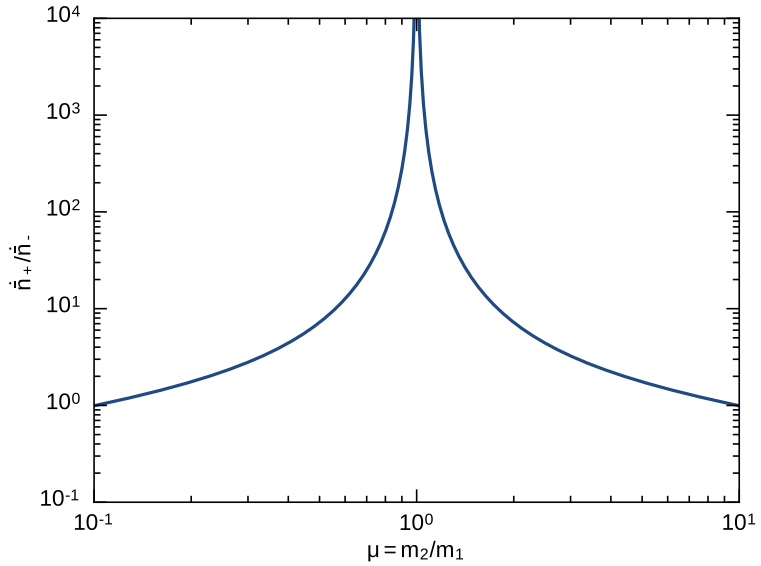


Figure 4.9: The ratio of the in- and out-of-phase heating rates of a two-ion crystal as a function of mass ratio $\mu = \frac{m_2}{m_1}$, assuming a white electric field noise spectral density. The gain from using the out-of-phase mode versus the in-phase mode for quantum logic spectroscopy decreases as $\mu$ changes from 1.

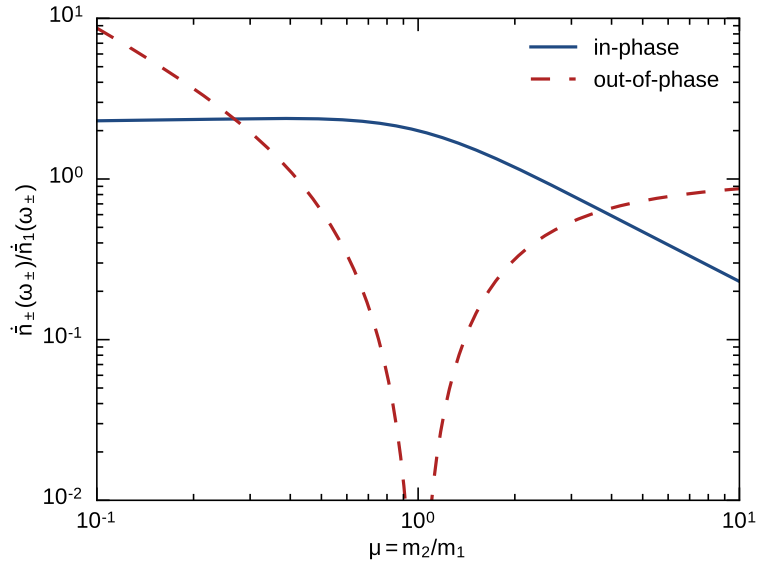


Figure 4.10: Plotted are the scaling factors relating the heating rates of the in- and out-of-phase modes to the rate of a single ion at the same frequency, given by Equation 4.32.

excitation seen on the red sideband will be due to population not in the ground state. By comparing the heights of the two sidebands, we can extract the average motional quantum number of the ion

We start with the assumption that after sideband cooling the ion, it is thermally distributed according to the Boltzmann distribution. This yields the probability to be located in a specific $n$-state

$$P_n = \frac{\bar{n}^n}{(\bar{n}+1)^{n+1}} \tag{4.33}$$

If the ion is initially in the ground state and the light field is on resonance, the population of the blue sideband evolves as

$$\rho_{bsb} \simeq \sum_{n=0}^{\infty} P_n \sin^2\left(\sqrt{n+1}\eta\Omega\frac{t}{2}\right) \tag{4.34}$$

The population of the red sideband, on the other hand, will evolve as

$$\rho_{rsb} \simeq \sum_{n=1}^{\infty} P_n \sin^2\left(\sqrt{n}\eta\Omega\frac{t}{2}\right) \tag{4.35}$$

We can rewrite the sum on the red sideband as

$$\rho_{rsb} \simeq \sum_{n=0}^{\infty} \frac{\bar{n}}{\bar{n}+1} P_n \sin^2\left(\sqrt{n+1}\eta\Omega\frac{t}{2}\right) \tag{4.36}$$

which means that the ratio between the two sidebands gives

$$\frac{\rho_{rsb}}{\rho_{bsb}} = \frac{\bar{n}}{\bar{n}+1} \tag{4.37}$$

Finally, this means that

$$\bar{n} = \frac{\rho_{rsb}}{\rho_{bsb} - \rho_{rsb}} \tag{4.38}$$

It should be stressed that Equation 4.38 is only correct if the ion's motional distribution is thermal.

### 4.4.1 Two ions

For two ions of different species, the motional state measurement can be carried out for each mode individually using the same technique as the single ion[3]. If we have two ions of the same species, and the field interacts with both of them, the measurement of the motional state must be modified based on the equations in Table 3.1. The modified measurement is done by considering the ratio of $P_{rsb}(\uparrow\uparrow)$ and $P_{bsb}(\uparrow\uparrow)$.

For a thermal distribution

$$P_{rsb}(\uparrow\uparrow) \simeq \sum_{n=2}^{\infty} P_n \frac{n(n-1)}{(2n-1)^2}\left[1-\cos(g_r\eta_{\pm}\Omega_0\frac{t}{2})\right]^2 \tag{4.39}$$

and

$$P_{bsb}(\uparrow\uparrow) \simeq \sum_{n=0}^{\infty} P_n \frac{(n+1)(n+2)}{(2n+3)^2}\left[1-\cos(g_b\eta_{\pm}\Omega_0\frac{t}{2})\right]^2 \tag{4.40}$$

[3]Assuming no coupling between the modes, the thermal distribution of each can be determined independently of the other. While there will be two sums of thermal distributions for determining the sideband height, the sum over the distribution of the mode not being measured appears equally in each sideband, and thus cancels. See Appendix C.3.

As in the single ion case, we can shift the sum of the red sideband probability, but in this case by two. Taking the ratio of these probabilities, we obtain

$$\frac{P_{rsb}(\uparrow\uparrow)}{P_{bsb}(\uparrow\uparrow)} = \left(\frac{\bar{n}}{\bar{n}+1}\right)^2 \tag{4.41}$$

and thus

$$\bar{n} = \frac{\sqrt{P_{rsb}(\uparrow\uparrow)}}{\sqrt{P_{bsb}(\uparrow\uparrow)} - \sqrt{P_{rsb}(\uparrow\uparrow)}} \tag{4.42}$$

This is a similar expression to Equation 4.38, but we are much less sensitive to small $\bar{n}$, as population in $|\downarrow\downarrow, n = 1\rangle$ cannot contribute to $P_{rsb}(\uparrow\uparrow)$.

### 4.4.2 Temperature

Often when we are evaluating cold-ion results, we talk about temperature. But how is temperature defined, especially for a trapped ion in a room temperature environment? What does it mean if I say an ion mode is sub-millikelvin or sub-microkelvin?

In this thesis, when I talk about the temperature of the sideband-cooled single ion, we are generally talking about the temperature of the axial mode with the assumption that the population of this mode is Boltzmann distributed between the harmonic levels. This means that the probability $P_n$ of finding the ion in a specific $n$ state is determined by the Boltzmann distribution

$$P_n = \frac{e^{\frac{-E_n}{k_B T}}}{Q} \tag{4.43}$$

where $Q$ is the partition function of a quantum harmonic oscillator. Inserting $Q$ and solving for $T$ gives

$$T = \frac{-\hbar\omega_z}{k_B \log(1 - P_0)} \tag{4.44}$$

This also applies to talking about the axial temperature of one of the modes of a two-ion crystal. In terms of the average motional occupation number $\bar{n}$, $P_n$ is given by

$$P_n = \frac{\bar{n}^n}{(\bar{n}+1)^{n+1}} \tag{4.45}$$

In literature there are other ways of defining temperature of a single ion. One other popular way to define temperature in the axial direction is as

$$\frac{1}{2}k_B T = E_{kin} \tag{4.46}$$

and is really just a way of describing the kinetic energy of the ion. This is useful for describing non-thermal distributions or zero-point kinetic energy in terms of a 'temperature.'

# Part II

# Ions in Aarhus

# Introduction

As mentioned in the Introduction, in order to study a single molecular ion, we co-trap them with a single atomic ion. In the experiments in Aarhus, we wish to study the molecular ion $^{24}MgH^+$ by sympathetically cooling it by cooling $^{40}Ca^+$. $^{40}Ca^+$ and $^{24}MgH^+$ are not, however, two-level ions. Thus the cooling methods are more complex than those described in the previous section, though the basic physics still applies.

This part consists of two chapters which describe the cooling and detection of these ions. Chapter 5 describes how we apply the methods of Doppler and sideband cooling of Chapter 4 to a real multilevel ion like $^{40}Ca^+$, and gives experimental results for these cooling methods. Further, it explains how in practice we can detect the internal state of $^{40}Ca^+$.

Chapter 6 discusses how cooling and detection of $^{24}MgH^+$ will be accomplished. The cooling methods include cooling of both internal and external degrees of freedom, with the internal degrees of freedom primarily cooled by direct interaction with $^{24}MgH^+$, and with the external degrees of freedom cooled sympathetically by $^{40}Ca^+$. Finally, it discusses how we will implement the detection of transitions in $^{24}MgH^+$.

# Chapter 5

# Cooling and detection of $^{40}Ca^{+}$

## 5.1 $^{40}Ca^{+}$ structure

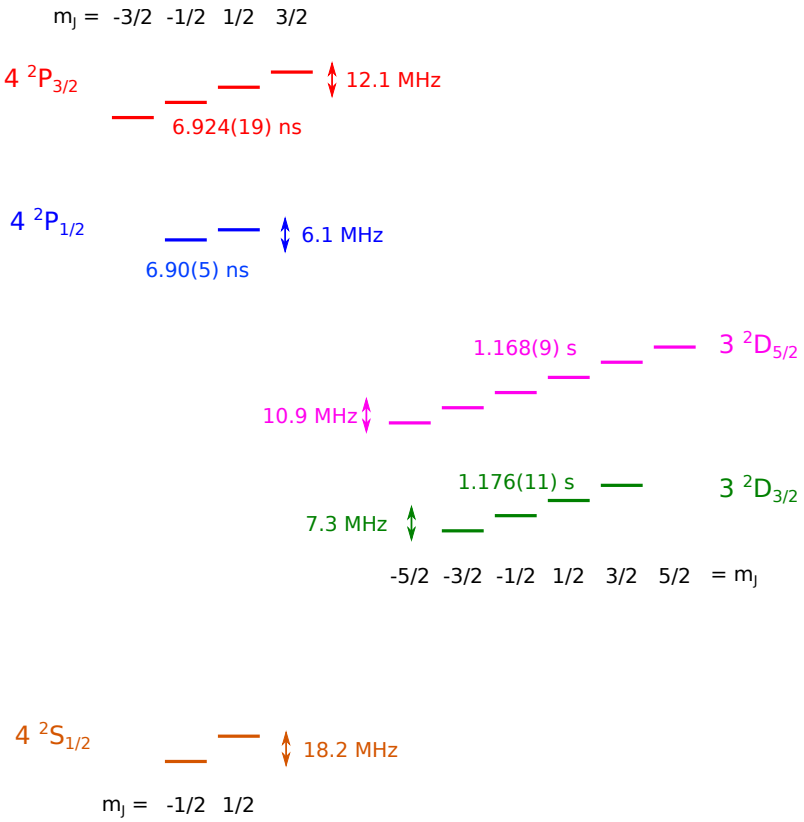


Figure 5.1: Level structure of $^{40}Ca^{+}$, showing lifetimes and Zeeman splittings of the fine structure. The Zeeman splittings are calculated for a magnetic field of 6.5 G, which is a typical field in our experiment.

As can be seen from Figure 5.1 , $^{40}Ca^{+}$ is not a two-level atom. It has S, P, and D levels, which undergo fine structure splitting. Full state, transition, and lifetime data along with references can

| State | $m_J$ | $\frac{d\nu}{dB}$[MHz G$^{-1}$] |
|---|---|---|
| $^2S_{1/2}$ | $\pm 1/2$ | $\pm 1.40$ |
| $^2P_{1/2}$ | $\pm 1/2$ | $\pm 0.47$ |
| $^2P_{3/2}$ | $\pm 1/2$ | $\pm 0.93$ |
| | $\pm 3/2$ | $\pm 2.80$ |
| $^2D_{3/2}$ | $\pm 1/2$ | $\pm 0.56$ |
| | $\pm 3/2$ | $\pm 1.68$ |
| $^2D_{5/2}$ | $\pm 1/2$ | $\pm 0.84$ |
| | $\pm 3/2$ | $\pm 2.52$ |
| | $\pm 5/2$ | $\pm 4.20$ |

Table 5.1: Zeeman splittings in MHz G$^{-1}$ for the levels in in the $^{40}Ca^{+}$ ion.

be found in Appendix A.

In the presence of a magnetic field, the fine structure of $^{40}Ca^{+}$ undergoes additional Zeeman splitting. The Zeeman splitting arises due to the interaction of the magnetic moment due to the electron's angular momentum with a magnetic field. At low fields, the Zeeman splitting is given by

$$\Delta E = \mu_B g_J B m_J \tag{5.1}$$

where $\mu_B$ is the Bohr magneton $\mu_B = \frac{e\hbar}{2m_e}$ and where $g_J$ is the Landé g-factor, expressed as

$$g_J \simeq \frac{3}{2} + \frac{S(S+1) - L(L+1)}{2J(J+1)} \tag{5.2}$$

The direction along which B points defines the quantization axis for the ion, which in our experiment is perpendicular to the z-axis and 45° to the x and y axes. A table of frequency shifts per Gauss, $\frac{d\nu}{dB}$, for each level is given in Table 5.1.

## 5.2 Doppler cooling and fluorescence detection

To produce $^{40}Ca^{+}$, an atom oven of Ca is heated to about 570 K and the atoms form an effusive beam, out of which they are photoionized (see section 7.5). To bring these ions at 570 K down to mK temperatures, we perform Doppler cooling.

The scheme for Doppler cooling in $^{40}Ca^{+}$ is presented in Figure 5.2. Doppler cooling is performed on the 397 nm dipole-allowed $^2S_{1/2} \rightarrow {}^2P_{1/2}$ transition. This transition has a linewidth $\Gamma/(2\pi) = 21.57(15)$ MHz [98], which is much larger than our typical axial frequencies of less than 1 MHz, and thus suitable for the Doppler cooling regime. For a cooling beam propagating at 45° to all trap axes, the Doppler temperature in the z-direction $T_{D_z} \simeq 0.5$ mK, as calculated from Equation 4.18.

The $^2S_{1/2}$ and $^2P_{1/2}$ do not form a two-level system, as $^2P_{1/2}$ state has another decay channel to the $^2D_{3/2}$ state. While decay to the $^2S_{1/2}$ state dominates with a branching ratio of 0.94 [99], the $^2D_{3/2}$ state has a long lifetime of 1.2 s compared to the 6.9 ns lifetime of the $^2P_{1/2}$ state, which means that if the ion falls into this state, the scattering (and thus cooling) rate is reduced by nearly 9 orders of magnitude, effectively halting cooling. To prevent the ion from getting stuck in the $^2D_{3/2}$ state during Doppler cooling, a laser at 866 nm serves to repump out of the $^2D_{3/2}$ level back to the $^2P_{1/2}$ level, where it can decay back to the $^2S_{1/2}$ level.

In addition to decay to other fine structure levels, we must take into account the Zeeman splitting of the $^2S_{1/2}$ and $^2P_{1/2}$ levels. We typically work at magnetic fields of 6.5 G. This results in a

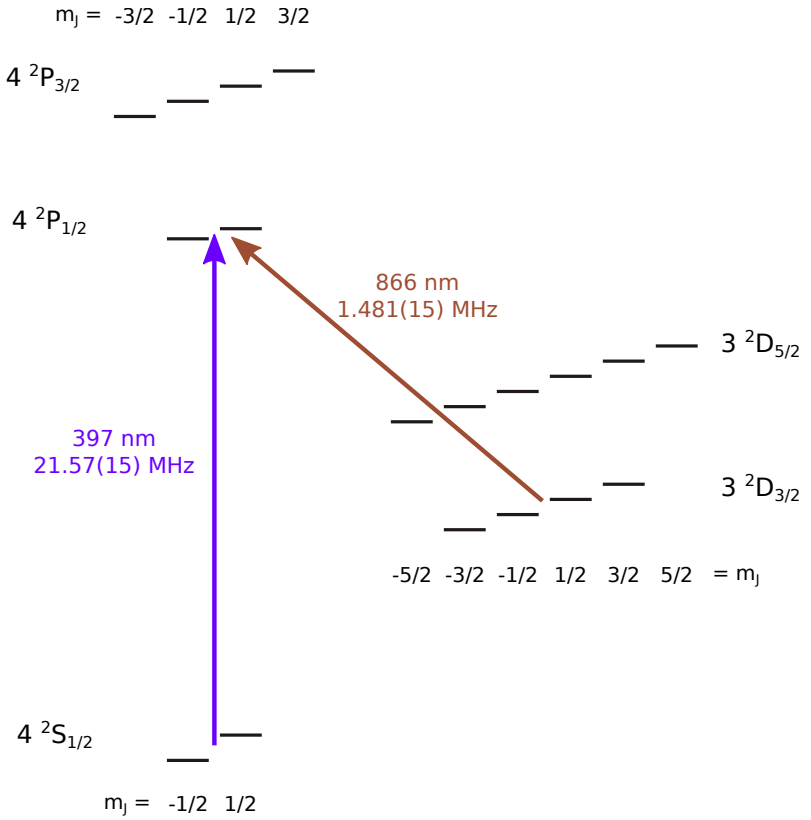


Figure 5.2: The Doppler cooling system in $^{40}Ca^{+}$. A light field at 866 nm is used to pump out of the $^2D_{3/2}$ state to close the cooling cycle, creating an effective 2-level system. The listed frequencies give the linewidth $\Gamma$ of the transition.

splitting of 18.2 MHz of the $^2S_{1/2}$ state, and a splitting of 6.1 MHz of the $^2P_{1/2}$ state. $\Delta m_J = \pm 1$ transitions (driven by $\sigma$-polarized light[1]) and $\Delta m_J = 0$ (driven by $\pi$-polarized light) will have different transition frequencies. Table 5.2 summarizes the shift of the transition frequency between different $m_J$ from the unperturbed transition frequency. We can see that if we choose to use $\sigma$-polarized light for Doppler cooling, the difference between the two transition frequencies will be 24.4 MHz. This is broader than the transition linewidth, and thus a bad choice. We instead cool using $\pi$-polarized light, whose transitions have a separation of 12 MHz. This Zeeman splitting effectively broadens the transition[2], bringing the Doppler temperature closer to $T_{D_z} = 0.75$ mK.

The polarization of the 866 nm laser is also important. With $\pi$-polarized light, it cannot drive transitions from the $^2D_{3/2}$, $m_J = \pm 3/2$ levels, so they would be dark. Additionally, in the absence of a magnetic field (or with the wrong field), dark states can form even using $\sigma$-polarized light [100]. We use a combination of light polarized at 45° to the quantization axis and magnetic fields to destabilize the dark states.

[1] $\sigma$-polarized light here refers to linearly-polarized light with a polarization perpendicular to the quantization axis, which in this case is the magnetic field. This polarization drives both $\Delta m = \pm 1$ transitions. $\sigma_{+(-)}$ light refers to circularly-polarized light propagating along the quantization axis, which drives $\Delta m_J = +(-)1$, $|g\rangle \rightarrow |e\rangle$ transitions. $\pi$-polarized light refers to light polarized parallel to the quantization axis, which drives only $\Delta m_J = 0$ transitions

[2] The width of the transition is more complicated than this. First, this is no longer a Lorentzian. Second, the powers of both the 397 nm and 866 nm lasers will contribute to the actual width.

| $^2S_{1/2}$ | $^2P_{1/2}$ | $\Delta\omega/(2\pi)$ [MHz] |
|---|---|---|
| -1/2 | -1/2 | 6.0 |
| -1/2 | 1/2 | 12.2 |
| 1/2 | -1/2 | $-12.2$ |
| 1/2 | 1/2 | $-6.0$ |

Table 5.2: Change of the transition frequency from the unperturbed frequency due to Zeeman splitting for transitions between different $m_J$ for Doppler cooling.

Since the Doppler cooling transition has a high scattering rate, it is also possible to use it for fluorescence detection. The scattered 397 nm photons are collected into an imaging system (see section 7.3), and the ions are imaged using a CCD camera. Thus, we can tell whether or not the $^2S_{1/2} \rightarrow {}^2P_{1/2}$ and $^2D_{3/2} \rightarrow {}^2P_{1/2}$ are being driven based on whether or not we can see the ion.

In practice, we employ two different steps of Doppler cooling: one at higher intensity, sufficient for fluorescence detection, and one at lower intensity, to reach the Doppler limit and avoid imparting a kick on the ion due to fast turn-off of the radiation pressure. Currently, the total Doppler cooling time used in our experiments is 2 ms.

## 5.3 Sideband cooling

The $^2S_{1/2} \rightarrow {}^2D_{5/2}$ transition is a dipole-forbidden quadrupole transition at 729 nm. This transition is ideal for sideband cooling due to its sub-Hertz linewidth[3]. The condition that $\Gamma \ll \omega_z$ is easily satisfied, as axial frequencies in our trap are on the order of hundreds of kHz. The long lifetime of the $^2D_{5/2}$ state means, however, that effective cooling would be impossible if we were to wait for it to decay. We speed up the process by coupling the $^2D_{5/2}$ state to the $^2P_{3/2}$ state using light at 854 nm. This scheme is illustrated in Figure 5.3.

Specifically, we use the Zeeman transition $^2S_{1/2}$, $m_J = -1/2 \rightarrow {}^2D_{5/2}$, $m_J = -5/2$ to carry out sideband cooling. This transition is chosen because of its nearly closed scheme. Figure 5.3 shows this in the left image. From the $^2D_{5/2}$ $m_J = -5/2$ state, it can only be excited via the 854 nm transition to the $^2P_{3/2}$ $m_J = -3/2$ state. From here, if the ion decays back to the $^2S_{1/2}$ state (branching ratio 0.9347(3) [103]), it can only decay to $m_J = -1/2$, the initial state.

The ion can, however, decay instead to the $^2D_{5/2}$ or $^2D_{3/2}$ levels with branching ratios of 0.0587(2) and 0.006 61(4) respectively [103]. This is shown in Figure 5.3. When the ion is pumped back out of the $^2D_{5/2}$ and $^2D_{3/2}$, it can end up in either $^2S_{1/2}$ $m_J = \pm 1/2$.

After Doppler cooling, the ion is in a mixture of $^2S_{1/2}$ $m_J = \pm 1/2$. For effective sideband cooling, we must initialize the ion in the $m_J = -1/2$ state. It is also necessary to employ state initialization during the sideband cooling procedure, due to the mixing that can occur due to decays to the D levels.

There are two ways to implement sideband cooling: a pulsed and a continuous scheme. Both have been used in the experiments presented in this thesis. This section covers how pulsed sideband cooling, continuous sideband cooling, and state initialization work.

### 5.3.1 Pulsed scheme

In a pulsed scheme, the light at 729 nm and the light at 854 nm is alternately applied. This means that population is transferred to the $^2D_{5/2}$ state on the red sideband using light at 729 nm and

[3] This is not the only transition suitable for sideband cooling in $^{40}Ca^{+}$. Other schemes include cooling using the $^2S_{1/2} \rightarrow {}^2D_{3/2}$ 732 nm transition [101], or Raman sideband cooling on the 397 nm transition [81, 102].

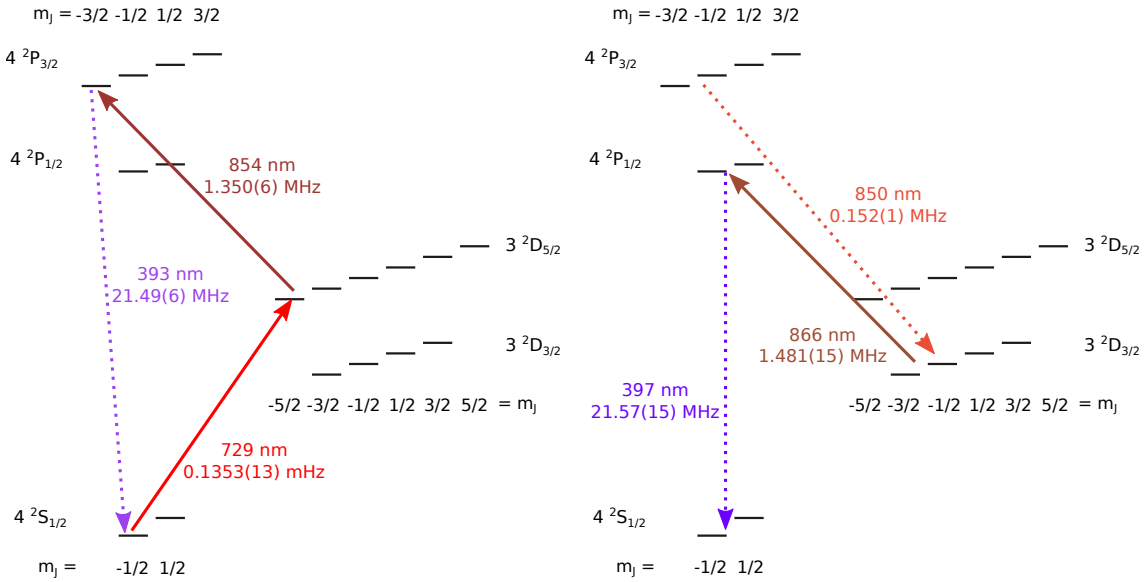


Figure 5.3: The sideband cooling scheme in $^{40}Ca^{+}$. The listed frequencies are the linewidth $\Gamma$ of the transition. **Left:** Red sideband transitions are driven on the $^2S_{1/2}$, $m_J = -1/2 \rightarrow {}^2D_{5/2}$, $m_J = -5/2$ transition at 729 nm. Light at 854 nm couples $^2D_{5/2}$ to $^2P_{3/2}$, speeding up the cooling process. Due to selection rules, only $^2D_{5/2}$, $m_J = -5/2 \rightarrow {}^2P_{3/2}$, $m_J = -3/2$ can be driven. From the $^2P_{3/2}$, $m_J = -3/2$ state, if the ion decays to the $^2S_{1/2}$ state (which it does with high probability), it can only decay to the $m_J = -1/2$ state, at which point the process can restart. **Right:** From the $^2P_{3/2}$ state, decay can also occur either back to the $^2D_{5/2}$ state, or to the $^2D_{3/2}$ state. A light field at 866 nm pumps the ion out of the $^2D_{3/2}$ state. Either of these decays and subsequent repumps can cause the ion to end up finally in either $m_J$ state in the $^2S_{1/2}$ level.

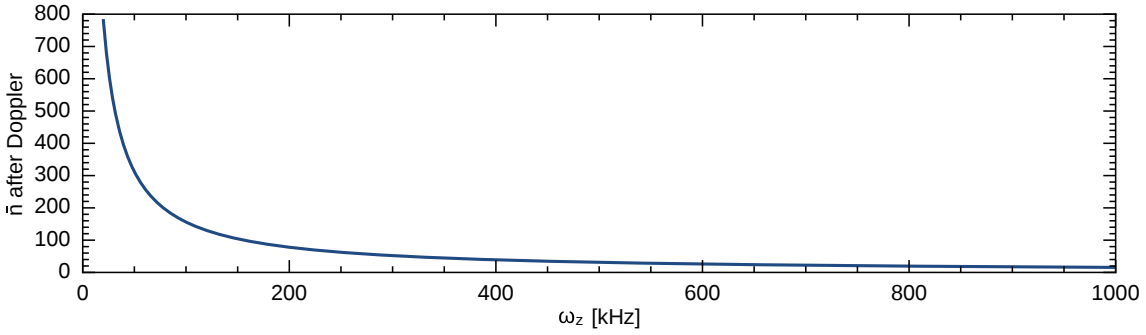


Figure 5.4: $\bar{n}$ after Doppler cooling for variable $\omega_z$.

pumped back to the $^2P_{3/2}$ with the field at 854 nm. The ion decays back to the $^2S_{1/2}$, and thus the process starts anew.

After Doppler cooling, the ion is in a thermal distribution with $\bar{n} \simeq \frac{\Gamma}{2\omega_z}$ (Equation 4.19). This is thus dependent on $\omega_z$ as shown in Figure 5.4, a plot of $\bar{n}$ after Doppler cooling for typical axial frequencies[4]. Thus, the lower $\omega_z$, the more we need to cool to reach the ground state of motion.

[4] Assuming a Zeeman-broadened linewidth.

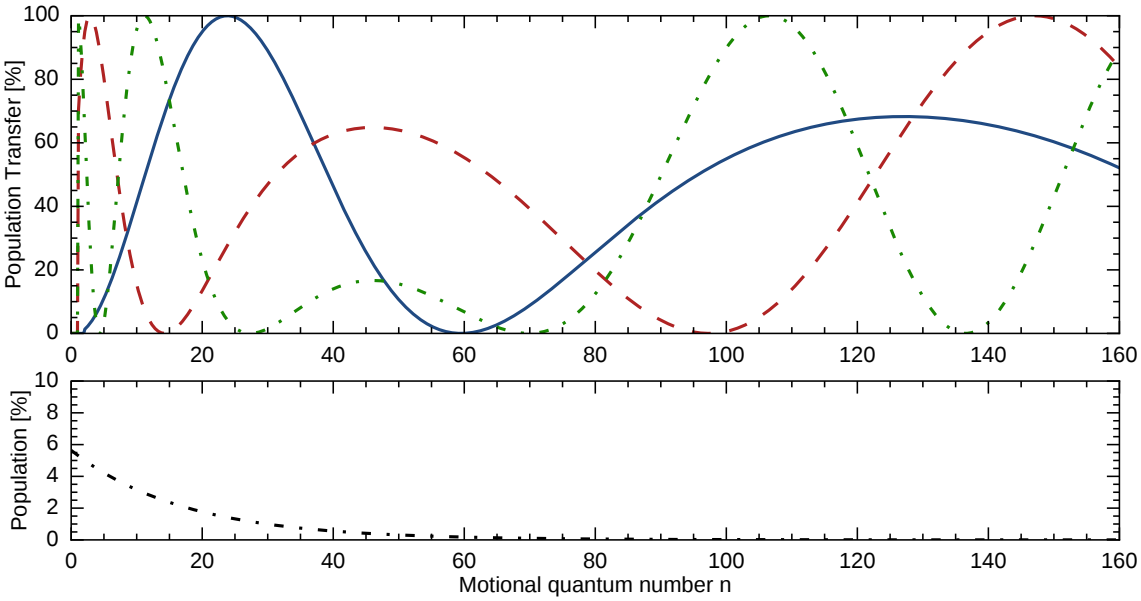


Figure 5.5: **Top:** Population transfer on the second red sideband, the first red sideband, both with $\Omega_0/(2\pi) = 92\,\text{kHz}$, and the low intensity first red sideband, with $\Omega_0/(2\pi) = 20\,\text{kHz}$, for cooling at $\omega_z/(2\pi) = 509\,\text{kHz}$, $\eta = 0.136$. **Bottom:** $P_n$ after Doppler cooling for the same trap paramters.

To more efficiently move population from high $n$ to low $n$, we make use of higher order sidebands. In our experiment, we first couple on the $2^{\text{nd}}$ red sideband before moving to the $1^{\text{st}}$ sideband. The $1^{\text{st}}$ red sideband then serves to pump population to low $n$. In the last step, we couple again on the $1^{\text{st}}$ red sideband, but at low intensity to reduce off-resonant scattering.

The efficiency of the population transfer to the excited state for a fixed pulse time and intensity is motional-state dependent, and assuming resonance is given by

$$p_{ee,n} = \sin^2\left(\Omega_{n,s}\frac{t}{2}\right) \tag{5.3}$$

This is plotted in Figure 5.5 for $\omega_z/(2\pi) = 509\,\text{kHz}$, corresponding to the Lamb Dicke parameter $\eta = .136$. The vacuum Rabi frequency for the $2^{\text{nd}}$ and $1^{\text{st}}$ sidebands is $\Omega_0/(2\pi) = 92\,\text{kHz}$ with pulse times $t = 30\,\mu\text{s}$ and $t = 25\,\mu\text{s}$, respectively. The low intensity red sideband has parameters $\Omega_0/(2\pi) = 20\,\text{kHz}$ and $t = 180\,\mu\text{s}$[5]. This corresponds to a $\pi$-pulse for $n = 1$ on the red sideband.

The first thing we see looking at Figure 5.5 is its strong dependence on the motional quantum number. In a sequence, pulses on the $2^{\text{nd}}$ red sideband occur first. Each pulse transfers population in $n \to n-2$ with the efficiency shown in the plot[6]. If we are considering a starting population $n < 60$, then this is capable of pumping the population down to $n = 0$ if the initial $n$ was even, and to $n = 1$ if the initial population was odd, though the process is inefficient at low $n$ as can be seen in the plot. If the initial population starts instead at $n > 60$, population will get stuck at $n = 60$, since there is no population transfer at this $n$. The lower plot shows the percentage $P_n$

[5]These are actual parameters that were used in the experiment. The exact pulse timings and intensities have since changed due to cooling at different $\omega_z$, for example, but the timings are generally similar, with the Rabi frequencies lower for lower $\omega_z$.

[6]Neglecting off-resonant coupling and decays on sidebands.

after Doppler cooling. While the population at $n > 60$ is small, it is non-negligible at 3 % of the total population.

Next, we employ a series of pulses on the 1st red sideband, so each pulse causes a change in motion of $\Delta n = 1$. Population at $15 < n < 100$ will be moved to $n = 15$, and population lower than this could be pumped to the ground state. The amplitude of the 1st red sideband increases where the amplitude of the 2nd sideband decreases, such that population that was inefficiently pumped previously is now efficiently pumped.

The last step is to apply the low intensity red sideband, which takes population in the vicinity of $n = 0$ and transfers it to $n = 0$. Its pulse time is crafted to be a $\pi$-pulse for population in $n = 1$, and the intensity low as to minimize off-resonant scattering. It also peaks where the previous sideband had minima.

Population that was stuck in $n = 15$ after the second step still gets stuck before 0 at $n = 5$. One could either create an adaptive scheme, which sweeps either the pulse time or pulse power to move these minima, or, a technically simpler option, is to loop through this process again. It is possible to choose parameters differently such that there are fewer minima, however one makes trade-offs in coupling strength. It is generally sufficient to loop through the process twice to achieve a ground-state cooled ion[7]. One must take care, however, not to choose parameters where all three have minima in the same spot [44]. Another solution would be to use even higher order sidebands in the cooling scheme [46].

These minima due to $n\pi$-pulses are not the only minima we must worry about. Figure 5.6 shows $\Omega_{n,s}/\Omega_0$ for the 1st and 2nd sidebands for three different $\eta$, or $\omega_z$ (decreasing $\omega_z$ from the first plot down). As we increase $\eta$ (decrease $\omega_z$), we move farther and farther outside of the Lamb Dicke regime. Points of $\Omega_{n,s} = 0$ appear, and no matter the pulse time or power, we cannot couple on the sidebands at these $n$. For small $\eta$, these occur at high $n$ and thus are no concern. For larger $\eta$, both $\bar{n}$ after Doppler cooling increases and the minima move to lower $n$, working together to make sideband cooling a more complex process.

Because in the pulsed scheme we have two types of minima to be concerned with, to cool at lower $\omega_z$, it simplifies matters to move to the continuous sideband cooling scheme.

### 5.3.2 Continuous scheme

The other method is a continuous cooling scheme, where both 729 nm and 854 nm fields are on at the same time, with the light at 854 nm effectively broadening the linewidth of the transition [104]. In the low saturation limit, the upper level ($^2P_{3/2}$) can be adiabatically eliminated, and effective linewidth is given by[8]

$$\Gamma_{eff} = \frac{\Omega_{854}^2}{(\Gamma_{393} + \Gamma_{854})^2 + 4\delta_{729}^2}\Gamma_{393} \tag{5.4}$$

The 854 nm field contributes an extra AC Stark shift to the 729 nm transition, given by $\delta_{854}\frac{\Gamma_{eff}}{\Gamma_{397}}$ [91]. For optimal cooling, the 729 nm field should be tuned to the AC Stark-shifted resonance[9].

At this point, one could employ a similar rate equation analysis as presented in section 4.2 with modified $A_\pm$ terms, as described by [104]. However, this description is only valid in the

[7] 2 loops corresponded to an improvement of nearly 50% on the final $\bar{n}$ (as simulated), whereas three loops the improvement was negligible. Even for poorly chosen parameters where two of the minima nearly overlap, two loops results in an ion close to the ground state, with negligible improvement after a third loop. The simulations are equivalent to those detailed in [44, pg. 133].

[8] The coherence decay $\gamma$ from the optical Bloch equations is no longer given by $\Gamma/2$, however it is a good approximation for $^{40}Ca^+$ [104].

[9] This is an area in which we could gain in our sideband cooling procedure, since at the moment our sequence does not do this.

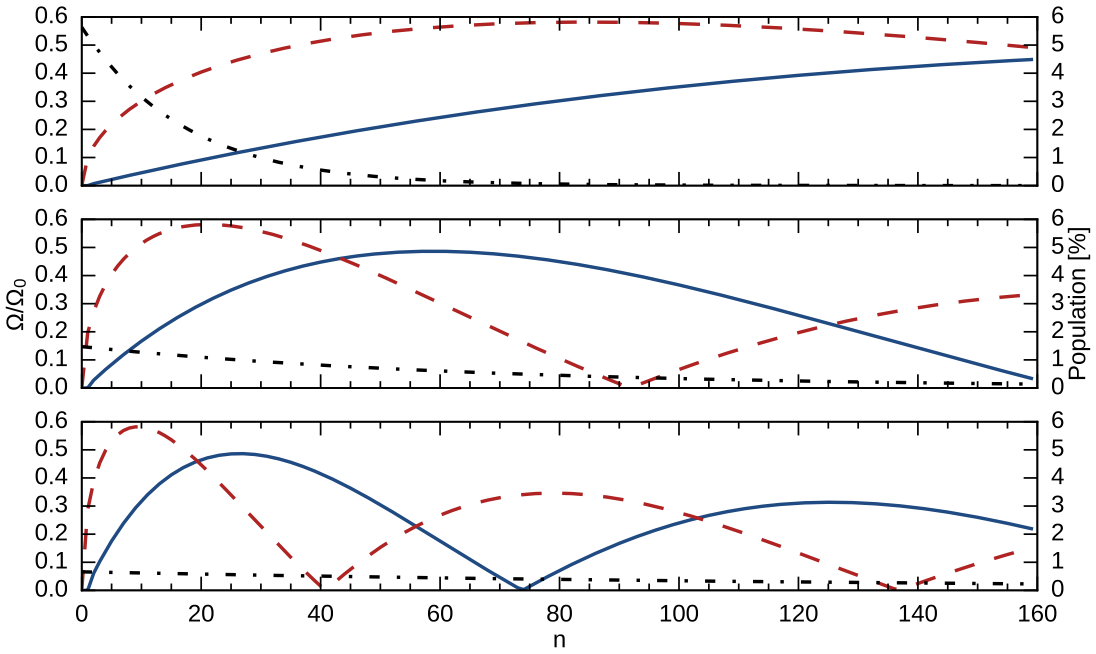


Figure 5.6: Plots of the normalized sideband Rabi frequency as a function of motional quantum number for Top: $\eta = 0.1$, $\omega_z/(2\pi) = 930\,\text{kHz}$. Middle: $\eta = 0.2$, $\omega_z/(2\pi) = 230\,\text{kHz}$. Bottom: $\eta = 0.3$, $\omega_z/(2\pi) = 100\,\text{kHz}$. ——— shows the second red sideband and – – – shows the first sideband (both left axis). - · - · - is referenced to the right axis and shows the population after Doppler cooling in each $n$ for a single $^{40}Ca^{+}$ at the corresponding $\omega_z$. Out of the Lamb Dicke regime, the sideband Rabi frequencies do not follow the simple formula. They can have regimes of 0 coupling even at high $n$.

Lamb Dicke regime, and as discussed in the previous section, we are at times not in the Lamb Dicke regime when we begin cooling. Thus, this description only gives us an end of cooling scenario. The end $\bar{n}$ is dependent on a number of free parameters: $\delta_{854}$, $\delta_{729}$, $\Omega_{854}$, $\Omega_{729}$, and $\omega_z$.

The qualitative picture shows us that by effectively broadening the linewidth of the transition, we sideband cool more quickly. Because the process does not rely on coherent dynamics, we do not get the 0 population transfer conditions presented in Figure 5.5. We do still get the 0 Rabi frequency points plotted in Figure 5.6, and thus must still use multiple sideband orders and iterations, depending on the exact starting conditions.

When we employ the continuous scheme, we leave the last stage at low intensity pulsed, as to most effectively transfer population from low $n$ without needing to perfectly optimize the AC Stark shifts and the exact 854 nm intensity and detuning.

### 5.3.3 State initialization

Preparation in the $^2S_{1/2}$, $m_J = -1/2$ state is achieved by driving the $^2S_{1/2}$, $m_J = -1/2 \rightarrow {}^2D_{5/2}$, $m_J = 3/2$ transition at 729 nm, and coupling to the $^2P_{3/2}$ at 854 nm. The level scheme looks similar to that of sideband cooling (Figure 5.3), but between different Zeeman sublevels. From the $^2D_{5/2}$, $m_J = 3/2$ state, the ion can be driven to the $^2P_{3/2}$, $m_J = 1/2, 3/2$ states. From the

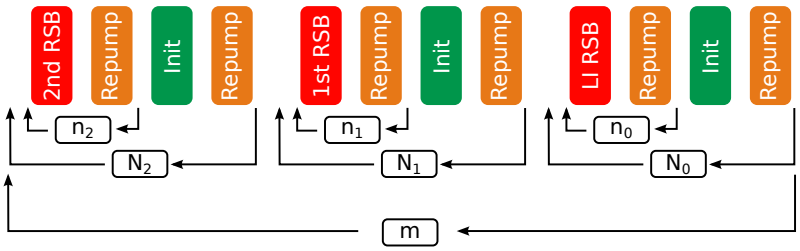


Figure 5.7: Schematic of the sideband cooling sequence.

$m_J = 1/2$ state, it can decay to the $^2S_{1/2}$, $m_J = -1/2$. Otherwise it ends up back in the $m_J = 1/2$ state and the process begins again. Because population is driven out of the $^2S_{1/2}$, $m_J = 1/2$ state but not from $m_J = -1/2$, eventually the population is optically pumped to the $^2S_{1/2}$, $m_J = -1/2$ state. This pumping is realized in a continuous scheme, with the 729 nm and 854 nm light on at the same time.

Initialization needs to happen within the sideband cooling sequence since the cooling cycle is not closed. Figure 5.7 shows the general format of the cooling. If the cooling method is a continuous method, both the 854 nm light and 729 nm light are turned on during the RSB (red sideband) stages. Otherwise, it is just the 729 nm. During the repump stages, the 854 nm and 866 nm fields are both on.

For each stage of the sideband cooling sequence, after $n_i$ cycles of sideband driving and repumping, we employ initialization. This is repeated $N_i$ times, where $i = 2$ for the $2^{\text{nd}}$ red sideband, $i = 1$ for the $1^{\text{st}}$ red sideband, and $i = 0$ refers to the low intensity sideband. The entire process is iterated $m$ times.

Our typical values are $n_{1,2} = 25$, $N_{1,2} = 5$, $n_0 = 5$, $N_0 = 2$, and $m = 2$. These numbers are overkill, chosen to be robust for changing parameters; the total time spent can be reduced by more than a factor of two if we keep the sideband cooling $\omega_z$ consistent[10]. For future experiments, this will be necessary. For continuous cooling, we could remove the loop over $n_i$ and increase the sideband time. We have tried this and seen that it works, but have continued using the mode of operation shown in Figure 5.7 such that switching back to a pulsed scheme is seamless.

#### Reverse initialization

If we wish to investigate Zeeman transitions from $^2S_{1/2}$, $m_J = 1/2$, we need to initialize this state instead. To implement this, we first complete the sideband cooling procedure. We can then drive a $\pi$-pulse on the carrier $^2S_{1/2}$, $m_J = -1/2 \rightarrow {}^2D_{5/2}$, $m_J = -3/2$ transition. We follow this pulse with 854 nm light to return the ion to the $^2S_{1/2}$ state. This is repeated 10 times to pump the ion into the $^2S_{1/2}$, $m_J = 1/2$ state.

### 5.3.4 Evaluation of cooling

We can simulate cooling, but final optimization is of course always carried out in the lab. Doppler cooling can be evaluated by probing multiple sideband orders on the 729 nm transition. This gives, on resonance,

$$\rho_{ee} = \sum_0^n P_n \sin^2\left(\Omega_{n,s}\frac{t}{2}\right) \tag{5.5}$$

[10] In fact, they already are much lower for two ion cooling.

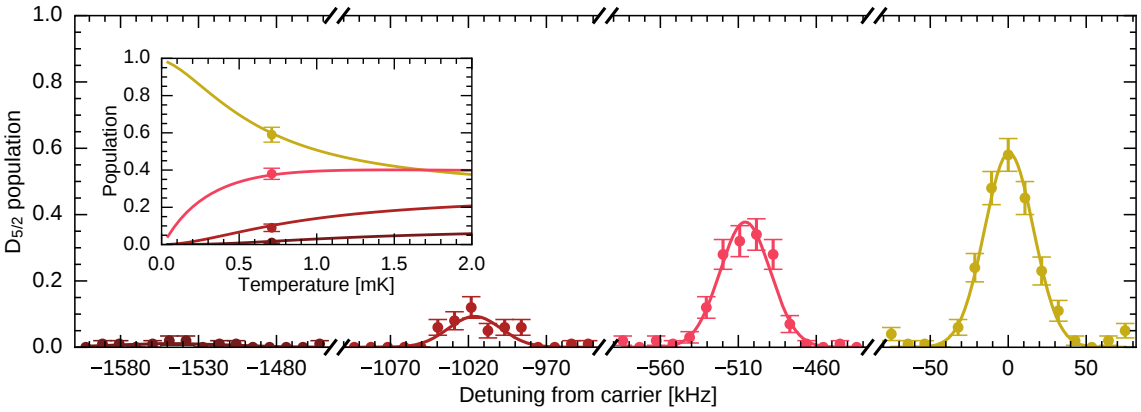


Figure 5.8: • Carrier, • 1st, • 2nd, and • 3rd red sidebands of a Doppler-cooled $^{40}Ca^{+}$ ion. The inset shows an approximate match to expected sideband heights for a thermal distribution with temperature $T = 0.71\,\mathrm{mK}$, where the points correspond to the sideband heights.

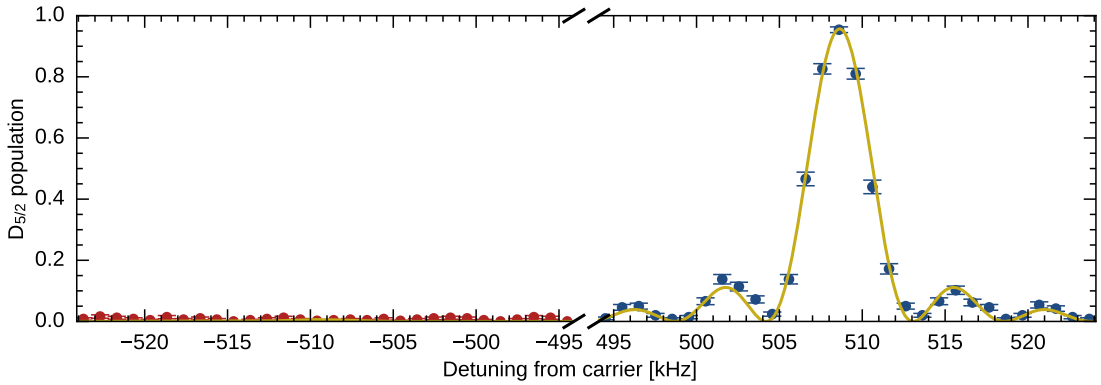


Figure 5.9: • Red and • blue sidebands of a sideband-cooled $^{40}Ca^{+}$ ion. This particular data set was taken using 500 detection trials rather than 100 for better resolution.

The sideband heights can thus be matched to a thermal distribution. Figure 5.8 shows a sideband spectrum after Doppler cooling, and the inset shows the heights of the sidebands compared to the thermal distribution. The Doppler-cooled temperature is thus approximately $T = 0.71\,\mathrm{mK}$, which matches well to the expected temperature including Zeeman splitting.

Sideband cooling can be evaluated using the method presented in section 4.4. Figure 5.9 shows a sideband-cooled spectrum for $\omega_z/(2\pi) = 509\,\mathrm{kHz}$, using the continuous scheme. The average motional occupation number after cooling $\bar{n} = 0.006(3)$, which corresponds to $P_0 = 99.4(3)\,\%$, and a temperature $T = 4.8(5)\,\mu\mathrm{K}$.

When the ion is prepared in nearly the ground state, Rabi flopping on the carrier has nearly 100% contrast, as shown in Figure 5.10. The single frequency and lack of decoherence on this timescale is a good indication that the ion is prepared in the ground state of motion.

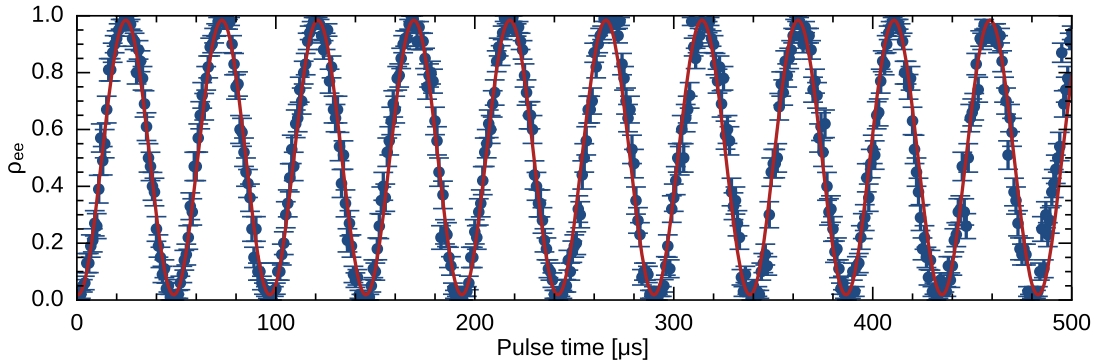


Figure 5.10: Carrier Rabi flopping after sideband cooling. • data, — fit. The fitted amplitude is 0.484(8).

## 5.4 Shelving

Detection in $^{40}Ca^{+}$ is performed using the electron shelving[11] method. The long lifetime of the $^{2}D_{5/2}$ state (1.168(9) s) means that, compared to the linewidth (and thus scattering rate limit) of the 397 nm transition, the ion does not decay in the time it takes to collect fluorescence information. If the ion has been shelved, the ion will stay in the $^{2}D_{5/2}$ state and thus can't fluoresce at 397 nm, so the ion will look dark on the CCD camera. If the ion has not been shelved, the ion will fluoresce and will be visible to the camera. Thus, we have direct access to $\rho_{ee}$ on the 729 nm transition. The level diagram corresponding to a shelved ion is shown in Figure 5.11.

Of course, for any single measurement of the ion, it will be either light or dark. $\rho_{ee}$ is extracted statistically, by repeating the same measurement for $n$ trials to extract the probability of the ion being dark. A typical $n$ for our experiment is 100 trials.

[11] Proposed and coined by Dehmelt in 1975 [13].

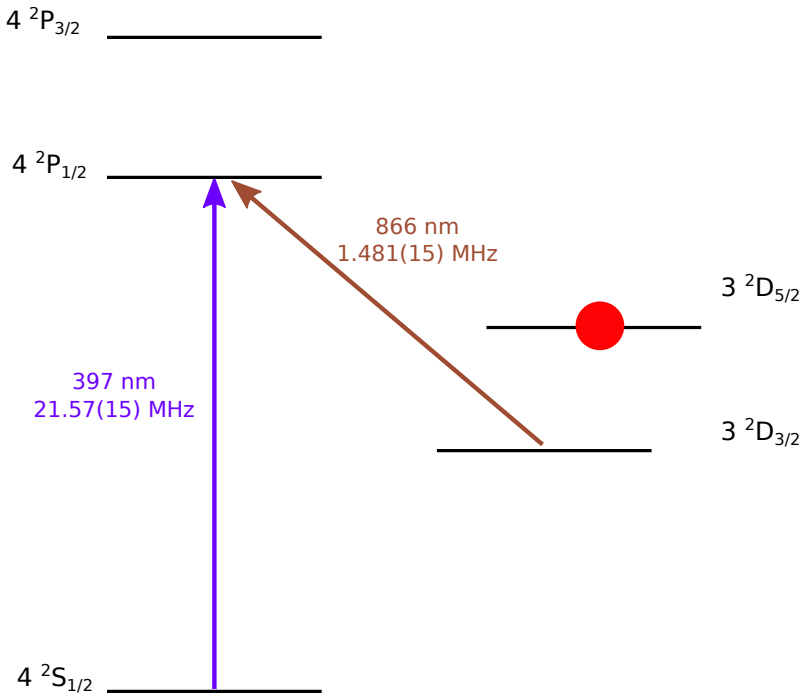


Figure 5.11: Level diagram showing shelving detection. When the ion is in the $^2D_{5/2}$ state, it cannot fluoresce at 397 nm, thus the ion looks dark.

# Chapter 6

# Cooling and detection of $^{24}MgH^+$

Although none of the experiments presented in this thesis include $^{24}MgH^+$, to understand the objectives it is important to understand the structure, cooling, and detection of the molecule in order to understand the motivation of the experiments.

## 6.1 $^{24}MgH^+$ Structure

The internal structure of molecules is more complex than atomic structure. In addition to electronic structure, they also have vibrational and rotational structure.

$^{24}MgH^+$ is a diatomic polar molecule. Its electronic structure is shown in Figure 6.1 (a). Its ground electronic state is $X^1\Sigma^+$, and the lowest electronic transition is $X^1\Sigma^+ \rightarrow A^1\Sigma^+$ with a wavelength of 281 nm, or 1061 THz. Zooming into the ground electronic state in Figure 6.1 (b), we see the vibrational spectrum. Each vibrational state splits into rotational states. The lowest rovibrational transitions ($|v = 0\rangle \rightarrow |v = 1\rangle$) have wavelengths of about 6 µm, or 50 THz. The rotational states, denoted by $J$, have a splitting characterized by the rotational constant $B \simeq 190$ GHz [105].

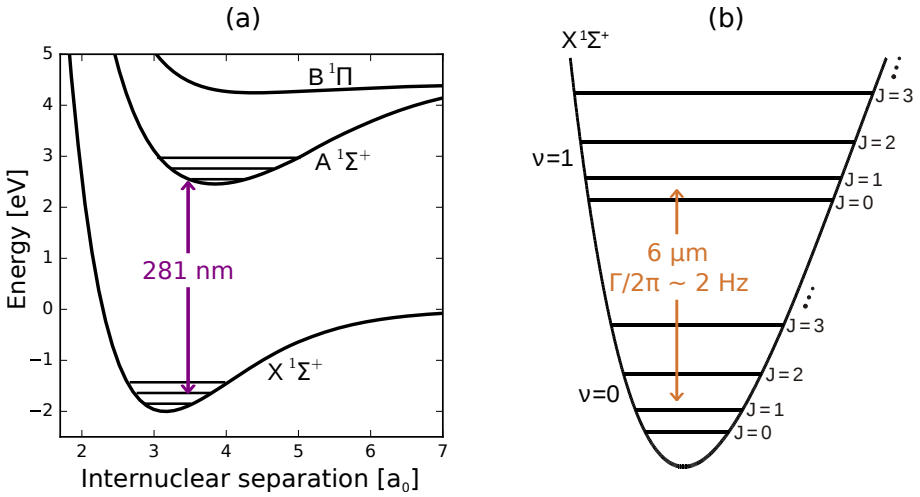


Figure 6.1: Internal level structure of $^{24}MgH^+$. **(a)**: The lowest-lying singlet electronic states. **(b)**: Zoom in of the electronic ground state to see the lowest-lying vibrational and rotational states.

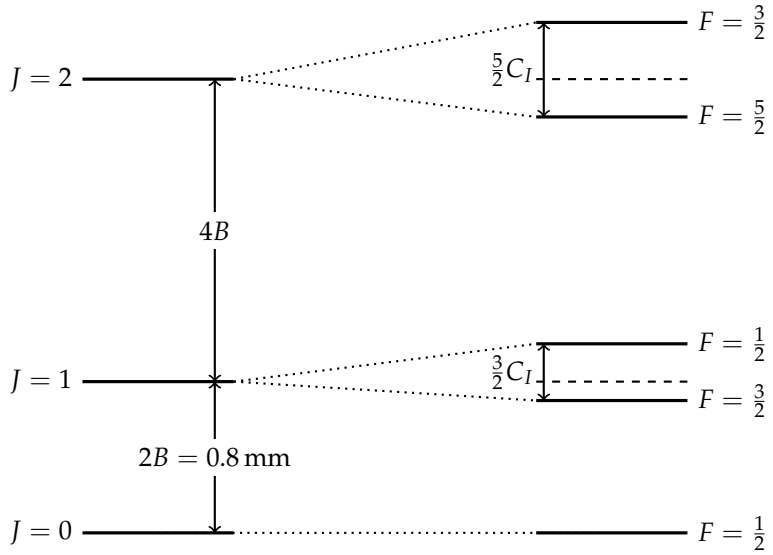


Figure 6.2: Hyperfine structure of $^{24}MgH^+$.

The rotational level energies are given by

$$E_J = \hbar B J(J+1) \tag{6.1}$$

Thus the separation between $J = 0$ and $J = 1$ is 0.38 THz, or a wavelength of 0.8 mm.

$^{24}MgH^+$ has nuclear spin $I = 1/2$, and thus has hyperfine structure. The energy of the hyperfine structure is given by

$$\Delta E_J = -h\frac{C_I}{2}(F(F+1) - I(I+1) - J(J+1)) \tag{6.2}$$

where $C_I = 18.1$ kHz [106] is the spin-rotation constant for $^{24}MgH^+$. The splitting of the rotational levels into the hyperfine structure is represented schematically in Figure 6.2. Further, when the molecule is placed in a magnetic field $B$, the hyperfine structure undergoes Zeeman splitting. The Zeeman splitting in $^{24}MgH^+$ can be calculated by diagonalizing the Hamiltonian

$$H = -hC_I\hat{I}\cdot\hat{J} - g_p\mu_N\hat{I}\cdot B - g_{rot}\mu_N\hat{J}\cdot B \tag{6.3}$$

where $g_p$ is the proton g-factor, $g_{rot} \simeq -0.08$ [106] is the rotational g-factor, and $\mu_N = \frac{e\hbar}{2m_p}$ is the nuclear magneton, where $m_p$ is the mass of the proton. The first term is the hyperfine Hamiltonian, and second two terms are the Zeeman components. This Hamiltonian can be simplified by defining the B-field along the $z'$-axis[1] and expanding $\hat{I}\cdot\hat{J}$ into the $z'$-components and the ladder operators. The resulting Zeeman splitting is shown in Figure 6.3, where each plot shows the frequency difference from $E_J/h$.

[1] I've written $z'$ as to not confuse this axis with the trap axis. This is merely to use the standard definitions of the angular momentum operators.

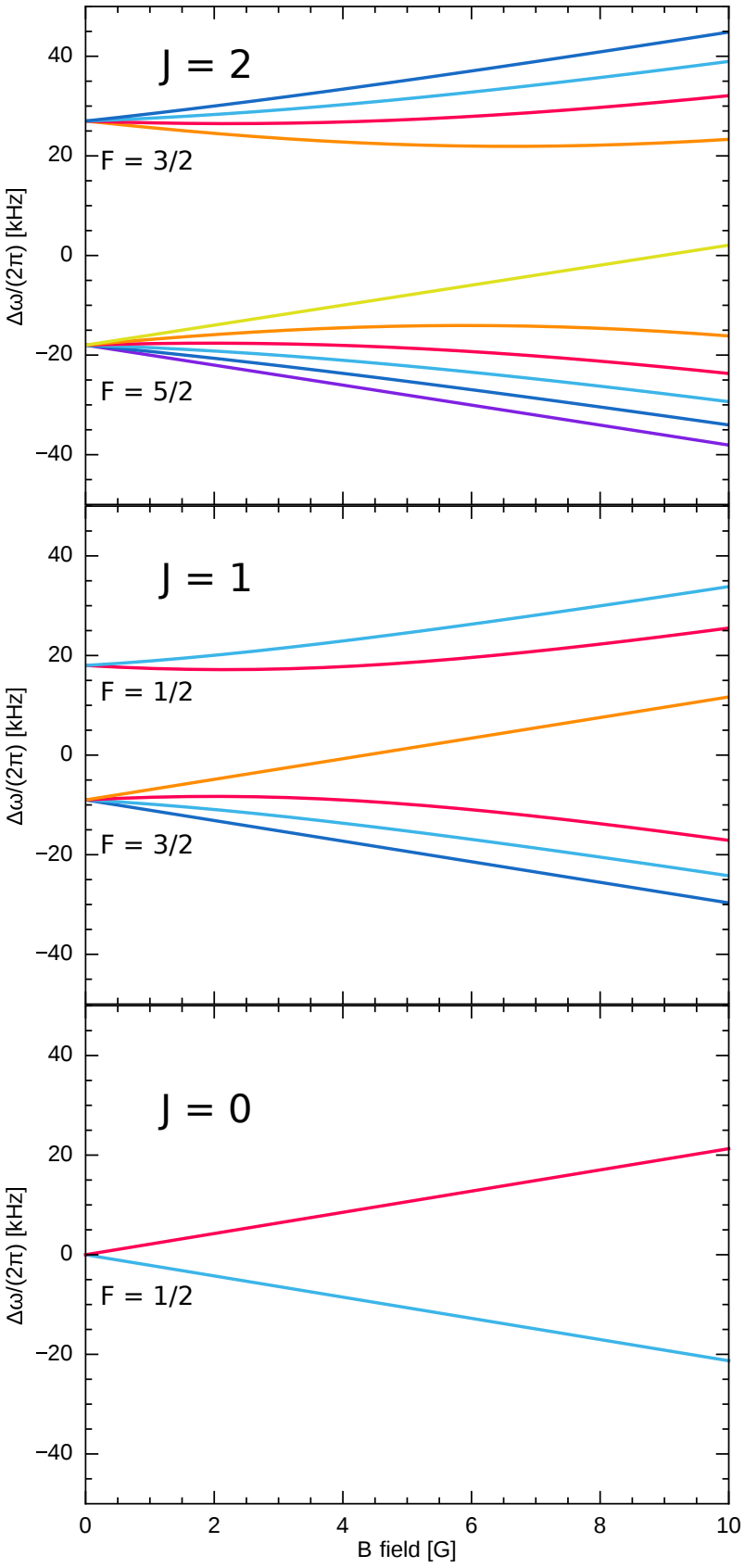


Figure 6.3: Zeeman splitting of the hyperfine levels $F$ of the rotational levels $J$ in $^{24}MgH^{+}$. The 'hot' colors show negative $m_F$ and the 'cold' colors show positive $m_F$.

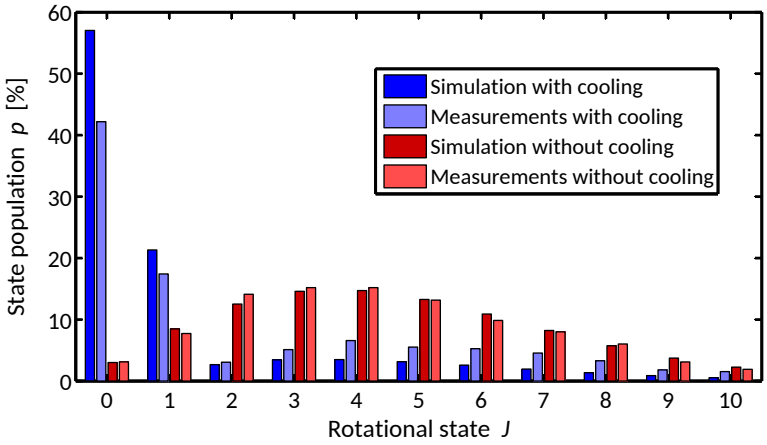


Figure 6.4: Rotational population distribution before and after employing rotational cooling, compared to rate equation theory. Results and figure reproduced from A. Hansen's thesis [108].

## 6.2 Preparing internal degrees of freedom

At room temperature, $^{24}MgH^+$ is found in its ground electronic state. With a vibrational constant of about 50 THz, at room temperature the $^{24}MgH^+$ is also in the ground vibrational state with a likelihood of more than 99.9 %. It is, however, distributed between the rotational levels. Figure 6.4 shows the room temperature distribution of $^{24}MgH^+$ between the rotational states in red. Sympathetic cooling (section 6.3) is effective at cooling the external motion of the molecule, but it is not effective at cooling the rotation [107]. Thus, it is necessary to employ other techniques to prepare the ion in a specific rotational state.

One technique used for cooling the rotational degree of freedom in molecular ions is buffer gas cooling. Buffer gas cooling is employed either by using a leaked in buffer gas, generally in a cryogenic environment [109], or by using clouds of laser-cooled atoms [41]. Buffer gas cooling is not species dependent[2], and helium buffer-gas cooling as been demonstrated with great success in $^{24}MgH^+$, with a ground state population of nearly 0.8 after about one second for a single ion [43]. Our trap is not equipped for using either leaked-in buffer gases or laser-cooled clouds, though in our group a cryogenic trap is currently being constructed in which this technique can be employed.

Another method is to employ rotational cooling by optical pumping. This species-specific method has been previously employed in $^{24}Mg^+$-$^{24}MgH^+$ Coulomb crystals in Aarhus [40], and other schemes have been implemented in a few other species as well [42, 111]. The scheme for $^{24}MgH^+$, proposed by Vogelius *et al.* [112], is pictured in Figure 6.5. A laser tuned to 6.2 µm pumps population from $|v = 0, J = 2\rangle \rightarrow |v = 1, J = 1\rangle$. From this point, $|v = 1, J = 1\rangle$ can decay either to $|v = 0, J = 0\rangle$ or to $|v = 0, J = 2\rangle$. If the ion decays to $|v = 0, J = 2\rangle$, it gets pumped back again.

Blackbody radiation couples the rotational states, and the blackbody rates are higher for higher rotational states. The blackbody radiation couples population from higher states into $|v = 0, J = 2\rangle$, allowing it to be pumped into $|v = 0, J = 0\rangle$. Of course, blackbody radiation

[2]The mass ratio between the gas and the species does effect the cooling, and should be $\lesssim 1$ [110], but the same buffer gas could be used to cool multiple species.

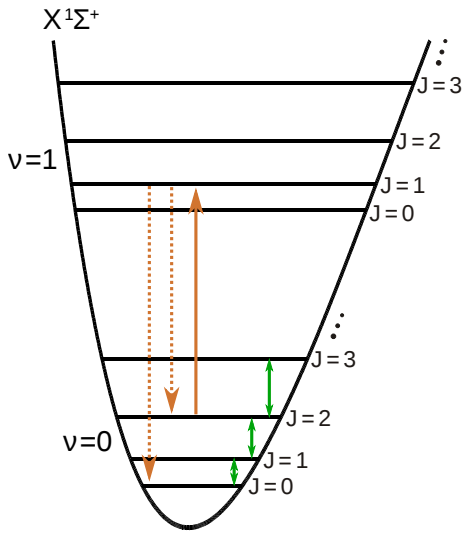


Figure 6.5: Diagram showing the rotational cooling scheme. A 6.2 µm laser drives the $|v = 0, J = 2\rangle \rightarrow |v = 1, J = 1\rangle$ transition. The dotted lines indicate the decay paths, and the green arrows indicate blackbody coupling.

also limits the final rotational state population, as population is coupled out of the ground state. The final population compared to the initial is shown in Figure 6.4. The entire process takes about 60 s [113].

While the population increases dramatically, this method does not prepare us with near 100 % in any state. The solution to this problem is to perform probabilistic state preparation via state projection. One method is to perform successive state-selective dissociation measurements. By attempting to dissociate multiple times from $|v = 0, J > 0\rangle$, and not having a dissociation event, the population is projected into $|v = 0, J = 0\rangle$. This is problematic with a single ion since every time it is dissociated, we need to load a new ion. This is very time intensive and impractical.

Another solution is to use quantum logic spectroscopy [48] (subsection 6.4.1) to map information about the internal state onto the motion of a $^{40}Ca^{+}$-$^{24}MgH^{+}$ crystal [50,51]. If we interweave $\pi$-pulses on a blue sideband transitions in $^{24}MgH^{+}$ and detections in $^{40}Ca^{+}$, we can detect when a transition occurs. By sampling multiple rotational states, we can 'find' the state of $^{24}MgH^{+}$[3].

Once we see a change in motional state, we know what state $^{24}MgH^{+}$ is in, and can move it to where we want it. We are in the midst of developing a technique that uses a femtosecond frequency comb to drive Raman transitions between rotational states. Using this technique, we will be able to prepare any rotational state within $\Delta J = 2$ of the initial. For more information on how a frequency comb can be used to drive Raman transitions, see [114,115].

## 6.3 Sympathetic cooling

The general absence of closed, fast cycling transitions in molecular ions means that direct Doppler and sideband cooling are typically not possible. Though we cannot directly cool the $^{24}MgH^{+}$, we can sympathetically cool it by cooling co-trapped $^{40}Ca^{+}$.

[3] Or, rather, project into that state.

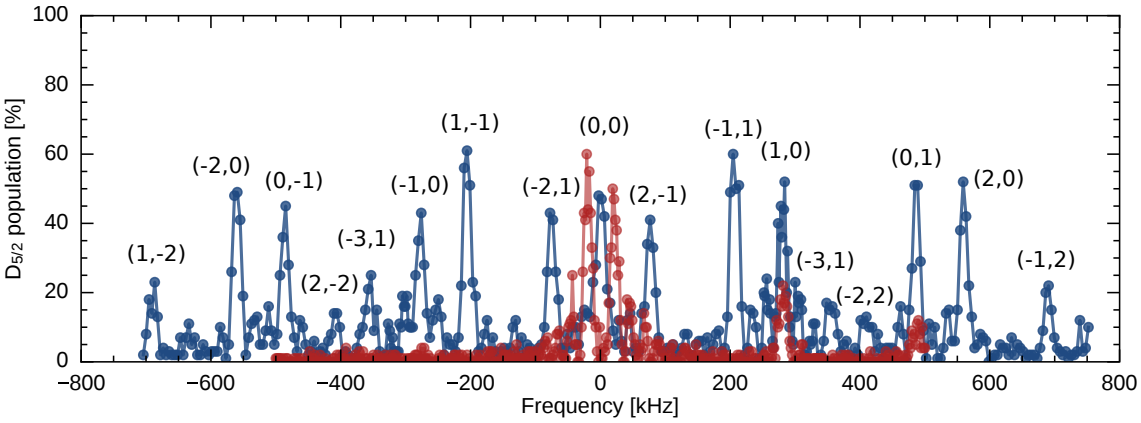


Figure 6.6: Sideband spectrum of $^{40}Ca^+$-$^{42}Ca^+$ for • Doppler-cooled or • sideband-cooled ions. The numbers refer to the sideband orders in terms of $(n_+, n_-)$.

Sympathetic cooling was first suggested by Wineland, *et al.* in 1978 [83], employed in Penning traps in 1980 on different $Mg^+$ isotopes [116], and on different species, $^9Be^+$ and $^{198}Hg^+$, in 1986 [21]. The next year it was implemented in Paul traps to cool crystals of 2-4 ions[4]. Since, sympathetic cooling has been used extensively to cool both atomic and molecular ions [118], allowing for the study of otherwise inaccessible ions. Most recently, it has been employed in two ion chains with one atomic ion and one molecular ion [44–46], enabling the implementation of high resolution spectroscopy [47, 49].

The idea of sympathetic cooling is a simple one: two species are trapped together in a crystal. Due to the Coulomb interaction combined with the trapping potential, they share motional modes (section 2.2). Changing the motion of one species thus influences the motion of the other. Therefore, if we cool the motion of one species, we also cool the motion of the other. This principle can be applied both to Doppler and sideband cooling. As such, we can cool $^{24}MgH^+$ down to the ground state of motion by employing both Doppler and sideband cooling on $^{40}Ca^+$.

Sympathetic sideband cooling [119] works under the same principle of sideband cooling: removing motional quanta by addressing the red motional sidebands. With two ions, however, there are two axial frequencies, $\omega_+$ and $\omega_-$. The blue trace in Figure 6.6 shows the sideband spectrum of a Doppler-cooled $^{40}Ca^+$-$^{42}Ca^+$ crystal[5]. The sideband structure is much more complex than in the single ion case as sidebands form at any integer multiple combination of the two frequencies.

To cool the two ions down to the ground state in one of these modes, we must address the red sidebands of that mode on one of the two ions. For the in-phase mode, this corresponds to (-2,0), and (-1,0) for the second and first red sidebands, and (0, -2) and (0, -1) for the out-of-phase sidebands. To cool both modes, we must address the red sideband of both modes on one of the two ions. In practice, we interleave cooling pulses[6] on each mode, such that in Figure 5.7 each sideband-repump pair would be followed by one of the other mode. The red trace in Figure 6.6 shows a sideband-cooled spectrum, and the complex peak structure has been cooled out. The multiple peaks around the carrier are a result of over-driving the carrier transition.

[4] All ions were $^{198}Hg^+$ [117], but the cooling beam was focused as to address only a single ion, thus this is still sympathetic cooling.

[5] $^{42}Ca^+$ does not fluoresce at the same frequency as $^{40}Ca^+$, and thus is a dark ion. By cooling $^{40}Ca^+$, we cool $^{42}Ca^+$ sympathetically.

[6] In both the continuous and pulsed schemes.

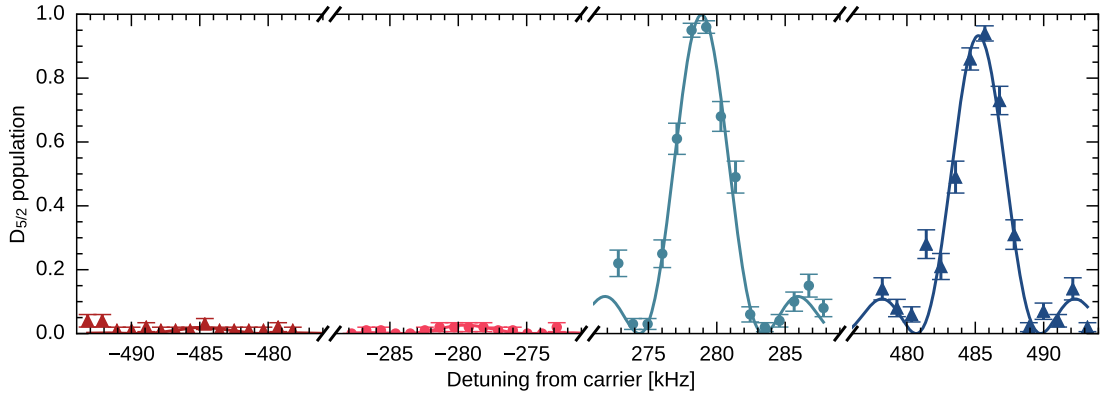


Figure 6.7: • , • In-phase and • , • out-of-phase sidebands for a sideband-cooled $^{40}Ca^{+}$-$^{42}Ca^{+}$ crystal. The lines show a fit of a Rabi line shape to the data. Both in- and out-of-phase data was taken with a pulse corresponding to a $\pi$-pulse on the respective mode.

Figure 6.7 shows the first order in- and out-of-phase sidebands of a sympathetically cooled $^{40}Ca^{+}$-$^{42}Ca^{+}$ crystal. The motional occupation of the in-phase mode is $\bar{n}_{+} = 0.027(10)$ ($P_0 = 97.4(9)$), and the thermal occupation of the out-of-phase mode is $\bar{n}_{-} = 0.021(15)$ ($P_0 = 97.9(14)$). For these plots, parameters for each mode from Figure 5.7 were $n_{1,2} = 10$, $N_{1,2} = 5$, $n_0 = 6$, $N_0 = 2$, and $m = 2$. Naturally, in order to study $^{24}MgH^{+}$, we will have to sideband cool $^{40}Ca^{+}$-$^{24}MgH^{+}$. This will require somewhat different parameters due to the changing eigenvectors, frequencies, and Lamb-Dicke parameters, but sympathetic cooling of lighter-mass species with even larger mass ratios has been previously demonstrated [120].

## 6.4 Detection of $^{24}MgH^{+}$

The absence of closed cycling transitions in $^{24}MgH^{+}$ also means that we cannot perform fluorescence detection on $^{24}MgH^{+}$. In order to perform rovibrational spectroscopy, we need to be able to detect changes in the internal state of $^{24}MgH^{+}$. Previously in our group, the internal state of $^{24}MgH^{+}$ was determined using destructive rotational state selective dissociation [37, 121, 122], called 1+1 resonance-enhanced multi-photon dissociation (REMPD). These experiments were carried out on large Coulomb crystals; thus statistics could be built up over fewer experimental cycles.

The large Coulomb crystals are not, however, cooled into the Lamb Dicke regime, and thus suffer from Doppler broadening, limiting spectroscopic resolution. Further, the ions in the outer shells experience more micromotion than those at the center, and thus the second order Doppler shift limits spectroscopic precision. Lastly, between the many motional modes and the presence of micromotion, one cannot practically sideband-cool a large crystal. The need to switch to single molecular ions is evident, but dissociation detection is impractical with a single ion, as one would have to reload with every dissociation.

A better solution is to use the co-trapped $^{40}Ca^{+}$ as a sensor for the state of $^{24}MgH^{+}$. This works by using the coupled motion of the ions to detect motional transitions in $^{24}MgH^{+}$ by measuring the sidebands of $^{40}Ca^{+}$. This technique is called quantum logic spectroscopy (QLS) [48].

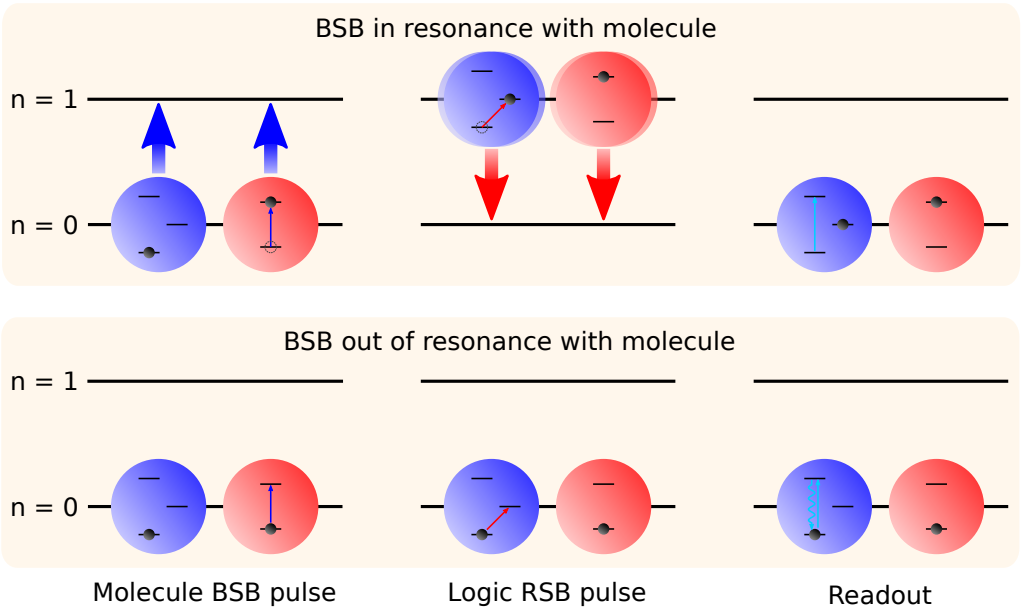


Figure 6.8: QLS scheme: $^{40}Ca^+$ is shown in blue, with a simplified level structure shown inside of it ($^2S_{1/2}$, $^2P_{3/2}$, $^2D_{5/2}$). The molecular ion is shown in red.

### 6.4.1 Quantum logic spectroscopy

The technique of QLS was first proposed and demonstrated by Schmidt, *et al.* at NIST in 2005 [48]. It has opened the doors to the precision spectroscopic study of ions which to not have an easily accessible cooling transition. It has been used to great end in atomic ions for metrology, and quantum logic-based $^{27}Al^+$ clocks are some of the best in the world [16, 19]. In terms of molecular ions, this technique has been implemented for $^{24}MgH^+$ at PTB[7] [49] and for $CaH^+$ at NIST[8] [47].

QLS is a technique that is used to track the internal state of a non-fluorescing ion by monitoring the motional state of a co-trapped fluorescing ion. Because the two ions have coupled motion, driving a sideband transition in the non-fluorescing ion will cause both the non-fluorescing ion and the fluorescing ion to have a motional state change. We are most sensitive to motional state changes when we are cooled to the ground state of motion.

The following details a basic QLS experiment. I use the notation $|i\rangle_a|i\rangle_m|n\rangle$, where $a$ (atomic) refers to the $^{40}Ca^+$, $m$ (molecular) refers to $^{24}MgH^+$, and the internal state $i$ can be $g$, for ground, or $e$ for excited for either ion. For simplicity, we only consider one motional mode with quantum number $n$. The description follows Figure 6.8, where the first point in each step refers to the top part of the image, and the second point refers to the bottom section of the image.

1. Prepare the shared motion in the motional ground state via sympathetic sideband cooling: $|g\rangle_a|g\rangle_m|0\rangle$.
2. Probe the molecular ion near the transition you wish to see. To first order, either:
   - The ion makes a transition on the blue sideband, and the motional state increases by one quanta: $|g\rangle_a|g\rangle_m|0\rangle \rightarrow |g\rangle_a|e\rangle_m|1\rangle$.

[7] Used for electronic spectroscopy.
[8] Used to manipulate the Zeeman and hyperfine states.

- The ion does not transition on the blue sideband, so the motion remains in the ground state: $|g\rangle_a|g\rangle_m|0\rangle$.

3. Perform a $\pi$-pulse on the red sideband of the atomic ion's shelving transition.Depending on the previous step, either:
   - If the motional state increased in the previous step, the ion will transition, shelving: $|g\rangle_a|e\rangle_m|1\rangle \rightarrow |e\rangle_a|e\rangle_m|0\rangle$.
   - If the motion was in the ground state, the red sideband does not exist, and nothing will happen: $|g\rangle_a|g\rangle_m|0\rangle$.
4. Perform detection of the atomic ion.
   - If the ion is shelved ($|e\rangle_a$), it will not fluoresce.
   - If the ion did not transition($|g\rangle_a$), it will fluoresce.

In short, if the atomic ion does not fluoresce in the last step, it made a transition, and if it does, it did not. By running this sequence many times and scanning the detuning of the spectroscopy laser, one can resolve the blue sideband transition. One can also probe carrier transitions by first transitioning on the $^{24}MgH^+$ carrier $|g\rangle_a|g\rangle_m|0\rangle \rightarrow |g\rangle_a|e\rangle_m|0\rangle$, and then driving a red sideband on the $^{24}MgH^+$ to $|g\rangle_a|g\rangle_m|1\rangle$. The sequence is identical from this point forward. The red sideband can also be probed by preparing in $|n = 1\rangle$, for example.

This sequence can be used for spectroscopy even if it is not possible to implement a coherent pulse on the sideband. If we drive $^{24}MgH^+$ sidebands using an incoherent light source, we still have excitation out of the ground state, and thus will detect a signal on $^{40}Ca^+$. This extension of QLS has been termed photon-recoil spectroscopy [123] and sympathetic heating spectroscopy[9] [125] and in both cases was implemented in atomic ions. In an attempt to avoid confusion between terms, I will refer to all techniques as QLS, and clarify what situation I am referring to.

Since QLS relies on a high probability of the ion being in the ground state of motion if a transition did not occur, it is important that the heating rate of the trap is small compared to the interaction time of the ion[10]. Because QLS is carried out on only one of the two axial modes, we can choose the mode with the lower heating rate: the out-of-phase mode. In a $^{40}Ca^+$-$^{24}MgH^+$ crystal, this mode has a heating rate 3.5 times lower than single ion would at the same frequency $\omega_-$.

The only caveat is that the heating of the in-phase mode influences the Rabi frequency of the out-of-phase mode. Thus, as the in-phase mode heats, the signal height of the out-of-phase mode reduces (see Appendix C.3). This only becomes significant at high $\bar{n}$, and the lower the $\eta$, the less it contributes.

## 6.5 Adiabatic cooling

The challenge of using QLS to perform direct vibrational spectroscopy is that QLS requires driving sideband transitions on the vibrational transitions. Vibrational transitions in $^{24}MgH^+$ are in the mid-IR ($\simeq 6\,\mu m$), and these photons carry nearly an order of magnitude less momentum than photons at 729 nm. Thus, compared to exciting a carrier transition, it is much more difficult to excite a sideband transition in $^{24}MgH^+$ than in $^{40}Ca^+$.

[9] Here the experiment was carried out without sideband cooling and detection was based on fluorescence levels. Their suggestion for ground state cooled ions was termed quantum sympathetic heating spectroscopy [124].

[10] It should be noted that QLS schemes also exist for ions which are not sideband cooled [33].

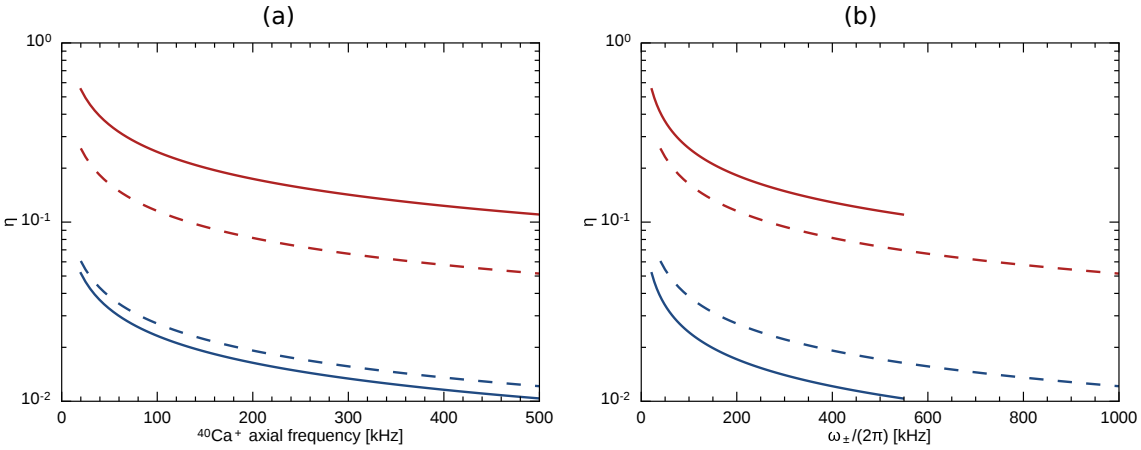


Figure 6.9: The Lamb Dicke parameter of a $^{40}Ca^{+}$-$^{24}MgH^{+}$ two-ion chain as a function of **(a):** the equivalent single $^{40}Ca^{+}$ ion frequency, and **(b):** $\omega_{\pm}$. In each, the red curves show $\eta_{\pm}$ for driving a 729 nm transition in $^{40}Ca^{+}$, and the blue curves show $\eta_{\pm}$ for driving a 6.2 µm transition in $^{24}MgH^{+}$. The solid lines are $\eta_{+}$, and the dotted are $\eta_{-}$.

A solution to this problem can be found by comparing the Lamb Dicke parameters for $^{24}MgH^{+}$ versus $^{40}Ca^{+}$. The scattering rate on a sideband is proportional to the square of the Lamb Dicke parameter, which is given for a two ion crystal by Equation 3.32. The important point is that

$$\eta^2 \propto \frac{k^2}{\omega_{\pm}} \tag{6.4}$$

While we cannot control the wavelength of the transition, we can control the axial frequency. Thus, by lowering the axial frequency, we can increase the sideband scattering rate. The axial frequency dependence of the $^{40}Ca^{+}$ and $^{24}MgH^{+}$ $\eta$'s is shown in Figure 6.9.

As explained in section 5.3, sideband cooling becomes much more complex as the Lamb Dicke parameter increases. Further, as the axial frequency decreases, the spectral resolution of the sideband spectrum decreases. Most notably, the $2^{nd}$ order in-phase sidebands become closer and closer to the $1^{st}$ order out-of-phase sidebands. Figure 6.10 shows how the $(2\omega_{+} - \omega_{-})/\omega_1$ changes as a function of mass-ratio. Thus, we do not want to perform operations on $^{40}Ca^{+}$ at low $\omega_{\pm}$. The solution is to sideband cool at high $\omega_{\pm}$, adiabatically lower $\omega_{\pm}$, perform the spectroscopy pulse on $^{24}MgH^{+}$, and adiabatically raise $\omega_{\pm}$ before measuring the sideband on $^{40}Ca^{+}$. This process of adiabatically opening the trap potential is called adiabatic cooling. It is called cooling because if we lower the axial frequency without changing the motional quantum number $n$, the energy given by the harmonic Hamiltonian decreases

$$E_{ho} = \hbar\omega_z \left(n + \frac{1}{2}\right) \tag{6.5}$$

We can see as well from Equation 4.44 that decreasing $\omega_z$ lowers the temperature of the ion in the z-direction.

For a frequency ramp to be adiabatic, it must not change the motional occupation of the harmonic oscillator. The condition for this is given by

$$\beta \simeq \frac{\dot{\omega}_z}{\omega_z^2} \ll 1 \tag{6.6}$$

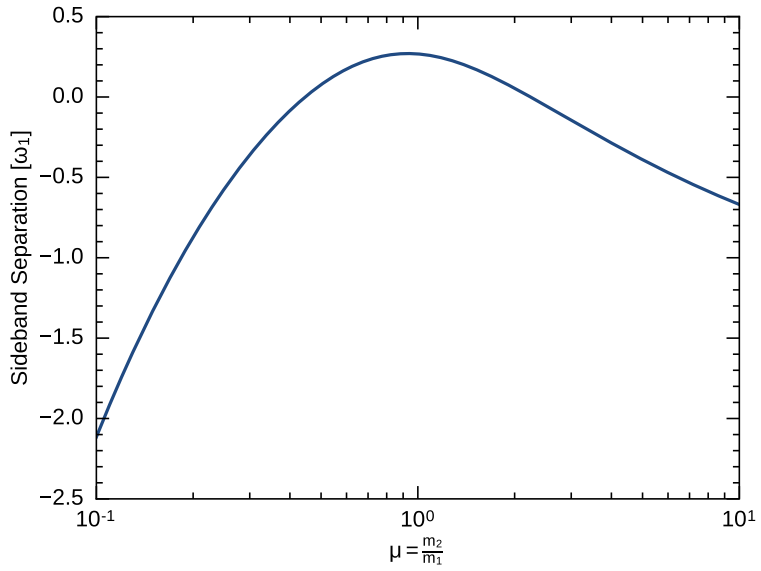


Figure 6.10: Separation between the second in-phase sideband and the first out-of-phase sideband, as a function of mass ratio $\mu$, in units of $\omega_1$, the axial frequency of a single ion of mass $m_1$.

From this expression, it is evident that the shape of the frequency ramp will impact the evolution of $\beta$ in time. Y. Guberman [126] looked into the adiabaticity of different shape ramps—square-root, exponential, and constant adiabaticity—by calculating the expected gain in motional quanta, $\Delta\bar{n}$ for three different ramp shapes. He solves each numerically, and provides analytical approximations for the results.

These three frequency ramp shapes are shown in Figure 6.11. Experimentally, we reduce $\omega_z$ by lowering $V_{end}$. This makes a frequency ramp with a square-root time dependence interesting because it corresponds to a linear voltage ramp. It was found that this ramp type far under performs the other two. This is not unexpected, as the rate-of-change of frequency stays constant, but the frequency decreases. Thus, it becomes harder and harder to fulfill the adiabaticity condition as the ramp decreases in frequency.

An exponential time dependence is also of interest. It is a shape that naturally arises from electronic filtering, though in a one-sided direction[11]. The last, and perhaps most obvious choice, is a ramp shape that keeps the adiabaticity parameter $\beta$ constant. Defining $\omega_{z,t}$ as the axial frequency at the top of the ramp, $\omega_{z,b}$ as the frequency at the bottom of the ramp, and $\alpha = \frac{\omega_{z,b}}{\omega_{z,t}}$, the functional form of the ramp is given by

$$\omega_z(t) = \frac{\omega_{z,t}}{1 + \frac{t}{t_r}(\frac{1}{\alpha} - 1)} \tag{6.7}$$

where $t_r$ is the time it takes to complete the ramp.

Figure 6.12 compares for variable $t_r$ the heating of an exponential ramp and a constant adiabaticity ramp for a ramp with $\omega_{z,t}/(2\pi) = 284\,\text{kHz}$ and $\omega_{z,b}/(2\pi) = 22\,\text{kHz}$, which corresponds

[11] A capacitive filter will cause initial voltage changes to happen quickly, and final voltages changes to happen slowly. This means that for decreasing the frequency, this ramp does well to fulfill the adiabaticity condition, but upwards it does not.

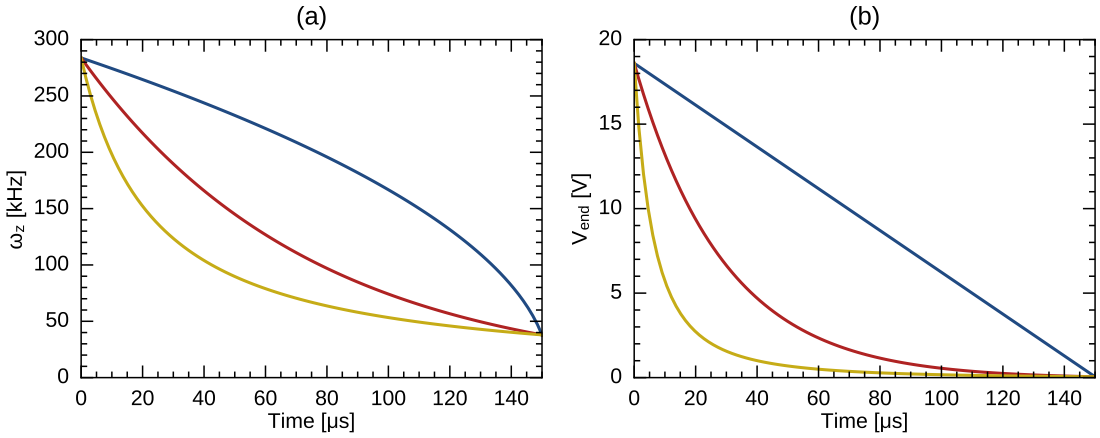


Figure 6.11: **(a):** Three different types of frequency ramps from $\omega_{z,t}284\,\text{kHz}$ to $\omega_{z,b}22\,\text{kHz}$ in 150 µs, with square-root ramp, exponential ramp, and constant adiabaticity ramp. **(b):** the corresponding voltage ramps.

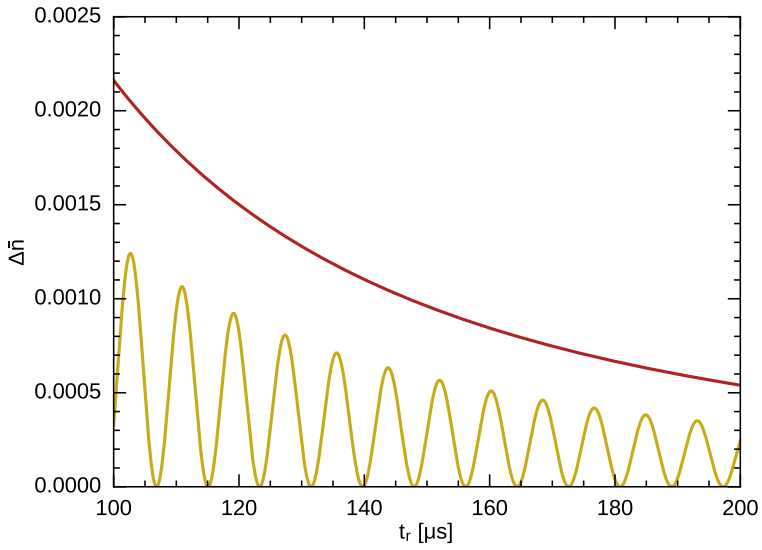


Figure 6.12: Expected $\Delta n$ for a ramp with $\omega_{z,t}/2\pi = 284\,\text{kHz}$ and $\omega_{z,b}/2\pi = 22\,\text{kHz}$, with exponential ramp and constant adiabaticity ramp.

to $V_{end} = 18.6\,\mathrm{V}$ to $0.05\,\mathrm{V}$. The heating of a square-root ramp with these parameters gives more than a quanta of heating. Because the constant adiabaticity ramp out-performs the exponential ramp[12], we choose to implement the constant adiabaticity ramp.

The heating of the the constant adiabaticity ramp has the form [126]

$$\bar{n} = \frac{1}{4}\left(\frac{1}{\omega_f t_f}\right)^2 (1-\alpha)^2 \sin^2\left(\omega_f t_f \frac{\log(\alpha)}{1-\alpha}\right) \tag{6.8}$$

[12]Noted in numerical simulations of the exponential ramp, a sinusoidal form is also seen, however in the exponential case the oscillations are centered around the line.

# Part III

# Experimental Setup

# Introduction

The full experimental setup for our ion trap experiments is extensive, spanning several rooms, with the trap setup in one room and the laser systems in other rooms. Nine months into my PhD we had the joy of moving our labs from one basement to another[13]. Thankfully, all of the optics stayed on the tables, but nearly every cable had to be labeled, unplugged, and moved. Free space beam paths had to be reworked, and many fibers had to be strung. The benefit of moving, however, was brand new lab facilities spread over 11 rooms and a much better understanding of the apparatus. Figure 6.13 shows on the left, the old lab, in the center, our trap table being lowered by a crane into the basement, and on the right, the central laser room of our new lab.

There are many aspects to an ion trap experimental setup, thus this part is broken into several chapters. Chapter 7 covers the setup on the trap table. This consists of the trap which sits inside of the vacuum chamber surrounded by an optical table for guiding laser beams into the chamber. Above the chamber sits the imaging system, which enables us to see the ion fluorescence. Also covered in this chapter is the magnetic field used to control the Zeeman splitting of the ions. Lastly, I discuss means of production of the ions.

Chapter 8 covers the laser systems used in the experiment and Chapter 9 covers the electronics used to provide voltages on the trap electrodes. Lastly, Chapter 10 discusses the experimental control system.

Figure 6.13: **Left:** the old lab. **Center:** the trap table is lowered by a crane to the basement. **Right:** the central laser lab in the new lab. Typically in the new lab, all tables are surrounded by curtains.

[13] "We moved a few things around in the lab...and the lab."

# Chapter 7

# Trap setup

## 7.1 Trap

As described in Chapter 2, we trap ions in a linear Paul trap. The trap in our setup was designed by Niels Kjærgaard circa 2000 [127]. Figure 7.1 shows a photograph of the trap.

The dimensions of the trap, given in Table 7.1, were chosen such that the potential seen by a large crystal would be approximately harmonic. This was achieved by choosing the ratio of $R/r_0$ (as defined in Figure 2.1) such that close to the axis, the potential is nearly perfectly quadrupolar [65, 128]. The length of the central electrodes, combined with the long endcap electrodes, was chosen such that the harmonic approximation of the DC confinement would hold over a scale of mm's [127] away from the trap center. It speaks to the versatility of this trap that it can be used for experiments of both large crystals and single ions.

The trap electrodes are constructed of 12 sections of gold-coated stainless steel rods, insulated from one another by Macor. The 12 electrodes are split into four rods of three pieces, with the four rods mounted in Macor. The construction of a single rod is show in Figure 7.2.

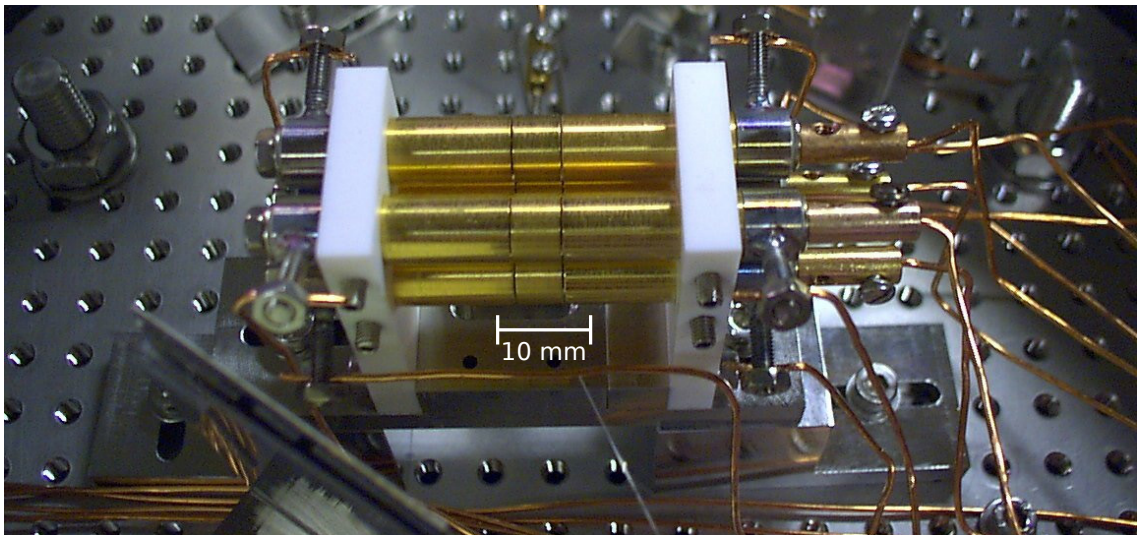


Figure 7.1: A photograph of the linear Paul trap used in the experiments presented in the thesis. Figure from N. Kjærgaard [127].

| Geometric trap paramters | |
|---|---|
| $z_0$ | 2.70 mm |
| $r_0$ | 3.50 mm |
| $R$ | 4.00 mm |
| $z_e$ | 20.00 mm |
| $\kappa$ | 0.248 |

| Typical trapping parameters | | |
|---|---|---|
| | Single Ion | Two Ions |
| $a$ | 0.023 | 0.007 |
| $q$ | 0.49 | 0.34 |
| $V_{RF}$ | 1090 $V_{pp}$ | 750 $V_{pp}$ |
| $V_{end}$ | 60 V | 18.6 V |
| $\omega_r$ | 730 kHz | 525 kHz |
| $\omega_z$ | 509.1 kHz | 283.7 kHz |
| $\Omega_{RF}$ | $2\pi\times4.682$ MHz | |

Table 7.1: Trap parameters. $q$ values and $V_{RF}$ are calculated from spectra of the radial modes. The geometric parameters refer to the parameters defined in Figure 2.1. Ion frequencies $\omega_z$, $\omega_r$ refer to the measured frequencies for $^{40}Ca^+$ ions at the voltages listed.

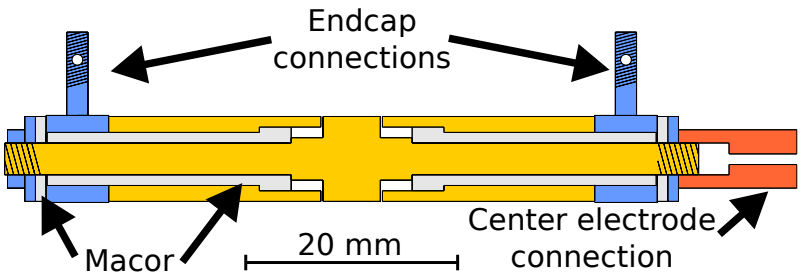


Figure 7.2: Construction of a single rod of the ion trap. The yellow sections are gold-coated stainless steel. Figure from N. Kjærgaard [127].

The voltages, $V_{end}$ and $V_{RF}$, that are applied to the trap change depending on the experimental situation, and are tabulated in Table 7.1. Lower voltages were chosen for the two-ion case for several reasons:

- The Lamb Dicke parameter(s) $\eta$ is smaller in a two-ion crystal than for a single ion, so $\omega_z$ can be smaller and achieve the same $\eta$.
- With a two-ion crystal, we saw that the ions had a tendency to decrystalize from an axial crystal and rotate in the radial plane. We found that this was alleviated by lowering $V_{RF}$, possibly as a result of lowering the $q$ parameter. This lowers $\omega_r$, and to keep the ions crystallized axially, $\omega_r > \omega_z$ must be fulfilled. Thus, must $V_{end}$ also be lowered.
- For $^{24}MgH^+$, the single ion voltages are the very end of the stability region, as shown in Figure 7.3. In other words, q would be even higher for $^{24}MgH^+$.

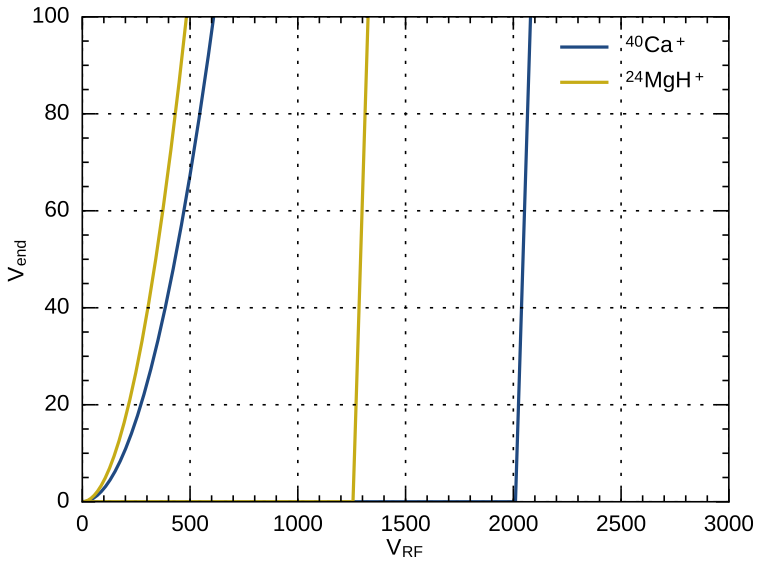


Figure 7.3: Stability diagram in terms of the trap voltages for $^{40}Ca^{+}$ and $^{24}MgH^{+}$.

For the experiments presented, precise knowledge of $\omega_z$ at a range of $V_{end}$ is required. To calibrate $\omega_z\,(V_{end})$, we take advantage of the fact that the cooling beam exerts light pressure on the ion. By pulsing the cooling beam, we create a driven harmonic oscillator. When the beam is pulsed at the frequency $\omega_z$, the ion is excited and appears blurry on the camera. For each measurement, the power of the pulsed cooling beam is reduced to the lowest possible where we can still see the ion, to reduce the influence of the cooling force on the oscillation. Using this method, we can extract $\omega_z$ to about 100 Hz precision [102]. We then fit

$$\omega_z\,(V_{end}) = \sqrt{\frac{2Q\kappa \times A(V_{end}+B)}{mz_0^2}} \tag{7.1}$$

to the measured $\omega_z$, with fit variable parameters $A$ and $B$. A plot showing the measurements and fit is given in Figure 7.4. The plot shows two sets of data, taken 10 months apart, whose fit parameters agree. The $a$ trap parameter is calculated from the measured $\omega_z$ as per Equation 2.8.

For $\omega_r$, the radial spectrum was measured by resolving the motional sidebands in the radial direction after only Doppler cooling. $V_{RF}$ is then calculated with the measurements of both $\omega_r$ and $\omega_z$. The $q$ parameter is then also calculated from these frequencies as per Equation 2.8.

## 7.2 Vacuum chamber

To isolate the ion trap from background gas collisions, the trap is placed in the center of a vacuum chamber. The chamber has not been opened for more than 10 years, so the only thing required to maintain vacuum is an ion getter pump[1]. The pressure is monitored by an ion gauge[2], and typical background pressures are $2 \times 10^{-10}$ mbar as reported by the ion gauge. The vacuum system

[1] Leybold IZ 270
[2] AML UHV Bayard-Alpert

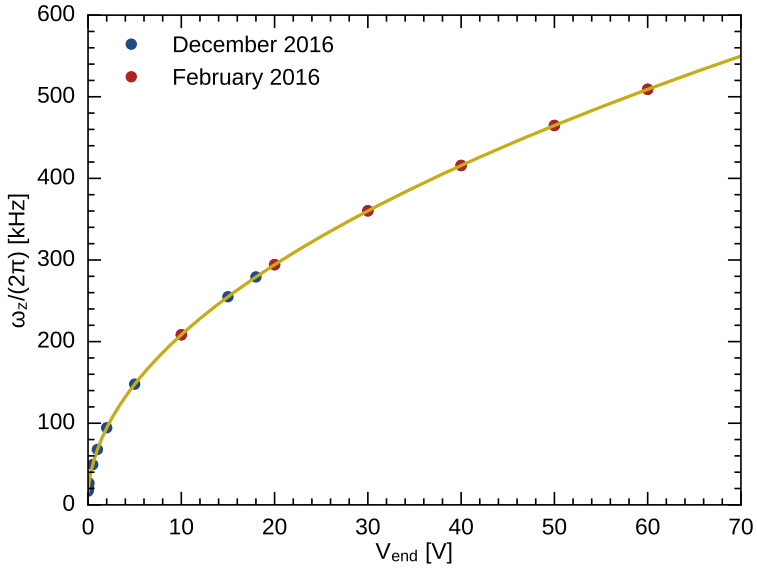


Figure 7.4: Curve showing the calibration of $\omega_z$. Measurements are for a single $^{40}Ca^+$. The fit follows Equation 7.1 and the parameters for the curve are $A = 1.045\,85(5)$ and $B = 0.0650(1)$ V. This fit is to the data in December. For every point in February, there is a corresponding point for December.

further is equipped with a leak value such that gas (e.g. $H_2$) can be leaked in to facilitate reactions with atomic ions to form molecular ions.

The chamber is mounted such that it is surrounded by an optical table, and has 7 ports around the circumference for optical access, 8 ports for other purposes, as well as one port on top for imaging access. A photograph of the chamber surrounded by the optical table is shown in Figure 7.5, a diagram shown from the top is in Figure 7.6, and an image of the inside of the chamber is in Figure 7.7. The optical ports are fused silica, aside from the two 45° ports which are made of $CaF_2$ to allow for optical access with the 6 µm quantum cascade laser for vibrational spectroscopy and rotational cooling of $^{24}MgH^+$.

The ports not used for optical access serve other purposes, as labeled in Figure 7.6, and understanding the inside of the chamber shown in Figure 7.7 can help us understand what they are for. The ion trap sits in the middle of the chamber. The trap electrodes need to be provided with RF and DC voltages, which are sourced through the trap feedthrough which can be seen at the center top of the photo.

The atom ovens (see section 7.5 for more on the production of ions) containing Mg and Ca are shown in the right hand side of the chamber. The atom beams are skimmed by two skimmers, and the beams can be blocked by a mechanical shutter, moveable from outside the chamber. The current for heating these ovens comes in through a feedthrough, and the outputs of two oven thermocouples are sent through the same feedthrough. Not visible in Figure 7.7 is the ion gauge filament.

The alignment fiber can be moved into the trap via a translation stage from outside the chamber, such that the end of the fiber is in the center of the trap. This is useful for rough alignment of the laser beams to the ion position, as it is easier to see scattered light from the fiber than a signal from the ion, as the fiber has a 125 µm diameter. It is also helpful for positioning the imaging

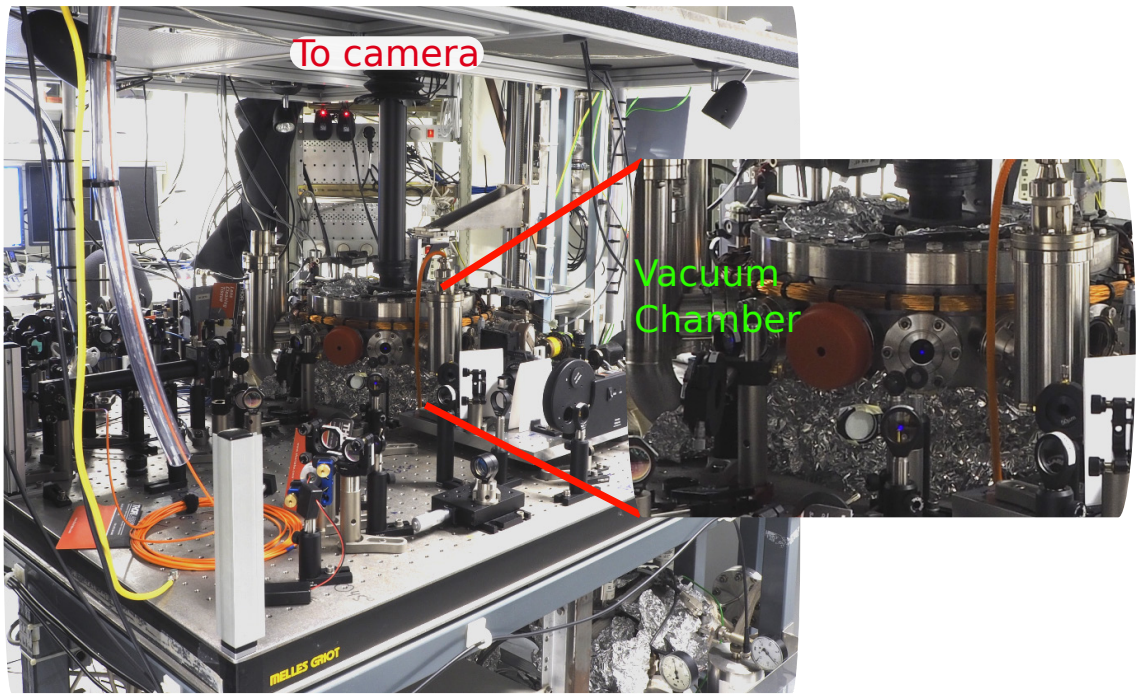


Figure 7.5: Photograph of the trap optical table, with the vacuum chamber in the center.

system to be roughly centered on the ion.

Also pictured in Figure 7.7 is an electron gun. This, along with the rest gas analyzer (RGA), and liquid nitrogen container are not used in the experiments presented in this thesis. Lastly, a lens for focusing into a photomultiplier tube (PMT) for detection is shown in Figure 7.7. This is not currently used, but we may wish to use it in the future.

## 7.3 Imaging system

The imaging system looks down on the ion from above through the top viewport of the vacuum chamber. It is constructed of a lens, an image intensifier, and a camera. The entirety of the imaging system is mounted on a tower, and its height is adjustable using a motor. The tower is mounted to the frame of the trap optical table.

A schematic of the imaging system is presented in Figure 7.8. The lens used is a custom-made compound lens with a focal length of 70 mm and a numerical aperture of 0.28. The lens is placed approximately 7.5 cm away from the ion, just above the top viewport, and is mounted on a translation stage with micrometer screws for precision positioning. About one meter higher, the ion image is focused onto an image intensifier[3]. The output of the image intensifier is focused by another lens[4] onto a CCD camera[5]. The image intensifier is powered by homebuilt electronics[6], and can be gated down to 1 ns.

[3]Proxitronic, BV 2581 BY-V 1N
[4]Nikon AF Micro Nikkor 60mm f/2.8D
[5]PCO Sensicam QE
[6]By Erik Søndergaard

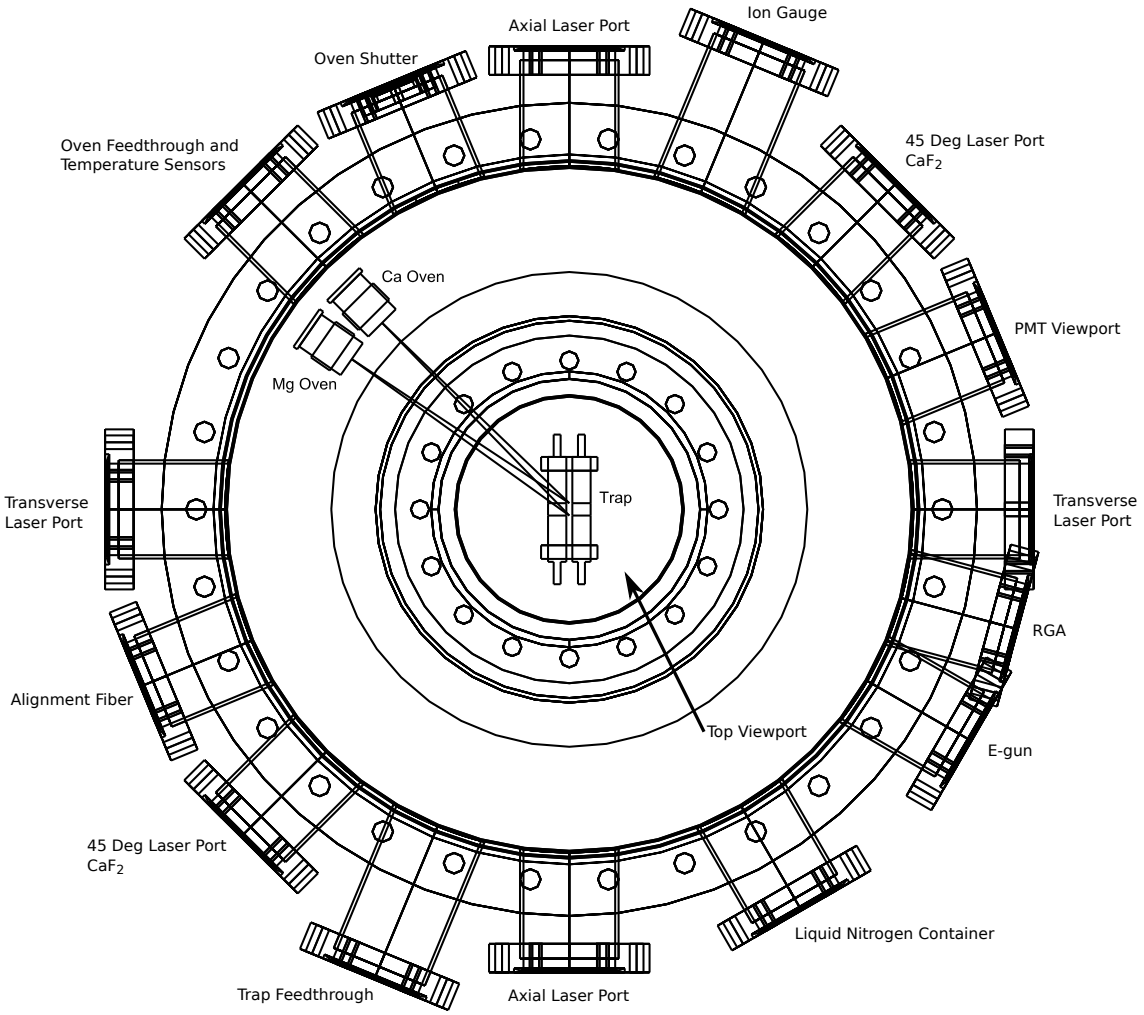


Figure 7.6: Overhead schematic of the vacuum chamber. Figure from N. Kjærgaard [127].

The magnification of the imaging system is calibrated by measuring the distance between two axially-aligned ions at varying axial frequencies, as the absolute distance between two ions can be calculated if one knows the axial frequency. Images of the ions are shown in Figure 7.9 (a). The distance between them in pixels is found by fitting the intensity distribution across the images to a sum of Lorentzians, shown in Figure 7.9 (b).

Equation 2.14 from section 2.2 gives the equilibrium distance $z_{eq}$ of two ions. If we measure this distance in CCD pixels, we get the expression

$$z_{eq}[pix] = A\left(\frac{2e^2/4\pi\epsilon_0}{m\omega_z^2}\right)^{\frac{1}{3}} \tag{7.2}$$

where A is the number of pixels per meter. By fitting the measured pixel separation versus axial frequency with Equation 7.2 (Figure 7.9 (c)), we obtain $A = 0.677(3)\,\text{pixels}/\mu\text{m}$, which is $\frac{1}{A} = 1.477(2)\,\mu\text{m}/\text{pixel}$. The size of each CCD pixel is $6.45\,\mu\text{m} \times 6.45\,\mu\text{m}$, giving a total system magnification of $M = 4.4$.

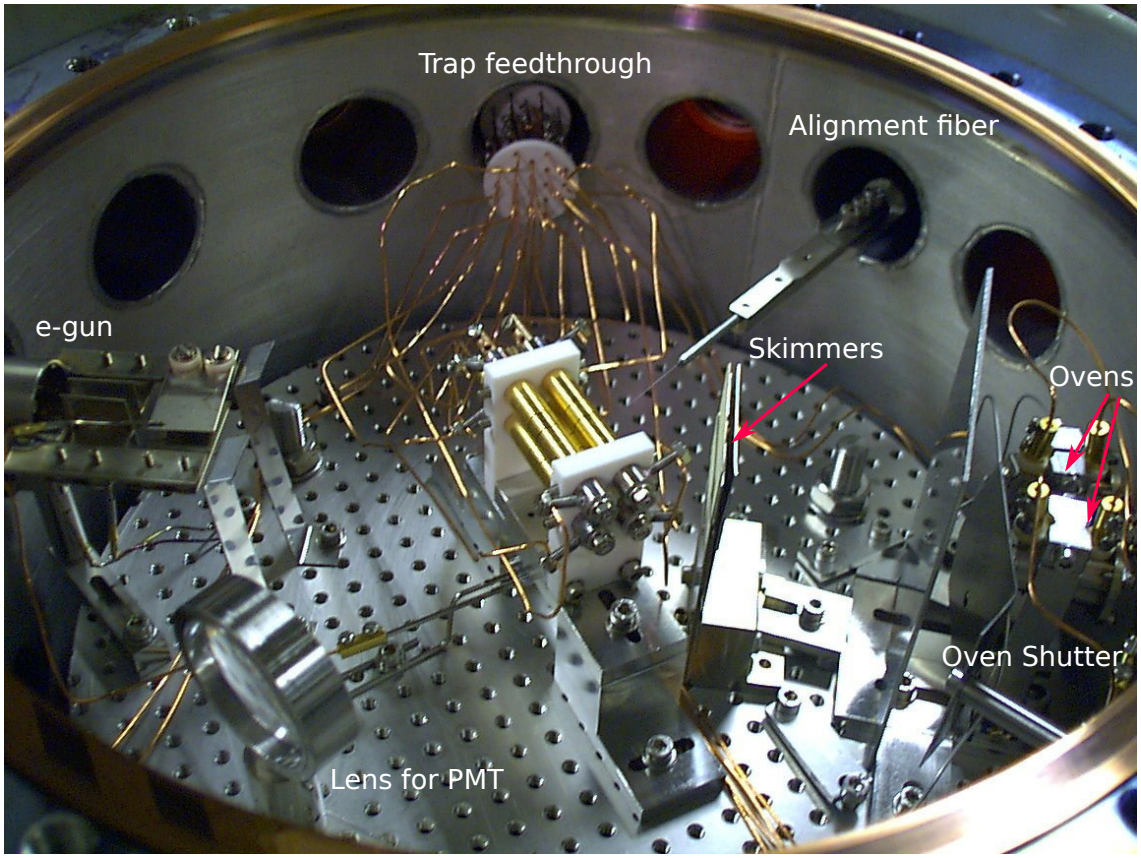


Figure 7.7: The inside of the trap vacuum chamber. Photo from N. Kjærgaard [127].

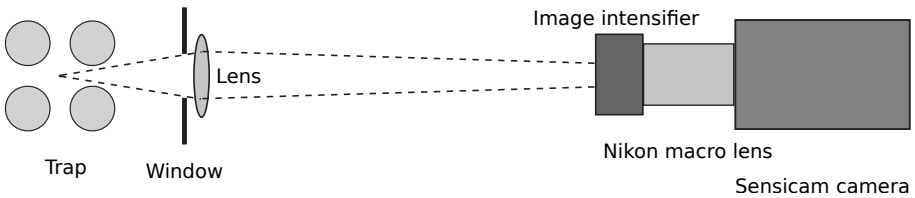


Figure 7.8: Schematic of the imaging system. In the setup, the camera is above the trap (vertical).

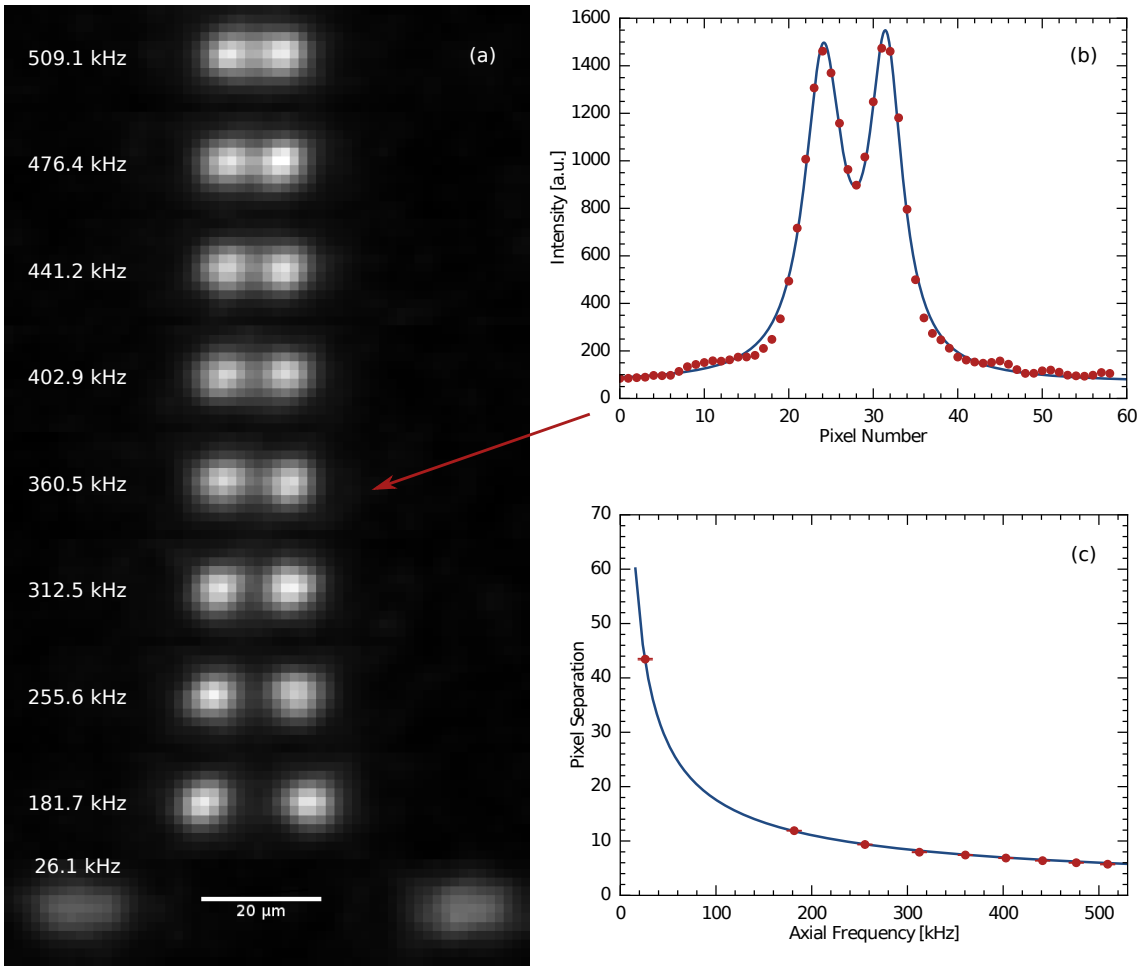


Figure 7.9: Magnification calibration **(a)** Images of two ions at varying axial frequencies $\omega_+/(2\pi)$. **(b)** Intensity profile of the image at $\omega_+/2\pi = 360.5\,\text{kHz}$ as a function of horizontal pixel number. The intensity is fit to a sum of two Lorenzians. (c) shows the fitted ion separation as a function of $\omega_+/(2\pi)$, and the fit with Equation 7.2.

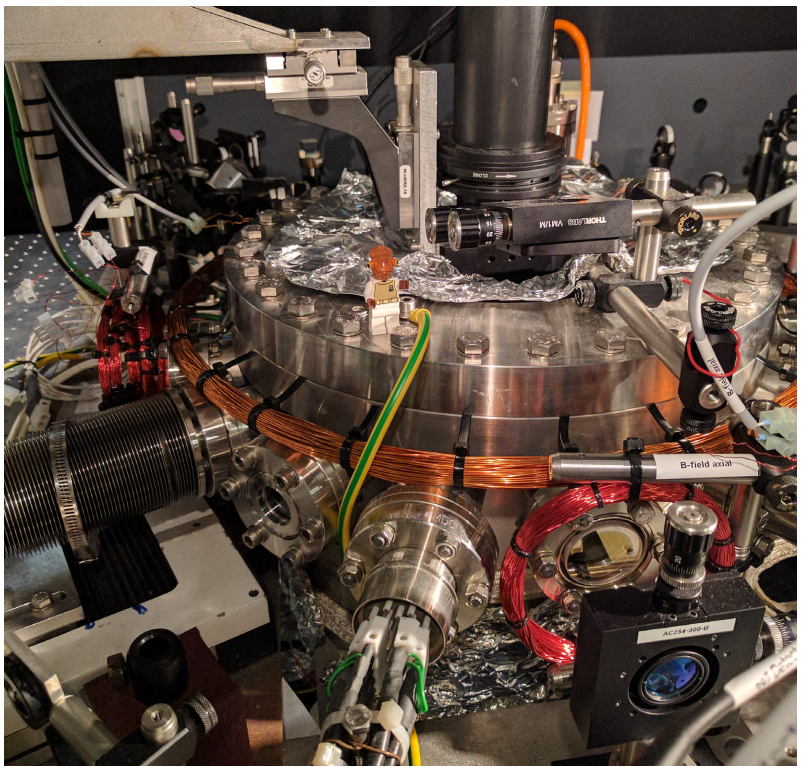


Figure 7.10: Photograph showing magnetic field coils. The orange coil wrapped around the trap provides the quantization axis magnetic field. The two red coils, one in the front and one on the left, provide angular magnetic field compensation. The coil for AC magnetic field compensation sits underneath the tin foil, on top of the top viewport.

## 7.4 Magnetic field

The magnetic field used to control the Zeeman splitting in $^{40}Ca^{+}$ is produced by a coil that sits on the vacuum chamber, shown in Figure 7.10. The magnetic field that the ion sees from this coil defines the quantization axis, which is perpendicular to the trap axis, and is oriented vertically in the lab frame. The coil is composed of 100 turns of copper wire with a diameter of 42 cm. The vertical distance of the coil to the ion is approximately 4.5 cm. The magnetic field at the ion is approximately $3\,\mathrm{G\,A^{-1}}$, as measured on the ion by measuring two $^2S_{1/2} \rightarrow {}^2D_{5/2}$ transitions with different $m_J$ and using Table 5.1 to calculate the field. Typically we run experiments with a magnetic field of about 6.5 G, accomplished by running the coil at a fixed current of 2.170 A, provided by a low-noise current source[7]. The rated current ripple on this supply is $200\,\mu A_{rms}$ [129]. This corresponds to magnetic field fluctuation of $600\,\mu G_{rms}$.

To adjust for a tilt in the magnetic field due to stray fields, the earth's field, and imperfect coil placement, two smaller coils are placed such that their magnetic fields point in perpendicular horizontal directions. The coils are wrapped around viewports, as seen in Figure 7.10, and have 400 windings each at a diameter of 10 cm. They sit 23 cm away from the ion.

The compensation of the field tilt is done by taking advantage of the fact that for a dipole transition, $\pi$-polarized light only drives transitions where $\Delta m = 0$. We can set the polarization of the

[7] Toellner TOE 8852-32

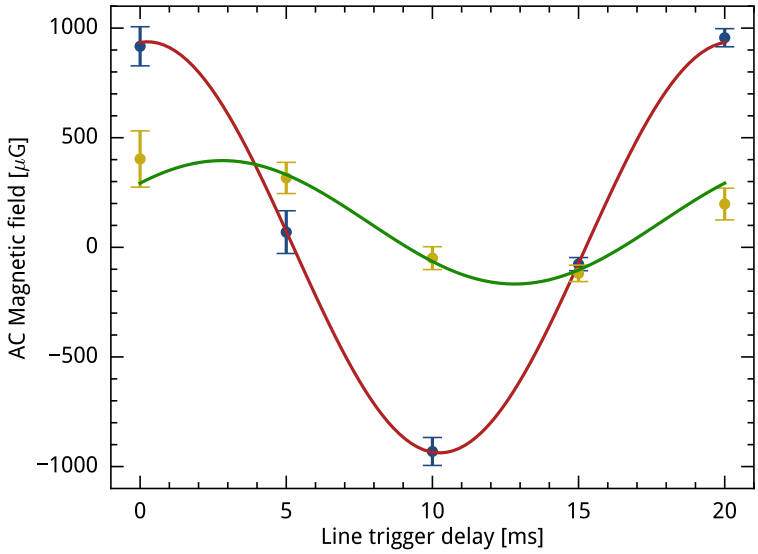


Figure 7.11: Comparison of the 50 Hz magnetic field noise at the ion before and after compensation, as measured on the $^2S_{1/2}$, $m_J = -1/2 \rightarrow {}^2D_{5/2}$, $m_J = -5/2$ transition.

866 nm repump beam to vertical. The smaller the angle between the polarization and the magnetic field, the less effective the 866 nm beam will be at repumping as the ions get trapped in dark states [100]. The crystal's fluorescence will therefore decrease. By monitoring the fluorescence of the crystal while scanning the current to the compensation coils, it is possible to adjust the direction of the field at the ion to be vertical. The currents of the coils after adjustment are 224 mA in the trap's axial direction, and 454 mA in the radial direction, corresponding to a magnetic field at the ion of 219 mG and 109 mG, respectively. The compensation is good within 5 mG.

Because the frequencies of the transitions used for sideband cooling and shelving are dependent on magnetic field, it is important that the magnetic field is stable during measurements. The AC wall voltage at 50 Hz means that there is a lot of 50 Hz magnetic radiation in the lab. To combat the changing field over time, we do two things. One is that we line-trigger our experiment, that is, always start it at the same point during the AC line. This means that the sequences are repeatable. However, since a sequence consists of many parts, and various sequences may not have identical timing, the field changes over the course of a measurement, or between two different types of measurement. Ideally, then, we reduce this magnetic field noise as much as possible.

We compensate the AC magnetic field using an additional coil (approx. 100 turns, 7 cm from the ion, 18 cm diameter) that sits on top of the chamber's top viewport. A phase-shifted and amplitude-adjusted AC line is fed into this coil. The amplitude and phase shift are experimentally adjusted until the 50 Hz oscillation of the transition frequencies is minimal. Figure 7.11 shows a plot of the AC magnetic field noise as a function of relative delay from the line trigger before and after compensation, as calculated from the $^2S_{1/2}$, $m_J = -1/2 \rightarrow {}^2D_{5/2}$, $m_J = -5/2$ (shelving) transition frequency using Table 5.1. The pre-compensation amplitude is 938(12) μG and the post compensation amplitude is 280(70) μG. This corresponds to 2.62(3) kHz and 0.8(2) kHz on the shelving transition.

It is also important that the field and the field compensation stay consistent over time. Figure 7.12 shows the calculated magnetic field over the course of 6 hours overnight (when the field is more stable). This measurement was taken by measuring the $^2S_{1/2}$, $m_J = -1/2 \rightarrow {}^2D_{5/2}$, $m_J =$

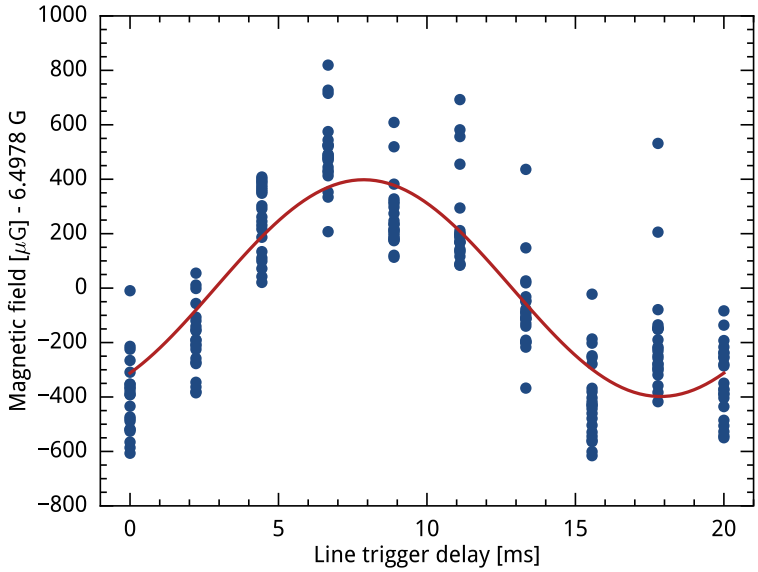


Figure 7.12: Magnetic field as a function of relative delay from the line trigger, taken over the course of 6 hours at night. The field is calculated by measuring the $^2S_{1/2}$, $m_J = -1/2 \rightarrow {}^2D_{5/2}$, $m_J = 3/2$ and $^2S_{1/2}$, $m_J = 1/2 \rightarrow {}^2D_{5/2}$, $m_J = -3/2$ transition frequencies. The fit puts the 50 Hz noise amplitude at 400(20) µG.

3/2 and $^2S_{1/2}$, $m_J = 1/2 \rightarrow {}^2D_{5/2}$, $m_J = -3/2$ transitions consecutively and taking the difference $\Delta\nu$ of the two frequencies for varying delay times with respect to the AC phase. This is expressed mathematically as

$$\begin{aligned} \nu_{\pm 2} &= \nu_{729} \pm \left( \frac{d\nu}{dB}\{^2S_{1/2}\}B + \frac{d\nu}{dB}\{^2D_{5/2}, \pm 3/2\}B \right) \\ \Delta\nu &= \nu_{+2} - \nu_{-2} \\ &= 2B \left( \frac{d\nu}{dB}\{^2S_{1/2}\} + \frac{d\nu}{dB}\{^2D_{5/2}, \pm 3/2\} \right) \end{aligned} \tag{7.3}$$

where $\nu_{729}$ is the non-Zeeman-shifted frequency of the $^2S_{1/2} \rightarrow {}^2D_{5/2}$ transition, $\nu_{\pm 2}$ refers to the measured frequencies of the specific $\Delta m_J = \pm 2$ transitions mentioned above, and $\frac{d\nu}{dB}$ for the relevant states comes from Table 5.1. These two transitions were chosen since the difference between them is dependent on only two shifts and the magnetic field. By subtracting the two transition frequencies, shifts due to laser frequency drift drop out.

The amplitude of the 50 Hz noise is 400(20) µG and is consistent throughout the night. The point spread in Figure 7.12 is not obviously correlated with time and could be due to small, frequent field shifts or laser frequency fluctuations on the time scale of a measurement. It could also be related to the voltage ripple rating of the supply, though the datasheet is not specific about the frequency of the ripple, and rather gives a frequency range. It is unlikely that ripple at high frequencies is the issue, as the spectroscopy peak would be comparably broad, which we do not see.

During the day and over time, we see that the magnetic field is much less stable than over the course of a single night, changing by up to 6 mG in a day due to sudden jumps. Nights, on

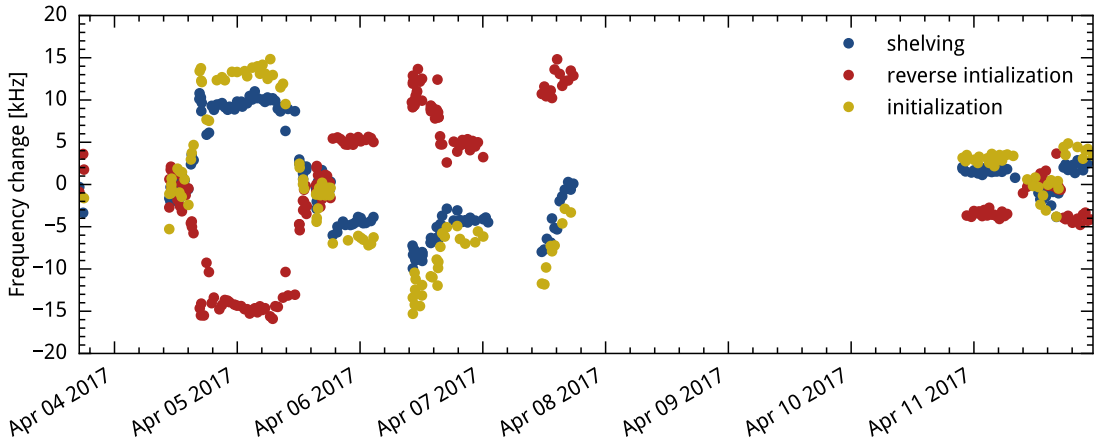


Figure 7.13: Measured shift of the transition frequencies of three transitions. The near perfect anti-correlation of the initialization and reverse initialization transitions indicates that the magnetic field is changing, and the laser frequency is constant. Note that the transition frequencies are often stable at night, with midnight corresponding to the date markers.

the other hand, see a stability on the order of the point spread shown, around 400 µG. For the shelving transition, this corresponds to shifts on the order of 1 kHz. Figure 7.13 shows a series over the course of several days of measurements of three transitions: the $^2S_{1/2}$, $m_J = -1/2 \rightarrow {}^2D_{5/2}$, $m_J = -5/2$ shelving transition, the $^2S_{1/2}$, $m_J = -1/2 \rightarrow {}^2D_{5/2}$, $m_J = 3/2$ reverse initialization transition, and the $^2S_{1/2}$, $m_J = 1/2 \rightarrow {}^2D_{5/2}$, $m_J = -3/2$ initialization transition. We can see that the transition frequencies of the reverse initialization and initialization transitions follow one another oppositely, meaning that frequency shifts are due to magnetic field changes. The flat sections of transition frequencies almost exclusively occur at night. Thus, when possible, measurements were taken at night.

## 7.5 Ion production

Two atom ovens sit inside the vacuum chamber, shown in Figure 7.7 and schematically in Figure 7.6. The ovens are made from hollow graphite cylinders, one of which contains Ca and the other of which contains Mg. The ovens are heated by running current through tungsten wire coiled around the cylinder. The heated atoms effuse out of a 1 mm hole in the oven forming an atom beam, which is collimated by skimmers [130] between the ovens and the trap such that the atoms do not contaminate the electrodes. The divergence angle after the skimmers is 23 mrad.

The oven temperatures are measured by thermocouples placed on the graphite cylinders. This signal from the thermocouples is measured by thermocouple readers[8] connected to an Arduino. The Arduino communicates via USB with a Raspberry Pi. The Raspberry Pi logs the temperature data to an online database[9], and maintains a a locally-accessible website which gives the current temperature of the ovens. A plot showing the warm up of the ovens when current is applied only to the Ca oven[10] is shown in Figure 7.14.

[8] MAX31850K
[9] PostgreSQL
[10] None of the experimental results in this thesis deal with $^{24}Mg^+$, but it is integral for future experiments with $^{24}MgH^+$

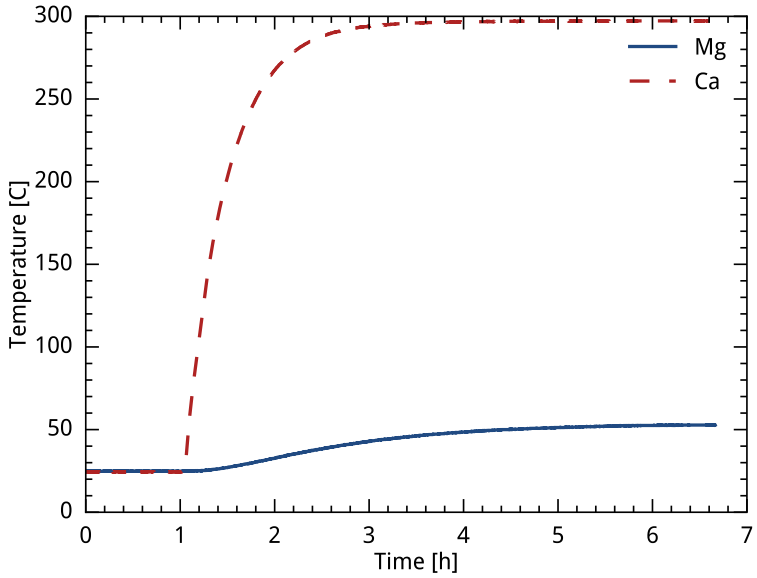


Figure 7.14: Warm up of the Ca oven. The Mg oven also warms slightly due to its proximity to the Ca oven.

Typically to load $^{40}Ca^+$, we run the oven at 5 A, which heats the oven to 300 °C (573 K). This gives a vapor pressure of $4.5 \times 10^{-8}$ mbar, as shown in Figure 7.15. For loading single $^{40}Ca^+$ ions, this is sufficient to load within a few ms. However, to ionize $^{42}Ca$, which has an abundance of 0.647 % compared to 96.941 % for $^{40}Ca$, it is easier if the temperature is increased to 400 °C (673 K), giving a factor of 100 in vapor pressure. This is the difference between waiting minutes versus seconds to load a single ion. A table of the isotope abundances is given in Appendix A.

We use resonance-enhanced two-photon ionization to isotope-selectively ionize Ca and Mg. This technique was pioneered by our group in Aarhus [132–134]. The atom beams propagate at a 45° angle to the trap axis. The photoionization beam propagates perpendicular to the atom beams to minimize Doppler broadening, and they meet in the center of the trap.

A diagram of the ionization processes is shown in Figure 7.16. To photoionize Ca, a laser at 272 nm is used to resonantly excite the atom from $4s^2\ ^1S_0 \rightarrow 4s5p\ ^1P_1$. This resonant step is how the process is isotope selective[11]. At this point, the atom can either be ionized by 272 nm or 397 nm light, or the atom can decay to $4s3p\ ^1D_2$. From $4s3p\ ^1D_2$ the atom can be ionized by 272 nm light. It should be noted that this is not the sole isotope-selective photoionization scheme, and other schemes are used in other groups [135–137].

For Mg, the resonant excitation step is at 285 nm [132] and excites $3s^2\ ^1S_0 \rightarrow 3s3p\ ^1P_1$. The atom can then be ionized by either 280 nm light (Doppler cooling for $^{24}Mg^+$) or 285 nm light.

The formation of $^{24}MgH^+$ is accomplished by ionizing Mg and Doppler cooling it. $H_2$ is then leaked into the chamber. The $H_2$ gas reacts with $^{24}Mg^+$ when it is in the excited $^3p^2P_{3/2}$ state (the upper state of the Doppler cooling transition), creating $^{24}MgH^+$ [23].

[11] The isotope selectivity of this process was studied by Mortensen [130, 134]. A table covering the isotope shifts is provided in Appendix A.

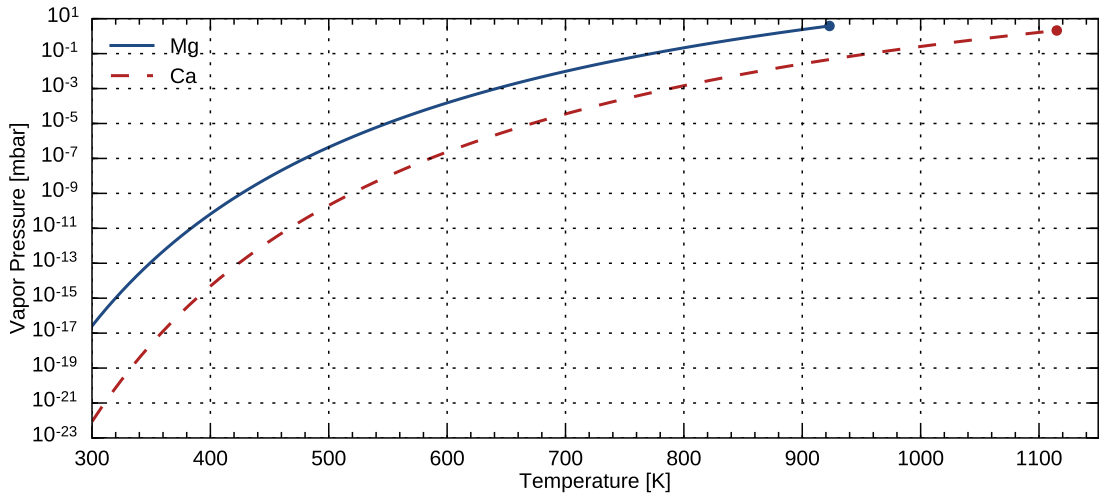


Figure 7.15: Vapor pressure of Mg and Ca as a function of temperature. The endpoints show the melting points. Derived from [131].

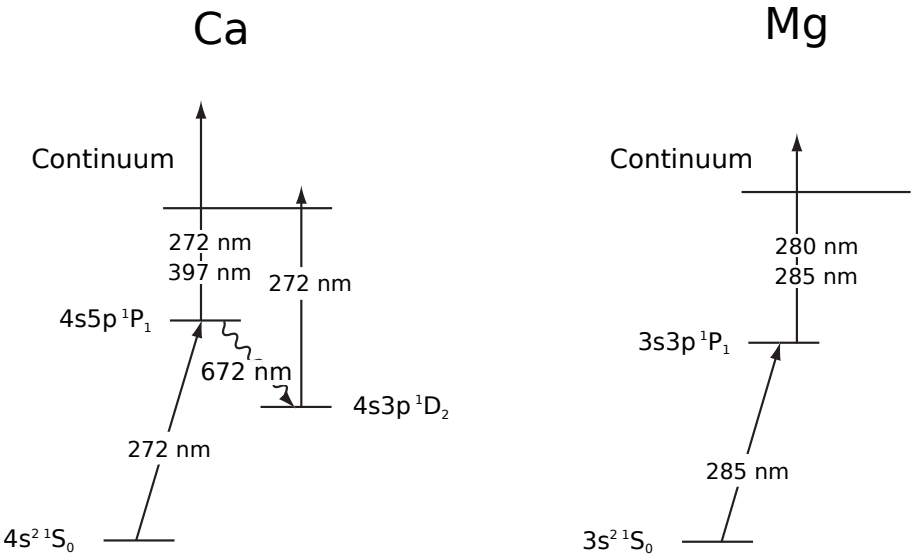


Figure 7.16: The Ca and Mg photoionization schemes.

# Chapter 8

# Laser systems

To probe coherent dynamics of ions, we need coherent light sources. For our experiments we use lasers to provide coherent electromagnetic fields. An overview of the beam geometry into the trap is presented in Figure 8.1.

This chapter covers the many lasers we use to control the internal and external states of the $^{40}Ca^{+}$ ion, along with the tools we use to lock the lasers to specific wavelengths. The lasers for $^{24}Mg^{+}$ and $^{24}MgH^{+}$ are not presented as they are not used in the experiments detailed in this thesis.

## 8.1 Wavemeter

An invaluable tool in our lab is a fiber-coupled wavemeter[1], which uses a Fizeau interferometer to measure the wavelength of the light coupled into it. The wavemeter is used with two fiber switches, one for wavelengths less than and one for wavelengths greater than 630 nm, each with 7 usable inputs. The switches iterate through their inputs to be read on the wavemeter, allowing for 14 lasers to be referenced on the same wavemeter at once. The wavemeter is automatically calibrated to a stabilized HeNe laser.

The wavemeter interfaces with 8 proportional-integral-derivative (PID) controller modules, which create an error signal from the measured frequency and can be used to feedback to the lasers and stabilize their frequency to within a few MHz. Many of our lasers are stabilized in this way.

## 8.2 272 nm

As discussed in section 7.5, photoionization of Ca is achieved using a 272 nm beam. Light at this wavelength is produced by frequency-doubling twice from 1088 nm light. The laser which produces 1088 nm light is a Koheras Boostix fiber laser with approximately one watt output power. The light is frequency-doubled to 544 nm in a butterfly cavity, the details of which can be found in Peter Herskind's thesis [138].

The light from 544 nm is split off into two branches. The majority goes to a second butterfly doubling cavity, which frequency-doubles the light to 272 nm. The details of this cavity can be found in Anders Hansen's thesis [108]. The cavity output mode is cleaned up by focusing through a pinhole, and the light is sent from one room to another in free space via a series of platforms. The total distance it must travel to the trap is on the order of 13 meters. The free space beam path

[1] Ångstrom WS-U

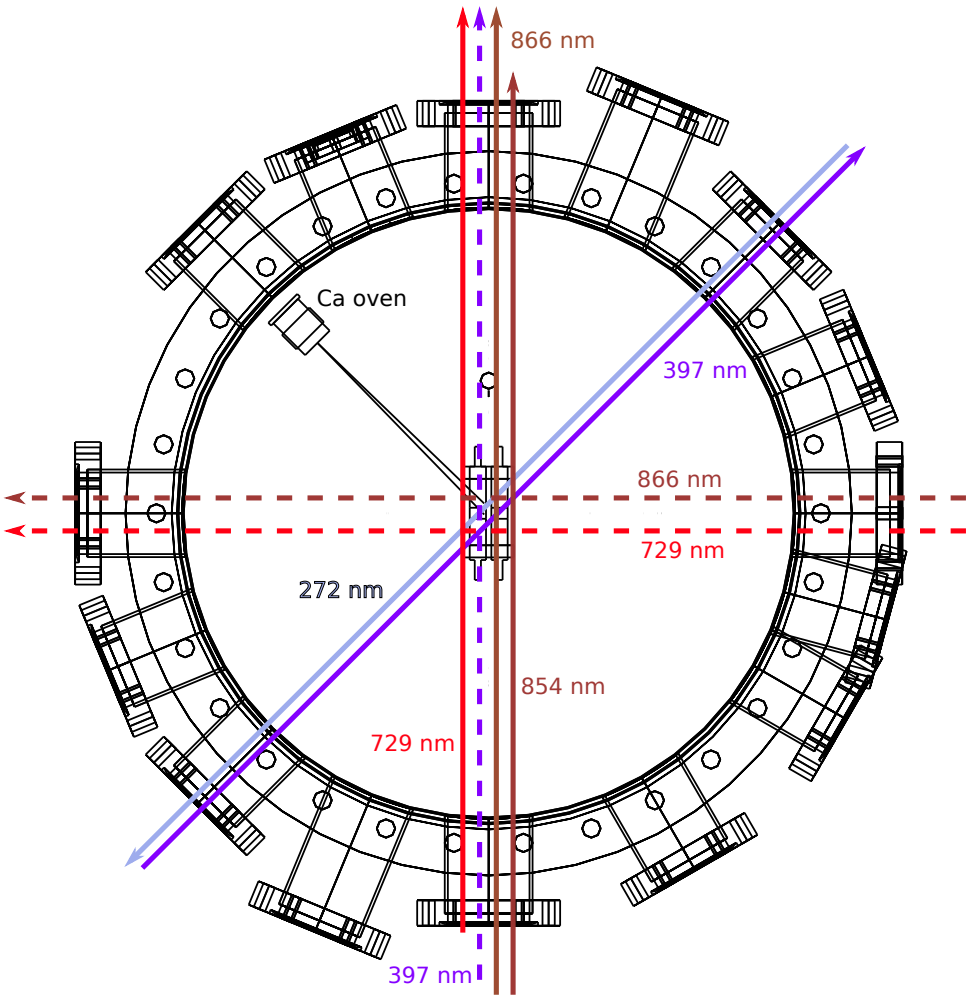


Figure 8.1: Geometry of the beampaths into the vacuum chamber. The solid lines indicate the geometry used in the experiments presented in this thesis, while the dashed lines indicate optional geometries.

is necessary due to the lack of available fibers capable of transmitting 272 nm light without heavy losses.

The second 544 nm branch is sent to the wavemeter. The wavemeter is used to stabilize the laser frequency by feeding back on the laser piezo. Thus, while the wavemeter produces its error signal from the green 544 nm light, it acts on the fiber laser and thus stabilizes the 1088 nm output. The end effect is that the 272 nm light is stable, which is necessary for isotope-selective ionization.

The 272 nm light must be shared between all four traps in the Aarhus Ion Trap group. This is accomplished using motorized flip mirrors[2] which are controlled by a Raspberry Pi. The position can be set by an online interface.

To load a small number of ions, we must be able to pulse the 272 nm light. We block the beam on one of the platforms using a home-built mechanical shutter [139]. The shutter can be TTL

[2]Thorlabs MFF101/M

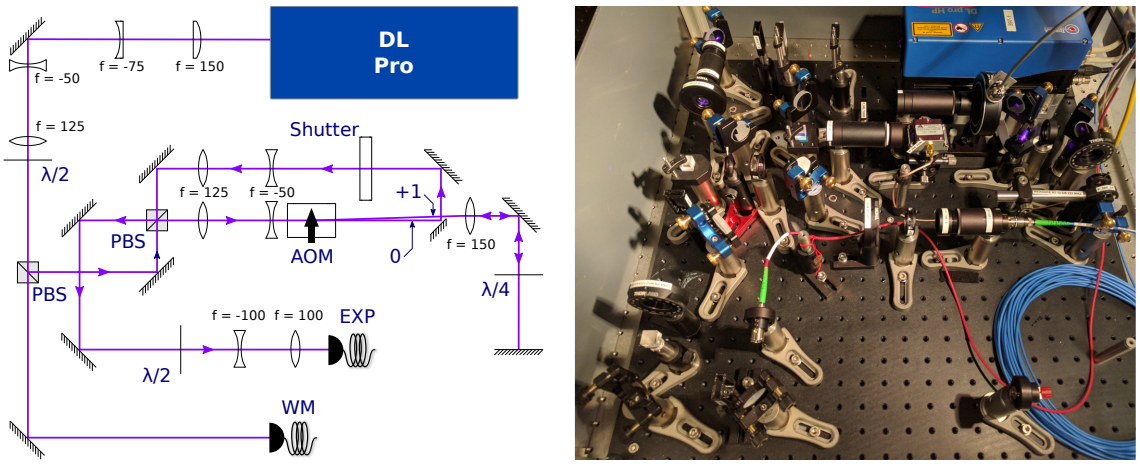


Figure 8.2: Diagram and photograph of the 397 nm setup.

controlled (good for computer control), or it can be set to be always open or always closed by a mechanical switch.

## 8.3 397 nm

The 397 nm Doppler cooling beam is produced by a Toptica DL Pro diode laser with output powers ranging between typical values of 17 mW and 30 mW, depending on the current setting. The output is split into two branches: a wavemeter branch, and an experimental branch, with 80 % of the light going to the experimental branch. The remaining power enters the wavemeter branch, where it is coupled into a single mode fiber that goes to the wavemeter, which is used to stabilize the output wavelength. A diagram of the optical setup is shown in Figure 8.2.

In the experimental branch, the light is sent through a double-pass acousto-optic modulator (AOM) centered at 250 MHz. The AOM is used for both pulse switching and frequency control in experimental sequences. The double-passed +1 order light is used for Doppler cooling and readout in a normal ion experiment. The frequency of this beam is thus detuned to the optimal $-\Gamma/2$ for Doppler cooling.

The RF drive applied to the AOM is provided by a home-built 4-channel DDS[3], of which two channels are used for the 397 nm AOM, one at high power, and one at lower power, both used in Doppler cooling. The DDS outputs are sent through RF switches, which are switched by TTL pulses provided by the PPG (see section 10.2) such that the 397 nm beam can be pulsed with precise timing within a sequence.

When the ion is very hot, the optimally tuned 397 nm beam has little cooling effect on the ion. The ion is hot when loading, and can become hot as the result of collisions with background gas during regular experiments. In situations such as these, it is very helpful to have a far-detuned 397 nm beam to help cool the ion.

We create a far-red-detuned beam (400 MHz to 500 MHz detuned) by directing the single-passed zero-order beam of the AOM through a TTL-controlled mechanical shutter[4] and recombining it with the shifted light. The mechanical shutter is normally closed, but can be opened to cool the ion when it is dark. The 0-order and double-passed beams are recombined in a polarizing

[3] Designed and built by Frank Mikkelsen of our electronics department.
[4] Uniblitz LS2

beam splitter (PBS) and coupled into a single mode polarization maintaining fiber which goes to the trap.

Once on the trap table, the light is focused into the trap on a path at 45° to the trap axis. Optionally, if we are working with large crystals, we can instead send the beam down the trap axis, or have a combination of axial and 45° beams. This is chosen such that we can cool all three directions of motion. The light is $\pi$-polarized, for the reasons described in section 5.2.

## 8.4 854 and 866 nm

Both the 866 and 854 nm repump beams are produced by homebuilt external cavity diode lasers (ECDL) in Littrow configuration, frequency stabilized by the wavemeter. Each beam is shuttered by single-pass AOMs centered at 270 MHz, of which we use the -1 order for the 854 nm beam, and the +1 order for the 866 nm beam. The two AOMs are driven by the remaining two channels of the same DDS as is used for the 397 nm laser, and the RF voltages to the AOMs are switched by TTL-controlled RF switches. Each beam is coupled into separate single mode polarization maintaining fibers, which go to the trap table. On the trap table, the 854 and 866 nm beams are combined, and the polarizations are rotated to 45° with respect to the quantization axis. The combined beam is sent down the trap axis.

We have the use of another homebuilt 866 nm diode laser which we can send to the trap radially. This laser can be used for the magnetic field compensation described in section 7.4.

## 8.5 729 nm

The 729 nm beam is used for sideband cooling and for shelving on the $^2S_{1/2} \rightarrow {}^2D_{5/2}$ transition, as presented in Chapter 5. The narrow linewidth of this transition, coupled with the need for sideband resolution means that this laser needs to not only be stable, but narrow linewidth, with at least $\Gamma_L \ll \omega_z$. How narrow the laser linewidth is will impact the coherence time. We aim for 1 kHz or less. We use a cavity to narrow and stabilize this laser, and then reference the laser to an optical frequency comb to correct for long-term drift. I will first discuss the general optical layout, before moving onto the stabilization.

The 729 nm beam is produced by a Toptica TA Pro laser, within which the laser light is generated by a diode laser and amplified by a tapered amplifier (TA). The typical output power of this laser is 375 mW, which is split into 4 branches: an experimental branch, a cavity branch, a wavemeter branch, and a comb reference branch. These four branches are pictured in Figure 8.3.

85 % of the optical output power of the laser is used for the experimental branch. The experimental branch consists of a double-passed AOM centered at 200 MHz. The RF drive for the AOM is provided by a DDS output on the PPG (see section 10.2). The double-passed +1 order is beam-shaped and coupled into a single-mode polarization maintaining fiber and sent to the trap table, where the typical maximal power is 55 mW.

On the trap table, the beam is sent through the trap axially. The polarization is set to 45° to the magnetic field. This enables us to drive $\Delta m_J = \pm 1, \pm 2$ transitions (see Appendix C.2 for the geometry dependent coupling strengths of the quadrupole transition). It is also possible to send the 729 nm beam radially by using a flip mirror. This allows us to investigate the radial oscillation modes of the ions.

The cavity branch consists of a double-passed AOM centered at 600 MHz. The double-passed -1 order light is coupled into a single mode polarization maintaining fiber, which goes to the cavity (subsection 8.5.1). The AOM is driven by an amplified frequency generator[5].

[5] Rohde & Schwarz SML02

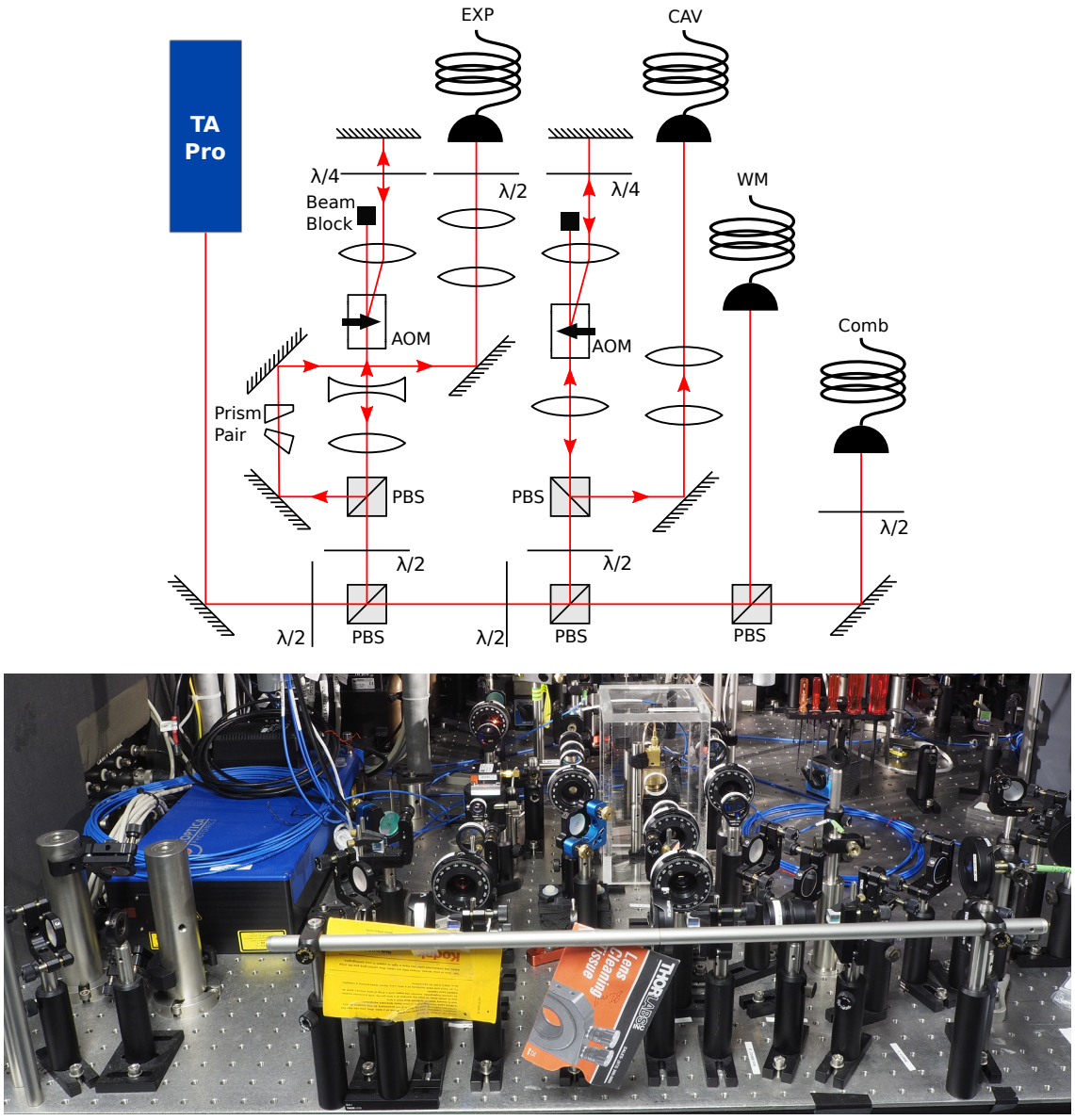


Figure 8.3: Diagram and photograph of the 729 optical setup. The branches are EXP: experimental, CAV: cavity, WM: wavemeter, and Comb. The prism pair is used for beam shaping.

The wavemeter branch is used to couple less than 1 mW of the light into a single mode fiber that terminates at the wavemeter. The wavemeter is used only to monitor the frequency of the light, and does not play a role in stabilization, as the wavemeter does not have the resolution nor the bandwidth to narrow the laser linewidth to the kHz level.

Lastly, the comb branch consists only of coupling into a single mode polarization maintaining fiber, which terminates at the frequency comb. The frequency comb setup is detailed in subsection 8.5.2.

### 8.5.1 Cavity stabilization

The 729 nm laser is locked and frequency-narrowed by a reference cavity in a Pound-Drever-Hall (PDH) scheme [140]. The cavity has a length of 250 mm, is vibration isolated and temperature stabilized, has a free spectral range of 600 MHz, and a measured finesse of 3240(10). Detailed construction details and characterization of the cavity are described in Gregers Poulsen's thesis [44]. The sidebands for PDH locking are generated at 20 MHz by an electro-optic modulator (EOM).

The cavity is only resonant at specific frequencies, separated by the free spectral range of the cavity. This resonant frequency may not be the same frequency as the $^2S_{1/2} \rightarrow {}^2D_{5/2}$ transition in $^{40}Ca^+$. The cavity AOM combined with the experiment AOM are used to shift the laser frequency into resonance with the ion. If the cavity AOM frequency is given by $\nu_{cav}$, and the experimental AOM frequency is given by $\nu_{exp}$, then compared to the resonant cavity frequency $\nu_{res}$, the frequency at the ion will be

$$\nu_{ion} = \nu_{res} + 2\nu_{exp} + 2\nu_{cav} \tag{8.1}$$

The factors of 2 are by virtue of the double pass setups, and the signs take into account their respective AOM diffraction orders.

### 8.5.2 Comb stabilization

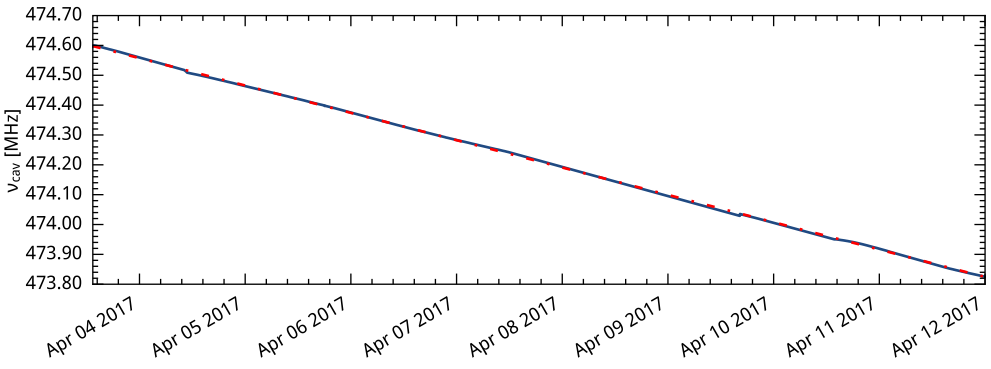


Figure 8.4: ——— shows the adjustment of $\nu_{cav}$ over the course of the week. A fit - - - gives the slope as $-1.06\,\mathrm{Hz\,s^{-1}}$, which corresponds to a cavity drift of $-2.12\,\mathrm{Hz\,s^{-1}}$, or $-7.6\,\mathrm{kHz\,h^{-1}}$

.

While the cavity keeps the laser linewidth narrow and frequency stable for short times, the cavity resonance drifts over time at a rate of $7.6\,\mathrm{kHz\,h^{-1}}$, so it cannot be used as an absolute reference. One option to compensate for this drift is to frequently measure the transition frequency on the ion, and follow the drift with the experimental AOM. We have a convenient other option, and

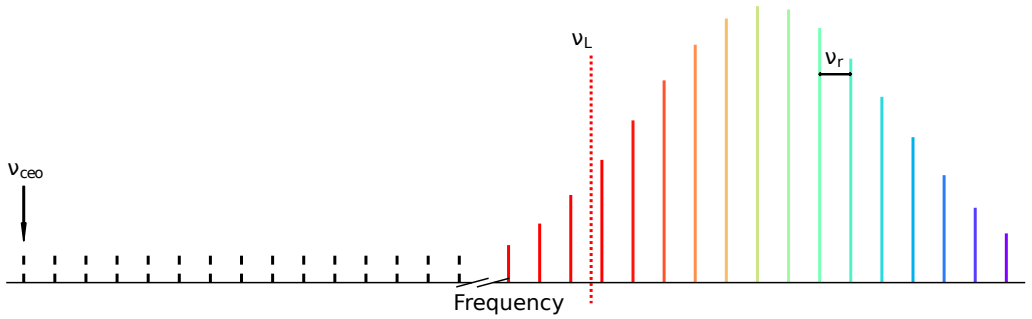


Figure 8.5: Representation of an optical frequency comb. The dashed line shows the cw-laser referenced to the comb.

that is to reference the frequency of the laser to an optical frequency comb. This allows us to keep consistent experimental AOM frequencies over months and enables us to take measurements that take hours without being dependent on remeasuring the transition frequency.

The basic idea is to use a frequency comb (described below) to constantly monitor the frequency of the 729 nm laser. As the cavity drifts, the lock of the laser follows, and the comb sees a changing frequency. We can feed back on that information, changing the cavity AOM frequency $\nu_{cav}$ to keep the laser frequency constant. The software[6] performing this feedback checks the frequency of the 729 nm laser every 30 s and updates $\nu_{cav}$. The software is limited to an update of maximum 100 Hz for $\nu_{cav}$, to prevent bad readings from having a big impact on the laser frequency. The software also checks to make sure the comb is locked, the wavemeter reading is reasonable, and the beatnote of the laser with the comb has sufficent signal-to-noise to trust the calculated frequency. If anything is deemed 'not okay,' then the cavity AOM frequency correction defaults to a set amount based on a linear fit to the cavity drift over time.

In 2005, John Hall and Theodor Hänsch were awarded the Nobel prize "for their contributions to the development of laser-based precision spectroscopy, including the optical frequency comb technique [141]." Their development of stabilized octave-spanning optical frequency combs enabled the generation and measurement of optical frequencies at unprecedented levels. Much of the information in this section is based on [142, 143].

A frequency comb is generated by pulsing a laser lasing at frequency $\nu_c$ at a stabilized repetition rate $\nu_r$. In the time domain, this looks similar to a series of delta functions separated by a fixed time. Thus, when we move into the frequency domain, it looks like a series of delta functions separated by a fixed frequency. This series of delta functions is called a comb, and each delta is called a tooth. Of course, in reality the pulses are not delta functions, but are instead pulses of finite width in time, but the idea holds. Thus, the comb intensity spectrum is shaped by the spectrum of the pulsed laser. The frequency space representation of a frequency comb is shown in Figure 8.5.

If $\nu_r$ is not an integer factor of $\nu_c$, the electric field in the pulse will not always have the same phase. This results in a shift between zero-frequency and the first comb tooth[7], called the carrier envelope offset (CEO), denoted by $\nu_{ceo}$. The frequency of any comb tooth number $n$ is thus given by

$$\nu_n = n\nu_r + \nu_{ceo} \tag{8.2}$$

One can determine $\nu_{ceo}$ if the frequency comb is octave-spanning by frequency-doubling the comb. If one doubles a comb tooth $n$ at the red end of the spectrum, the doubled tooth will

[6] Implemented by Steffen Meyer.
[7] This 'first comb tooth' is the tooth closest to zero-frequency if the teeth are extrapolated out to zero.

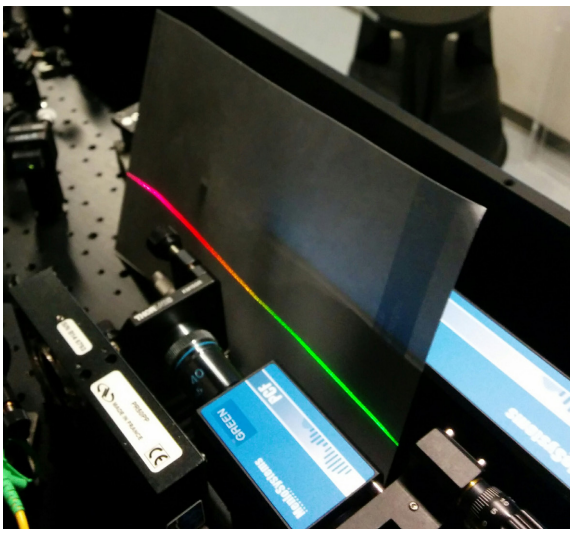


Figure 8.6: A photograph of the spectrum generated by broadening the comb in the green PCF. The spectrum is spread in space by reflecting it off a grating.

overlap with tooth $2n$ at the blue end of the spectrum, resulting in beating between the two teeth with beat frequency

$$\nu_{b_{ceo}} = 2n\nu_r + 2\nu_{ceo} - (2n\nu_r + \nu_{ceo}) = \nu_{ceo} \tag{8.3}$$

This beat can be detected on a photodetector, and thus the CEO can be stabilized.

If both the CEO and the repetition rate are locked, the comb teeth stay stable. Thus, a frequency comb can be thought of as a ruler in frequency space, where the teeth of the comb are similar to the markings on a ruler. By monitoring the beat $\nu_{b_L}$ of a laser of frequency $\nu_L$ with the $n^{th}$ comb tooth, we can measure the laser's frequency relative to the comb tooth's. If we know what number $n$ the tooth is, we can calculate the absolute frequency of the laser,

$$\nu_L = n\nu_r \pm \nu_{ceo} \pm \nu_{b_L} \tag{8.4}$$

where the sign for the beat depends on which side of the comb tooth the laser sits on (determined by changing $\nu_r$). Figure 8.5 shows the laser frequency lower than the nearest comb tooth, which corresponds to a negative sign for $\nu_{b_L}$. The sign of the CEO depends on whether the doubled tooth has a larger or smaller frequency than the comb tooth with which it is beating (can be determined by changing the $\nu_{ceo}$).

### Menlo frequency comb

The Menlo frequency comb[8] is a commercial frequency comb which can be used to measure the frequency of lasers in the 550 nm to 2100 nm range[9]. The basis of the frequency comb is a mode-locked erbium-doped fiber laser with a center wavelength of 1550 nm and repetition rate of order 250 MHz. The output of the fiber laser is sent into three branches, all three of which amplify the signal using erbium-doped fiber amplifiers (EDFA). One of the branches then spectrally broadens the pulse using a highly non-linear fiber (HNLF), producing the comb in the 1050 nm to 2100 nm

[8] MenloSystems FC1500-250-WG

[9] The comb is a shared resource of LASERLAB.DK. Our group takes primary care of it.

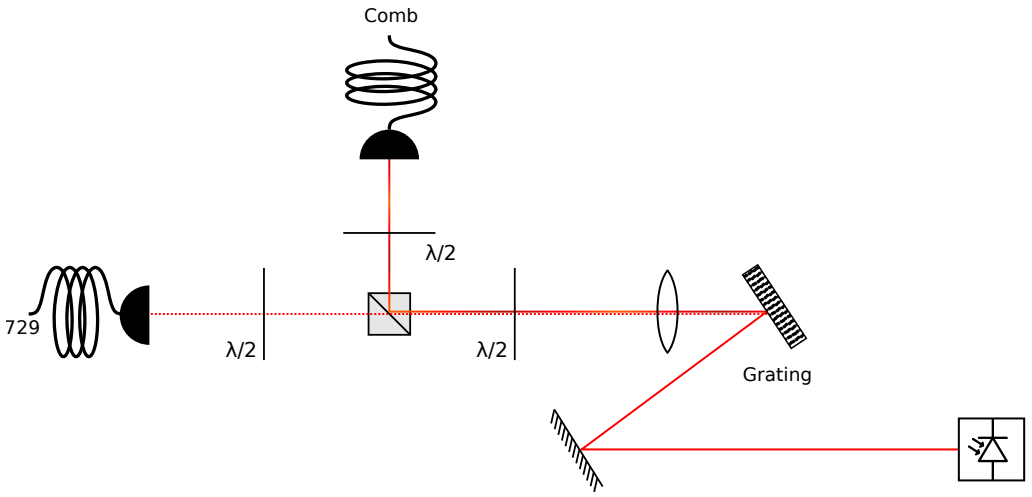


Figure 8.7: Beat detection setup for the 729 nm laser with the comb. The light from the two sources is power-balanced and overlapped in a polarizing beam splitter (PBS) by adjusting their polarizations with waveplates. The power to the detector is optimized by another waveplate and PBS pair. The combined beam is reflected off a grating to spread the comb spectrum, such that only the light closest to the 729 nm beam in frequency is overlapped with it. The beam is then reflected into a photodetector for beat note detection.

range. Another branch broadens and doubles the spectrum for CEO beat detection and stabilization. The last branch doubles the spectrum, producing a visible spectrum comb centered at 780 nm. The broadening for the visible comb region can be done in two different photonic crystal fibers (PCF), a 'green' PCF for broadening into the visible, and a 'red' PCF for broadening in the near-infrared (NIR), depending on the wavelength needed. A photograph of the spectrum after having been broadened in the 'green' PCF and reflected off a grating is shown in Figure 8.6.

To measure the frequency of the 729 nm laser, we broaden the visible comb in the 'red' PCF, and beat the laser against it in a beat detection unit (BDU). The BDU at this wavelength is free space, and a schematic of it is shown in Figure 8.7.

We know the frequency of the 729 nm laser to a few MHz since we measure the frequency $\nu_{wm}$ on the wavemeter. By measuring $\nu_{b_L}$, $\nu_r$, and $\nu_{ceo}$, we can deduce the comb tooth number $n$. By using Table 8.1 in combination with Equation 8.4 (our signs are both -), we find $n = 1644166$.

We can check this calculation against the known $^2S_{1/2} \rightarrow {}^2D_{5/2}$ transition frequency $\nu_{729}$ by measuring the shelving transition frequency and magnetic field. The ion transition frequency, according to the comb, is calculated by

$$\nu_{729_{meas}} = n\nu_r - 2\nu_{ceo} - \nu_b + 2\nu_{exp} + \Delta\nu_{shelv} \tag{8.5}$$

where $2\nu_{exp}$ is the $2\times$ the experimental AOM frequency on resonance with the shelving transition, and $\Delta\nu_{shelv}$ is the shift of the shelving transition due to the Zeeman effect. This calculation brings us 6 kHz off from the known value of $\nu_{729}$. This discrepancy can be accounted for from two sources. The first is the DDS for the experimental AOM, which outputs frequencies about 4 kHz different from the programmed value. The second is the clock used to count $\nu_r$, which has discrete steps which correspond to 2 kHz at the 729 nm frequency.

Figure 8.8 shows the stability of $\nu_L$, $\nu_{ceo}$, $\nu_r$ and $\nu_b$ over the course of a week. $\nu_L$ here is the calculated transition frequency from the comb parameters. We see that the measurement stays

| | |
|---|---|
| $\nu_{wm}$ | 411.041 666 THz |
| $\nu_{ceo}$ | 20.000 000 0 MHz |
| $\nu_r$ | 250.000 140 697 MHz |
| $\nu_{L_b}$ | 21.3308 MHz |
| $n$ | 1644166 |
| $\nu_{729}$ [144] | 411.042 129 776 393 2(10) THz |
| $2\nu_{exp}$ | 441.576 MHz |
| $B$ | 6.5044 G |
| $\Delta\nu_{shelv}$ | −18.194 MHz |
| $\nu_L$ | 441.041 670 000 063 THz |

Table 8.1: Parameters for the calculation of the 729 nm laser frequency, and the measurement of the $^2S_{1/2} \rightarrow {}^2D_{5/2}$ transition frequency. Values are taken from the averages shown in Figure 8.8. $\nu_L$ refers to the average laser frequency calculated by the comb correction software. The software uses a slightly different value for $\nu_r$ so there is a slight discrepancy between the actual calculated value and the software calculated value.

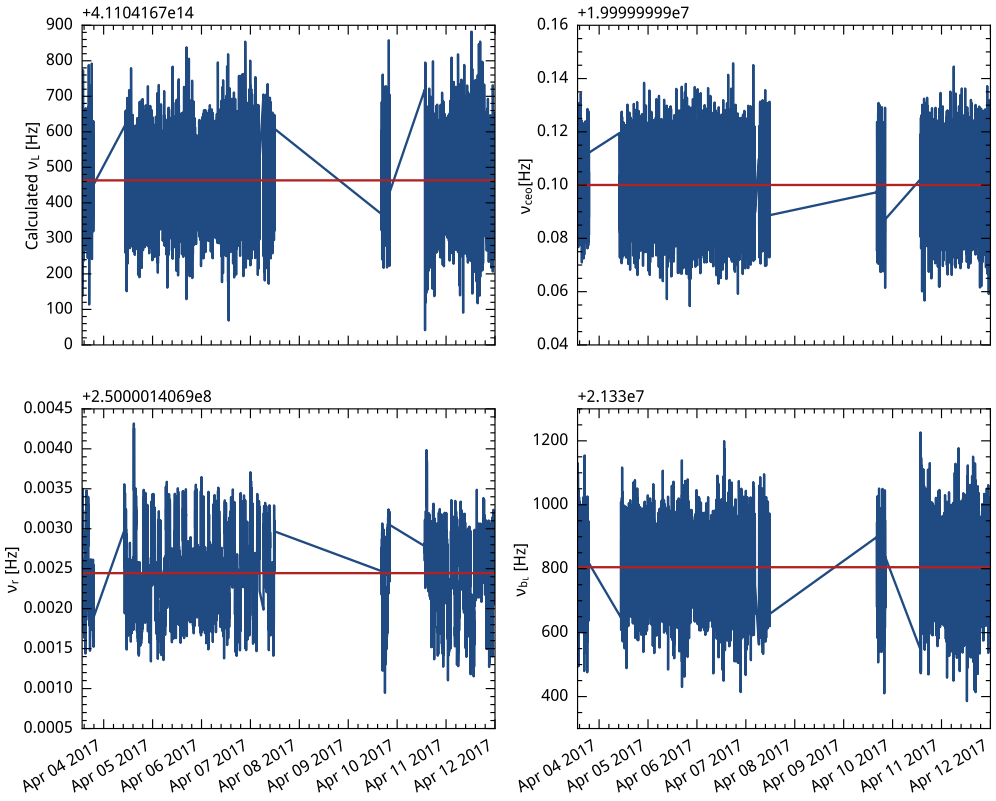


Figure 8.8: Measurements of $\nu_L$, $\nu_{ceo}$, $\nu_r$ and $\nu_b$ over the course of a week. $\nu_L$ is the calculated 729 nm frequency as the comb reports it. The red lines indicate the averages.

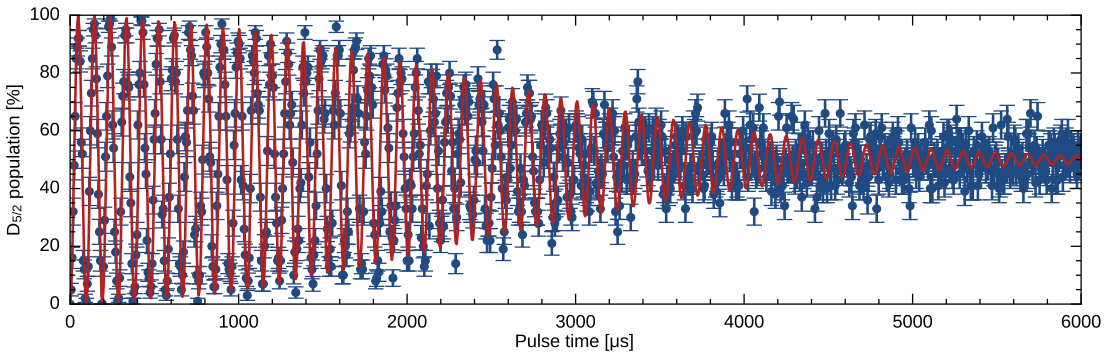


Figure 8.9: Rabi flopping on the shelving transition. ——— shows a sinusoidal function with a Gaussian decay.

stable for most times within 400 Hz. We can compare this measured frequency to the transition frequencies by comparing to Figure 7.13, which is taken for the same date range.

#### Acetylene-stabilized fiber laser

When the repetition rate of the comb is RF-locked, the width of the comb teeth is 270 kHz. This is too broad to stabilize the 729 nm laser to the 1 kHz level. To narrow the teeth, we optically lock the frequency comb to an erbium-doped fiber laser that is stabilized to an acetylene cell [145]. The stabilized laser[10] is a prototype developed at the Danish National Metrology Institute (DFM[11]). The stabilized laser is based on a Koheras BASIK X15[12] fiber laser which is fed back on from a saturated absorption spectroscopy of an acetylene cell [146]. The wavelength of the output is 1.54 µm. The stabilized laser has linewidth approximately 600 Hz on a 100 ms timescale and drifts less than 400 Hz per year, which is mitigated by referencing it to a GPS signal.

The optical lock of the comb is achieved by beating the stabilized laser with the comb, and keeping the beatnote constant by feeding back on the repetition rate. The linewidth of the comb teeth is narrowed to 1.05(9) kHz [145].

### 8.5.3 Rabi coherence

As mentioned, the linewidth must be narrow in order to resolve the sidebands and to have long coherence times. Figure 8.9 shows Rabi flopping out to 6 ms. The decay shape is Gaussian, and we see that the coherence begins to fall off at around 1 ms, falling to approximately 60 % contrast at 2 ms. We suspect that our limitation is magnetic field noise, and not the laser linewidth. In any case, 2 ms is much longer than our typical coherent operations on $^{40}Ca^{+}$, which take maximum 400 µs. We have already seen in Figure 5.10 that coherence is nearly perfectly maintained on this timescale.

[10] JPX 1603
[11] Dansk Fundamental Metrologi
[12] NKT Photonics

# Chapter 9

# Trap electronics

In our trap, each electrode can have both an RF and a DC potential applied to it. The RF and DC voltages are combined in an RF/DC mixer before being sent via a vacuum feedthrough to the trap. To have further control over DC ramp shapes and timing, the DC and RF/DC mixers were replaced during my PhD in order to reduce the ramp time for adiabatic cooling, requiring optimization and characterization. Full schematics of the electronics described in this section can be found in Appendix D.

## 9.1 RF/DC mixer

The RF/DC mixer was designed by Martin Stougaard from our electronics department, and was based on earlier mixers designed by Erik Søndergaard. It was first installed in our trap setup towards the beginning of my PhD in 2014, and replaced an older version to serve two purposes: decrease the cutoff of the DC filtering in order to speed up ramp times, and increase $\Omega_{RF}$ to allow for lower $q$ values.

The RF/DC mixer serves a number of purposes. The first is to combine the RF and the DC voltages, $V_{RF}$ and $V_{DC}$[1], so they can be delivered to each of the electrodes. The second is to split $V_{RF}$ into two 180°-shifted phases such that adjacent rods have opposite amplitudes. The third is to create the resonant circuit for $V_{RF}$ to be amplified for the frequency $\Omega_{RF}$. This is necessary to achieve the RF amplitudes of $1\,\mathrm{kV}_{pp}$ used in our experiments. The fourth is to provide filtering for the DC supply, such that the noise from the supply is reduced at the electrodes, and such that the RF does not bleed back into the DC supply.

### 9.1.1 Resonant circuit

The RF is coupled into the RF/DC mixer by a toriodal transformers which output two signals of opposite phases. Here we will look at a simplified version of the circuit for a single electrode. A simplified schematic for one of the phases is shown in Figure 9.1. This is an RLC resonator, where $Z_{in}$ is the input impedance, $R_p$ is the parasitic resistance in the circuit, and L is the inductance of the transformer. The capacitor $C_1$ is variable, and used to balance the two RF phases. The capacitor $C_{DC}$ couples the DC and the RF. The capacitor $C_t$ represents the electrode's capacitance with the trap as well as any parasitic capacitances as a result of the cabling and feedthrough after the output of the mixer. Thus, the capacitance of the trap itself influences the resonance of the circuit.

[1] Typically I refer to $V_{end}$, the endcap voltage. All electrodes can have different voltages, including the central electrodes, so it's faulty to give them only one name.

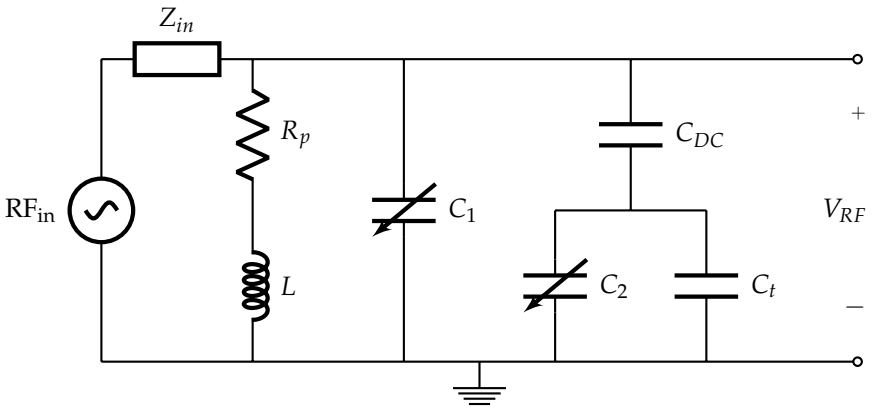


Figure 9.1: A model of the resonator for amplifying the RF voltage. All components other than the trap capacitance $C_t$ are contained within the RF/DC mixer.

This diagram is simplified. In reality, there are 12 electrodes. The first part of the circuit, before $C_{DC}$, is repeated twice for the two phases, and the capacitive side is repeated 6 times per phase. The various electrodes will see different capacitances, and the capacitance of each impacts the resonant circuit as a whole due to coupling between the branches.

Looking back to Figure 7.2 and Figure 7.1, we can see several sources of capacitance due to the trap. In Figure 7.2, we see that central electrode forms the inner cylinder of a cylindrical capacitor with the two endcap electrodes, coupling the resonant circuits of electrodes with the same phase. Figure 7.1 shows that adjacent rods form a small plate capacitor, coupling the circuits of opposite phase RF. Both of these capacitances will change the capacitive load on the circuit.

If the capacitance for each branch is different, the amplitudes and phases of the RF on the electrodes will differ, causing unwanted motion along the trap axis at the RF frequency. This axial micromotion can be compensated by the last capacitor, $C_2$. There is one for every electrode such that the capacitances can be balanced.

Our resonant circuit was designed to be operated at approximately $\Omega_{RF} = 2\pi \times 5\,\text{MHz}$. Micromotion compensation has shifted this frequency to $\Omega_{RF} = 2\pi \times 4.682\,\text{MHz}$.

### 9.1.2 Axial micromotion compensation

Axial micromotion compensation is achieved by balancing the capacitances between the electrodes. The capacitances are initially adjusted by balancing the amplitudes and phases of the RF of each channel as measured on the capacitively-coupled monitor output by an oscilloscope. This is an iterative adjustment process and only compensates to a point. The most sensitive measuring device is the ion itself.

The presence of micromotion gives rise to motional sidebands at the RF frequency. The coupling on the sidebands is given as Bessel functions [89]. This means that the coupling strength on an RF sideband could be zero, even when micromotion is not well compensated. This necessitates looking at many sidebands, and optimizing on the highest order sideband measurable.

To minimize micromotion, we probe the RF sidebands using the 729 nm beam on a Doppler-cooled ion. We check which is the highest order sideband where we can still see excitation, and focus first on that sideband. Next we ensure that we probe below saturating power and vary the pulse duration (a Rabi flopping measurement). If the micromotion sideband is greater than the 5th sideband, we park the pulse duration on the rising edge of the signal, such that when the micromotion is reduced, we see a reduction in signal height.By watching the signal height while

adjusting the capacitors on the RF/DC mixer, we can reduce the micromotion. Before moving on to the next sideband after reducing the signal height, we must check higher-order sidebands again to ensure we truly did reduce the micromotion. Once the sideband order is at 5 or below, we iterate through the capacitors, adjusting them only small amounts at one time while recording how much each was adjusted.

Throughout the process, it is necessary to adjust $\Omega_{RF}$, as the changing capacitance shifts the resonant frequency. Thankfully, once axial micromotion has been compensated, it does not need to be done again unless the RF/DC mixer is modified.

### 9.1.3 DC filtering

The DC voltages are filtered in the RF/DC mixer prior to mixing with the RF. A schematic of the filtering that a single channel sees is shown in Figure 9.2. Note that this schematic includes $R_{out}$, which is the output resistor of the DC supply itself. This is included since the filter is passive, so this resistor will change its overall filter characteristic. Figure 9.3 shows the transfer function of this filtering[2]. The value used for $C_t + C_2$ was 100 pF.

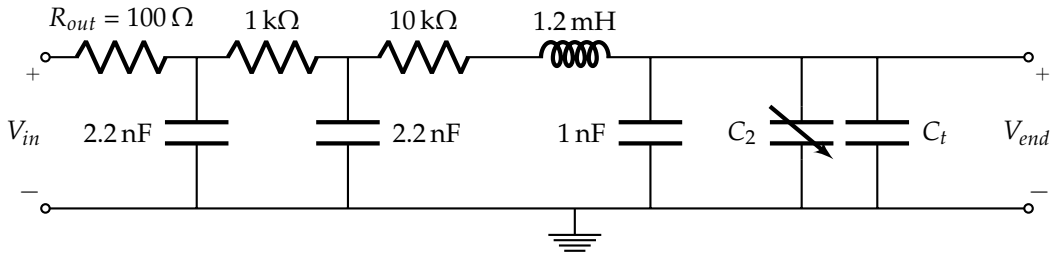


Figure 9.2: An approximate circuit diagram of the trap filtering for a single electrode. $V_{in}$ refers to the voltage directly out of the amplifier opamp. $R_{out}$ is the output resistor of the DC amplifiers, and the rest is contained within the mixer. $C_2$ and $C_t$ are the same components as in Figure 9.1, and the 1 µF capacitor is the same as $C_{DC}$.

## 9.2 RF supply

The RF is supplied by a two-channel function generator[3], and is further amplified by an RF amplifier[4]. Two-channel functionality of the generator allows easy synchronization of signals to the RF amplitude, for example, when performing radial micromotion compensation (see subsection 9.3.8). The RF amplifier is remarkable in that it can absorb reflections, and thus can be run with any load impedance (important since a trap is not 50 Ω).

## 9.3 DC supply

To carry out fast, controlled ramping, it was necessary to build a new DC supply. The requirements for this supply were ramps on the 100 µs timescale, control over the ramp shape, an ability

[2] While it is possible to calculate the transfer function by hand (I did), for analysis I used SPICE modeling through a python package ahkab [147].

[3] Keysight 33500B

[4] ENI 3100L

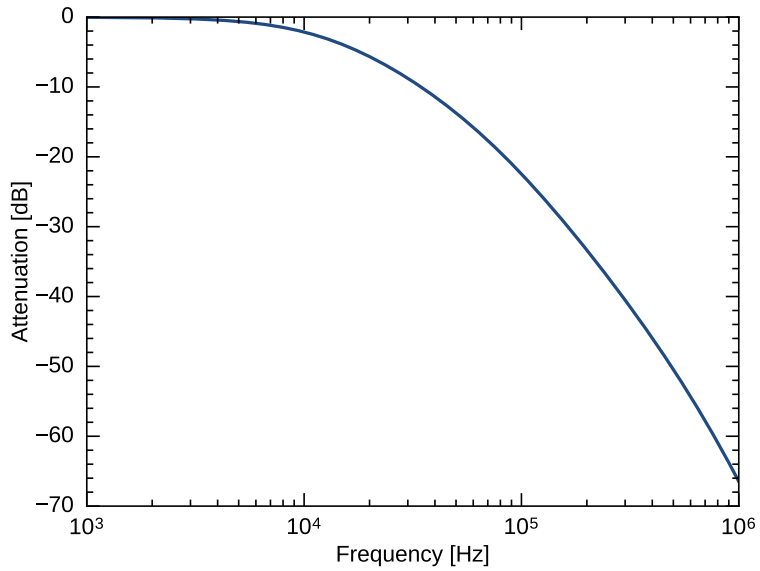


Figure 9.3: Plot of transfer function of the filtering of the DC signal in the RF/DC mixer.

to compensate radial micromotion throughout the ramp, programmable by way of our experimental control software qControl (section 10.1) while still precisely timed by our pulse generator (section 10.2), and have low noise and therefore low heating rates.

This section discusses the design and characterization of the new DC supply, the etherDAC, that I put together for our experiment. While the original electronic design was spear-headed by Gregers Poulsen, a former PhD and postdoc on the project, I constructed, programmed, debugged, and characterized the supply. I have since collaborated with Martin Stougaard at our electronics department to create further iterations to improve the output noise.

### 9.3.1 Overview

Though the etherDAC has gone through several iterations, the basic principles of operation have not changed, and thus it is possible to understand the basic idea of how all versions work with one description. A block diagram of the etherDAC 1.0 is shown in Figure 9.4. The basis of the etherDAC are 12 digital to analog converters (DACs). The DACs provide digitally-controllable voltages, which are set by binary sequences. The binary sequences needed to control the DACs are sent by a microcontroller, on which the many general purpose input/output (GPIO) ports available make it possible to update all 12 DACs simultaneously with independent signals. A TTL trigger input can tell the microcontroller when to send signals, allowing for precise timing.

The microcontroller cannot, however, connect to the internet. A Raspberry Pi instead acts as a server for the etherDAC and communicates with the microcontroller via serial peripheral interface (SPI)[5]. The Raspberry Pi can load multiple ramps onto the microcontroller to be triggered at a later time. Thus, the etherDAC can be pre-programmed over the network for later use during a sequence.

[5]SPI requires only three GPIO ports on each device.

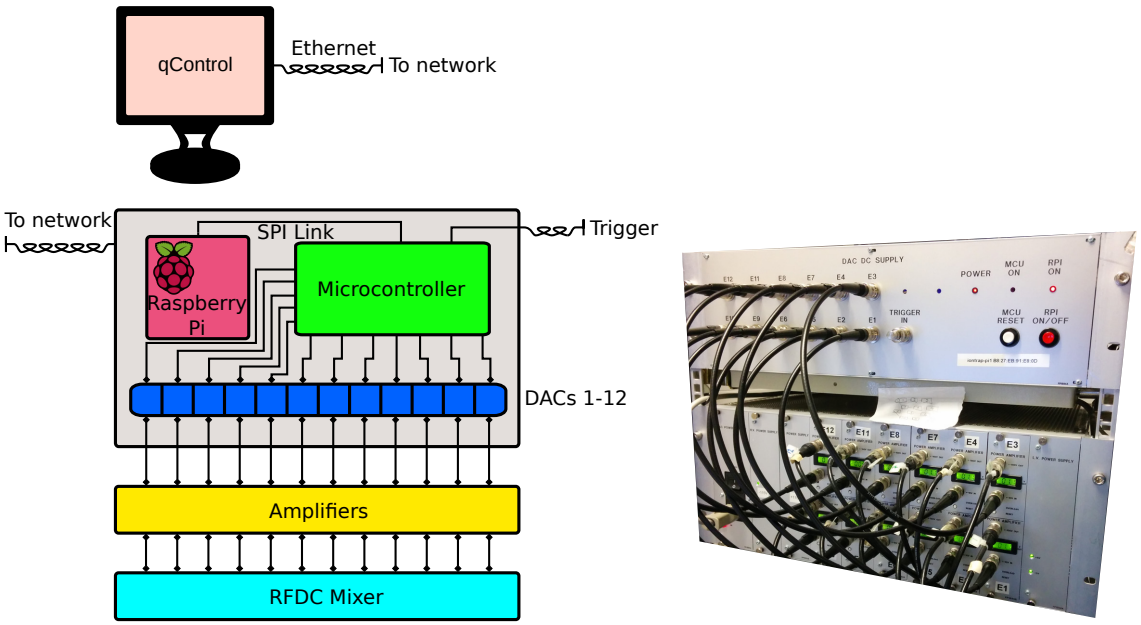


Figure 9.4: Block diagram of the etherDAC system. qControl interfaces with the etherDAC box via the network. Within the box, the Raspberry Pi acts as a server, and communicates voltage data to the microcontroller. The microcontroller updates the DACs when triggered. The voltages out of the DACs get sent first to an amplifier, then to the RF-DC mixer before making it to the trap electrodes. The photograph on the right shows the DAC and amplifier boxes mounted in a 19" rack in the lab.

In order to obtain high enough voltages to reach typical sideband cooling axial frequencies, it is necessary to amplify the DAC outputs. The outputs of the DACs are amplified by a factor of 10 using high voltage amplifiers[6].

### 9.3.2 The hardware

The exact hardware of the etherDAC differs depending on the version. etherDAC 1.0 was entirely constructed, debugged, and characterized by myself. etherDAC 2.0 was redesigned in a collaborative effort with Martin Stougaard, who modified the original designs and constructed the supply. Debugging was often collaborative, and characterization was carried out by myself.

#### etherDAC 1.0

In the etherDAC 1.0, the Raspberry Pi[7], microcontroller[8], and DACs are all housed in the same box, and the amplifiers are housed in a separate box, as shown in Figure 9.4.

The DAC box electronics have two types of home-mounted PCB boards: the main board, and the DAC boards. The main board houses the microcontroller, the voltage references, and the trigger-sensing electronics. The DAC boards each house two DACs along with output buffering and filtering electronics. The DAC boards are stackable, with jumper connections determining

[6] designed by Martin Stougaard from the electronics department.
[7] model B
[8] STM32F4

which microcontroller signal they respond to. The modular setup means that if a DAC board fails, it is straightforward to replace. The DAC boards are also connected to the same clock signal, thus they are time sychronized, updating simultaneously.

The Raspberry Pi is not mounted on either type of board, and is instead connected to the main board via a ribbon cable. The main board power and the Raspberry Pi power is provided by a $\pm 15\,\mathrm{V}, +5\,\mathrm{V}$ linear power supply[9].

The specific DACs used are Analog Devices AD5791. They were chosen for their low noise, high temperature stability, high slew and update rates, and short settling time[10]. Each output of each DAC is voltage-buffered and then filtered by an active lowpass filter with a cutoff frequency of 20 kHz. This filtering serves to filter out DAC update noise. The operational amplifiers (op-amp) used for both the buffer and filter are Analog Devices AD8676, which were also chosen for their low output noise[11].

The DACs are referenced to two voltage references at $-1\,\mathrm{V}$ and 10 V. Because we would like to have long term stability as well as precise knowledge of the voltage from our DACs, it is important that the voltage reference not drift. Furthermore, since we are more sensitive to drifts on the electrodes relative to one another (leading to increased micromotion) versus drifts occurring at the same level on all electrodes, all DACs are referenced to the same voltage reference. Lastly, noise on the voltage reference directly translates to noise on the DAC outputs, and therefore on the electrodes, so we used low-noise references.

In order to obtain stable reference voltages, a low drift 5 V voltage reference[12] was chosen. The 5 V is converted into the $-1\,\mathrm{V}$ and 10 V references using amplifiers constructed from Vishay DSMZ foil resistor dividers[13] and AD8676 op-amps. These resistor dividers are in a single package and resilient against temperature drifts.

The output noise of the LTC6655 reference drops from 90 nV at 1 kHz to 20 nV at 10 kHz. For both the positive and negative voltage references, this is filtered with a cutoff frequency of $f_c = 106\,\mathrm{Hz}$ before being used for the DACs. This brings the noise from the LTC6655 at the DAC down to the 10 nV level at 10 kHz.

The amplifiers are based on a high power op-amp made by Apex[14]. These op-amps have a low input noise of about $4.5\,\mathrm{nV}/\sqrt{\mathrm{Hz}}$. They have a factor of 10 amplification for DC voltages, which drops off as the frequency increases due to filtering in the amplifier circuit. The amplification as a function of frequency is shown in Figure 9.5.

#### etherDAC 2.0

The main difference between etherDAC 1.0 and etherDAC 2.0 is that the DACs were moved outside of the box housing the Raspberry Pi and microcontroller, and into the amplifier box. This was done to move the analog components as close together as possible to avoid picking up noise on the connections between them. It also served the purpose of moving the analog components away from the Raspberry Pi and the microcontroller, which are not designed to be low noise. The digital signals are now delivered to the DACs as differential signals to isolate the grounding of the two boxes.

Another difference is in the voltage reference for the DACs. This was changed to $-10\,\mathrm{V}$ and 10 V references, such that a commercial high precision chip[15] could be used for the reference.

[9] Power-One (now Bel Power Solutions) HBAA-40W-AG
[10] 7.5 $\mathrm{nV}/\sqrt{\mathrm{Hz}}$ noise, <0.05 ppm/°C, slew 50 $\mathrm{V\,\mu s^{-1}}$, 25 MHz update rate, 1 µs settling time
[11] 2.8 $\mathrm{nV}/\sqrt{\mathrm{Hz}}$ noise, <0.6 $\mathrm{\mu V\,°C^{-1}}$
[12] LTC6655, 2 ppm/°C
[13] DSMZ Z-foil, ± 0.05 ppm/°C, resistor ratio stability of 0.005%
[14] Apex PA90
[15] AD688ARWZ

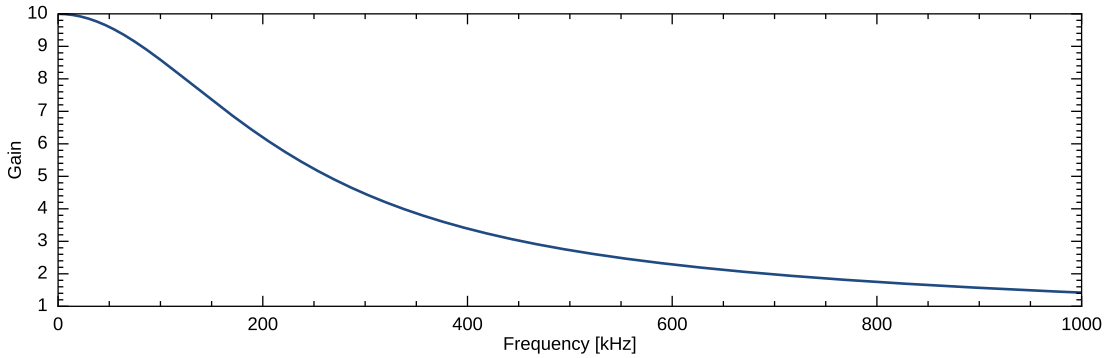


Figure 9.5: Gain of the DC amplifiers as a function of input signal frequency. The y-axis scale is linear.

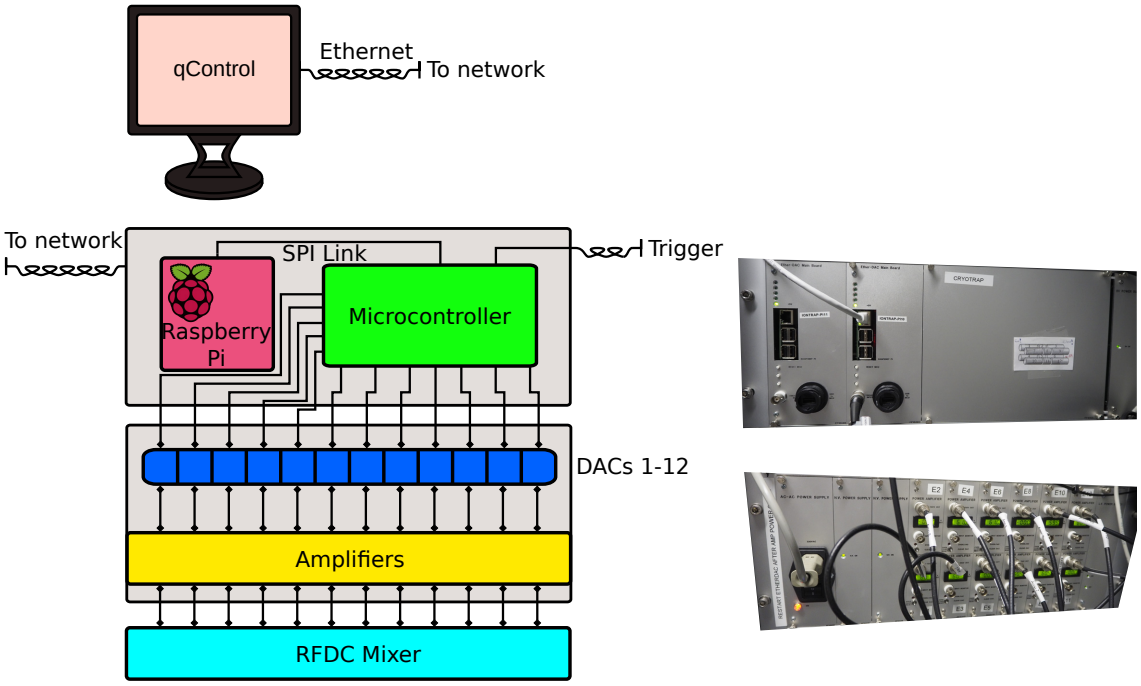


Figure 9.6: Block diagram and photograph of the etherDAC 2.0/2.1. The major difference is that the DACs are moved into the same box as the amplifiers.

Lastly, the filtering out of the DACs was changed from a 20 kHz cutoff to a 15 kHz cutoff.

#### etherDAC 2.1

The only difference between the etherDAC 2.0 and the etherDAC 2.1 is the addition of filtering at the output of the DAC chip. The filter at the DAC output was changed from a first order filter with a cutoff of 15 kHz with a 20 dB rolloff to a second order filter with a cutoff of 15 kHz with a 40 dB rolloff. This was changed because when ramping, it was possible to see DAC update 'glitches,' or noise due to bit switching, on the ramp, which caused significant heating on the ion when ramping. The addition of extra filtering sovled this problem.

### 9.3.3 The software

The software for the Raspberry Pi and the client for qControl are written in Python, and the microcontroller firmware is written in C. The Raspberry Pi- is responsible for all calculations, such as calculating ramps, the binary representation of the voltages, and more. It sends data transfer packets to the microcontroller via SPI that are 44 bytes in length. This can be split up as:

- 2 byte command - tells the microcontroller what function to do, for example, update the DACs, or add a voltage to the buffer
- 40 byte data - two bytes per bit, consisting of voltage data for all 12 DACs
- 1 byte 'continue' - tells the microcontroller if the update is part of a ramp and should continue updating
- 1 byte used only in the response, stating the length of the buffer, used to catch communication errors

The DAC has 20 bits, and there are 12 DACs. The way the firmware is set up, the microcontroller could control up to 15 DACs. The data part of transfer packet is split into 20 16-bit sections–16 bits for the 15 DACs plus one clock. The SPI data is organized as most significant bit to least significant bit, such that the first 16 bit section transferred is the most significant bits of all of the DACs, and the last 16 bit section transferred is the least significant bits of all of the DACs.

Once the microcontroller has received this data and added it to the buffer, it sends a response. This enables us to read data back out of the buffer if necessary. When the microcontroller updates the DACs, it breaks down the serial data into 16 20-bit packets, to be updated simultaneously to the DACs.

### 9.3.4 Ramping time

Before building a new supply, the old DC system was limited to ramp times of 1 ms with a settling time of 5 ms due to filtering in both the supply and the old RF/DC mixer. The new DACs were designed to be time-limited by the RF/DC mixer.

I measured the rise time of the new DC supply out of the RF/DC mixer by connecting a scope directly to the output. Note that this then neglects the added trap capacitance. The trap capacitance is on the order of 100 pF as compared to the 11 pF of the oscilloscope. However, this only makes a small difference in ramp time, so this measurement is a good baseline.

All channels were measured to have a 10-90% rise time of 37 µs. Figure 9.7 shows, in blue, the ramp measured out of electrode 10 as measured on the oscilloscope. The trace in red shows the predicted ramp based on a model of the entire circuit after the DAC chip, made in LTspice [148]. The modeled and measured ramps have similar behavior.

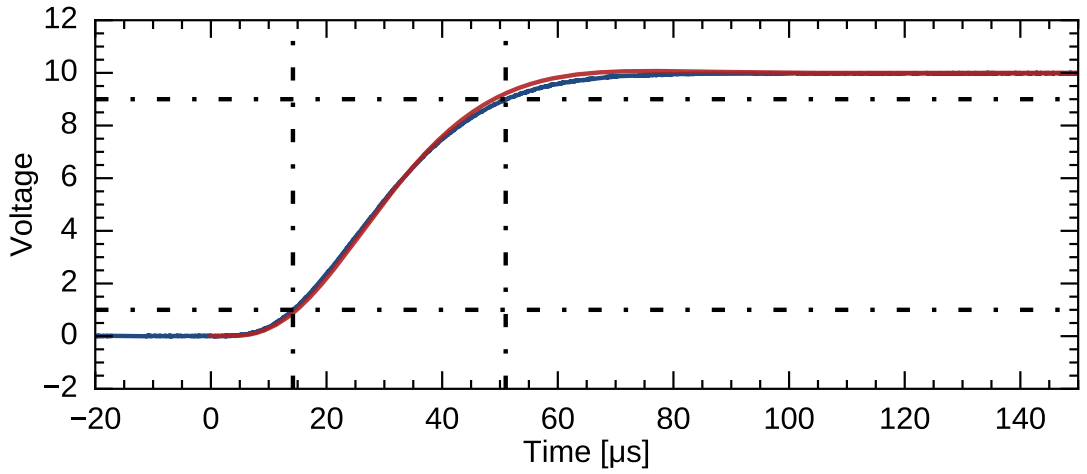


Figure 9.7: Measured and simulated single step ramp of the etherDAC, as measured out of the RF/DC mixer. The dashed lines indication the 10% to 90% rise times and voltages.

### 9.3.5 Ramp programming

We can program any shape of ramp into the etherDAC with the caveat of the fact that the filtering will modify its shape, and that it is limited by the update rate of the DAC. The update rate of the DACs is one update per 4.68 µs, or 214 kHz[16].

As discussed in section 6.5, the ramp shape that has the most potential to cause the least heating during ramping is a constant adiabaticity ramp. This shape in terms of voltage is given by

$$\begin{aligned} V(t) =& \frac{mz_0^2}{2\kappa e}\left(\frac{\omega_{z,t}}{1+\omega_{z,t}^2\gamma t}\right)^2 = V_0\left(\frac{1}{1+\omega_{z,t}^2\gamma t}\right)^2 \\ =& V_0\left(\frac{1}{1+\frac{t}{t_f}\left(\frac{1}{\alpha}-1\right)}\right)^2 \end{aligned} \tag{9.1}$$

Figure 9.8 shows scope traces of two ramps with this shape with different start and end voltages, but the same change in voltage and the same ramp time. We see that their shapes differ from one another. Ramps can be defined in two different ways: with a desired ramp time, or with a desired $\beta$. In both cases, both the axial frequency at the top of the ramp, $\omega_{z,t}$, and at the bottom of the ramp, $\omega_{z,b}$ must also be specified.

The user, often through qControl, specifies these parameters, and the etherDAC[17] calculates the ramp based on Equation 9.1. The etherDAC must, of course, program this ramp in a discrete

[16] Blakestad [149] sees that the update rate of the DAC can excite motion when $\omega_z$ is an integer multiple of the rate. We have not seen this, likely because we have much more aggressive filtering, smoothing the discrete steps. It is still worth keeping in mind, as it might be possible to increase the update rate, as the current rate is a consequence of how the microcontroller is programmed. Very fast DAC update rates of around 50 MHz in, for example, transport experiments, are achieved using FPGAs [150], another layer of complexity. This is beyond what we need.

[17] To be specific, the Raspberry Pi does the calculations.

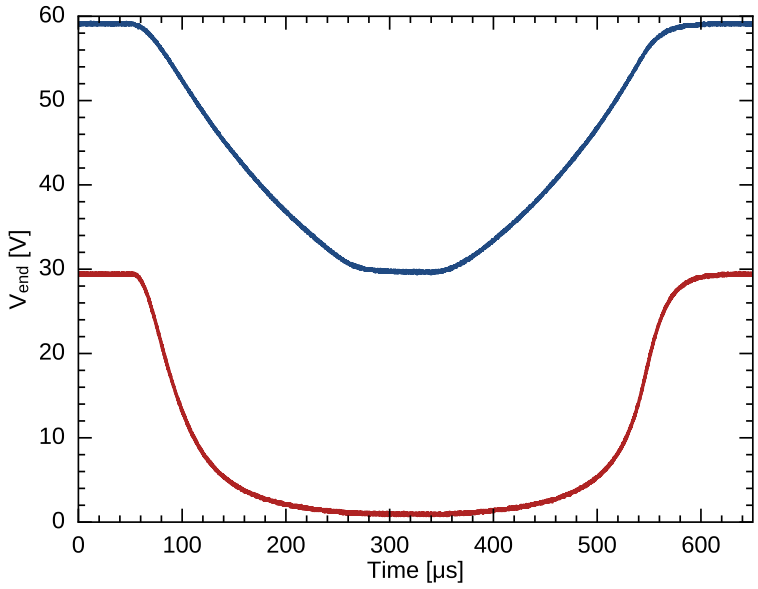


Figure 9.8: Scope traces of adiabatic-shaped etherDAC ramps, both with $t_r = 250\,\mu s$ but different voltage ranges (60 V to 30 V and 30 V to 0 V). This shows both a ramp down, a wait, and then a ramp back up again. The asymmetry is due to the DC filtering.

manner. Either by being provided $t_f$, or by calculating $t_f$ based on $\beta$, the etherDAC calculates how many steps fit into that time and rounds up. It then calculates the appropriate voltage at each time step based on Equation 9.1. From this calculation last step will always exactly hit or overshoot the intended $\omega_{z,b}$. The etherDAC forces the last step to go to the $\omega_{z,b}$. This way, the actual $\beta$ throughout the ramp will never exceed the intended $\beta$.

Figure 9.9 shows a pair of symmetric ramps: one down, and one up. The trace in dark blue shows the measured scope trace, and the traces in red and yellow show the expected ramp shapes based on the LTspice model. They match very well. Below, we see the input to the model, or rather the output of the DAC, which corresponds to the calculated adiabatic ramp shape as discretized into 4.68 µs steps. The orange corresponds to the actual time this occurs relative to the measured scope trace, and the light blue shows the curve time-shifted by 30 µs to overlap with the scope trace. The ramp is slower than the adiabatic shape at the top in both cases, however the shape at the bottom of the ramp follows well. The fact that the ramp is slower means that $\beta$ is not higher during that part of the ramp than it was intended to be. Because the ramp is slower than the programmed ramp, there is a built in settling time of $t_s$ = 150 µs past the ramp time. Simulation has shown that this is more than enough time to have less than 100 Hz variations in the axial frequency after this time at both the bottom and top of the ramp for typical ramps used in the experiment.

### 9.3.6 Triggering

The etherDAC can be used during an experiment by being pre-programmed with any ramps needed during a sequence, and then triggered with precise timing to start each ramp exactly when needed. Triggering is accomplished via a trigger input to the microcontroller, which the

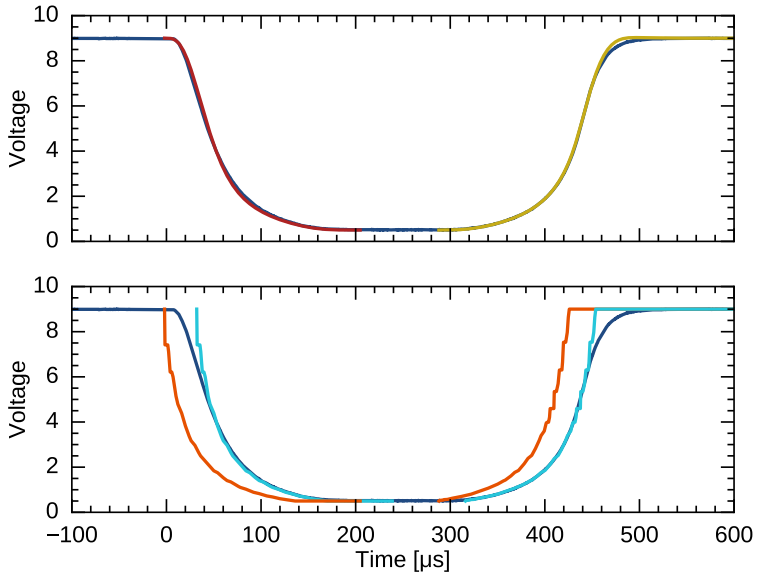


Figure 9.9: Ramps with $t_r$ = 140 µs, with ▬ showing the ramps measured with the scope out of the RF/DC mixer. **Top:** ▬ and ▬ show the simulated ramp shape for the same input ramp. **Bottom:** ▬ shows the programmed DAC ramps at the time they occurs, and ▬ shows them shifted in time to compare the programmed versus actual ramp shapes.

microcontroller always listens for so long as it is not in the middle of writing data out to the DACs.

I measured the time between trigger and ramp start for 12 ramps: 8 ramps at 0-2 V, 2 ramps from 0-60 V, and 2 ramps from 0-80 V. The measured time between trigger and ramp start was found to be 5.76(3) µs. Thus, we can count on ramps to occur at the same time during a sequence.

Triggering one ramp causes the entire programmed ramp to run. The updates stop at the end of the ramp, as indicated by the 'continue' bit changing from 1 to 0. Many ramps can be programmed into the buffer, and the next trigger will trigger the next ramp in the buffer. If the end of the buffer is reached, it wraps around such that the next trigger is the first ramp in the buffer. This means that for a sequence that requires two ramps for every measurement, the only two ramps need to be programmed in at the very beginning of the sequence, and not before individual measurements.

### 9.3.7 Noise measurements

As discussed in section 4.4, electric field noise at the frequency of the ion causes unwanted heating. As such, it was important to characterize the output noise of the DAC systems, especially as I made changes. Thus, I measured the noise spectral densities at the output of the three etherDAC versions. The implications of the measured noise spectral densities are discussed in Chapter 11.

Figure 9.10 shows the noise spectral density of the three different etherDAC versions. We can see that there was improvement of the output noise with each iteration. The noise spectra were measured using a spectrum analyzer[18], and the measurement limit, called the noise floor,

[18] Tektronix RSA5103B

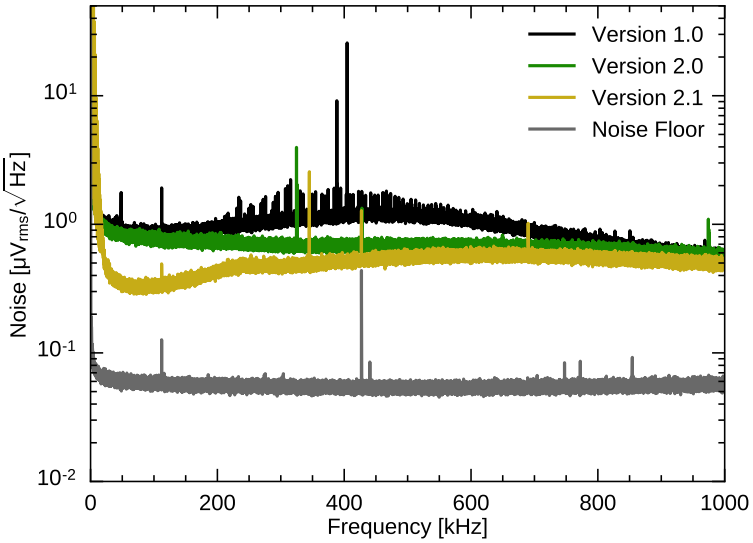


Figure 9.10: Comparison of the noise spectral densities out of the amplifiers of the three etherDAC versions. Also plotted is the measurement floor of the spectrum analyzer (noise floor).

is plotted in grey. For each, the noise is measured directly out of the amplifiers. The noise out of the DAC box (unamplified DACs) in etherDAC 1.0 was too low to measure with the spectrum analyzer, as the noise is below the noise floor. It was similarly not possible to measure the noise out of the RF/DC mixer, as the filtering causes the noise level to be too low to measure.

The noise spectrum of the etherDAC 1.0 amplifiers is limited by noise from the amplifier box, as the noise spectrum does not change regardless of whether it is loaded with the DACs, with a battery, or shorted across the input. Batteries have noise levels in the $50\,\mathrm{pV_{rms}}/\sqrt{\mathrm{Hz}}$ to $300\,\mathrm{pV_{rms}}/\sqrt{\mathrm{Hz}}$ range at 100 kHz [151]. Amplifying this noise by 10 (the maximal amplification, though at this frequency it's lower), this brings us nowhere near the measured noise level around $1\,\mu\mathrm{V_{rms}}/\sqrt{\mathrm{Hz}}$.

These three traces plotted were measured at a DAC output of 0 V. The noise spectrum changes only marginally, and only at low frequency, when loaded with a higher voltage. The spectrum analyzer can only measure with an offset of 5 V DC, so used a 0.1 µF capacitor in series with the output of the supplies to measure at higher voltages. This forms a high pass filter with the output resistance of the DC amplifiers $R_{out}$ and the 50 Ω input resistance of the spectrum analyzer. Figure 9.11 shows a circuit diagram of the filtering into the spectrum analyzer. The spectrum was corrected by using the transfer function of this circuit to calculate back to $V_{in}$.

It should be noted at the spectra of etherDAC 1.0 are not identical across all channels. They all have the same base shape, but the peaks in the 300 kHz to 600 kHz range are less pronounced in some channels.

### 9.3.8 Radial micromotion compensation

As discussed in section 2.1, along the trap axis the RF field cancels, creating an RF null line. If the ion sits in the center of the trap, the only micromotion it experiences is intrinsic, resulting from the fact that the ion cannot stay perfectly in the trap center. If the ion's equilibrium position is pushed away from the RF null by, for example, DC stray fields, it experiences excess micromotion

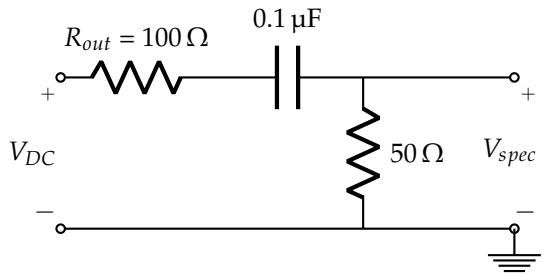


Figure 9.11: Diagram of the filter circuit for the spectrum analyzer. A 0.1 µF capacitor is placed between the DC amplifiers and the spectrum analyzer to create a filter with the passive components on either end. $R_{out}$ is the output resistor of the DC amplifiers, and the 50 Ω resistor corresponds to the input of the spectrum analyzer.

in the radial direction [89]. These stray fields can be compensated by adding offset voltages to the trap rods, in our case, to electrode triplets 1,2, and 3, and 4, 5, and 6, as labeled in Figure 2.1.

To compensate micromotion, we must be able to detect it. Looking at Figure 2.6, moving away from the trap center horizontally will result in vertical micromotion. Moving away from the trap center vertically will result in horizontal micromotion.

To detect horizontal micromotion, we can monitor the Doppler shift as a function of the RF phase. The fluorescence of the ion will increase as it is moving towards the Doppler cooling beam, as the effective detuning becomes closer to resonance. As it moves away from the beam, the fluorescence decreases. Thus, for larger amounts of micromotion there is a larger modulation of the fluorescence signal. This is the same type of detection method as presented in [89].

In practice we accomplish this measurement by gating the image intensifier at a 0.5 Hz frequency difference from $\Omega_{RF}$. The fluorescence signal from the camera then changes in time as we sample a full RF period over 2 seconds. This allows us to compensate micromotion in real time.

To detect micromotion in the vertical direction, we use the imaging system. If the ion is pushed off-center by a DC field in the horizontal direction, we will be able to see the ion move as we change the amplitude of $V_{RF}$ and the confinement of the ion becomes weaker or stronger. If the ion is centered, it will not move.

It is important for micromotion to be compensated at all voltages used in the experiment. We compensate for micromotion at $V_{end} = 60\,\mathrm{V}$ and at $V_{end} = 1\,\mathrm{V}$. We find that interpolating between (or extrapolating past) the compensation values found at these two voltages, we stay compensated at all voltages. We apply the calculated compensation voltages in every step in a ramp, keeping micromotion compensated.

### 9.3.9 Axial field compensation

DC offsets along the axial direction cause the ion to shift along the axis as $V_{end}$ is changed. During adiabatic ramping experiments, we want to ensure that the ion or ion pair's center does not move. Thus, we compensate axial DC offsets by applying a potential to electrodes 3, 6, 9, and 12, as labeled in Figure 2.1.

To determine the correct center location, we increase $V_{end}$ until the ion no longer moves along the axis (as seen on the imaging). The ion position is marked, and the $V_{end}$ reduced. Because the 397 nm laser exerts light pressure on the ion, it is also important to reduce this power until the ion no longer moves. The potential is then adjusted until the ion is centered.

# Chapter 10

# Sequence automation

Our experiment is largely automated. This chapter briefly discusses how experimental automation is accomplished.

## 10.1 Sequence building: qControl

All of our experiments are run via an experimental control program called qControl. qControl is a Python program that was started by Gregers Poulsen [44], and has been continuously modified by all PhD students and postdocs on the trap since. It takes care of saving all ion experimental data to both the computer and to a database, along with which it saves the configuration file of all of the settings. Thus it is simple to track changes in sequences from one to another.

Day to day use of qControl involves interacting with its GUI, which has pre-defined experimental sequences on which one can modify parameters. Each sequence is based on preexisting sequence blocks which are defined centrally. For example, Doppler cooling, sideband cooling, and readout are centrally defined, such that no matter what type of sequence one runs, the parameters stay consistent unless explicitly edited. Additionally, operations such as probe pulse (a 729 nm coherent pulse) is defined with variable inputs for the pulse length, amplitude, and frequency. Thus, building a sequence is quite straightforward.

There are a few aspects of the sequence building which I will cover in the following: readout, ion dark detection, and transition locators.

### 10.1.1 Readout

$^{40}Ca^{+}$ detection, or readout, is achieved through analysis of CCD images. During readout, the 397 nm and 866 nm Doppler cooling beams are used to probe the internal state of $^{40}Ca^{+}$. If the ion is shelved, it is dark, otherwise it is light. Readout takes 10 ms for exposure.

The experimental control program then analyzes the number of counts in a user-defined region of interest (ROI). If it is above a cutoff fluorescence, the ion is determined to be light, and if it is below, it is determined to be dark. Dark counts are registered as one count, and light counts as zero. Each data point consists of a sum of these counts, the number of which is dependent on the number of experimental cycles, normally 100.

The cutoff level is determined by a sequence which returns the fluorescence level of the ion with both the 397 nm and the 866 nm lasers on, and returns the fluorescence level without the 866 nm laser on. Without the 866 nm light, the ion is pumped into the $^{2}P_{3/2}$ state and is dark on the camera. The cutoff is then chosen to fall between the light and the dark counts. A histogram

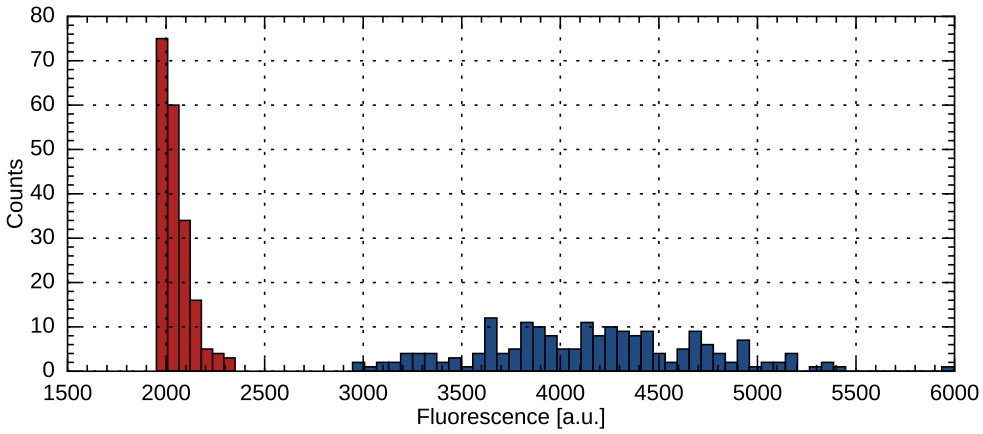


Figure 10.1: Histogram of the fluorescence signal when the ion is dark (red) and light (blue).

showing the light and dark counts can be found in Figure 10.1. We have near perfect detection fidelity.

### 10.1.2 Ion dark detection

Sometimes during a sequence, the ion will go dark for reasons unrelated to the experimental sequence. This could be because a laser came unlocked, or it could be because a collision knocked the ion into an orbit and it has not yet re-cooled. To combat these occurrences from being logged as false dark counts, we have implemented ion dark detection and processing.

Ion dark detection checks after every data point (typically 100 cycles[1]) that the ion is bright after repumping. If it is not, the data point is discarded[2], the ion is re-cooled using the far-detuned 397 nm beam, and the data point is retaken.

With two ions, the ion dark detection is more involved. For two $^{40}Ca^{+}$ ions, qControl uses two different thresholds: one that separates both being light from one being light, and one that separates one being light with both being dark. Readout is detected when both are dark, but ion dark detection checks if even one is dark. This way, if one ion has been kicked heated in orbit by a collision but the other is still cold, or if one of the ions has reacted, the experiment can discard this data. It is also chosen this way because with two-ion chains, the ions sometimes get stuck orbiting in the radial plane. This orbit has some residual fluorescence which is slightly higher than that of two dark ions[3].

For the mixed-species chains, one more check was added. This checks if the ion was sitting in the center of the ROI or if it was sitting out at the sides, its 'proper' location. If it sits in the center, the point is considered a false dark, the ion is re-cooled, and the data is retaken.

For the two-ion crystals, the re-cooling can be chosen to also implement a frequency ramp for both the axial and radial frequencies while cooling with the far-detuned 397 nm beam. This helps the ion recrystalize.

The last ion dark detection check is not a physical check but a processing check. qControl checks how many dark counts $d$ it gets in a row during a data point. If, given the total number of

[1] It is not implemented every cycle because it is quite time intensive, as we are using the camera and not a PMT for readout.

[2] These instances are logged.

[3] But barely. In most cases it would still readout as two dark ions.

dark counts measured, there is less than a 1 % chance that it measured $d$ dark counts in a row, the point is retaken.

### 10.1.3 Transition locator

In order to track magnetic field and laser drifts, we have implemented automatic transition locators. These are automatically enqueued every 10 minutes, and carry out carrier spectroscopy on the shelving transition ($^2S_{1/2}$, $m_J = -1/2 \rightarrow {}^2D_{5/2}$, $m_J = 5/2$), the intialization transition ($^2S_{1/2}$, $m_J = 1/2 \rightarrow {}^2D_{5/2}$, $m_J = -3/2$), and the reverse initialization transition ($^2S_{1/2}$, $m_J = -1/2 \rightarrow {}^2D_{5/2}$, $m_J = 3/2$). If the fit of the transition is good, the values are updated in qControl and saved to the database (as well as the raw spectroscopy scan). This allows us to evaluate the quality of data that we take, and judge if there were any shifts during measurement.

## 10.2 Sequence timing: the PPG

Within a sequence we have a number of components: Doppler cooling, initialization, sideband cooling, frequency ramping, probing, readout, and repumping. Each of these components must come in at specific time in a specific order. Each of these components consists of sub-components: laser pulses, voltage changes, and camera exposure. Each of the sub-components need to occur for a specific period of time, and their occurrence must be precisely timed in relation to the other sub-components.

We use a programmable pulse generator (PPG) to handle the timing of the experimental sequence. The PPG hardware and software are based on an open source PPG developed at MIT, NIST, MPQ, and Innsbruck, with input contributed from ion trap groups around the world [152–157]. The PPG uses field programmable gate arrays (FPGA) running at 100 MHz to control 32 TTL (transistor-transistor logic) outputs. As previously mentioned, these TTL outputs control the RF switches for the laser AOMs, the camera exposure, the etherDAC ramps, and anything else that needs timing during a sequence.

The PPG is also equipped with a DDS output with a range of 10 MHz to 350 MHz, which is used to control the 729 nm AOM, and thus the amplitude and frequency of the light at the experiment. The DDS is controlled with a dedicated FPGA which allows for phase continuous and coherent operations such as frequency and amplitude switching and sweeps.

Sequences are compiled by qControl[4] and sent to the PPG. Each data point (typically 100 cycles) consists of one program looped 100 times. After each cycle, the PPG waits for a trigger from the computer to confirm that fluorescence was recorded, before starting again. At each data point, qControl uploads a new pulse sequence (for example, with different pulse time or frequency) to the PPG. Sequence upload is achieved via fiber-optic link.

[4] using the open source API provided at [152, 155].

# Part IV

# Experiments with $Ca^+$

# Chapter 11

# Heating rates

The cause and reduction of heating rates in ion traps has been of great interest to the ion trap community, as the heating rate in a trap produces limitations in measurement precision, gate fidelity, and coherence times. Measurements of heating rates in Paul traps were presented as early as 1989 by Diedrich *et al.* [18], where the heating rate was considered in order to understand the limitations of their sideband cooling. In 1995, Monroe *et al.* [158] referred to this heating as anomalous heating, as the source of the heating was not well understood, and this term has been used widely in the literature since [93, 159–162].

The origins of heating in traps has since been studied for many different traps of varying geometry and environment, with at least a few papers published on the topic each year since 1998. While in many traps the dominant mechanism of heating is still unknown, there are some examples where the mechanism for the specific trap has been identified, from fluctuating patch potentials [160], to Johnson noise [163], to surface effects [164, 165] and contamination [166–169], to technical noise [170–173] and EM pickup [174, 175]. Needless to say, which heating mechanism is dominant is largely trap dependent.

The heating rates in our trap are of particular interest to us as heating limits our ability to perform quantum logic spectroscopy. Knowing the heating rates allows us to tailor the experiments such that we are not noise-limited. Understanding the origin of these rates is especially enticing, as it allows for improvement of the heating rate.

Heating rates were previously studied in our trap [44, 175], and were found to be independent of $\omega_z$, sitting just below $\dot{\bar{n}} = 1\,\mathrm{s}$. However, since these measurements were completed, the entire electronics system was swapped out for one with less filtering. In addition, the location of the lab moved. Thus, it was necessary to recharacterize and subsequently improve these rates.

In this chapter, I discuss the heating rate measurements carried out for both single ions and two ion crystals. In addition, I trace the origin of these heating rates to the noise from the DC supply, improve them, and am able to construct a model with which to predict further heating rates. Because we are concerned with the axial ion modes, all experiments undertaken in this chapter deal with the axial heating rates of the ions.

## 11.1 Single ion heating rates

To characterize the heating rates in our trap, we use a single $^{40}Ca^{+}$ ion as a baseline. This section covers the measured heating rates of a single $^{40}Ca^{+}$ ion, and the analysis into the origin of the heating.

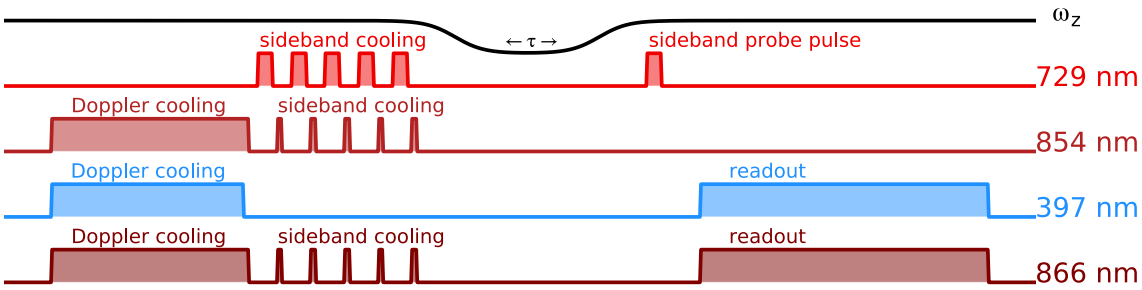


Figure 11.1: Sequence diagram of a heating rate measurement. The delay time $\tau$ is inserted at the bottom of the ramp. The sideband probe pulse alternates between exciting the red and the blue sidebands.

### 11.1.1 Experimental details

The goal of a heating rate measurement is to extract $\dot{\bar{n}}$. $\bar{n}$ can be measured using the sideband comparison method [94] of measuring motional state occupation described in 4.4. To measure the heating rate, one must study the evolution of $\bar{n}$ in time.

A schematic of the sequence used in heating rate measurements can be found in Figure 11.1. To understand the sequence, we will first not consider changing $\omega_z$ (the black curve). The first step is to cool the ion down to the ground state using a combination of Doppler and sideband cooling. At the end of this stage, the ion will be in the state $|g, \bar{n}_i\rangle$, where $\bar{n}_i \simeq 0$. The second step is to wait a variable time $\tau$. During this time, electric field noise will drive transitions between neighboring $|g, n\rangle$ at a rate $\dot{\bar{n}}$, without influencing the internal state. After this stage, the new state is $|g, \bar{n}(\tau)\rangle$. Lastly, the state $|g, \bar{n}(\tau)\rangle$ is probed by a sideband probe pulse. This pulse is tuned to either the red or the blue sideband of the shelving transition, and Equation 4.38 can be used to calculate $\bar{n}(\tau)$. After varying $\tau$, a plot of $\bar{n}(\tau)$ can be fit to a line. The extracted slope will give $\dot{\bar{n}}$, and an example is shown in Figure 11.2.

We wish to measure the heating rate at multiple frequencies to understand how the heating rate will affect quantum logic spectroscopy using adiabatic cooling. Optimizing sideband cooling at every $\omega_z$ is not necessary to carry out these measurements, as we can utilize the ability to change $\omega_z$ mid-measurement. This is where the curve for $\omega_z$ in Figure 11.1 comes in. After sideband cooling, we have the option of ramping from $\omega_z = \omega_{z,t}$ to $\omega_z = \omega_{z,b}$. The variable time delay $\tau$ is now placed at the bottom of the ramp such that we probe the evolution of $\bar{n}$ at $\omega_z = \omega_{z,b}$. The ion will heat in all parts of the sequence, however, the important part of the linear fit is the slope, and only heating picked up as a result of the change in $\tau$ will influence the slope. Thus the rate will valid for $\omega_{z,b}$.

The measurement of $\bar{n}$ is dependent only on the height of the sidebands. If the separation between the two sidebands is well-known, we can extract the heights of the sidebands by measuring only on the peaks. For the measurements presented in this section, $\bar{n}$ for each delay was measured by measuring the sideband heights at only one frequency per sideband, corresponding to the centers of the red and blue sideband. The pulse time used for the sidebands corresponded to a $\pi$-pulse on the blue sideband $|g, n = 0\rangle \rightarrow |e, n = 1\rangle$ transition, which also is a $\pi$-pulse for the red sideband $|g, n = 1\rangle \rightarrow |e, n = 0\rangle$ transition. Each sideband height measurement corresponds to 100 measurement trials, and each sideband height was measured 19 times[1], with the measurements interwoven between the sidebands such that correlations between sideband height changes could be tracked.

[1]The measurements taken for the unamplified DACs were only measured 9 times per sideband. This is the only dataset presented that is an exception.

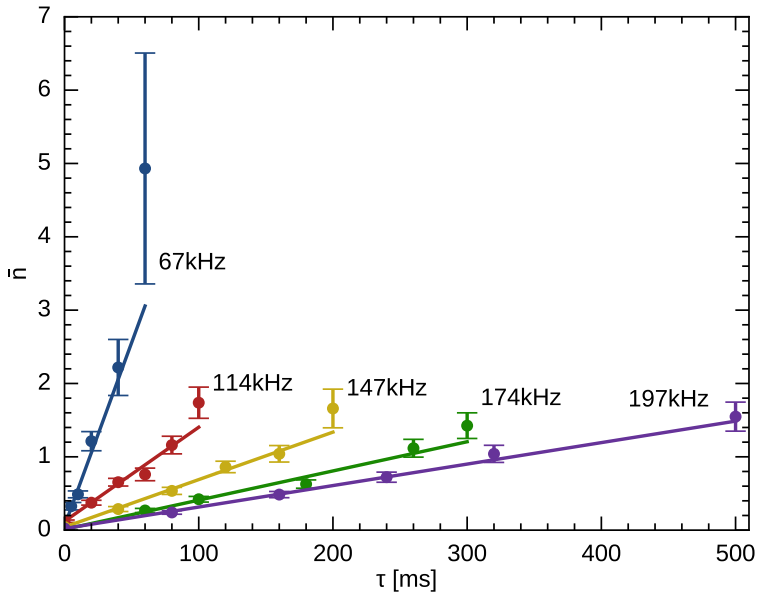


Figure 11.2: Heating rate measurements for five different axial frequencies. The points show the measured $\bar{n}$ for a specific delay time $\tau$, and the slope gives the heating rate. This dataset can be related to the heating rates for the unamplified DACs.

We can only use this measurement method if the laser frequency and magnetic field are stable over the course of a measurement. Because of the cavity and comb stabilization of the 729 nm laser, the laser frequency is not a problem. For magnetic field stability, heating rate measurements were typically taken over the course of a night such that the field was more stable. In addition to this, Equation 4.38 is independent to detuning, so as long as the magnetic field is constant over the course of the measurement of a single delay, it can shift small amounts between delays. To monitor when the field is shifting, measurements of the carrier shelving transition, the initialization transition, and the reverse initialization transition were taken before and after the measurement of each delay, and monitored for changes in frequency.

While separation between the two sidebands ideally is $2\omega_{z,t}$, AC Stark shifts (see subsection 3.2.1) can cause this separation to be slightly smaller. To ensure that we measured at the correct frequencies, the separation between the carrier and the blue sideband was fit prior to starting the measurements. The separation was further confirmed by measuring the sideband separation after having created the Fock state $|g, n = 1\rangle$ by applying a blue sideband pulse plus an 854 nm pulse prior to measurement.

### 11.1.2 Results

Heating rate measurements were carried out for all versions of the DC supply, and are summarized in Figure 11.3.

The black circles show the data for the first iteration of the DC supply, etherDAC 1.0. These measurements were taken before frequency ramping was fully implemented, so $\dot{n}$ was measured by sideband cooling and probing at each axial frequency. The pulsed sideband cooling scheme was adjusted separately for each axial frequency (keeping consistent timing but varying pulse

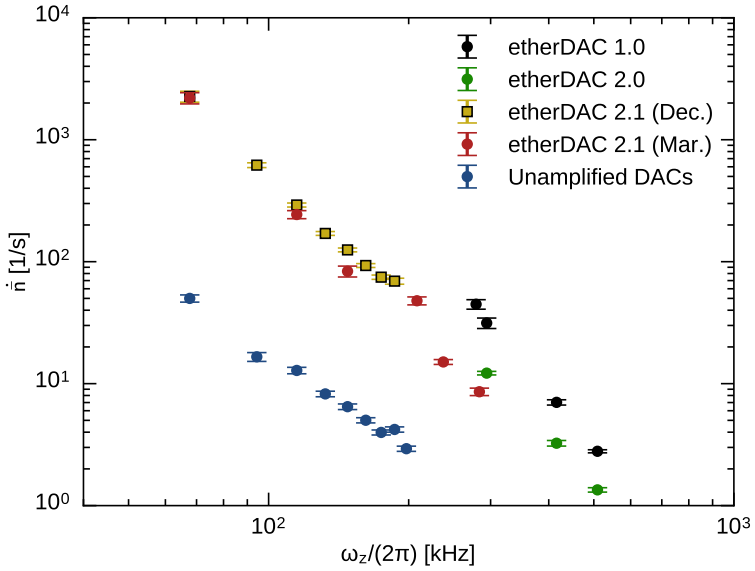


Figure 11.3: Heating rates versus $\omega_z$ of a single $^{40}Ca^+$ ion

| $\frac{\omega_z}{2\pi}$ [kHz] | $\dot{n}$ [$s^{-1}$] | | Ratio |
|---|---|---|---|
| | etherDAC 1.0 | etherDAC 2.0 | |
| 294.2 | 31(3) | 12.1(4) | 2.6(3) |
| 415.8 | 7.0(3) | 3.2(2) | 2.2(2) |
| 509.1 | 2.79(8) | 1.35(6) | 2.1(1) |

Table 11.1: Comparison of heating rates, showing the degree of improvement between two etherDAC supplies.

powers).

When we move the DAC chips from the digital box to the amplifier box to create etherDAC 2.0, we see a reduction of noise as shown in Figure 9.10. The green points in Figure 11.3 show the corresponding reduction in heating rate. These points were measured using the same method as for etherDAC 1.0. The ratio between the heating rates of etherDAC 1.0 and 2.0 is given in Table 11.1. These ratios correspond approximately to the square of the ratio between the two noise spectra shown in Figure 9.10, as one would expect if the heating is due to the DC supply.

The points in yellow and in red show the heating rate after extra filtering was added after the DACs, creating etherDAC 2.1. The corresponding noise spectrum is the yellow curve in Figure 9.10. For the points in yellow, the ion was sideband-cooled using a continuous scheme at 416 kHz, ramping down to $\omega_{z,b}$ in $t_r = 80\,\mu s$. This corresponds to the adiabaticity parameter $\beta = 0.025$ for the lowest frequency. The red points were taken four and a half months after the rates shown in yellow, showing remarkable consistency in heating rates over a long period of time. For these points, the ion was continuous sideband-cooled at 283 kHz before ramping in $t_r = 150\,\mu s$. This gives $\beta = 0.012$ for the ramp down to the lowest frequency, 67 kHz.

As discussed in subsection 9.3.7, the noise spectrum out of the unamplified DACs (DAC box) of etherDAC 1.0 was too low to measure on the spectrum analyzer. I was able to, however, measure heating rates when using only the unamplified DACs to provide the DC voltages to the

electrodes. This amounts to removing the amplifiers in Figure 9.4.

The blue points show the heating rates measured using the unamplified DACs as the DC supply. They were taken by sideband cooling using a continuous scheme at 198 kHz[2] and ramping to the measured frequency in 150 µs. For the lowest frequency, $\beta = 0.01$. These heating rates are more than an order of magnitude reduced from the amplified supply, with the absolute rates ranging from $\dot{\bar{n}} = 3\,\mathrm{s}^{-1}$ to $50\,\mathrm{s}^{-1}$ for $\omega_z/(2\pi) = 198\,\mathrm{kHz}$ to 68 kHz. It is clear that reducing the noise output of the DC supply impacts our heating rates. As calculated from Equation 4.29, the heating rate at $\omega_z/(2\pi) = 198\,\mathrm{kHz}$ corresponds to $S_E = 4 \times 10^{-15}\,\mathrm{V^2\,m^{-2}\,Hz^{-1}}$, which brings to similar electric field noise as was achieved previously in the trap with much stronger electronic filtering [175].

### 11.1.3 Heating from technical noise

Voltage noise at the output of the DC supply translates to electric field noise at the ion. This is because the supply noise from the output of the DC supply ends up as voltage noise on the electrodes. Voltage noise on the electrodes of course translates to electric field noise on the ion. This means that to have low heating rates, it's important to either have a low noise DC supply or a strongly filtered supply. For our experiment, the speed at which we want to ramp sets the limit to how much filtering is possible.

The voltage noise spectral density on the electrodes translates into the electric field noise spectral density on the ion (in the z-direction) by scaling it by the ion's characteristic length from the electrodes, D [93, 94, 160]

$$S_E = \frac{S_{V_{end}}}{D^2} \tag{11.1}$$

This characteristic distance describes how a voltage change on a single endcap electrode will change the electric field in the z-direction on the ion. In our trap, $D = 56\,\mathrm{mm}$, and was found by modeling the trap in SIMION[3].

As presented in Chapter 9, the output of the DC supply is filtered through the RF/DC mixer before going to the trap electrodes. This means that the noise is filtered as well by the characteristic of the RF/DC mixer. To relate the voltage out of the DC supply to the voltage at the trap electrodes, we must take into account the transfer function of the RF/DC mixer shown in Figure 9.3, denoted functionally as $F(\omega)$[4]. The DC supply noise shown in Figure 9.10 shows $\sqrt{S_{V_{DC}}}$. Thus,

$$S_E(\omega) = F^2(\omega)\frac{S_{V_{DC}}}{D^2} \tag{11.2}$$

Inserting Equation 11.2 into Equation 4.29, one obtains

$$\dot{\bar{n}}_{one} \simeq \frac{e^2}{4m\hbar\omega_z} F^2(\omega_z)\frac{S_{V_{DC}}}{D^2} \tag{11.3}$$

This equation is valid if the noise is on only one of the electrodes. We have 8 electrodes (the endcaps) contributing to axial heating. The voltage noise adds in quadrature, thus the noise spectral density will sum. Equation 11.3 becomes

$$\dot{\bar{n}} \simeq 8 \times \frac{e^2}{4m\hbar\omega_z} F^2(\omega_z)\frac{S_{V_{DC}}}{D^2} \tag{11.4}$$

[2] This is the frequency that corresponds to 9 V. The supply's voltage range is −1 V to 10 V, but I needed a buffer for micromotion offsets.

[3] Thank you to Julian Glässel, who helped me modify his trap's model to model my own.

[4] One note is that the filtering of the unamplified DAC supply differs slightly from $F(\omega)$ since the output of this supply does not have the 100 Ω resistor. This has been accounted for in calculations.

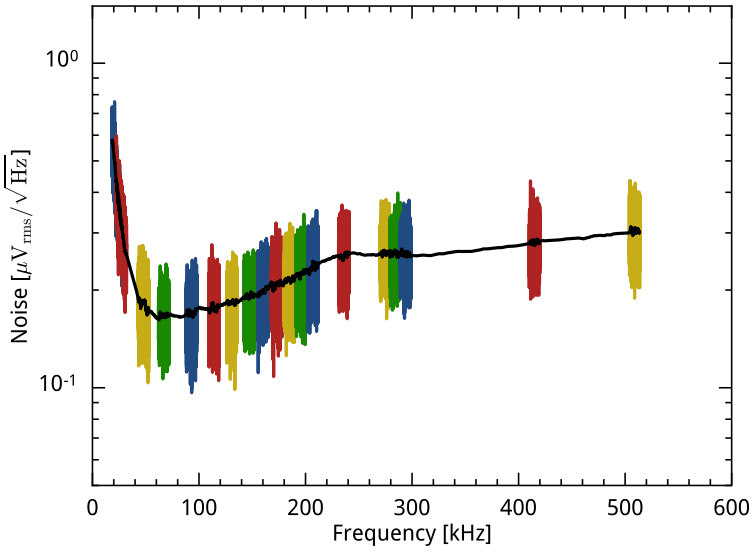


Figure 11.4: Noise out of etherDAC 2.1 amplifiers, with each colored section corresponding to a measurement where $V_{end}$ was set such that the center of the covered range was $\omega_z(V_{DC})$. For these measurements, the resolution bandwidth (RBW) of the spectrum analyzer was 10 Hz, and the measured signal corrected for this. The black line shows the smoothed noise signal.

### Comparison to DC supply noise

In order to optimize the DC supply, it is invaluable to understand how the noise out of the DC supply exactly influences the heating rates on the ion. Using the model presented in Equation 11.3, we can connect the measured noise spectra to the measured heating rates.

First, I remeasured the noise spectrum out of etherDAC 2.1 using a slightly different method than previously. Instead of measuring the spectra over a large range at a fixed endcap voltage, I measured small section of the spectrum while changing the endcap voltage such that I could see the noise spectrum 'as the ion would see it.' This meant having the same voltage loading the amplifiers as there would be during an experiment.

The endcap voltage is related to $\omega_z$ by Equation 2.4, and is shown characterized for our trap in Figure 7.4. Equation 7.1 gives us the functional form of $\omega_z(V_{end})$. To measure the noise spectra, I set $V_{end}$ and measured the noise spectra for a 10 kHz width around $\omega_z(V_{end})$. The $V_{end}$ values were chosen based on where the heating rates had been measured. The resulting spectrum is shown in Figure 11.4. The colored sections show the individual measurements of the noise for different $V_{end}$. The spectrum has been adjusted for the low pass filter used to measure on the spectrum analyzer (discussed in subsection 9.3.7). The black line shows the smoothed noise signal.

To relate this noise spectrum to the data, I fit the equation

$$\dot{\bar{n}} \simeq A \times 8 \times \frac{e^2}{4m\hbar\omega_z} F^2(\omega) \frac{S_{V_{end}}}{D^2} \tag{11.5}$$

for A, where this equation is based on Equation 11.4. This $A$ acts as a scaling parameter for the noise. The result of this fit is $A = 0.88$, and is shown in Figure 11.5 (a), where (b) shows the comparison to the other supplies. The line is obtained using the smoothed noise spectrum, and the shaded area around the fit line approximately corresponds to the width of the unsmoothed

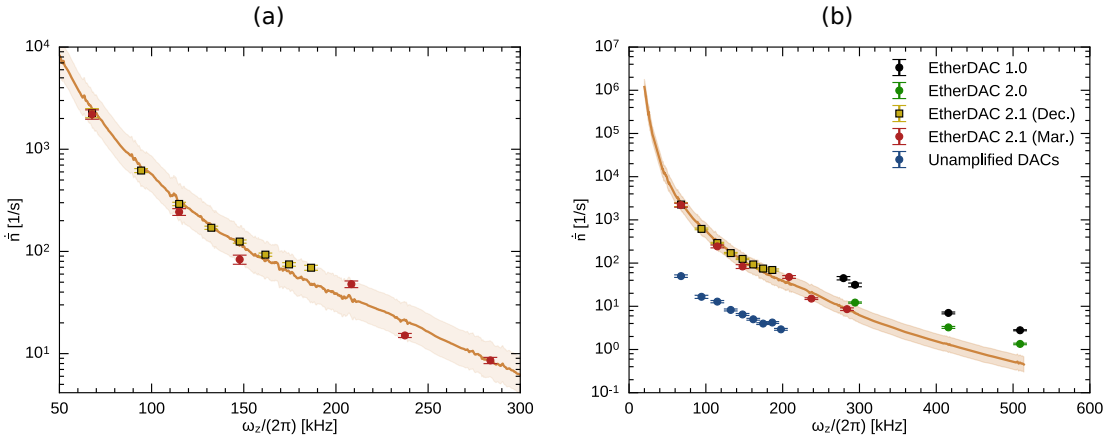


Figure 11.5: **(a):** Fit of Equation 11.5 to the heating rates using the noise spectrum pictured in Figure 11.4. The shaded area around the fit line corresponds to the width of the spectrum analyzer trace. Zoom in of the fit to the etherDAC 2.1 heating rates. **(b):** Comparison of the extrapolated fit to the other supply versions.

spectrum analyzer trace. We can see that the model well describes the trend of the data, with all points falling within the shaded region.

The scaling parameter is quite close to one. If one takes $\sqrt{A}$ to obtain a scaling factor instead for the voltage noise plotted in Figure 11.4, it is only 0.94. Its deviation from unity could be due to systematic error in the measurement of the noise spectrum. The measured noise spectrum is consistent, however, if it is measured at different resolution bandwidths (RBW)[5], the signal height changes even after correcting for the RBW. This scaling factor could also be related to the unknown parasitic and trap capacitances, $C_t$, combined with the variable capacitance $C_2$. For this calculation, it has been estimated at 100 pF.

Because the noise measurement is consistent when using the same spectrum analyzer settings, and the heating rates are consistent over time, one can use the spectrum analyzer measurement to predict the heating rates. This knowledge is invaluable for improving the DC supply. This also means that we know exactly where our heating rates are stemming from: technical noise. They are certainly not anomalous[6].

We can take this one step further and now predict the output noise of the unamplified DAC supply by back calculating from the measured heating rates. This produces the plot shown in Figure 11.6. This confirms what we had previously found: that the noise out of the DACs is low enough that we cannot measure it on the spectrum analyzer.

## 11.2 Two ion heating rates

To implement spectroscopy of $^{24}MgH^+$ using quantum logic spectroscopy, we need to understand how two-ion crystals heat in our experiment. To check if we can use heating rates of single $^{40}Ca^+$ to estimate heating rates on a two-ion crystal, I measured the heating rates of two types of two-ion crystals: $^{40}Ca^+$-$^{40}Ca^+$ and $^{40}Ca^+$-$^{42}Ca^+$.

[5]The RBW for this particular measurement was 10 Hz.

[6]One might even be tempted to say that they are... nomalous.

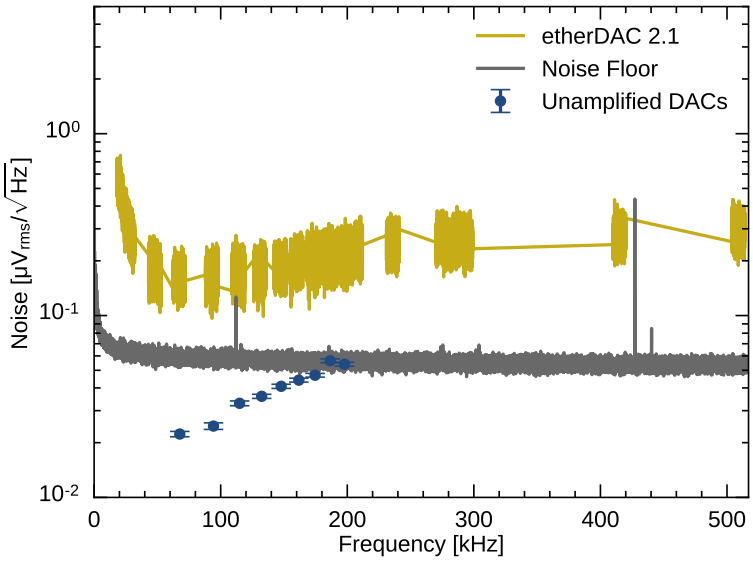


Figure 11.6: Comparison of the measured noise spectrum out of the etherDAC 2.1 amplifiers to the predicted noise spectrum of the unamplified DACs.

### 11.2.1 Experimental details

The basic experimental sequence for measuring two ion heating rates is the same as for the single ion case. In fact, the entire procedure is identical for measuring the in-phase heating rates of a two-ion crystal. Measuring the out-of-phase heating rates of two ion crystals was more challenging due to the heating rates being so small combined with an increased likelihood of the two ions decrystalizing with increased delay time $\tau$.

To measure the out-of-phase heating rates, I switched to measuring the sideband heights by fitting the peak over a range of detunings. Because decrystalization was a frequent occurrence, points were taken in groups of 10 trials, such that the ion dark detection would run more frequently, and less data would be lost when a dark ion was detected. 30 sets of 10 trials were taken per frequency (300 data trials total per point) and binned, with the groups of 10 more than 4 sigma from the mean being dropped as outliers. These points generally corresponded to groups of 10 where for every point, the ion was dark, but went light again prior to the ion dark detection.

Prior to using this technique, it was nearly impossible to take longer delays without a laser coming unlocked, the magnetic field shifting, or losing the ion. Even with this other scheme, the longest of these measurements took 5 hours to get a single delay data point (at a delay of 100 ms). Thus, only three delays were measured per $\omega_-$.

For all measurements, both in- and out-of-phase, sideband cooling occurred at 18.6 V before ramping to $\omega_\pm$ for the measurement in 150 µs. For the $^{40}Ca^+$-$^{40}Ca^+$ crystal, 18.6 V corresponds to $\omega_+/(2\pi) = 283.7$ kHz and $\omega_-/(2\pi) = 491.5$ kHz. For the $^{40}Ca^+$-$^{42}Ca^+$ crystal, this corresponds to $\omega_+/(2\pi) = 280.3$ kHz and $\omega_-/(2\pi) = 485.7$ kHz. The pulse times correspond to $\pi$-pulses on the blue sideband for $|g, n = 0\rangle$. For the $^{40}Ca^+$-$^{40}Ca^+$ case, this means the first instance of maximal probability $P_{bsb}(\uparrow\uparrow)$ as given in Table 3.1. The maximum peak height is $P_{bsb}(\uparrow\uparrow) = 0.89$. All measurements were carried out using the etherDAC 2.1.

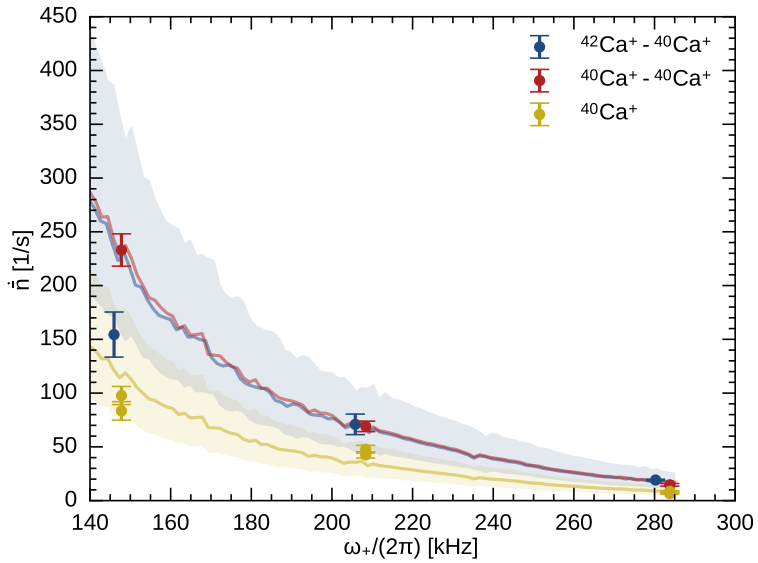


Figure 11.7: Heating rates of the in-phase modes of two-ion crystals with the lines derived from the single ion model. The points in yellow show the single ion measurements for comparison.

### 11.2.2 Results

In- and out-of-phase heating rates were measured for two types of two-ion crystals: a $^{40}Ca^{+}$-$^{40}Ca^{+}$ chain, and a $^{40}Ca^{+}$-$^{42}Ca^{+}$ chain. The measurements for the $^{40}Ca^{+}$-$^{40}Ca^{+}$ crystal are limited by the fact that we are sensitive only to $\Delta n = 2$ transitions (see subsection 4.4.1).

The measurements for the in-phase heating rates are summarized in Figure 11.7. Using Equation 4.32, we can predict the heating rates of the in-phase modes from the model developed in the previous section

$$\dot{\bar{n}}_{+}(\omega_{+}) = A \times 8 \times \frac{e^2}{4m\hbar\omega_z} F^2(\omega) \frac{S_{V_{DC}}}{D^2} \left( \beta_1^{\pm\prime} + \frac{\beta_2^{\pm\prime}}{\sqrt{\mu}} \right)^2 \tag{11.6}$$

where we use A = 0.88 as found in the single ion case. The red and blue lines in the plot are calculated from this model. For comparison, the rates for the single $^{40}Ca^{+}$ are shown in yellow.

Equation 11.6 assumes that the noise is spatially correlated. This is a reasonable assumption, given that ion separations range from 10 µm to 100 µm, and $D = 56$ mm is much larger.

The model calculated from the single ion case fits the two ion data as well. This is an indication that the assumption to treat the noise as spatially correlated is a valid assumption. This implies that we can use the single $^{40}Ca^{+}$ results to predict the heating rates in a $^{24}MgH^{+}$-$^{40}Ca^{+}$ chain.

As stated previously, the out-of-phase heating rates were more difficult to measure. For $^{40}Ca^{+}$-$^{40}Ca^{+}$ it was especially difficult owing to the decreased sensitivity dictated by Equation 4.41. Two measurements of $\bar{n}$ for out-of-phase heating rates are shown in Figure 11.8. These correspond to the delays $\tau = 0$ ms and $\tau = 100$ ms for the frequency $\omega_{-}/(2\pi) = 256.0$ kHz for a $^{40}Ca^{+}$-$^{40}Ca^{+}$ crystal. One can see that even after a delay of 100 ms, the red sideband has not grown much in height.

These are constructed from the binned data, and fit with an offset corresponding to the background noise. The background noise (related to the decrystalization) for each experiment type

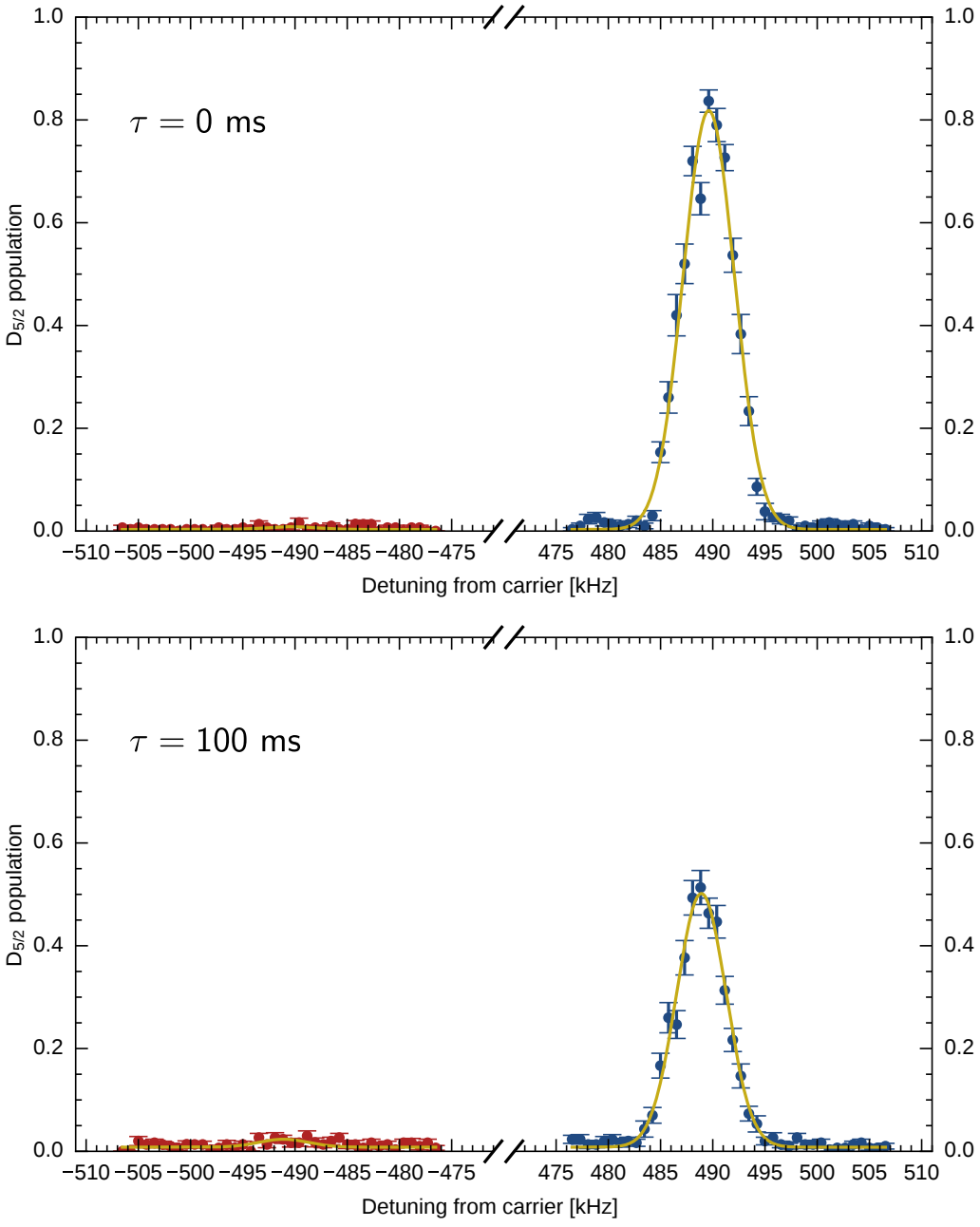


Figure 11.8: Out-of-phase sideband spectrum for $^{40}Ca^{+}$-$^{40}Ca^{+}$, with • showing the out-of-phase blue sideband and • showing the out-of-phase red sideband. These correspond to measurements of the heating rate at $\omega_{-}/(2\pi) = 256.0\,\text{kHz}$ with delays $\tau = 0\,\text{ms}$ and $\tau = 100\,\text{ms}$. They are constructed from the binned data.

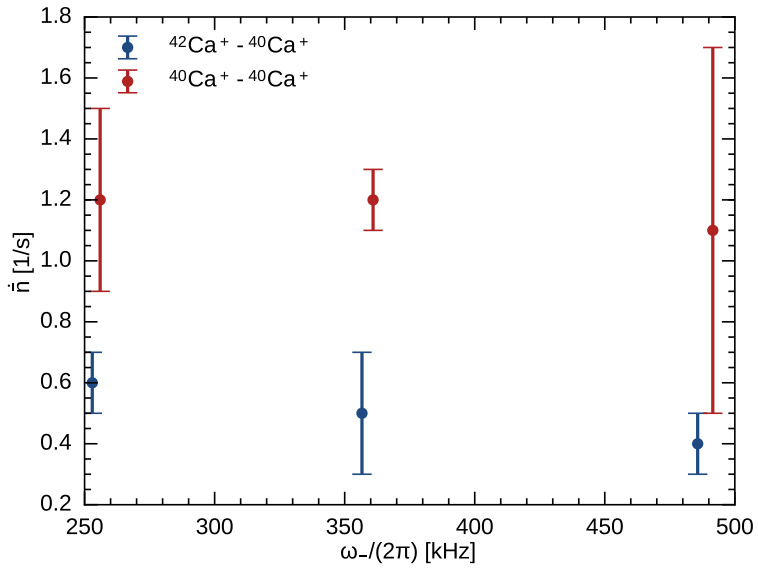


Figure 11.9: Out-of-phase heating rates of • $^{40}Ca^{+}$-$^{42}Ca^{+}$ and • $^{40}Ca^{+}$-$^{40}Ca^{+}$.

was characterized by running an identical experiment without inserting the probe pulse. The center frequency of the red sideband is constrained based on the center frequency of the blue sideband. The width of the red sideband in the fits is also constrained to be the same as the blue sideband, which in the limit of small $n$ is a decent approximation.

Figure 11.9 shows the results of the out-of-phase heating rate measurements on the two types of ion crystals. The expected heating rate of the out-of-phase mode of the $^{40}Ca^{+}$-$^{40}Ca^{+}$ crystal is $0\,s^{-1}$, and the expected heating rate for the $^{40}Ca^{+}$-$^{42}Ca^{+}$ crystal is dependent on frequency, and is two orders of magnitude smaller than what was measured.

There is a discrepancy between the two crystals, with the heating rates of the $^{40}Ca^{+}$-$^{40}Ca^{+}$ crystal about twice that of the $^{40}Ca^{+}$-$^{42}Ca^{+}$ crystal. This could mean that light leaking through the AOM at 397 nm could be responsible for these baseline heating rates, though one would expect to see a frequency dependence, which we do not see within error. Understanding the discrepancy between the heating of the two crystals would require further investigation.

It is worth noting that the measured heating rates, around $1.2\,s^{-1}$ for the $^{40}Ca^{+}$-$^{40}Ca^{+}$ crystal and about $0.5\,s^{-1}$ for the $^{40}Ca^{+}$-$^{42}Ca^{+}$ crystal, are similar in magnitude to the heating rates measured for single $^{40}Ca^{+}$ in the old setup. They similarly do not show a frequency dependence.

## 11.3 Conclusion

Heating rates were measured for a single $^{40}Ca^{+}$ at variable axial frequency for different versions of the DC supply. Technical noise was found to be the dominant cause of the heating rate, with the measured technical noise of the supply predicting the heating rates with only a 0.88 scaling factor on the noise spectral density. The largest decrease in the heating rates was more than an order of magnitude, and came when using the DAC supply without amplifiers, yielding heating rates ranging from $2.93(14)\,s^{-1}$ at $\omega_z/(2\pi) = 198\,kHz$ to $50(3)\,s^{-1}$ at $\omega_z/(2\pi) = 68\,kHz$. Measurements of the in-phase heating rates two-ion crystals showed good agreement with the

model developed for the single ion. The only discrepancy was with the out-of-phase heating rates, which seem to be limited by another process.

To gain the advantage of the improved heating rates when not using amplifiers in the DC supply, along with the spectral resolution gained with higher $\omega_z$, one could imagine building a DC supply with a larger DAC range, and offsetting the central electrodes negatively to gain even more in $\omega_z$. For example, a supply with $\pm 10\,\mathrm{V}$ could be used to reach the $18.6\,\mathrm{V}$ we normally operate at for two-ion experiments. The DACs currently used can have reference voltages up to $\pm 14\,\mathrm{V}$, so this could be potentially a minor modification.

# Chapter 12

# Adiabatic cooling

The classical process of adiabatic cooling is one that has long been understood. It is the phenomenon that as the pressure confining a gas is slowly decreased, the temperature of the gas decreases. It is found as a naturally occurring process in, for example, the formation of clouds. The quantum mechanical version of adiabatic cooling comes from the adiabatic reduction of the confinement of a well potential, allowing for the adiabatic expansion of a wavepacket. Adiabatic cooling has been used in quantum systems with a large number of particles, to, for example, reduce the temperature of gases of polar molecules [176], of beams of lithium atoms [177], and of plasmas of antiprotons [178], and to study phase transitions in ultracold gases [179, 180]. While adiabatic cooling of single ions was proposed as early as 1989 by Bergquist, *et al.* as a method for reducing the second-order Doppler shift [181], few experiments have been undertaken towards implementing adiabatic cooling.

Prior to the start of my PhD, adiabatic cooling was investigated on a single $^{40}Ca^{+}$ ion in Aarhus in both the Doppler and sideband-cooled regimes [44, 52]. In the sideband-cooled case, the best results were achieved for an axial frequency ramp from 583 kHz to 75 kHz, which took a total of 6 ms. The biggest limitation was the slow ramp time, which makes it inefficient to employ in an experiment with molecular ions.

This chapter presents the results of adiabatic cooling single $^{40}Ca^{+}$ ions and $^{40}Ca^{+}$-$^{42}Ca^{+}$ chains using the new electronics systems. The ramps employed have a ramp time of 290 µs, more than 20-times faster than those employed previously, and achieve lower frequencies–down to 41 kHz. The results presented in this chapter come from experiments on two different supplies: the etherDAC 2.1 and the unamplified DAC supplies. The first section covers the experiments undertaken with the etherDAC 2.1 supply, and the second section covers experiments undertaken with the unamplified DACs.

## 12.1 Experimental sequence

While the experimental sequence is by and large the same as that for the heating rates (with the sequence shown in Figure 11.1), the point of the experiments is fundamentally different. In the heating rate experiments, we are concerned with how much heating we pick up as a result of waiting variable delay times at the bottom of the ramp. So long as we can measure the change in the sideband heights for different delay times, we do not mind if we pick up consistent thermal excitation during the ramp as this just adds an offset to $\bar{n}$ which does not impact the rate. In adiabatic cooling experiments, we are interested in exactly how and why we pick up heating as the result of the frequency ramp, as we are interested in cooling the ion down as far as possible.

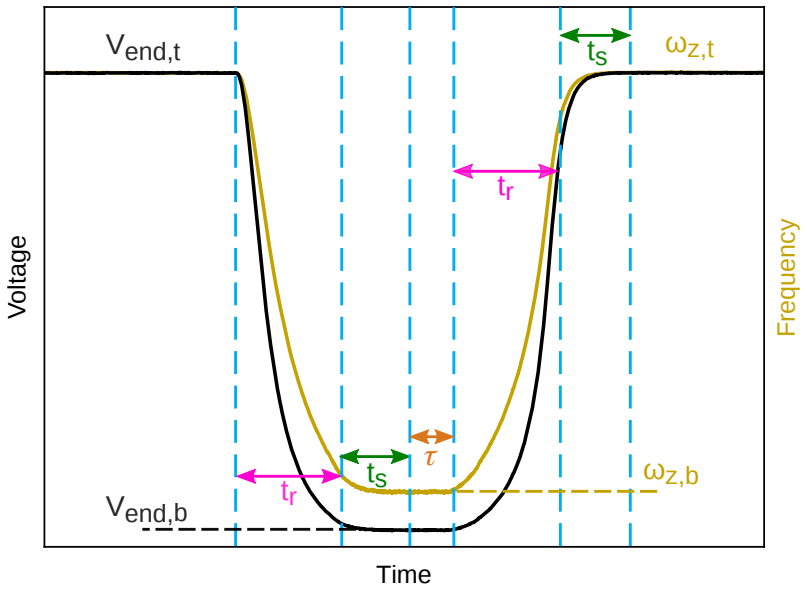


Figure 12.1: Voltage ramp from $V_{end,t}$ to $V_{end,b}$ showing the corresponding frequency ramp from $\omega_{z,t}$ to $\omega_{z,b}$. The ramp is programmed to take $t_r$, but due to the filtering in the electronics takes longer. A settling time $t_s = 150\,\mu s$ is used to ensure the ramp has time to reach its final value. There is an additionally optional wait time $\tau$ which can be added at the bottom of the ramp, which is 0 unless otherwise specified.

A generic ramp is shown in Figure 12.1. In a sequence, we ramp down to the target frequency $\omega_{z,b}$ from frequency $\omega_{z,t}$ by changing the voltage from $V_{end,t}$ to $V_{end,b}$. This is done with a constant adiabaticity ramp shape (see section 6.5 and subsection 9.3.5). The ramp takes time $t_r$, which is variable by the user, and takes time $t_s$ to settle due to the electronic filtering. After this point, the ramp is applied in the opposite direction, and after waiting for the voltage to settle, the red and blue sidebands are measured using a pulse time which corresponds to a $\pi$-pulse on the blue sideband. The sidebands are mapped out by a scan of the 729 nm frequency.

Though we are interested in the motional state of the ion at the bottom of the ramp[1], we measure the sideband heights at the top of the ramp. This is done for consistency and resolution. If we measure at the top of the ramp, we are always measuring at $\omega_{z,t}$, regardless of $\omega_{z,b}$. This means that the 729 nm intensity and/or pulse time can be kept constant.

The other reason is due to spectral resolution between modes. This is especially important for the two-ion case, where the first out-of-phase sidebands are located at $\delta = \pm\omega_-$, and the second in-phase sidebands are located at $\delta = \pm 2\omega_+$. The separation between these sidebands of course decreases as the potential decreases, as previously discussed in section 6.5.

It is thus simpler to measure at the top of the ramp, and is equivalent to what we would do in an experiment with $^{24}MgH^+$, as the measurement of $^{40}Ca^+$ would come at the top of the ramp. Thus, it is essential to know how much the ion heats as a result of ramping in both directions.

[1] Actually we are interested in the motional state both at the bottom and at the top, since spectroscopy occurs at the bottom but detection occurs at the top.

## 12.2 Temperature diagnostics

For each experiment presented, two sideband measurements are shown: one for a sideband-cooled (SBC) ion without a ramp as a baseline, and one for an ion which has been sideband- and further adiabatically-cooled. Because we measure at the top of the ramp, we must consider how we determine the temperature of the ion at the bottom of the ramp. If the process is perfectly adiabatic, we know that the temperature at the bottom of the ramp can be calculated from Equation 4.44, inserting $\omega_{z,b}$ for $\omega_z$, where

$$\begin{aligned} P_{0,top} &= P_{0,b} = \frac{1}{\bar{n}_{top}+1} \\ \bar{n}_{top} &= \bar{n}_b \end{aligned} \tag{12.1}$$

where $\bar{n}_{top}$ and $P_{0,top}$ are the measured average motional quantum state and population at the top of the ramp, and $\bar{n}_b$ and $P_{0,b}$ are the actual populations at the bottom of the ramp. Of course, $\bar{n}_{top}$ then also equals $\bar{n}_{SBC}$, where the latter is the motional occupation after sideband cooling.

However, if there is heating during the ramp, it is not so clear what the temperature at the bottom of the ramp is. There are two methods we can use to estimate the temperature. The first is to put an upper bound on the temperature at the bottom of the ramp. We do this by assigning the measured ground state population at the top of the ramp $P_{top}$ as the population at the bottom of the ramp. We can then calculate the temperature with Equation 12.1 using $P_0 = P_{top}$ and $\omega_z = \omega_{z,b}$. This maximum temperature $T_{b_{max}}$ assumes that all heating can be attributed to the ramp down.

Alternatively, we can make the assumption that half of the heating comes from half the ramp, and calculate $P_{0,b_h}$ and thus $T_{0,b_h}$ from $\bar{n}_{b_h} = \frac{\bar{n}_{SBC}+\bar{n}_{top}}{2}$. The assumption that half the heating comes from each ramp is not a perfect assumption, since the ramp, while programmed to be symmetric, is not perfectly symmetric due to electronic filtering. However, these two measurements, $T_{b_{max}}$ and $T_{b_h}$, give us an estimate of the temperature at the bottom of the ramp.

## 12.3 etherDAC 2.1

### 12.3.1 Single Ion

The measured sidebands of a ramping experiment with a single $^{40}Ca^+$ ion are shown in Figure 12.2, in conjunction with the measured sidebands after sideband cooling. The ramp used in this experiment went from $\omega_{z,t}/(2\pi) = 415.8\,\text{kHz}$ to $\omega_{z,b}/(2\pi) = 67.7\,\text{kHz}$, and had a ramp time of $t_r = 140\,\mu\text{s}$. The adiabaticity parameter $\beta$, as defined in Equation 6.6, for this ramp is $\beta = 0.014$. It must be noted that for this particular measurement, $t_s = 80\,\mu\text{s}$. In this case, the predicted deviation from $V_{end,b}$ is 0.04 %, which leads to a deviation from the fully-settled frequency by 13 Hz smaller than the frequency uncertainty. $t_s$ was changed to 150 µs for later experiments to ensure low deviations for all ramp shapes.

Looking at the figure, we see a large increase in the height of the red sideband. Evidently there is some heating occurring during the ramp. Looking at the quantitative results presented in Table 12.1, we see that the change in $n$ after the ramp is $\Delta\bar{n} = 0.33(4)$, which would lead to a large number of false detections if using quantum logic spectroscopy.

We must determine the cause of the heating if we wish to eliminate it. It could come from the ramp shape, from electronic noise in the trap, or from DAC update noise, which is the noise related to the periodic updates of the DAC voltages [149]. The expected gain in motional quanta for the programmed ramp shape can be predicted by Equation 6.8. Because the ramp does not perfectly match the programmed ramp due to filtering, we take the maximum within one period

| $\omega_{z,t}/(2\pi)$ [kHz] | $\omega_{z,b}/(2\pi)$ [kHz] | $t_r$ [µs] |
|---|---|---|
| 415.8 | 67.7 | 140 |

| $V_{end,t}$ [V] | $V_{end,b}$ [V] |
|---|---|
| 40.0 | 1.0 |

| | | $\bar{n}$ | $P_0$ [%] | $T$ [µK] |
|---|---|---|---|---|
| SBC | | 0.03(1) | 97.0(9) | 5.7(5) |
| Ramp | top | 0.36(4) | 73.3(13) | 15.1(6) |
| | $b_{max}$ | 0.36(4) | 73.3(13) | 2.45(15) |
| | $b_h$ | 0.20(2) | 83.5(15) | 1.8(1) |

Table 12.1: Ramp details and measurements for etherDAC 2.1 single ion ramping, for the measurement in Figure 12.2

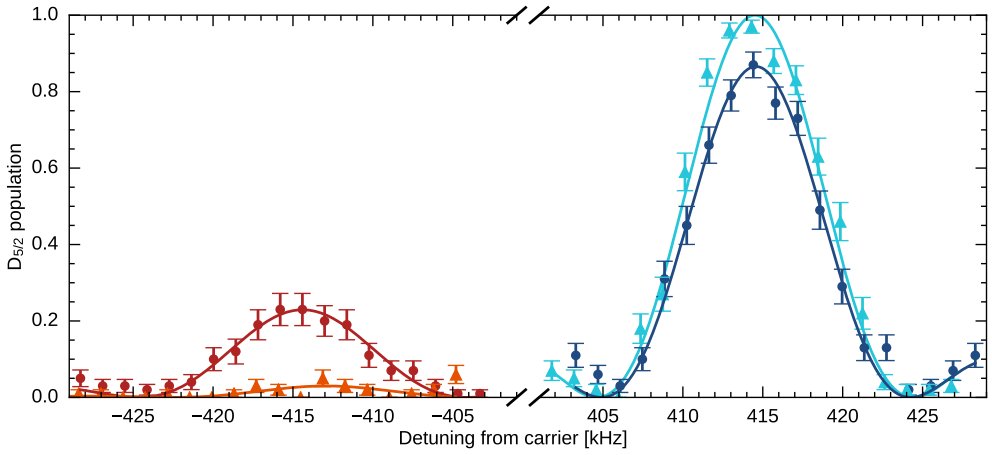


Figure 12.2: Sideband spectrum of a single $^{40}Ca^+$ comparing a sequence with no ramp (▲ red sideband, ▲ blue sideband) to a sequence with a ramp from $\omega_{z,t}/(2\pi) = 415.8\,\text{kHz}$ to $\omega_{z,b}/(2\pi) = 67.7\,\text{kHz}$ (● red sideband, ● blue sideband).

of the expected (see Figure 6.12). This gives an expected heating of $\Delta\bar{n} = 7 \times 10^{-5}$, which rules out heating from ramp shape as it is orders of magnitude different from what we measure. To diagnose if it is the result of electronic noise from the DC supply, we can understand this heating as an integration over the heating rates throughout the ramp.

### Integrated heating

One of the technical challenges with adiabatically ramping the frequency is that we become sensitive to electric field noise at all frequencies between $\omega_{z,t}$ and $\omega_{z,b}$. The number of motional quanta that we gain at a specific frequency $\omega_z$ depends on the heating rate $\dot{\bar{n}}(\omega_z)$ and the time $dt$ that we spend at that frequency. Thus, the total number of quanta gained during a ramp assuming

perfect adiabaticity is given by

$$\begin{aligned}\bar{n} &= \int_{t_0}^{t_f} \dot{\bar{n}}\left(\omega_z(t)\right) dt \\ &= \int_{t_0}^{t_f} \dot{\bar{n}}\left(\frac{\omega_{z,t}}{1+\frac{t}{t_r}(\frac{1}{\alpha}-1)}\right) dt\end{aligned} \tag{12.2}$$

where the equation for $\omega_z(t)$ comes from Equation 6.7, and as before $\alpha = \frac{\omega_{z,b}}{\omega_{z,t}}$.

We can numerically evaluate this equation using the model of the etherDAC 2.1 heating rates (Equation 11.5) to calculate the expected gain in quanta due to electric field noise for the data in Figure 12.2. This is not a perfect analysis since it assumes a perfect ramp (without filtering), but is sufficient as the ramp shape follows well at the bottom of the ramp where the majority of the heating occurs (see Figure 9.9). The analysis predicts $\bar{n}$ gained in this experiment to be $\Delta n = 0.28$, which accounts for the measured change in $\Delta\bar{n} = 0.33(4)$. The calculation of $\Delta n$ includes the expected heating due to the settling time.

Figure 12.3 further illustrates the agreement between the integrated heating and the measured $\bar{n}$ after ramping. It shows a series of measurements with a ramp time of $t_r = 500\,\mu s$, ramping from $\omega_{z,t}/(2\pi) = 415.8\,kHz$ to $\omega_{z,b}$. For these measurements, $\bar{n}$ was measured at the bottom of the ramp, with the pulse power varied to keep the sideband Rabi frequency constant. Each point corresponds to 5 measurements, except the point at $\omega_{z,b}/(2\pi) = 415.8\,kHz$, which consists of 10 measurements. The line shows the calculated gain in quanta as calculated using numerical integration combined with heating during $t_s$ and the pulse time[2]. The shaded width of the line corresponds to the shaded width in Figure 11.5[3]. The model predicts the results quite well, supporting the conclusion that the heating is due to the background noise of the DAC supply, and not due to non-adiabatic ramping or DAC update noise.

One consequence of being sensitive to noise throughout the spectrum is that if there are any sharp peaks in the noise spectrum, we will pick them up when ramping, with a sensitivity depending on how fast we ramp through them. We can use this then as a tool to diagnose noise in the system and remove it, a technique which I applied to our setup. By performing a binary search, I was able to locate when $\Delta\bar{n}$ jumped unexpectedly. Thus, I was able to locate a switched-mode power supply[4] which was injecting noise onto the line at 128 kHz, causing the ion to heat as it ramped through it. I was able to replace this supply[5], and then heating matched the expected as predicted by the etherDAC 2.1 heating rates.

### 12.3.2 Two Ions

As we saw in Chapter 11, the two modes of a two-ion crystal heat at different rates due to electric field noise, with the in-phase mode of the $^{40}Ca^{+}$-$^{42}Ca^{+}$ crystal heating at about twice the rate of a single ion, and the out-of-phase mode barely heating at all. Because of the high heating rates on the single ion, it is evident that adiabatic cooling with two ions on the in-phase mode will not be better. However, for our quantum logic spectroscopy scheme, we have the choice of either mode, thus it made sense to try adiabatic cooling on the out-of-phase mode of a two ion crystal[6].

I ran this experiment with a two ion chain consisting of $^{40}Ca^{+}$-$^{42}Ca^{+}$, which was chosen over a $^{40}Ca^{+}$-$^{40}Ca^{+}$ chain due to the limited motional state detection resolution in a $^{40}Ca^{+}$-$^{40}Ca^{+}$ chain

[2] Half the pulse time at the bottom of the ramp was used to give an estimate of the sideband height.

[3] Note that this has not been error-propagated, but rather carried through the calculation, as the signal from the spectrum analyzer would be had I not smoothed it.

[4] An XP PCM50US12 power supply for the camera. Other things that inject noise onto the line: Agilent oscilliscope DSO-X 2014A, at 64 kHz, and the spectrum analyzer, Tektronix RSA5103B at 112 kHz. These were turned off/unplugged

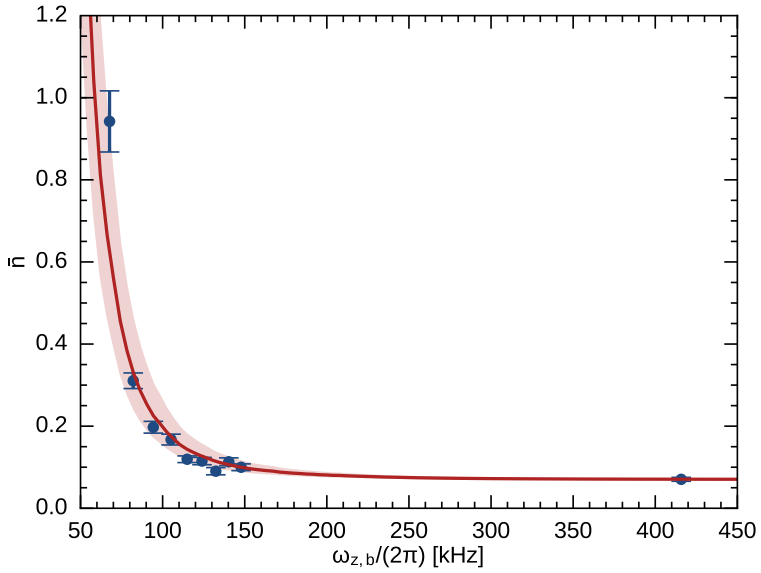


Figure 12.3: Motional quanta gained from ramping from $\omega_{z,t}/(2\pi) = 415\,\text{kHz}$ to $\omega_{z,b}$. Measurements • were taken with a pulse at the bottom of the ramp. Theory ——— was calculated from Equation 11.5 combined with the pulse timing.

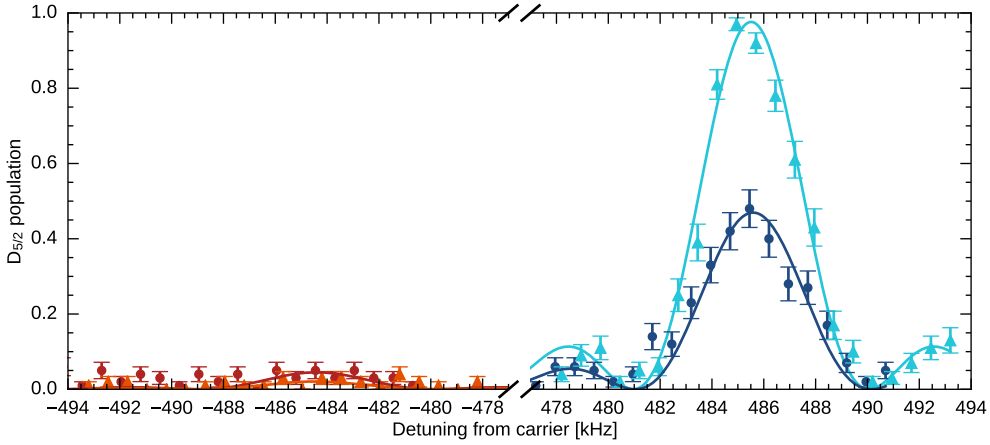


Figure 12.4: Out-of-phase sideband spectrum of a $^{40}Ca^{+}$-$^{42}Ca^{+}$ chain comparing a sequence with no ramp (▲ red sideband, ▲ blue sideband) to a sequence with a ramp from $\omega_{-,t}/(2\pi) = 485.7\,\text{kHz}$ to $\omega_{-,b}/(2\pi) = 40.7\,\text{kHz}$ (• red sideband, • blue sideband). The large drop in the sideband height is due to heating on the in-phase mode.

| $\omega_{-,t}/(2\pi)$ [kHz] | $\omega_{-,b}/(2\pi)$ [kHz] | $t_r$ [µs] |
|---|---|---|
| 485.7 | 40.7 | 140 |

| $V_{end,t}$ [V] | $V_{end,b}$ [V] |
|---|---|
| 18.6 | 0.07 |

| | | $\bar{n}$ | $P_0$ [%] | $T$ [µK] |
|---|---|---|---|---|
| SBC | | 0.022(9) | 97.9(9) | 6.1(7) |
| Ramp | top | 0.11(3) | 90(3) | 10.0(12) |
| | $b_{max}$ | 0.11(3) | 90(3) | 0.83(10) |
| | $b_h$ | 0.064(18) | 94.0(16) | 0.70(6) |

Table 12.2: Ramp details and measurements for etherDAC 2.1 two-ion out-of-phase mode ramping, for the measurement in Figure 12.4

(see subsection 4.4.1). Figure 12.4 shows the out-of-phase sideband spectra of sideband-cooled ions and the adiabatically-cooled ion, with a ramp from $\omega_-/(2\pi) = 485.7\,\text{kHz}$ to $\omega_-/(2\pi) = 40.7\,\text{kHz}$ in 140 µs, corresponding to $\beta = 0.026$. From Equation 6.8, the expected heating due to the ramp is $\Delta n = 2 \times 10^{-4}$. The ramp details and motional state diagnostics are presented in Table 12.2.

The change in motional quantum number as a result of the ramp is $\Delta n = 0.09(3)$, and is an improvement over the single ion case of $\Delta n = 0.33(4)$, and for a larger frequency range. The maximal temperature of the out-of-phase mode at the bottom of the ramp is $T_{b_{max}} = 0.83(10)\,\mu\text{K}$, which is about a factor of 7 lower than the temperature prior to adiabatic cooling.

Looking at Figure 12.4, we see that while the height of the red sideband does not change much, the blue sideband height is greatly reduced. This can be explained by the heating of the in-phase mode (see Appendix C.3). Because heating on the in-phase mode impacts the coupling on the out-of-phase mode, it is best if neither mode heats appreciably.

## 12.4 Unamplified DACs

For a $^{40}Ca^+$-$^{24}MgH^+$ crystal, it is especially relevant that the overall heating rate is low, since the mass ratio of $\mu = 25/40$ means that the out-of-phase mode heats only 1/3 as fast as the single ion at the same frequency[7] (see Figure 4.9). Thus, I switched to the unamplified DAC supply to have lower heating rates, and carried out single ion adiabatic cooling experiments.

Figure 12.5 shows the sideband-cooled versus adiabatically-cooled sideband spectra for a ramp with $\omega_{z,t}/(2\pi) = 197.7\,\text{kHz}$ to $\omega_{z,t}/(2\pi) = 49.66\,\text{kHz}$ and $t_r = 140\,\mu\text{s}$, with $\beta = 0.017$. The expected heating as per Equation 6.8 is $\Delta\bar{n} = 1 \times 10^{-4}$. Because heating rates were not measured down to this frequency for this supply, it is tough to predict the heating from DC supply noise. The motional state diagnostic results are presented in Table 12.3, and the gain in motional occupation from ramping is $\Delta\bar{n} = 0.04(2)$.

for subsequent measurements.

[5]With a benchtop linear supply.

[6]Of course, the heating rate of a $^{40}Ca^+$-$^{24}MgH^+$ out-of-phase mode is less strongly suppressed than the that of a similar-mass crystal, but testing first on a similar-mass crystal helps give a sense of the limitations.

[7]For the same voltage, this ratio is higher since $\omega_- > \omega_+$, but the ratio will be voltage-dependent.

| $\omega_{z,t}/(2\pi)$ [kHz] | $\omega_{z,b}/(2\pi)$ [kHz] | $t_r$ [µs] |
|---|---|---|
| 197.7 | 49.66 | 140 |

| $V_{end,t}$ [V] | $V_{end,b}$ [V] |
|---|---|
| 9.0 | 0.5 |

| | | $\bar{n}$ | $P_0$ [%] | $T$ [µK] |
|---|---|---|---|---|
| SBC | | 0.023(11) | 98(1) | 2.5(3) |
| Ramp | top | 0.06(2) | 94(2) | 3.3(4) |
| | $b_{max}$ | 0.06(2) | 94(2) | 0.82(10) |
| | $b_h$ | 0.041(12) | 96.1(12) | 0.60(5) |

Table 12.3: Ramp details and measurements for unamplified DC supply single ion ramping, for the measurement in Figure 12.5. These refer to the thermal values, and do not include the coherent state analysis.

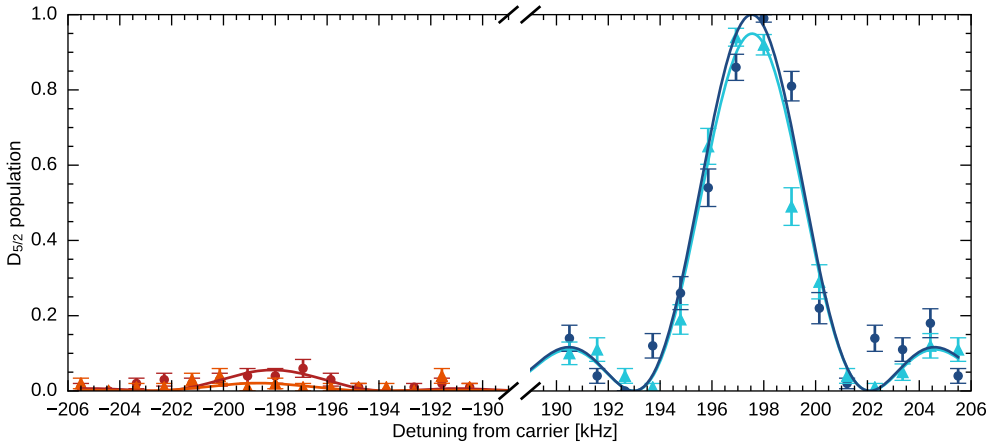


Figure 12.5: Sideband spectrum of single $^{40}Ca^+$ comparing a sequence with no ramp (▲ red sideband, ▲ blue sideband) to a sequence with a ramp from $\omega_{z,t}/(2\pi) = 197.7\,\text{kHz}$ to $\omega_{z,b}/(2\pi) = 49.66\,\text{kHz}$ (● red sideband, ● blue sideband).

This is a low amount of heating, with very low temperatures at the bottom of the ramp, and it looked like it should be no trouble to go lower. However, these measurements, though very reproducible, were suspicious, as changing the ramp time by only 1 µs resulted in sidebands that showed much more heating. Inserting a probe pulse at the bottom of the ramp resulted in an unexpectedly high red sideband as well.

I found the cause of these discrepancies by inserting delay times $\tau$ at the bottom of the ramp at intervals less than $2\pi/\omega_{z,b}$, such that it would be sensitive to any coherent dynamics at the bottom of the ramp. The results of this measurement are plotted in Figure 12.6. Lo and behold, the sideband height is $\tau$-dependent. There is a coherent oscillation of the ion at the bottom of the ramp.

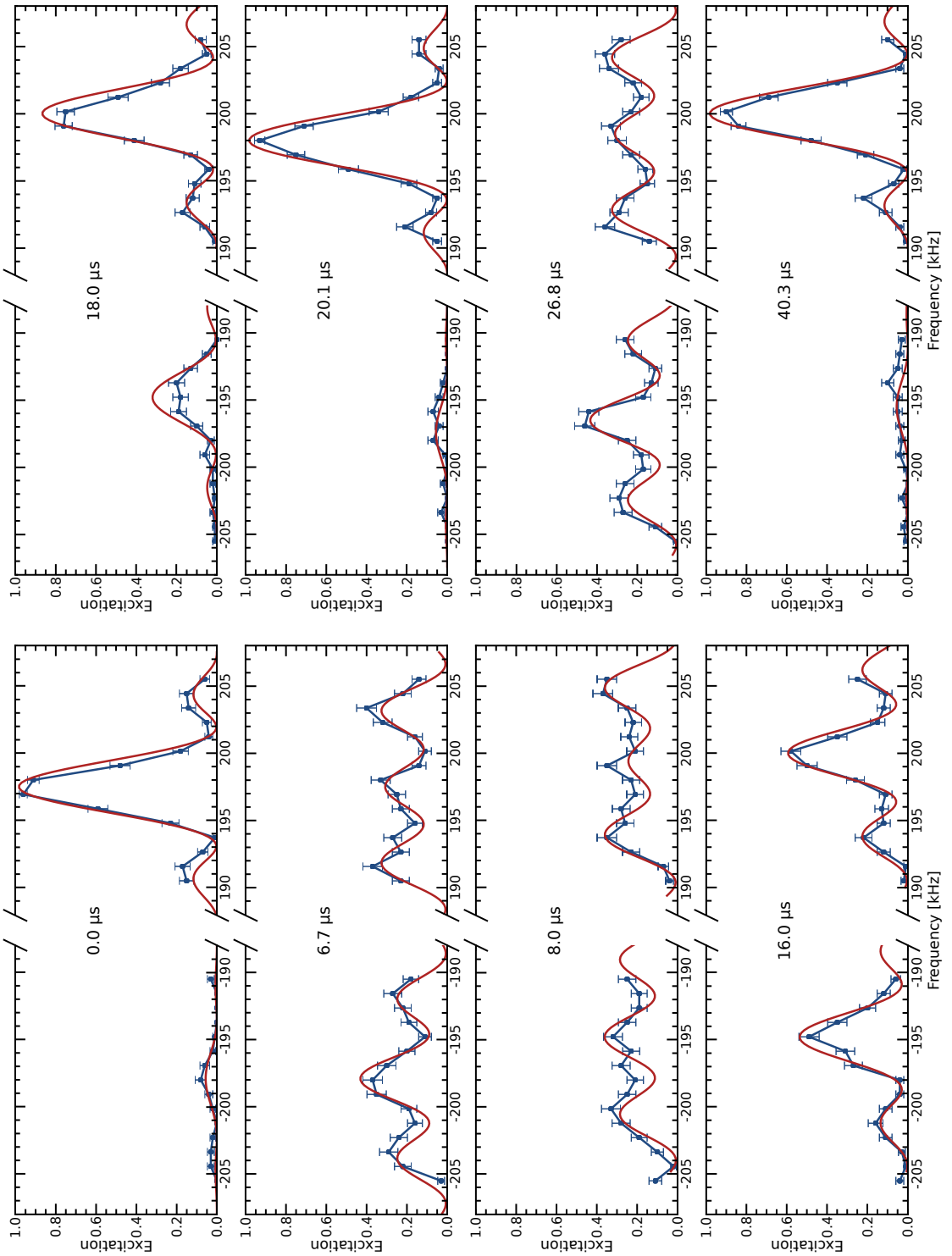


Figure 12.6: Plot of evolution of the sidebands as measured at the top of the ramp described in Table 12.3 for varying $\tau$, the time spent at the bottom of the ramp. • shows the experimental data, and — shows the predicted evolution based on the theory provided in subsection 12.4.1, with $\alpha' = 0.96$ and $\bar{n}_{th} = 0.06$.

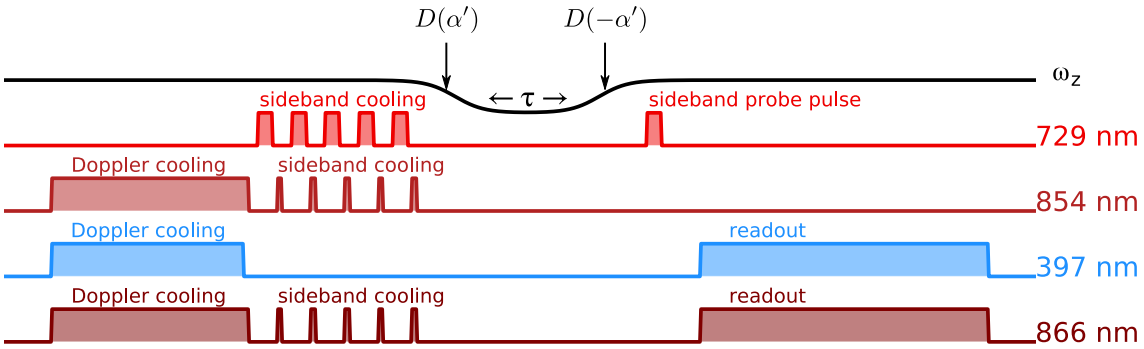


Figure 12.7: Pulse sequence for the adiabatic cooling experiments, showing approximately when the displacement operator acts.

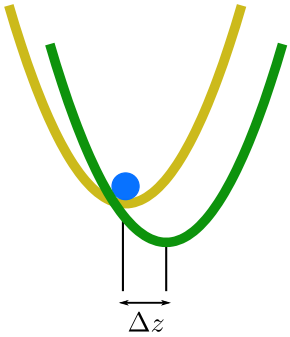


Figure 12.8: The displacement operator corresponds to a displacement of $\Delta z$ in space.

### 12.4.1 Coherent state generation

Assume we are creating a coherent state with the DC supply. We have two kicks of the ion, with the first corresponding to the ramp down, and the second kick corresponding to the ramp up. The first kick corresponds to the displacement operator $D(\alpha')$, where $\alpha'$ is related to the amplitude of the kick[8], and

$$D(\alpha') = e^{\alpha' a^\dagger - \alpha'^* a} \tag{12.3}$$

If we assume the kicks are symmetric, the second kick corresponds to the displacement operator $D(-\alpha')$. We assume this based on the measurement, where the second kick, after a 0 time delay $\tau$, returns the ion to the initial state. This is shown schematically in Figure 12.7. Physically, a displacement operator corresponds to a physical translation, which can be pictured as either the well or the ion being displaced by distance

$$\Delta z = \alpha' \sqrt{\frac{2\hbar}{m\omega_z}} \tag{12.4}$$

This is shown schematically in Figure 12.8.

[8]Coherent states typically use the parameter $\alpha$ to describe the amplitude of the kick, where $\bar{n} = |\alpha|^2$. I've used $\alpha'$ so it is not confused with the ramp $\alpha = \frac{\omega_{z,b}}{\omega_{z,t}}$, as they are unrelated.

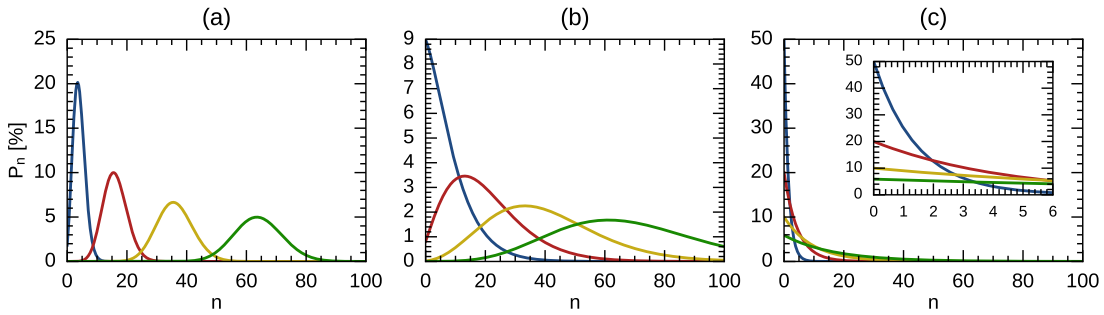


Figure 12.9: Comparison of distributions with $\bar{n} =$ 1, 4, 9, and 16 for a **(a):** coherent state, **(b):** thermocoherent state with $\bar{n}_{th} = 4$ and $\bar{n}_c = \bar{n}$, and **(c):** thermal distribution. The inset shows a zoomed-in view. Note that the y-axis changes scale between the three plots.

The population of a coherent state $|\alpha'\rangle$ is given by

$$P_c(n) = \frac{e^{-|\alpha'|^2}|\alpha'|^{2n}}{n!} \tag{12.5}$$

The time evolution of $|\alpha'\rangle$ can be described as $|\alpha(t)\rangle$, where

$$\alpha'(t) = \alpha'_0 e^{-i\omega_{z,b}t} \tag{12.6}$$

where $\omega_{z,b}$ refers to the axial frequency at the bottom of the ramp.

The first kick comes in at $t = 0$, corresponding to the coherent state

$$|b(t)\rangle \equiv D(\alpha')|0\rangle = |\alpha'_0 e^{-i\omega_{z,b}t}\rangle \tag{12.7}$$

assuming we started in the ground state. $|b\rangle$ refers to the state at the bottom of the ramp. We then wait a time of $\tau$ before the second kick comes in, and the state after the second kick is given by

$$|top(0)\rangle \equiv D(-\alpha')|b(\tau)\rangle = |\alpha'_0 e^{-i\omega_{z,b}\tau} - \alpha'_0\rangle \tag{12.8}$$

where $|top\rangle$ refers to the state at the top of the ramp. What we are sensitive to when measuring the sidebands is the population $P(n)$. Because this population is not time-dependent, the time dependence of $|top\rangle$ is neglected.

As seen in Equation 12.5, the population is dependent on $|\alpha'|^2 = \bar{n}_c$, the average occupation for the coherent state. For the state $|top\rangle$ this is given by

$$\bar{n}_{c,t}(\tau;\alpha'_0) = |\alpha'_0 e^{-i\omega_{z,b}\tau} - \alpha'_0|^2 = 2\alpha'^2_0(1 - \cos(\omega_{z,b}\tau)) \tag{12.9}$$

thus the population of $|top\rangle$ is

$$P_{c,t}(n) = \frac{e^{-\bar{n}_{c,t}}|\bar{n}_{c,t}|^n}{n!} \tag{12.10}$$

This population is shown graphically in Figure 12.9 (a).

Of course, the initial state is not perfectly prepared in $|0\rangle$, but is rather prepared in a thermal state, characterized by $\bar{n}_{th}$. The action of the displacement operator on a thermal state creates a

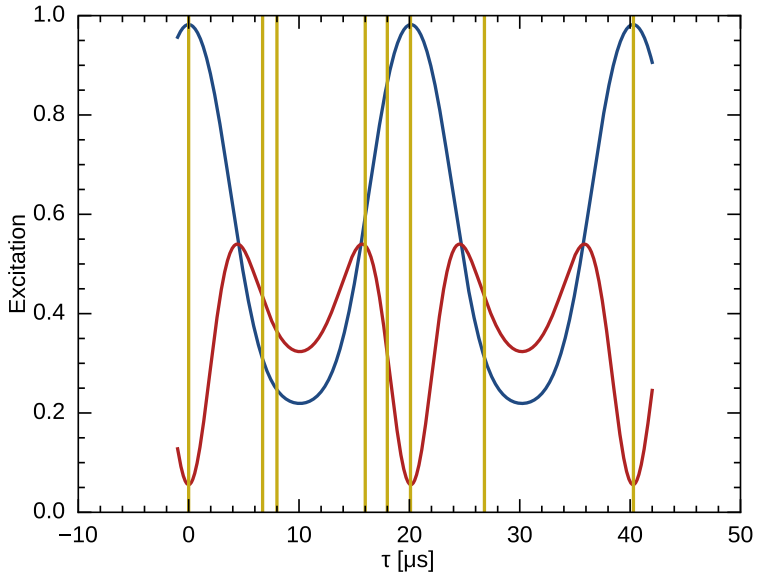


Figure 12.10: Evolution of the height of the center of the red and blue sidebands as a function of delay time $\tau$. The yellow lines indicate the $\tau$'s for which measurements are shown.

thermocoherent state, or Glauber-Lachs state [182–185]. The probability distribution of $|t\rangle$ assuming an initial thermal state is given by

$$P_{GL,t}(n) = \frac{\bar{n}_{th}^n}{(1+\bar{n}_{th})^{1+n}} \exp\left(\frac{-\bar{n}_{c,t}}{1+\bar{n}_{th}}\right) L_n\left(\frac{-\bar{n}_{c,t}}{\bar{n}_{th}(\bar{n}_{th}+1)}\right) \tag{12.11}$$

where $L_n$ is the Laguerre polynomial. This population distribution is shown graphically in Figure 12.9 (b), compared to a coherent distribution in (a) and a thermal distribution in (c). For $\bar{n}_c \gg \bar{n}_{th}$, this function reduces to the coherent state population, and for $\bar{n}_{th} \gg \bar{n}_c$, it reduces to the thermal distribution.

A sideband spectra of state $|top\rangle$ with this probability distribution will have a functional form of

$$\rho_{ee}(t) = \sum_{n=0}^{\infty} P_{GL,t}(n;\tau,\alpha_0,\bar{n}_{th}) \frac{\Omega_{n,s}^2}{\Omega_{n,s}^2+\delta_s^2} \sin^2\left(\sqrt{\Omega_{n,s}^2+\delta_s^2}\frac{t}{2}\right) \tag{12.12}$$

where the Rabi frequencies and detuning are defined as in Equation 3.28.

We can use this model to mimic the results obtained when probing the sideband transition after a variable $\tau$, as in Figure 12.6, where the red curves show the calculated population. The parameters used for the model (in red), are $\alpha' = 0.96$ and $\bar{n}_{th} = 0.06$, and the model mimics the data remarkably well. As the time increases, the state evolves from a typical sideband-cooled spectrum to a coherent state and back to a thermal state again. Figure 12.10 shows the expected evolution of the sideband height as a function of $\tau$ for this model, and the yellow lines show the time delays for which corresponding data is shown in Figure 12.6.

### 12.4.2 Implications

The agreement between the model and the data shows that we are creating a coherent state for the parameters presented in Table 12.3. We are not yet certain what is causing the displacement—it

is something to be investigated. As per Equation 12.4, $\alpha' = 0.96$ corresponds to a displacement of only 49 nm at $\omega_{z,t}/(2\pi) = 197.7$ kHz, or a displacement of 96 nm at $\omega_{z,t}/(2\pi) = 49.66$ kHz. Exactly where the displacement happens during the ramp is unclear, since if the rest of the ramp is adiabatic, it could happen anywhere. We are only sensitive to the dynamics at the bottom of the ramp because that is where we are applying the time delay, so it's where we see the evolution of the state.

As such, the creation of a coherent state is an effective meter of measuring $\omega_z$ at the bottom of the ramp. One can see the periodicity of the measurements by comparing the plots in Figure 12.6 with $\tau = 0\,\mu$s, $\tau = 20.1\,\mu$s, and $\tau = 40.3\,\mu$s, which represent zero, one, and two periods of oscillation at 49.66 kHz. At each period, the state comes almost perfectly back to the initial state. If we were to instead measure on the steepest slopes in Figure 12.10 out to long delays, we would be very sensitive to the value of $\omega_{z,b}$.

Though the motional distribution of the ion at the bottom of the ramp is not in the ground state of motion, the ion is not hot in the sense that the coherent motion is reversible. The thermal mixing, that is, the irreversible increase in motional quantum number, is sub-microkelvin. Because the coherent kick can be counteracted, the coherent motion does not preclude implementation of broadband quantum logic spectroscopy (covered in Chapter 14). If the time at the bottom of the ramp is chosen such that the state is returned to the initial, if no transitions occur, the state remains unchanged at the top of the ramp. If excitation occurs at the bottom of the ramp, then the state will be changed, and detection at the top of the ramp will reflect that. Aside from being demonstrated in this work, the ability to reverse the generation of coherent states of trapped ions has been shown in, for example, the context of ion transport [186], for very large coherent states [79], and in long chains of ions [187]. Having shown the ability to recreate the initial state for this specific case, we should be able to do the same for different ramp parameters.

Lastly, since the motion is coherent though the ramp itself should be adiabatic, it means that it is preventable. By diagnosing the cause of the coherent kick, we should be able to remove it.

## 12.5 Conclusion

I have presented adiabatic cooling experiments for two different DC supplies with total ramp times of $t_r + t_s = 290\,\mu$s–20 times faster than was previously achieved [52]. Single ion experiments on the amplified etherDAC 2.1 show that in order to reach very low $\omega_z$, it is necessary to lower the heating rate. Experiments with a two ion chain of $^{40}Ca^+$-$^{42}Ca^+$ show that adiabatic cooling of the out-of-phase mode is possible. In this experiment the axial frequency was reduced by nearly a factor of 12, down to $\omega_- = 40.7$ kHz with heating of only $\Delta\bar{n} = 0.09(3)$ observed after lowering and raising the frequency. The maximal out-of-phase mode temperature of the ion at the bottom of the ramp of the out-of-phase mode was found to be $0.83(10)\,\mu$K, a factor of 7 reduced from the initial temperature. This system with a cold out-of-phase mode and a hot in-phase mode can be used for studying cold collisions, which I will discuss in Chapter 15.

Experiments with the unamplified DAC supply show the promise of using an even lower noise supply for control of trap voltages. Experiments employing a ramp down to 50 kHz showed only $\Delta n = 0.04(2)$ for the ramp down and up again. Coherent excitation during the ramp means, however, that the ion is in a higher motional state at the bottom of the ramp. Because this motion is reversible, we expect that broadband vibrational spectroscopy will still work, so long as our experiment is precisely timed to return the ion to its initial state. For other experiments that rely on low kinetic energies, however, this coherent kick would need to be eliminated.

# Part V

# Future experiments with $^{24}MgH^+$

# Chapter 13

# Narrow spectroscopy

A far future goal of ours is to implement direct rovibrational spectroscopy in $^{24}MgH^+$ in a regime where the sidebands of the transition are resolved. In this regime we will be able to coherently manipulate the rovibrational states, allowing for state preparation, and, in the limit where the laser linewidth is much smaller than that of the molecular transition, achieve the highest resolution spectroscopy. The fundamental limit of spectroscopic resolution is given by the linewidths of the transitions, which are on the Hz-level. We would, on the other hand, be happy to resolve the hyperfine and Zeeman substructure of the rovibrational levels, a level of resolution already about $10^5$-times better than current knowledge [105]. With a narrow scheme come a few complications, especially considering the level structure of $^{24}MgH^+$. In this section, I consider what sort of properties, such as linewidth and power, we will need in a narrow 6 µm laser, such that we can begin working toward this goal. Further, I discuss some schemes that have already been implemented in other groups to narrow quantum cascade lasers (QCL), the type of laser that provides our 6 µm beam.

## 13.1 Experimental procedure

The basic experimental procedure is the same as that presented in subsection 6.4.1. As a reminder, we first cool the ion chain down to the ground state of motion. In order to detect a transition in $^{24}MgH^+$ on $^{40}Ca^+$, one must change the motional quantum state of the ion chain by driving a blue sideband transition in $^{24}MgH^+$. Detection is then carried out on the $^{40}Ca^+$ ion, where, if the ion has transitioned to the upper state, the red sideband of the $^{40}Ca^+$ ion can be driven with a $\pi$-pulse on the $|g, n = 1\rangle \rightarrow |e, n = 0\rangle$ transition. In an ideal experiment, where the ground-state cooled red sideband of the $^{40}Ca^+$ ion has zero coupling strength, the $\pi$-pulse gives 100 % transfer to the excited state, meaning that detection of a transition in $^{24}MgH^+$ is perfectly mapped onto the $^{40}Ca^+$ signal.

In an experiment, the detection will not, of course, be perfectly one-to-one due to ion heating and transfer efficiency, but the signal-to-noise of a $\pi$-pulse on the $^{40}Ca^+$ ion can be well characterized prior to starting spectroscopy on $^{24}MgH^+$. The blue sideband $\pi$-pulse time on the $^{24}MgH^+$ ion, on the other hand, can be predicted from the power, beam size, and coupling strength, but to be able to apply a true $\pi$-pulse, we must find the transition by scanning the frequency. Once the sideband has been located, Rabi flopping can be performed to determine the $\pi$-time.

Finding the blue sideband is already a form of spectroscopy, where we can determine that the carrier is $\omega_z$ away. However, because AC Stark shifts cause the sideband to shift due to off-resonant coupling on the carrier, for the highest resolution spectroscopy it is advantageous

to perform spectroscopy on the $^{24}MgH^+$ carrier transition. This works by first trying to drive a transition on the carrier, and then attempting to drive a blue sideband $\pi$-pulse. At this point we know the exact frequency of the blue sideband, so that stays constant, but the carrier frequency is swept. If the ion was excited on the carrier, the blue sideband cannot couple, whereas if it was not excited, the sideband will couple, and transfer population into $n = 1$. Final detection is carried out on $^{40}Ca^+$, and we will get an inverted signal compared to the previous case. Thus, the carrier is mapped onto the $^{40}Ca^+$ ion via the $^{24}MgH^+$ blue sideband.

We can also use the blue sideband transition to perform state preparation of higher vibrational levels. For state preparation, we do not need to use the carrier transition, only the sideband transition. By performing a $\pi$-pulse on the blue sideband, we can transfer all population from a lower rovibrational state to an upper one, or vice versa. We can then check that our preparation was successful by measuring the red sideband on the $^{40}Ca^+$ transition. We can even perform this state preparation if we can resolve the blue sideband but cannot drive a perfect $\pi$-pulse, as the red sideband in $^{40}Ca^+$ can only be excited if the ion has transitioned to the upper level. If detection on the red sideband of $^{40}Ca^+$ has perfect fidelity, we project the state of the $^{24}MgH^+$ ion into the upper level by measuring an excitation on the red sideband [50, 51].

## 13.2 Linewidth, power, and pulse time

As shown in Chapter 6, $^{24}MgH^+$ has rotational levels which split into hyperfine structure, and then further split into Zeeman levels. The splittings of the two hyperfine states within a rotational level are given by $(2J + 1) \times 9\,\text{kHz}$, except for $|J = 0\rangle$, which does not split. The splitting of the Zeeman states depends on the field and the $F$ and $m_F$ quantum numbers, but is on the order of a few kHz, up to about 10 kHz for typical fields on the order of 6 G. These splittings are smaller than $\omega_z$ and will ultimately determine the linewidths, powers, and pulse times we can use and still resolve these levels.

The cases with the fewest transitions to consider are the transitions between $|J = 0\rangle$ and $|J = 1\rangle$ with $\Delta v = 1$. The $|J = 0\rangle$ state consists only of $F = 1/2$ which splits into two $m_F$ states, and the $|J = 1\rangle$ state consists of $F = 1/2$ and $F = 3/2$. These two hyperfine states split into 2 and 4 states respectively[1]. These splittings are shown in Figure 13.1. This gives rise to 10 allowed transitions, each with Rabi frequencies dependent on Clebsch-Gordan coefficients. If we do not resolve the structure, then we may not be able to drive a $\pi$-pulse on either the carrier or sidebands since we could drive multiple transitions at different rates. This limits the signal height and detection efficiency of carrier spectroscopy.

Rovibrational state preparation does not, on the other hand, need all of the transitions to be resolved if we do not mind which substate the population ends up in, as a perfect $\pi$-pulse is not necessary as described above. This means that for state preparation of rovibrational states, the laser requirements are less strict than for spectroscopy, so we will take spectroscopy as an example to give stricter bounds on the laser requirements.

If we start state-prepared in a specific $m_F$ state, then this cuts down on the number of possible transitions. State preparation can be carried out by driving Raman transitions between the rotational levels and Zeeman substates using a femtosecond frequency comb, a method we are currently developing[2]. If we further choose our polarization to be either $\sigma$ or $\pi$, we are sensitive to even fewer transitions. If we want to be able to access every allowed hyperfine transition, we have to have a linewidth which is narrower than the smallest spacing between allowed transitions. At $B = 6.5\,\text{G}$, $|v = 0, J = 0\rangle \rightarrow |v = 1, J = 1\rangle$, the smallest spacing is for $\sigma$ polarized light

[1] Here I use the quantum numbers for the weak-field Zeeman, though at $B = 6.5\,\text{G}$, we are in the intermediate regime.
[2] Chou, et al. show Zeeman state preparation $CaH^+$ in [47].

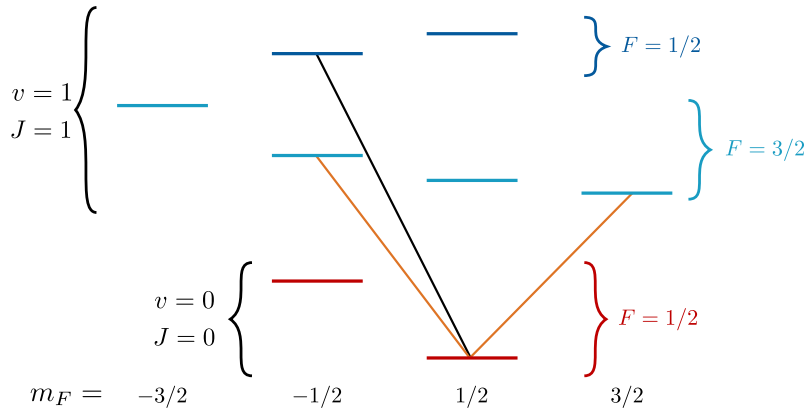


Figure 13.1: Diagram showing the levels for $|v = 0, J = 0\rangle$ (red) and $|v = 1, J = 1\rangle$ (blues). The rovibrational levels are split by approximately 50 THz, versus the splittings between the substates, which are 10 kHz-level. The three marked transitions are the $\sigma$ transitions from the $|v = 0, J = 0, F = 1/2, m_F = 1/2\rangle$ state. In orange are the two separated by 12 kHz (see text).

from $|F = 1/2, m_F = 1/2\rangle$ to states $|F = 3/2, m_F = -1/2\rangle$ and $|F = 3/2, m_F = 3/2\rangle$. These two transitions are separated by 11 kHz. To resolve these two transitions, we must have a linewidth smaller than their spacing. We must also then use Rabi frequencies smaller than the spacing, which puts bounds on the maximum power and pulse time. A Rabi frequency of a few kHz can be used for these specific transitions. The Rabi frequency dictates the $\pi$-pulse time, which for a Rabi frequency of 1 kHz is 500 µs. For the pulse to be coherent, the linewidth of the laser must then also be on the same order.

For sidebands, in addition to thinking about nearby transitions, we need to consider the width of the carrier transition. The Lamb Dicke parameters for these transitions are very small, on the order of $\eta = 0.02$. Thus, a 1 kHz Rabi frequency on the sideband results in a 50 kHz Rabi frequency on the carrier. We must keep the carrier Rabi frequency smaller than the sideband spacing.

To get order-of-magnitude powers, carrier and sideband Rabi frequencies have been calculated for a beam waist of 500 µm for a few rovibrational transitions, and are presented in Table 13.1. To get the strengths of individual transitions between substates, one would need to modify the powers by the transition strengths. Because the powers that we need to achieve are very low compared to what we expect to be able to achieve in the trap[3], there is no gain for $^{24}MgH^+$ to use adiabatic cooling for this type of spectroscopy. It could, however, be helpful in non-polar molecules, where quadrupole transitions must be driven, and it is difficult to produce the required power.

### 13.2.1 AC Stark shifts

With the pulse power we need to consider AC Stark shifts on top of power broadening. For carrier transitions, the primary contribution to the AC Stark shift will be due to nearby hyperfine transitions. For example, consider the two transitions given above. For a power corresponding to Rabi frequency $\Omega$ on the $\Delta m_F = 1$ transition, the Rabi frequency on the other transition will be given by $\Omega' = \frac{C'}{C}\Omega$, where $C$ and $C'$ are the Clebsch-Gordan coefficients of the $\Delta m_F = 1$ and $\Delta m_F = -1$ transitions, respectively. The $\Delta m_F = 1$ transition has a higher transition frequency,

[3] We expect to be able to get on the order of 20 mW of power, though we have not tried this yet.

| $J \to J'$ | $I_{sat}$ [W cm$^{-2}$] | $P_c$ [μW] | $P_{sb}$[μW] |
|---|---|---|---|
| $0 \to 1$ | $5.7 \times 10^{-13}$ | 0.011 | 42 |
| $1 \to 0$ | $1.4 \times 10^{-12}$ | 0.0017 | 6.6 |
| $1 \to 2$ | $7.5 \times 10^{-13}$ | 0.0068 | 25 |
| $2 \to 1$ | $8.4 \times 10^{-13}$ | 0.0046 | 18 |
| $2 \to 3$ | $8.9 \times 10^{-13}$ | 0.0051 | 18 |
| $3 \to 2$ | $6.8 \times 10^{-13}$ | 0.0067 | 26 |
| $3 \to 4$ | $1.0 \times 10^{-12}$ | 0.0041 | 15 |

Table 13.1: Saturation intensities for rovibrational transitions $|v = 0, J\rangle \to |v' = 1, J'\rangle$, along with the powers $P_c$ and $P_{sb}$ needed for Rabi frequencies of 1 kHz on the carrier and the blue sideband, respectively, assuming typical sideband cooling axial frequency (567 kHz on the out-of-phase mode).

and thus will be blue-detuned by 12 kHz from the $\Delta m_F = -1$ transition. This causes a shift of the $\Delta m_F = 1$ transition by $\frac{\Omega'^2}{4\delta}$ towards the $\Delta m = -1$ transition, where $\delta = 2\pi \times 12$ kHz. Likewise, as we scan over the $\Delta m = -1$ transition using the same power, we will see a shift of $\frac{\Omega^2}{4\delta}$ towards the $\Delta m_F = 1$ transition. Thus, the peaks shift together by a total of $\left(1 + \left(\frac{C'}{C}\right)^2\right) \frac{\Omega^2}{4\delta}$. For a sense of how large this shift is, for a 1 kHz Rabi frequency and taking all Clebsch-Gordan coefficients to be order 1, the shift for each peak is only 21 Hz. This shift could be further reduced by using a lower Rabi frequency.

On top of shifts from nearby sidebands, the sideband will also be shifted by all transitions' carriers. Due to the small Lamb Dicke parameter, this is a much bigger effect. For the carrier transition of the sideband transition being driven, the shift is given by $\frac{\Omega_{sb}^2}{2\eta^2\omega_z}$ towards the carrier, as both the upper and lower levels will shift. For the other nearby transitions, only the lower level contributes to the shift of the sideband, thus the contribution is given by $\left(\frac{C'}{C}\right)^2 \frac{\Omega_{sb}^2}{4\eta^2\omega_z}$.

For the three $\sigma$ transitions from $|J = 0, F = 1/2, m_F = 1/2\rangle$ at 6.5 G, the shift of the blue sideband due only to the carriers is on the order of 7 kHz towards the carrier for a sideband Rabi frequency of 1 kHz. This shift grows as the square of the sideband Rabi frequency, and is not greatly dependent on $\omega_z$. The magnitude of the shift is of course also dependent on which transition you are driving. If we try to drive a sideband pulse on the lowest frequency transition, the blue sideband will be more strongly affected by the other carriers, as they will be closer in frequency to the sideband. In these cases, it may be worth using the red sideband instead for QLS. This could be implemented either for carrier spectroscopy, where driving a red sideband from the excited state causes an increase in motional quantum number, or by first preparing the ions in $n = 1$.

## 13.3 Narrowing the quantum cascade laser

Currently, our QCL[4] has a linewidth on the (rough) order of 5 MHz, which isn't even on the same order of magnitude as $\omega_z$, let alone the kHz-level we need for narrow spectroscopy. For broadband spectroscopy, which I describe in the next section, this is no problem, but in order to implement narrow spectroscopy, we will have to implement a linewidth narrowing scheme.

[4] Daylight Solutions CW-MHF

One might consider building a cavity for the 6 µm light, similar to narrowing the 729 nm laser. This is unfortunately extremely difficult, due to the lack of available optical elements at 6 µm. Thus, we must use other techniques. There have been a few groups that have successfully narrowed the linewidth of quantum cascade lasers to a point that we could use [188, 189], some even to sub-Hertz linewidths [190]. One group which has narrowed a 5.4 µm QCL down to 60 Hz is the group of Stephan Schiller in Düsseldorf [189]. I had the opportunity to briefly visit their group and learn more about their setup.

In Düsseldorf, sum frequency generation (SFG) between mid-IR (5.4 µm) QCL light and 1.5 µm light from a fiber laser is performed in an orientation-patterned GaAs crystal, producing a near infrared wavelength (1.2 µm), a much easier wavelength to stabilize. The upconverted light is sent into a stable cavity, the signal from which is used to lock the QCL. This is not enough to stabilize the QCL, since the QCL is then only as stable as the fiber laser. The fiber laser is in turn locked to an optical frequency comb. Due to other very high precision lasers and cavities for locking their frequency comb, this lock is extremely stable, and they are able to achieve a 60 Hz linewidth of their QCL.

In Aarhus, we could amplify the output of the acetylene-stabilized fiber laser at 1.54 for upconversion with the 6 µm QCL light. The 1.5 µm fiber laser light combined with 6 µm light from the QCL produces light at approximately 1.2 µm. The upconverted light could then ideally be locked to the comb. Due to the linewidth of the acetylene-stabilized fiber laser (which also locks the comb), our narrowed linewidth would be limited to about 1 kHz. To narrow further, we would need to narrow the fiber laser output using a cavity, which should in turn also narrow the comb.

Locking to the comb may, however, be a challenge, as in Düsseldorf I learned that they struggled to achieve the bandwidth needed for the lock, and thus opted to use a cavity instead. Argence, *et al.* were able to narrow a QCL down to sub-Hz by locking to a comb. They, however, implemented this by using two combs generated by the same source, shifted in wavelength, one of which was used to perform the SFG. We must determine whether we can achieve the bandwidth necessary to narrow our laser. If we cannot achieve a high enough bandwidth, we will need to build a cavity for the 1.2 µm light.

## 13.4 Conclusion

The rovibrational level structure of $^{24}MgH^+$ has hyperfine splitting and Zeeman structure which causes transitions to be closely spaced, on the 10's of kHz level. We expect to be able to resolve this structure if we have a laser with linewidth on the order of 1 kHz. These splittings also put limitations on the pulse power and times, limiting Rabi frequencies on close-spaced transitions to the 1 kHz-level as well. This will require narrowing the quantum cascade laser, which has a linewidth on the 5 MHz level. This procedure will entail sum frequency generation with a stabilized telecom-wavelength laser, with the upconverted light used for stabilization of the QCL.

The rovibrational transitions in $^{24}MgH^+$ are only known to about 1.5 GHz precision [105]. Trying to search for the transition with a 1 kHz narrow laser is extremely difficult. Thus, this begs for another technique to hunt down the transition.

# Chapter 14

# Broadband spectroscopy

The ultimate spectroscopic resolution for rovibrational spectroscopy of $^{24}MgH^+$ will come by using a laser with a linewidth on the order of the molecular transitions, which are on the Hz-level. These transition frequencies, on the other hand, are only known to around 1.5 GHz precision [105]. Trying to find a Hz-linewidth transition in a GHz-wide space is like trying to find a needle in a haystack. We therefore need a technique to be able to pinpoint the location of these transitions with increasingly better resolution.

The laser that we will use to perform vibrational spectroscopy is a 6 µm quantum cascade laser (QCL). Our solution is to broaden the laser linewidth by modulating the current of QCL. We will interact with any motional sidebands within the linewidth of the laser, causing the ion to heat. We can thus measure this heating as an increase in scattering on the red sideband of the $^{40}Ca^+$ ion in a quantum logic spectroscopy QLS scheme. We can progressively decrease the modulation to pinpoint the locations of the transitions before moving to a narrow regime.

The proposed experiment is as follows, and is depicted in Figure 14.1:

1. Sympathetically cool a $^{40}Ca^+$-$^{24}MgH^+$ crystal down to the ground state of motion.
2. Adiabatically cool the $^{40}Ca^+$-$^{24}MgH^+$ crystal.
3. Illuminate the crystal with broadband radiation for time $t_{exp}$.
4. Adiabatically increase the potential.
5. Detect the motional state on $^{40}Ca^+$.

This chapter describes the calculations I have done to predict the experimental illumination time, $t_{exp}$, needed in such an experiment, as well as model the impact of adiabatic cooling on $t_{exp}$. I further apply the heating rate model from Chapter 11 to understand the experimental limitations for detection.

## 14.1 Model

When an atomic or molecular system is driven by broadband radiation, the evolution of the state populations in time can be modeled by Einstein A and B rate equations, as presented in subsection 3.1.2. These rate equations are a good approximation under the condition that the fastest rate in the system is much smaller than the linewidth $\Gamma_L$ of the driving field [191]. This is a classical

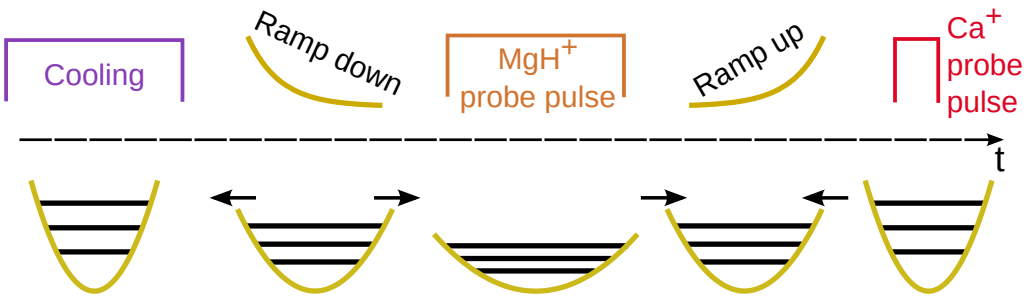


Figure 14.1: Experimental sequence for broadband spectroscopy of $^{24}MgH^+$.

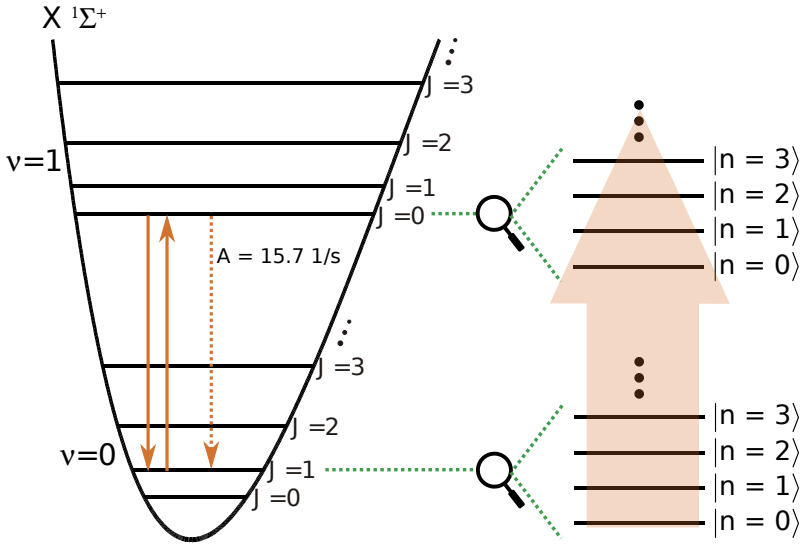


Figure 14.2: In the model system, I excite the $|v = 0, J = 1\rangle \rightarrow |v = 1, J = 0\rangle$ transition, which is closed. This can be separated into a two-level system with $N_-$ motional states. Because the radiation is broadband, it interacts with multiple sideband transitions.

model, and a more complete model would need to take into account the full Hamiltonian. However this model should give us a sense of the expected timescales. In this section I will describe how I set up rate equations to predict the experimental time needed for scattering.

To demonstrate how broadband radiation can be used to find transitions in molecular ions, I have simulated the experiment for exciting the closed transition $|v = 0, J = 1\rangle \rightarrow |v = 1, J = 0\rangle$. This transition has a frequency of 48.62 THz, corresponding to a wavelength of 6.16 µm [105]. The Einstein A parameter is given by the linewidth of the transition $A = \Gamma^{1,0}_{0,1} = 15.7\,\mathrm{s}^{-}1$ [106]. I chose this transition as a starting point such that decay into non-interacting states could be neglected.

Decay is not the only way the rotational states can mix. Blackbody radiation couples $|v = 0, J = 1\rangle$ to $|v = 0, J = 0\rangle$ and $|v = 0, J = 2\rangle$, and couples $|v = 1, J = 0\rangle$ to $|v = 1, J = 1\rangle$. The blackbody spectral energy density is given by Planck's radiation law

$$\rho(\omega) = \frac{\hbar\omega^3}{\pi^2 c^3} \frac{1}{e^{\hbar\omega/(k_B T)} - 1} \tag{14.1}$$

where $T$ is the temperature of the environment. The rates at which population is driven between

these levels can be calculated using Equation 3.20 combined with Equation 14.1 and are given by

$$R_{ge} = \frac{g_e}{g_g} \frac{1}{e^{\hbar\omega_{ge}/(k_B T)} - 1} A_{eg} \tag{14.2}$$

where the degeneracy is given by $g = 2(J+1)$.

At $T = 300\,\mathrm{K}$, these rates are nearly two orders of magnitude smaller than $\Gamma_{0,1}^{1,0}$. Because the dynamics we wish to model occur on a timescale faster than $\Gamma_{0,1}^{1,0}$, we can neglect blackbody coupling and approximate the internal states as a two level system where $|g\rangle \equiv |v = 0, J = 1\rangle$ and $|e\rangle \equiv |v = 1, J = 0\rangle$, as shown in Figure 14.2. Of course, these rotational states also have a hyperfine and Zeeman splitting, but because it is smaller than even $\omega_{\pm}$, we can approximate it as a single state[1].

The axial motion of the two-ion crystal of course adds another level of complexity. As a result, the system splits into $2N_+N_-$ states, where $N$ is the number of motional states considered for each mode. The states can then be written as $|i\rangle_a|i\rangle_m|n\rangle_+|n\rangle_-$, where again $i$ stands for the internal state of the atomic ($a$) or molecular ($m$) ion. As described in subsection 6.4.1, it is advantageous to use the out-of-phase mode of motion for QLS, so for simplicity's sake, I will explain the model for this mode only.

Now that we've set up our state space, we can set up our rate equations. The rate equations take into account absorption, stimulated emission, and spontaneous decay on the carrier and sidebands up to second order. The starting condition for QLS is that the ions start in the ground state of motion, so the system starts in $|g\rangle_m|0\rangle_-$. When the broadband light interacts with the molecule, light scatters on the carrier and on the sidebands. The upwards rate for the carrier is characterized by

$$R_{\uparrow,\Delta n=0} = B_{ge}\rho_L(\omega_{ge}) \tag{14.3}$$

where $B_{ge}$ is given by Equation 3.20 and $\rho_L(\omega_{ge})$ is the energy spectral density of the laser at the ion. The first sideband transitions are approximately scaled by $\eta_-^2(n+1)$ (blue) and $\eta_-^2 n$ (red), resulting in

$$\begin{aligned} R_{\uparrow,\Delta n=1} &= \eta_-^2(n+1)B_{ge}\rho_L(\omega_{ge}+\omega_-) \\ R_{\uparrow,\Delta n=-1} &= \eta_-^2(n)B_{ge}\rho_L(\omega_{ge}-\omega_-) \end{aligned} \tag{14.4}$$

Coupling on the second sidebands is approximately given by

$$\begin{aligned} R_{\uparrow,\Delta n=2} &= \eta_-^4(n+1)(n+2)B_{ge}\rho_L(\omega_{ge}+2\omega_-) \\ R_{\uparrow,\Delta n=-2} &= \eta_-^4(n)(n-1)B_{ge}\rho_L(\omega_{ge}-2\omega_-) \end{aligned} \tag{14.5}$$

The simulations use the full expression for scaling, given by (see Equation 3.27)

$$s(\eta) = \left(e^{-\frac{\eta^2}{2}}\eta^{|s|}\sqrt{\frac{n_<!}{n_>!}}L_{n_<}^{|s|}(\eta^2)\right)^2 \tag{14.6}$$

The downward rates are obtained by relating the upwards and downwards B parameters, as shown in Equation 3.20. The decay terms are modeled on the carrier just as the decay rate,

[1] We do need to consider polarization. In this case, we assume we choose a polarization that drives all transitions.

$A_{\downarrow,0} = \Gamma^{1,0}_{0,1}$. On the sidebands, the decays are modified similarly to the sidebands [192], with

$$\begin{aligned} A_{\uparrow,\Delta n=1} &= \alpha\eta_-^2(n+1)A_{\downarrow,0} \\ A_{\uparrow,\Delta n=-1} &= \alpha\eta_-^2(n)A_{\downarrow,0} \\ A_{\uparrow,\Delta n=2} &= \tilde{\alpha}\eta_-^4(n+1)(n+2)A_{\downarrow,0} \\ A_{\uparrow,\Delta n=-2} &= \tilde{\alpha}\eta_-^4(n)(n-1)A_{\downarrow,0} \end{aligned} \tag{14.7}$$

The factor $\alpha$ is the same factor as used in the description for Doppler cooling (section 4.1), and describes the probability that a decay contributes a kick along the axis. Here it is taken as isotropic, or $\alpha = 1/3$. $\tilde{\alpha} = 1/5$ describes the likelihood that a decay contributes a change of $\Delta n = 2$.

The rate equations are built then as

$$\begin{aligned} \frac{d}{dt}|g,n\rangle = &-(R_{\uparrow,0}+R_{\uparrow,1}+R_{\uparrow,2})|g,n\rangle + (R_{\downarrow,0}+A_{\downarrow,0})|e,n\rangle \\ &+(R_{\downarrow,1}+A_{\downarrow,1})|e,n+1\rangle + (R_{\downarrow,-1}+A_{\downarrow,-1})|e,n-1\rangle \\ &+(R_{\downarrow,2}+A_{\downarrow,2})|e,n+2\rangle + (R_{\downarrow,-2}+A_{\downarrow,-2})|e,n-2\rangle \end{aligned} \tag{14.8}$$

where $\frac{d}{dt}|e,n\rangle$ is built in a similar manner.

The laser energy spectral density has been modeled as a Gaussian[2]

$$\rho_L(\omega) = \frac{I}{c}\frac{1}{\sigma\sqrt{2\pi}}e^{\frac{-(\omega-\omega_L)^2}{(2\sigma^2)}} \tag{14.9}$$

where $\omega_L$ is the laser center frequency, $I$ is the intensity, and

$$\sigma = \Gamma_L\sqrt{8\log(2)} \tag{14.10}$$

where $\Gamma_L$ refers to the FWHM of the laser.

## 14.2 Results

I calculated the rate equations for variable $\omega_-$ with laser parameters of 10 mW of laser power, a 500 µm waist, and $\Gamma_L = 10$ MHz. All of these numbers are reasonable to obtain in the lab. The intensity with these parameters is $I = 2.5\,\mathrm{W\,cm^{-2}}$, compared to the saturation intensity $I_{sat} = 1.39\times10^{-12}\,\mathrm{W\,cm^{-2}}$.

As an example, the calculated time evolution of the motional states for $\omega_- = 424$ kHz is shown in Figure 14.3. This figure plots the evolution of the motional states independent of the internal state of the molecule, as in a real experiment we do not detect whether we are in the $|g\rangle$ and $|e\rangle$ states[3]. The curve in red shows the population not in the ground state, $P_{n\neq0} = 1 - P_0$, increasing in time. All levels reach a steady-state occupation of 0.2 because the model was limited to $N_- = 5$.

To understand how adiabatic cooling changes the experimental time, we must define a time when we have "enough" population in $P_{n\neq0}$. I define an $t_{exp}$ at 90% of the $t_{exp} = 0.90P_{n\neq0,ss}$.

[2]The exact choice of lineshape function here does not make a large difference in the calculations, as the intensity does not change to first order over the width of the sidebands. The exact lineshape in the experiment will depend on the way the current is modulated.

[3]This would require resolving the sidebands.

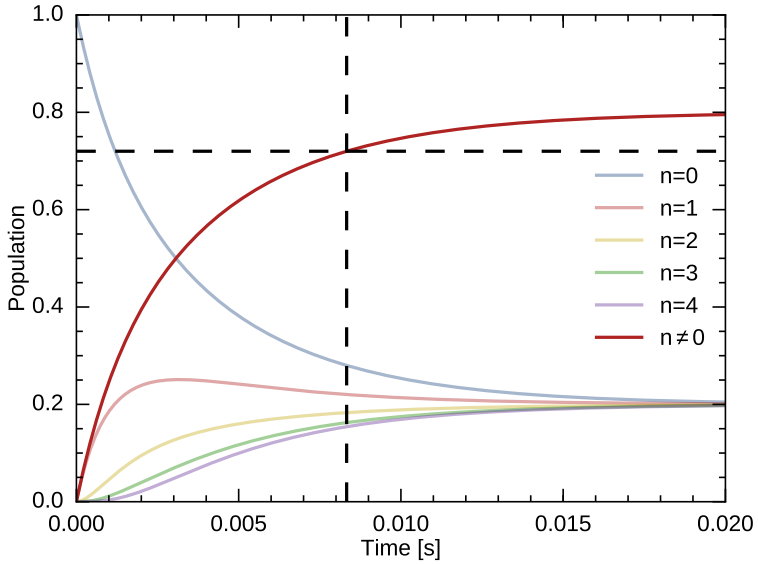


Figure 14.3: The evolution of the motional states of a ground-state cooled $^{40}Ca^{+}$-$^{24}MgH^{+}$ crystal when driving vibrational transitions in $^{24}MgH^{+}$ using a broad laser. The dashed lines indicate the location of $t_{exp}$ and the corresponding population.

For this axial frequency, $t_{exp} = 8.3\,\text{ms}$. This time is on the order of the time it takes to do readout of $^{40}Ca^{+}$. This means that it is a non-negligible additional time in our experimental sequence, so ideally we would like to lower it. We do that by varying $\omega_{-}$.

Figure 14.4 (a) shows the calculated $t_{exp}$ for the axial frequency range $20\,\text{kHz} \leq \omega_{-}/(2\pi) \leq 600\,\text{kHz}$. The red dot indicates which point comes from Figure 14.3. We immediately see that decreasing $\omega_{-}$ reduces $t_{exp}$. It is also evident from the linear characteristic of the result that transitions on the first sidebands dominate. In fact, the same result is obtained when the system is modeled without second sideband coupling or spontaneous decay. This is expected, as the Lamb Dicke parameter at $\omega_{-} = 20\,\text{kHz}$ is only $\eta_{-} = 0.086$ (see Figure 6.9).

The next step is to consider how much heating occurs on the ion due to electric field noise from the DC supply, as this will create noise in our signal. Combining Equation 4.32, relating the heating rate of the out-of-phase mode to that of a single ion, with the model in Chapter 11, we can predict the heating rate of the out-of-phase mode of the $^{40}Ca^{+}$-$^{24}MgH^{+}$ crystal. To get a measure of the number of quanta gained from from heating during an experiment, we can multiply the rate and the time to get

$$n_{heat} = \dot{\bar{n}} t_{exp} \tag{14.11}$$

Figure 14.4 (b) shows how the predicted $n_{heat}$ changes as a function of $\omega_{-}$ for both the amplified (etherDAC 2.1) and unamplified DC supplies. We see that as $t_{exp}$ decreases, $n_{heat}$ increases due to higher heating rates at low $\omega_{-}$. We can work with an increase in heating so long as the increase only contributes a small signal compared to the signal from the spectroscopy. At $t_{exp}$, $\bar{n} = 0.58$, so as long as we are much smaller than that, detection should be possible. For the etherDAC 2.1, this means we can ramp down to between 100 and 200 kHz and still resolve a signal. For the unamplified DACs, we do not hit this limit within the range of measured heating rates.

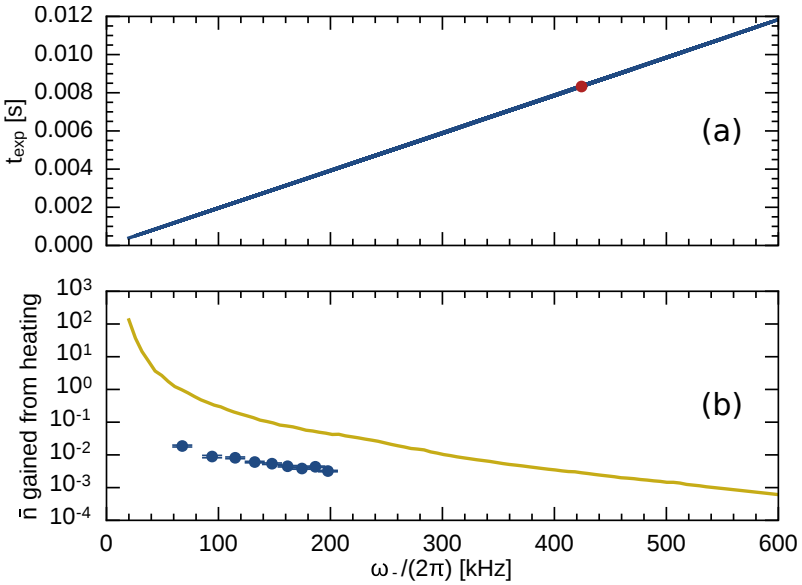


Figure 14.4: **(a):** Plot of $t_{exp}$ as a function of $\omega_-$ for the experimental parameters provided in the text. • corresponds to the case presented in Figure 14.3. **(b):** The number of quanta gained as a result of unwanted heating during the experimental time $t_{exp}$, as calculated from the heating rate model ——— for etherDAC 2.1 and results • for the unamplified DACs, as presented in Chapter 11.

### 14.2.1 Signal strength

In the experiment, the signal is given by the measured height of the resolved red sideband transition in $^{40}Ca^+$. Because we do not have a pure state, we cannot have a perfect $\pi$-pulse on $^{40}Ca^+$. The question is how high is the measured signal, and how does it evolve in time.

Figure 14.5 (a) shows the time evolution of the height of the red sideband for as a function of $t_{MgH}$, the illumination time of $^{24}MgH^+$, at axial frequency $\omega_- = 424\,\text{kHz}$. The colors show the detection pulse time on the $^{40}Ca^+$ ion, $t_{Ca}/t_\pi$ where $t_\pi$ is the $\pi$-pulse time for the $^{40}Ca^+$ blue sideband transition $|g\rangle_a|0\rangle_- \rightarrow |e\rangle_a|1\rangle_-$. The black line shows $t_{exp}$. One can see that the pulse time can be chosen to exploit different features. The highest red sidebands can be reached with pulse times around $t_{\text{Ca}} = 0.3t_\pi$, but require long excitation times on $^{24}MgH^+$ of 20 ms[4]. The gain from exciting $^{24}MgH^+$ longer than about 5 ms is minimal compared to the initial increase[5]. On the other hand, one can choose a pulse time that maximizes the height of the sideband for very short excitation times. For this case, $t_{\text{Ca}} = t_\pi$ is the preferred pulse time. The disadvantage of this choice is that the maximal possible sideband height is low, at just over 40 %.

At $t_{exp}$, the pulse time that maximizes the sideband height is approximately $t_{\text{Ca}} = 0.5t_\pi$. At this point, the sideband height is just leveling off with a height of 53 %. To determine if the heating from the DC supply is low enough, the signal is compared to the noise by subtracting the sideband height from heating from the sideband height from excitation.

The expected heating at $\omega_-/(2\pi) = 424\,\text{kHz}$ is very small at $t_{exp}$, and corresponds only to 0.3 % excitation on the red sideband for a pulse time $t_{Ca} = 0.5t_\pi$. For comparison, Figure 14.6 (a) shows the red sideband height for a pulse time $t_{Ca} = 0.5t_\pi$ compared to the background side-

[4]Because this is only modeled for 5 states, the population levels off.
[5]The 'gain' time shifts to $t_{exp}$ for when considering more states.

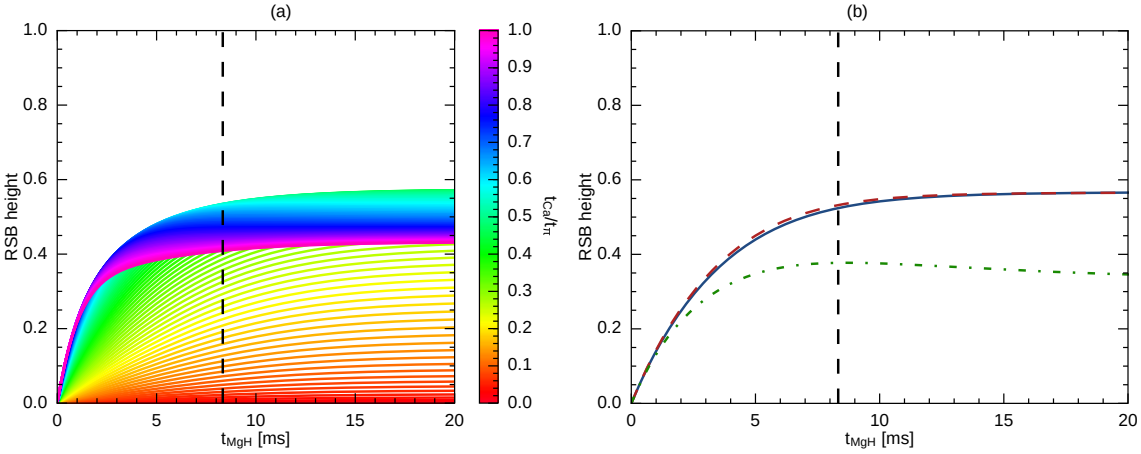


Figure 14.5: **(a):** Out-of-phase $^{40}Ca^{+}$ red sideband height as a function of time for $\omega_{-}/(2\pi) = 424\,\text{kHz}$ for variable $t_{Ca}/t_{\pi}$. ▬ ▬ shows $t_{exp}$. **(b):** ▬ ▬ shows the same signal as in (a) but for $t_{Ca} = 0.5t_{\pi}$, ▬ shows it considering the in-phase $^{24}MgH^{+}$ excitation's modification to the Rabi frequency (see Appendix C.3), and ▪ ▪ shows the effect of a heating rate on the in-phase mode 10 times that of what occurs due to optical heating.

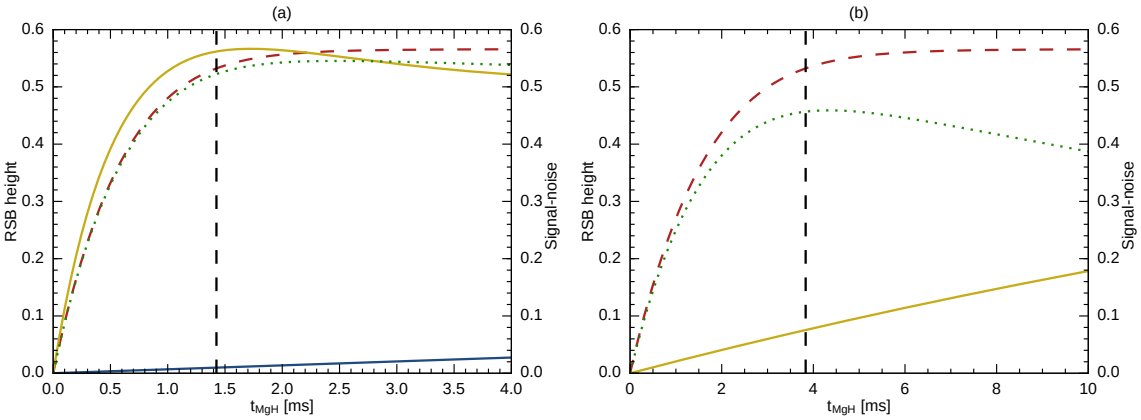


Figure 14.6: Comparison of signal and noise for a pulse time $t_{Ca} = 0.5t_{\pi}$ at **(a):** $\omega_{-}/(2\pi) = 68\,\text{kHz}$ and **(b):** $\omega_{-}/(2\pi) = 195\,\text{kHz}$. $^{40}Ca^{+}$ red sideband pulse height (left axis) due to ▬ ▬ excitation on the out-of-phase mode of $^{24}MgH^{+}$, ▬ heating from etherDAC 2.1, and ▬ heating from the unamplified DC supply. ▪▪▪▪ shows the difference between **(a):** ▬ ▬ and ▬ , or **(b):** ▬ ▬ and ▬ , and is referenced to the right axis.

band height from heating due to the DC supply for both the etherDAC 2.1 and the unamplified supply at $\omega_-/(2\pi) = 68\,\text{kHz}$. We see that while the heating from etherDAC 2.1 would make spectroscopy impossible, the heating from the unamplified supply is low compared to the signal height. At $t_{exp}$, the signal-noise difference is approximately the same height as the signal. The noise influences the measurement almost not at all, thus the unamplified DAC supply is well suited for this measurement.

Figure 14.6 (b) shows the signal minus the noise at $\omega_-/(2\pi) = 195\,\text{kHz}$ for comparison. The heating from the unamplified DACs is so small in this case that it is not plotted. We see that even though the heating from the etherDAC 2.1 contributes a non-negligible sideband height due to heating, the height of the signal-noise difference at $t_{exp}$ is still high at about 0.45. Thus it is possible to use etherDAC 2.1 for moderate ramp depth.

Lastly, we must consider that we have a two-ion crystal, and that the sideband height depends on the temperature of both modes. I modeled the excitation rate on the in-phase mode as well, and used it to calculate the modified out-of-phase red sideband height of $^{40}Ca^+$, shown in Figure 14.5 (b). This only takes into account excitation on $^{24}MgH^+$ from the light field, and not heating from the DC supply. However, to get a sense of how extra heating impacts the out-of-phase sideband height, I also modeled the height for a heating rate 10 times of that of the optical heating to get a sense of how the signal is impacted. The resulting signal is shown in green.

We see that the heating from the light field only slightly changes the height of the sideband. Heating on the in-phase mode is stronger than on the out-of-phase mode and while this heating will not create false signal, it will decrease the signal height (see Appendix C.3). Though this rate will still be much lower than the one displayed in green, it is optimal to stay cold on both modes.

## 14.3 Discussion

Looking at Figure 14.4, we see that there is a linear increase of $t_{exp}$ with increasing $\omega_-$. Thus, we can reduce the experimental time by adiabatically cooling. But how much?

For typical sideband cooling of a two-ion crystal, $V_{end} = 18.6\,\text{V}$. This corresponds to $\omega_-/(2\pi) = 568\,\text{kHz}$ for the $^{24}MgH^+$-$^{40}Ca^+$ crystal. $t_{exp}$ for this frequency is 11 ms. The lowest frequency with a measured heating rate for the unamplified DAC is $\omega_-/(2\pi) = 68\,\text{kHz}$. $t_{exp}$ for this frequency is about 1.4 ms. This is nearly an order of magnitude improvement in probe time. Given how low the expected heating will be at this low frequency, it looks promising that we could decrease $\omega_-$ even further.

While we can use the etherDAC 2.1 as well, we cannot cool as far. The most promising system is an unamplified DAC supply, with an extended voltage range to enable sideband cooling at higher $\omega_z$, allowing for more efficient cooling. It should be emphasized that to implement this change would be relatively simple, as it requires changing out only one voltage reference to have a $-10\,\text{V}$ to $10\,\text{V}$ supply, a large enough range to achieve 18.6 V.

We can implement the experiment even if we have a coherent excitation from the ramp, so long as the timing is chosen such that the kick on the way up counteracts the kick on the way down. Thus, if the ion is not excited, the ion will return to the initial state, whereas if excitation occurs, the ion will not return to the initial state. The ability to reform the initial state after a coherent excitation has been demonstrated even on a 42 ion Doppler-cooled chain on the ms timescale [187], thus we expect that this should be possible in our system as well.

Notably, the experimental time is much faster than the decay rate. The spectroscopy technique actually benefits from driving the transition above saturation, as the stimulated emission contributes to optical heating of the ion. Because we do not rely on spontaneous decay, and, in fact, are orders of magnitude faster, this technique can be applied to a transition which is not closed.

Because the excitation is broadband, we can probe $^{24}MgH^+$ during the entirety of the ramp. Thus, by illuminating the molecular ion at the start of the ramp, the ramp time is not entirely 'lost' time in the experimental sequence. It is almost possible to not consider the ramp time at all in the sequence, as it is faster than $t_{exp}$. This would not be the case with the previous supply, where ramps took 6 ms, as the time to ramp would be longer than $t_{exp}$.

## 14.4 Experimental outlook

From an experimental point of view, there are a few challenges we need to take into account. In a perfect world, we would have a perfect two-level atom, with no possibility of coupling into other states. While I have discussed why for a first model we can approximate this molecule as a two-level system, that does not mean that we can neglect this experimentally.

The first consideration is that while a trapped $^{24}MgH^+$ ion is in the electronic and vibrational ground states, it is distributed in the rotational levels, as discussed in section 6.2. To carry out this experiment, we can either prepare the state via rotational cooling or another state preparation method, or carry out the measurement on the room temperature distribution. Because the starting populations of $|v = 0, J = 0\rangle$ and $|v = 0, J = 1\rangle$ are less than 10 %, rotational cooling would make a signal much easier to measure.

Rotational cooling takes, however, a good 60 seconds to complete, and does not even allow us 100% preparation (experimentally, only about 35 % in $|J = 0\rangle$ and 15 % in $|(J = 1)\rangle$[6] [40]). It requires using the same laser as the one used for the spectroscopy, so on top of these 60 seconds is the tuning time of the laser between transitions. If we do rotational cooling, it is advantageous to do it as infrequently as possible. Ideally, of course, we use a projection scheme and prepare in $|v = 0, J = 1\rangle$, but even this takes time to 'find' the ion. This is where the blackbody rates come in[7], as they tell us how long it takes to re-thermalize. The blackbody rates between the lowest lying rotational states are on the order of $0.1\,s^{-1}$. We need to do as many repetitions of a measurement in succession as possible before re-thermalization occurs to build up statistics. This incentivizes being able to carry out this measurement as fast as possible.

Since the rovibrational state does not get prepared before every measurement, there will be a correlation between measurements. If the molecular ion is prepared in the correct rotational state, if you measure a signal on the first measurement, you will be more likely to measure it a second time. On the other hand, you are not prepared in the correct state, you will never measure a signal no matter how much you try.

These correlations can be used to help distinguish a signal from noise. Dark counts as a result of a transition in $^{24}MgH^+$ will occur correlated in time, whereas dark counts as a result of heating we be evenly distributed over time. We run into complications, however, when we consider that we also get dark counts as a result of collisions and decrystalization, which result in correlated dark counts which we would normally retake.

We can eliminate this problem by inverting our detection scheme, as shown schematically in Figure 14.7. After attempting to drive a transition in $^{24}MgH^+$, the $^{40}Ca^+$ ion will be in the state $|g, n\rangle$ with $|g\rangle$ being the $^2S_{1/2}$ state. In the scheme presented in subsection 6.4.1, we would then try to drive a red sideband transition and see if it is dark, where a dark count would be a positive indicator of transitions in $^{24}MgH^+$. We flip this scheme by preparing $^{40}Ca^+$ in $|e, n\rangle$ (the $^2D_{5/2}$ state) before detecting the motional state. We can prepare this state with nearly 100% efficiency using rapid adiabatic passage[8] [193–195]. We then use a blue sideband pulse to transfer

[6] One could instead pump from $|v = 0, J = 3\rangle$ to prepare more population in $|J = 1\rangle$

[7] For transitions that are not closed, we also need to take into account the spontaneous decay.

[8] Rapid adiabatic passage (RAP) is a technique where the detuning is swept over the transition and nearly 100 % population transfer from $|g\rangle \rightarrow |e\rangle$ occurs. We have already implemented it on the 729 nm transition in $^{40}Ca^+$.

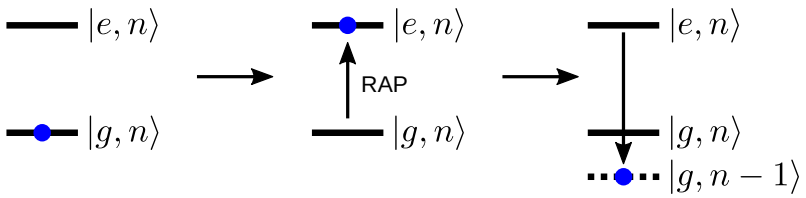


Figure 14.7: Proposed modification to the detection scheme. After probing $^{24}MgH^+$, rapid adiabatic passage (RAP) can be used to prepare $^{40}Ca^+$ in the excited state. A blue sideband pulse can then be used for detection. If the motional state is $n = 0$, it cannot couple and the ion will be dark. If it couples, the ion is light.

$|e,n\rangle \rightarrow |g,n-1\rangle$. This only couples if the ion is not in the ground state of motion. Thus, a positive detection event corresponds to the ion being in the $^2S_{1/2}$ state, which fluoresces during readout. A dark count due to decrystalization or collisions will thus only cause missed signal, rather than false signal, allowing us to rely on the correlation between events. These counts can still be controlled for by checking after some number of points that the ions are still there, however they are less detrimental to the signal.

To correlate the signal, it is important that we get as many measurements as possible before the ion re-thermalizes. With a blackbody rate of $0.1\,s^{-1}$, we have one second in which we keep the population with a 90 % chance. How many measurements can we carry out in one second?

Currently Doppler cooling takes 2 ms, sideband cooling[9] takes 40 ms, a $^{40}Ca^+$ sideband pulse is on the order of 100 µs, and readout takes 10 ms. If we stay at high axial frequency, $t_{exp} = 10$ ms is about 17 % of the total experiment time. With this pulse time, we could have a maximum of about 16 measurements[10] within the second. If we include the ramp, then we only need about 1.4 ms pulse time, corresponding to 19 measurements in the second.

This does not seem like a large increase. However, with improvements in sideband cooling time, $t_{exp}$ becomes a larger and larger percentage of the total experimental time. We must also consider if it makes sense to carry out these measurements with a photomultiplier tube instead of a CCD camera. We are also not limited to the 1 s time, this is just a chunk of time in which the population stays relatively constant. We can also measure continuously without state preparation. To build up correlation statistics, the measurement rate must be as fast as possible, and every ms counts.

In considering transitions other than $|v = 0, J = 1\rangle \rightarrow |v = 1, J = 0\rangle$, we have to consider the branching ratio of the spontaneous decay. For example, if we want to do spectroscopy on $|v = 0, J = 0\rangle \rightarrow |v = 1, J = 1\rangle$, then the ion will decay to the state $|v = 0, J = 2\rangle$ 60% of the time. For these measurements, it would be helpful to use the femtosecond comb-driven Raman transitions between rotational states to shift population back to $|v = 0, J = 0\rangle$. In this case, it would not have to be a full state preparation scheme, merely a few pulses driving from $|v = 0, J = 2\rangle \rightarrow |v = 0, J = 0\rangle$.

## 14.5 Conclusion

By exciting rovibrational transitions using broadband radiation, we will be able to perform spectroscopy that improves the precision of the transition frequencies by at least two orders of magnitude. The detection benefits from exciting the $^{24}MgH^+$ transition above saturation, and the

[9] Of two modes.

[10] If they are run exactly back to back. We can run the experiment without line triggering if we power broaden a bit on the 729 nm pulse, and ensure that the 50 Hz line is well compensated prior to measuring.

technique does not rely on spontaneous decay. As such, the pulse time is at least an order of magnitude faster than what would be required for one spontaneous decay.

The simulations indicate that by employing adiabatic cooling, we will be able to reduce the probe time of $^{24}MgH^+$ by an order of magnitude, from 10 ms to 1 ms. Using our unamplified DC supply, we can carry out this measurement with negligible heating of the ion from electronic noise, and full range can be achieved by replacing only one voltage reference. Having full voltage range enables us to take advantage of more efficient sideband cooling at higher $\omega_z$.

Ultimately, to build up measurement correlation statistics, it is advantageous to have each section of the experimental sequence as short as possible. By building up correlation statistics, it should be possible to perform these measurements without state preparation.

# Chapter 15

# Conclusion and Outlook

This thesis presents the implementation of adiabatic cooling of trapped ions for the purpose of rovibrational spectroscopy of molecular ions. Adiabatic cooling is implemented by ramping the axial trap potential, which is determined by DC voltages. Previously, the ramping time was limited to a total time of 6 ms due to electronic filtering. This led to the construction of a new DC supply, the etherDAC, that I built, tested, and programmed. With this supply, ramps of arbitrary shape can be remotely programmed into the supply, with limitations on the shape coming from the update rate of 4.68 µs and the electronic filtering. The electronic filtering leads to a step function rise-time of 37 µs, a factor nearly 30 faster than the previous supply. The output noise of the amplified supply was reduced from about $1\,\mu V_{rms}/\sqrt{Hz}$ to about $0.5\,\mu V_{rms}/\sqrt{Hz}$ for a typical axial frequency range by subsequent redesign of the supply.

Reduction of this noise is crucial for non-destructive detection of rovibrational transitions in molecular ions, as electronic noise causes unwanted heating of the ions. Thus, I measured the heating rates of a single $^{40}Ca^+$ ion for axial frequencies ranging from 509 kHz to 68 kHz for four versions of the DC supply. For the third version, the etherDAC 2.1, the output noise of the supply as measured by a spectrum analyzer was directly correlated to the measured heating rates. The noise spectral density was further used to predict the heating rates of the in-phase modes of $^{40}Ca^+$-$^{40}Ca^+$ and $^{40}Ca^+$-$^{42}Ca^+$, which showed good agreement with the data. The heating rates of the out-of-phase modes of the crystals were on the $1\,s^{-1}$ level, and seemed to be due to a different heating process.

The largest decrease in heating rates came as the result of switching from using a supply with an amplified output to using one without. The heating rates from the unamplified supply were more than an order of magnitude reduced from those of etherDAC 2.1, producing rates ranging from $2.93(14)\,s^{-1}$ at $\omega_z/(2\pi) = 198$ kHz to $50(3)\,s^{-1}$ at $\omega_z/(2\pi) = 68$ kHz. Back calculating the predicted output noise from the heating rate measurements shows that the output noise of this supply is less than $0.07\,\mu V_{rms}/\sqrt{Hz}$.

Adiabatic cooling experiments were carried out for two iterations of the DC supply: the etherDAC 2.1 and the unamplified supply. These experiments employed ramps with total ramp times of 290 µs, 20-times faster than with the old supply. I showed that temperatures achieved with a single $^{40}Ca^+$ ion in experiments using the etherDAC 2.1 were limited by heating due to the supply, as the gain in motional quantum number could be predicted from the heating rate measurements. Because the out-of-phase mode of a $^{40}Ca^+$-$^{42}Ca^+$ chain has a very low heating rate, adiabatic cooling of the out-of-phase mode was possible. For this experiment, I demonstrated a ramp from 486 kHz to 41 kHz, a factor of 12 reduction in axial frequency, with minimal excess heating on the out-of-phase mode. The maximal temperature of the out-of-phase mode of the ion at the bottom of the ramp was calculated to be $0.83(10)$ µK, corresponding to a factor of about 7

decrease in temperature from the top of the ramp to the bottom.

For the unamplified supply, I demonstrated frequency ramping of a single $^{40}Ca^+$ ion. While the measured increase in motional quantum number was low, I showed that a coherent kick was causing the ion to be excited at the bottom of the ramp while an opposite coherent kick was returning the ion to its initial state before measurement. This interesting result should not be a problem for rovibrational spectroscopy of $^{24}MgH^+$ so long as the kicks can be repeatably timed.

Ultimately, rovibrational spectroscopy of $^{24}MgH^+$ will be performed using a laser that has been narrowed to resolve the hyperfine structure and Zeeman structure of $^{24}MgH^+$, which requires a linewidth of about 1 kHz. However, using this narrow of a laser to search for transitions known only to the GHz would be impractical, thus I have presented calculations for quantum logic spectroscopy of $^{24}MgH^+$ using broadband laser radiation, which indicate that using adiabatic cooling can decrease the illumination time of the molecular ion by a factor of 10 for typical experimental parameters. This corresponds to an illumination time of about 1 ms. Taking into account the measured heating rates, I find that, for the fastest illumination times (lowest $\omega_z$), it is necessary to use a low-noise supply such as the unamplified supply to have a large enough difference between the $^{40}Ca^+$ red sideband height due to optical excitation and the background red sideband height. It should be possible to carry out this experiment with a thermal rotational distribution by employing fast loops of the experimental sequence, and tracking correlations between measurements.

## 15.1 Near future outlook

In order to implement broadband spectroscopy on $^{24}MgH^+$, the following tasks must be undertaken

- Increase the range of the unamplified DC supply. This is not strictly necessary, but should allow for much more efficient sideband cooling, and is relatively simple, only requiring changing one voltage reference
- Check reproducibility of coherent kick due to ramp for experimental timescales. If it is not reproducible, we must eliminate it.
- Optimize sideband cooling with $^{24}MgH^+$.
- Switch from a camera for readout to a PMT to increase the speed of detection.
- Setup the quantum cascade laser beamline.

Another notable experiment which we are working towards is femtosecond-driven Raman transitions between rotational levels. The details of how one can drive transitions in ions and molecular ions using a frequency comb are presented in [114, 115]. For $^{24}MgH^+$, these levels are spaced by approximately THz, and the Raman transitions will be driven via the off-resonant coupling of the field to the first excited electronic state. We have used this technique to measure the splitting between the $Ca^+$ $D$-fine structure states. The use of this technique will greatly aid in the rovibrational spectroscopy sequences, as it will allow us to prepare population in a specific rotational state. However, these transitions similarly suffer from the fact that the transition frequencies are known only to the GHz level. We can begin by using broadband rovibrational spectroscopy to measure the transition frequency of two rovibrational transitions with a shared upper level. Taking the difference between these two transitions will yield a better estimate of the splitting between these two rotational levels.

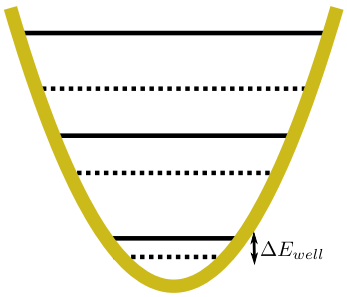


Figure 15.1: The zero-point energy of the ion is mass-dependent, so when an ion reacts to form a heavier mass ion, the zero-point energy decreases.

## 15.2 Other applications of adiabatic cooling

Aside from rovibrational spectroscopy, there are other experiments that we have been considering undertaking using adiabatic cooling. As discussed in the thesis, the opening of the trap potential causes both the spacing between motional levels and the zero-point energy to decrease, as is evident from the energy of a harmonic oscillator

$$E_{ho} = \hbar\omega_z \left(n + \frac{1}{2}\right) \tag{15.1}$$

which also amounts to a decrease in the kinetic energy.

These reductions have a number of applications to cold chemistry and collision studies. The collision energy is an important parameter in the dynamics of a chemical reaction, and at ultralow collision energies, it becomes possible to observe quantum effects. These include s-wave reactive scattering, tunneling, and reactive resonances [29]. Combining cold ions with cold atoms in hybrid traps, it is possible to tune collision energies to the 10 mK regime [196], and in a few cases, the 10 µK regime [197]. Using hybrid trap techniques combining with adiabatic cooling gives the prospect of tuning collision energies to another order of magnitude or more lower. Even in a 'perfectly' ground-state-cooled ion, adiabatic cooling reduces the collision energy by reducing the zero-point energy. Of course, for chemical reactions the collision energy depends on the ion motion in all three directions; thus, it would be necessary to implement adiabatic cooling also for the RF trapping field. All of these techniques, combined with internal state preparation of a molecular ion, could lead to a wealth of reaction studies at a large range of collision energies for state-prepared reactions. The new cryogenic trap setup being constructed in Aarhus will have magneto-optical trap capabilities, and thus will have the capability of studying this realm of physical chemistry.

Another application to cold chemistry is in the tuning of the thermodynamics of chemical reactions. When an ion and a neutral react, a heavier-mass product is formed and the zero-point energy of the well shifts lower, as $\omega_z \propto \frac{1}{\sqrt{m}}$. This shift, $\Delta E_{well}$ is illustrated in Figure 15.1. Now imagine that you have a typically endothermic reaction between a generic ion and neutral. If $\Delta E_{well}$ is larger than the gain in energy from the reaction, $\Delta E_{endo}$, then the reaction in the trap is actually exothermic in nature rather than endothermic. By employing adiabatic cooling, one could tune a reaction between being exo- and endothermic.

Adiabatic cooling of a two-ion crystal is an interesting tool for collision studies. The closer the spacing between motional energy levels, the more sensitive we are to small recoils as a result of a collision, as the limit of what we can detect is $\hbar\omega_z$. We propose using a two-ion crystal to measure small recoils in a range of collision energies, by using the out-of-phase mode as a meter

for the recoil energy, and the in-phase mode to adjust the collision energy. For example, by only Doppler-cooling the in-phase mode, the collision energy at the axial frequency used for cooling is on the order of a millikelvin. On the out-of-phase sideband-cooled mode, however, we are sensitive to recoils on the order of $T = \frac{\hbar\omega_-}{k_B} = 20\,\mu\text{K}$, where $\omega_-$ is the out-of-phase axial frequency. By employing adiabatic cooling, we both lower the collision energy and increase the sensitivity, which both change linearly with $\omega_-$. At a low axial frequencies, we can tune the collision energy by waiting for the in-phase mode to heat, while the out-of-phase mode stays cold. The collision energy could be further tuned by sideband-cooling the in-phase mode and the radial modes, to allow studies at low collision energy. As a result, we have access to a range of recoil energies over a large range of collision energies.

Another possible application is for vibrational sensing. If an ion trap were constructed to oscillate at a specific frequency, a trapped ion could be used to detect very low amplitude vibrations at that frequency, detected as heating of the ion. By using adiabatic-cooling, one can take advantage of the ability to sideband-cool at high frequency but detect at much lower frequency. Of course, heating from other sources would need to be reduced. One could use a combination of heavier mass ions (as to be less sensitive to electric field noise) with clever electronic filtering at the frequency of interest in order to reduce the heating from electric field noise and be able to sense in perhaps the mid to high audio range.

Aside from the main application of my thesis, rovibrational spectroscopy, I have suggested several exciting future applications. Adiabatic cooling is thus a method that enables the study of new physics across a number of disciplines, and we should look forward to seeing what it uncovers.

# Appendices

# Appendix A

# The calcium ion

## A.1 Ca isotopes

| Isotope | Abundance |
|---|---|
| 40 | 96.941(156) % |
| 42 | 0.647(23) % |
| 43 | 0.135(10) % |
| 44 | 2.086(110) % |
| 46 | 0.004(3) % |
| 48 | 0.187(21) % |

Table A.1: Isotope abundances from [198].

## A.2 $Ca^+$ structure and transitions

| Transition | Wavelength [nm] | Frequency [THz] | $\Gamma/2\pi$ |
|---|---|---|---|
| $4\,^2S_{1/2} - 4\,^2P_{1/2}$ | 397 | 755.222 765 896(88) [f] | 21.57(15) MHz [a] |
| $4\,^2S_{1/2} - 4\,^2P_{3/2}$ | 393 | 761.905 012 599(82) [e] | 21.49(6) MHz [b] |
| $3\,^2D_{3/2} - 4\,^2P_{1/2}$ | 866 | 346.000 234 867(96) [g] | 1.481(15) MHz [a] |
| $3\,^2D_{3/2} - 4\,^2P_{3/2}$ | 850 | 352.682 481 57(15) [h] | 0.152(1) MHz [a] |
| $3\,^2D_{5/2} - 4\,^2P_{3/2}$ | 854 | 350.862 882 55(15) [h] | 1.350(6) MHz [b] |
| $4\,^2S_{1/2} - 3\,^2D_{5/2}$ | 729 | 411.042 129 776 393 2(10) [c] | 136.3(10) mHz [d] |
| $3\,^2D_{3/2} - 3\,^2D_{5/2}$ | D-fine | 1 819 599 021 504(37) [i] | |
| $4\,^2S_{1/2} - 3\,^2D_{3/2}$ | 732 | 409.222 530 754 889(37) [h] | 135.3(13) mHz [d] |

[a] Ref. [98]
[b] Ref. [103]
[c] Ref. [200]
[d] Ref. [144]
[e] Ref. [201]
[f] Ref. [123]
[g] Ref. [202]
[h] calculated from ref [123, 201, 202]
[i] Ref. [203]

Table A.2: Transition data for $^{40}Ca^+$. Courtesy of Steffen Meyer.

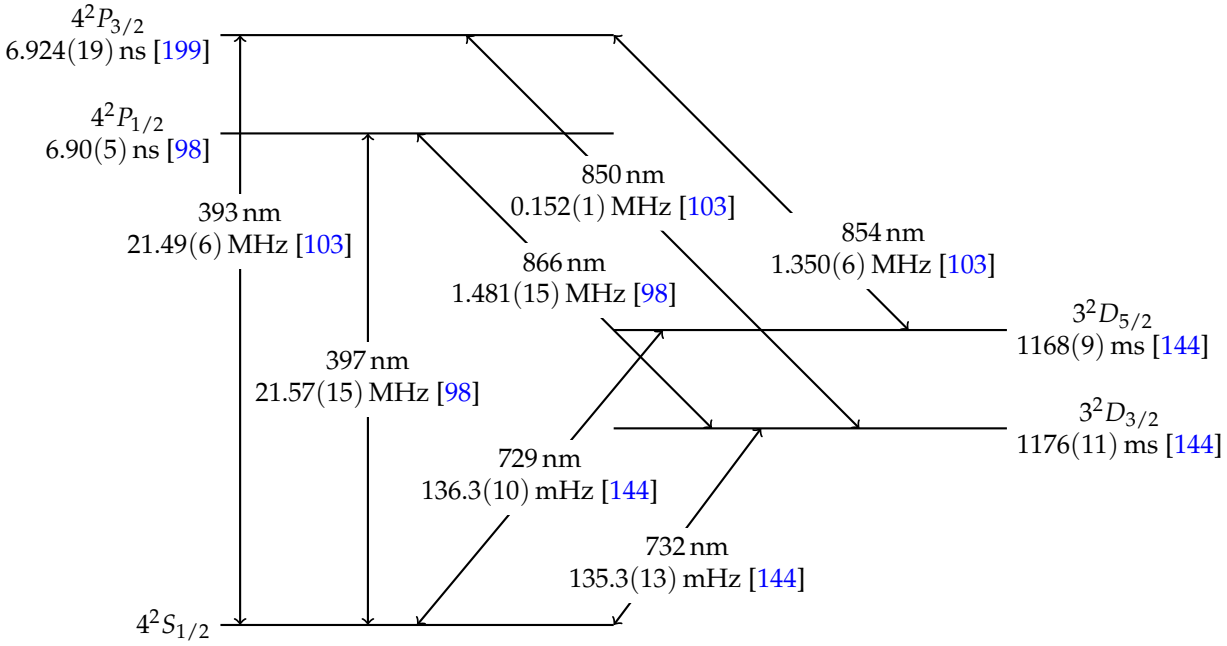


Figure A.1: The level structure of $^{40}Ca^+$. Courtesy of [68].

| Transition | [nm] | 42 | 44 | 46 | 48 |
|---|---|---|---|---|---|
| Ionization | 272 | +967(9) [e] | +1879(14) [e] | +2746(16) [e] | +3528(16) [e] |
| $4\,^2S_{1/2} - 4\,^2P_{1/2}$ | 397 | +425.706(94) [b] | +849.534(74) [b] | +1287(3) [d] | +1705.389(60) [b] |
| $4\,^2S_{1/2} - 4\,^2P_{3/2}$ | 393 | +425.932(71) [a] | +850.231(65) [a] | +1292(18) [d] | +1707.945(67) [a] |
| $4\,^2P_{1/2} - 4\,^2P_{3/2}$ | P-fine | +0.226(118) [a] | +0.697(98) [a] | | +2.556(90) [a] |
| $3\,^2D_{3/2} - 4\,^2P_{1/2}$ | 866 | −2349.974(99) [b] | −4498.883(80) [b] | | −8297.769(81) [b] |
| $3\,^2D_{3/2} - 4\,^2P_{3/2}$ | 850 | −2352.2(21) [c] | −4498.7(30) [c] | | −8297.7(58) [c] |
| $3\,^2D_{5/2} - 4\,^2P_{3/2}$ | 854 | −2350.4(43) [c] | −4495.2(43) [c] | | −8287.8(70) [c] |

[a] Ref. [201]
[b] Ref. [202]
[c] Ref. [204]
[d] Ref. [205]
[e] Ref. [134]

Table A.3: Calcium isotope shifts in MHz, courtesy of Steffen Meyer.

Clebsch-Gordan Coefficients

| | $4S_{1/2}, -1/2$ | $4S_{1/2}, +1/2$ |
|---|---|---|
| $4P_{1/2}, -1/2$ | $-\sqrt{1/3}$ | $\sqrt{2/3}$ |
| $4P_{1/2}, +1/2$ | $-\sqrt{2/3}$ | $\sqrt{1/3}$ |
| $4P_{3/2}, -3/2$ | 1 | - |
| $4P_{3/2}, -1/2$ | $\sqrt{2/3}$ | $\sqrt{1/3}$ |
| $4P_{3/2}, +1/2$ | $\sqrt{1/3}$ | $\sqrt{2/3}$ |
| $4P_{3/2}, +3/2$ | - | 1 |

| | $3D_{3/2}, -3/2$ | $3D_{3/2}, -1/2$ | $3D_{3/2}, +1/2$ | $3D_{3/2}, +3/2$ |
|---|---|---|---|---|
| $4P_{1/2}, -1/2$ | $\sqrt{1/2}$ | $-\sqrt{1/3}$ | $\sqrt{1/6}$ | - |
| $4P_{1/2}, +1/2$ | - | $\sqrt{1/6}$ | $-\sqrt{1/3}$ | $\sqrt{1/2}$ |
| $4P_{3/2}, -3/2$ | $-\sqrt{3/5}$ | $\sqrt{2/5}$ | - | - |
| $4P_{3/2}, -1/2$ | $-\sqrt{2/5}$ | $-\sqrt{1/15}$ | $\sqrt{8/15}$ | - |
| $4P_{3/2}, +1/2$ | - | $-\sqrt{8/15}$ | $\sqrt{1/15}$ | $\sqrt{2/5}$ |
| $4P_{3/2}, +3/2$ | - | - | $-\sqrt{2/5}$ | $\sqrt{3/5}$ |

| | $4P_{3/2}, -3/2$ | $4P_{3/2}, -1/2$ | $4P_{3/2}, +1/2$ | $4P_{3/2}, +3/2$ |
|---|---|---|---|---|
| $3D_{5/2}, -5/2$ | $\sqrt{2/3}$ | - | - | - |
| $3D_{5/2}, -3/2$ | $-\sqrt{4/15}$ | $\sqrt{2/5}$ | - | - |
| $3D_{5/2}, -1/2$ | $\sqrt{1/15}$ | $-\sqrt{2/5}$ | $\sqrt{1/5}$ | - |
| $3D_{5/2}, +1/2$ | - | $\sqrt{1/5}$ | $-\sqrt{2/5}$ | $\sqrt{1/15}$ |
| $3D_{5/2}, +3/2$ | - | - | $\sqrt{2/5}$ | $-\sqrt{4/15}$ |
| $3D_{5/2}, +5/2$ | - | - | - | $\sqrt{2/3}$ |

Table A.4: Clebsch-Gordan coefficients. Adapted from [138].

Landé g-factors for Zeeman splitting

| State | $g_J$ |
|---|---|
| $^2S_{1/2}$ | 2 |
| $^2P_{1/2}$ | 2/3 |
| $^2P_{3/2}$ | 4/3 |
| $^2D_{3/2}$ | 4/5 |
| $^2D_{5/2}$ | 6/5 |

Table A.5: Landé g-factors $g_J$, given by $g_J \simeq \frac{3}{2} + \frac{S(S+1)-L(L+1)}{2J(J+1)}$, for the $^{40}Ca^+$ ion. See section 5.1 for information on calculating the Zeeman splitting.

# Appendix B

# The $^{24}MgH^+$ ion

The R branch, transitions which have $\Delta J = 1$, is denoted by $R_v(J)$, where $v$ and $J$ refer to the lower state. The P branch, transitions which have $\Delta J = -1$, is denoted by $P_v(J)$, where $v$ and $J$ refer to the lower state.

| Transition | Wavenumber [$cm^{-1}$] | Vac. wavelength [μm] | Frequency [THz] |
|---|---|---|---|
| $R_0(0)$ | 12.59 | 794.53 | 0.377 |
| $R_0(1)$ | 25.16 | 397.54 | 0.754 |
| $R_0(2)$ | 37.82 | 264.43 | 1.134 |
| $R_0(3)$ | 50.19 | 199.23 | 1.505 |
| $R_0(4)$ | 62.85 | 159.12 | 1.884 |
| $R_0(5)$ | 75.22 | 132.95 | 2.255 |
| $R_0(6)$ | 87.66 | 114.07 | 2.628 |
| $R_0(7)$ | 99.95 | 100.05 | 2.997 |
| $R_0(8)$ | 112.30 | 89.05 | 3.367 |
| $R_0(9)$ | 124.45 | 80.35 | 3.731 |

Table B.1: Transition data for the lowest-lying rotational transitions. Calculated from [105], table reproduced (and corrected) from [108]. The error on wavenumber is 0.05 $cm^{-1}$.

| Transition | Wavenumber [$cm^{-1}$] | Vac. wavelength [nm] | Frequency [THz] |
|---|---|---|---|
| $P_1(5)$ | 1568.03 | 6377.45 | 47.008 |
| $P_1(4)$ | 1582.06 | 6320.89 | 47.429 |
| $P_1(3)$ | 1595.56 | 6267.41 | 47.834 |
| $P_1(2)$ | 1608.96 | 6215.19 | 48.235 |
| $P_1(1)$ | 1621.77 | 6166.11 | 48.619 |
| $R_1(0)$ | 1646.70 | 6072.74 | 49.367 |
| $R_1(1)$ | 1658.53 | 6029.44 | 49.721 |
| $R_1(2)$ | 1670.07 | 5987.79 | 50.067 |
| $R_1(3)$ | 1681.07 | 5948.61 | 50.397 |
| $R_1(4)$ | 1691.86 | 5910.67 | 50.721 |

Table B.2: Transition data for the lowest-lying rotational transitions. Calculated from [105]. Table reproduced (and corrected) from [108]. The error on wavenumber is 0.05 $cm^{-1}$.

| $\|v, J\rangle_{\text{ini}}$ | | $\Delta v = 0$ | | -1 | | -2 | | -3 | | -4 | |
|---|---|---|---|---|---|---|---|---|---|---|---|
| $v$ | $J$ | $\Delta J = -1$ | 1 | -1 | 1 | -1 | 1 | -1 | 1 | -1 | 1 |
| 0 | 0 | | | | | | | | | | |
| | 1 | 0.0023 | | | | | | | | | |
| | 2 | 0.022 | | | | | | | | | |
| | 3 | 0.081 | | | | | | | | | |
| | 4 | 0.199 | | | | | | | | | |
| | 5 | 0.396 | | | | | | | | | |
| | 6 | 0.691 | | | | | | | | | |
| | 7 | 1.104 | | | | | | | | | |
| | 8 | 1.652 | | | | | | | | | |
| 1 | 0 | | | | 15.753 | | | | | | |
| | 1 | 0.0020 | | 6.139 | 9.701 | | | | | | |
| | 2 | 0.020 | | 7.955 | 8.059 | | | | | | |
| | 3 | 0.070 | | 9.195 | 7.079 | | | | | | |
| | 4 | 0.172 | | 10.277 | 6.345 | | | | | | |
| | 5 | 0.343 | | 11.316 | 5.740 | | | | | | |
| | 6 | 0.599 | | 12.358 | 5.219 | | | | | | |
| | 7 | 0.957 | | 13.424 | 4.760 | | | | | | |
| | 8 | 1.430 | | 14.527 | 4.349 | | | | | | |
| 2 | 0 | | | | 36.614 | | 2.676 | | | | |
| | 1 | 0.0017 | | 14.061 | 22.721 | 0.802 | 1.872 | | | | |
| | 2 | 0.017 | | 18.093 | 19.025 | 0.907 | 1.762 | | | | |
| | 3 | 0.060 | | 20.773 | 16.851 | 0.911 | 1.750 | | | | |
| | 4 | 0.147 | | 23.065 | 15.231 | 0.883 | 1.769 | | | | |
| | 5 | 0.293 | | 25.237 | 13.899 | 0.839 | 1.800 | | | | |
| | 6 | 0.511 | | 27.392 | 12.750 | 0.787 | 1.838 | | | | |
| | 7 | 0.816 | | 29.579 | 11.735 | 0.731 | 1.878 | | | | |
| | 8 | 1.220 | | 31.826 | 10.825 | 0.672 | 1.918 | | | | |
| 3 | 0 | | | | 61.632 | | 5.918 | | 0.633 | | |
| | 1 | 0.0015 | | 23.391 | 38.480 | 1.741 | 4.172 | 0.202 | 0.431 | | |
| | 2 | 0.014 | | 29.927 | 32.422 | 1.947 | 3.953 | 0.236 | 0.396 | | |
| | 3 | 0.050 | | 34.167 | 28.899 | 1.934 | 3.949 | 0.247 | 0.385 | | |
| | 4 | 0.124 | | 37.731 | 26.289 | 1.847 | 4.012 | 0.250 | 0.382 | | |
| | 5 | 0.246 | | 41.063 | 24.147 | 1.728 | 4.103 | 0.248 | 0.382 | | |
| | 6 | 0.429 | | 44.335 | 22.299 | 1.592 | 4.205 | 0.245 | 0.383 | | |
| | 7 | 0.684 | | 47.630 | 20.661 | 1.448 | 4.311 | 0.241 | 0.386 | | |
| | 8 | 1.021 | | 50.991 | 19.186 | 1.300 | 4.417 | 0.235 | 0.390 | | |
| 4 | 0 | | | | 89.030 | | 7.861 | | 2.501 | | 0.053 |
| | 1 | NC | | 33.466 | 55.856 | 2.245 | 5.609 | 0.795 | 1.704 | 0.017 | 0.036 |
| | 2 | NC | | 42.614 | 47.292 | 2.466 | 5.372 | 0.931 | 1.567 | 0.020 | 0.033 |
| | 3 | NC | | 48.423 | 42.360 | 2.399 | 5.417 | 0.972 | 1.523 | 0.021 | 0.032 |
| | 4 | NC | | 53.224 | 38.723 | 2.237 | 5.549 | 0.981 | 1.509 | 0.021 | 0.031 |
| | 5 | NC | | 57.656 | 35.742 | 2.035 | 5.715 | 0.975 | 1.510 | 0.021 | 0.031 |
| | 6 | NC | | 61.966 | 33.167 | 1.816 | 5.893 | 0.961 | 1.517 | 0.021 | 0.031 |
| | 7 | NC | | 66.268 | 30.879 | 1.589 | 6.073 | 0.942 | 1.529 | 0.021 | 0.031 |
| | 8 | NC | | 70.624 | 28.812 | 1.364 | 6.249 | 0.920 | 1.543 | 0.021 | 0.032 |

Table B.3: Einstein $A$ coefficients for low-lying rovibrational transitions, in $\text{Hz}^{-1}$. Calculations by Frank Jensen [106]. Table reproduced from [108].

# Appendix C

# Rabi Frequencies

The following appendix explains how to calculate Rabi frequencies for dipole and quadrupole transitions. These two sections follow primarily [70,206]. It also explains, in a two-ion crystal, the influence of other modes on one mode's Rabi frequency.

For the following sections, if the $z$-axis is defined along the B-field such that $B = B_0(0,0,1)$, the polarization is defined as

$$\boldsymbol{\epsilon_i} = (\cos\gamma\cos\phi, \sin\gamma, -\cos\gamma sin\phi) \tag{C.1}$$

where $\gamma$ is the angle between the polarization and $B$, and $\phi$ is the angle between $k$ and $B$.

## C.1 Dipole transitions

For dipole transitions between lower state $|j, m_j\rangle$ and upper state $|j', m_j'\rangle$, the vacuum Rabi frequency is given by [70,206]

$$\Omega_0 = \frac{eE}{\hbar}\langle j, m_j|\hat{r_i}|j', m_j'\rangle\boldsymbol{\epsilon_i} \tag{C.2}$$

where

$$\begin{aligned}\langle j, m_j|\hat{r_i}|j', m_j'\rangle\boldsymbol{\epsilon_i} &= \sum_{q=-1}^{1}\langle j, m_j|rC_q^{(1)}|j', m_j'\rangle {c_i}^{(q)}\boldsymbol{\epsilon_i} \\ &= (-1)^{(j'-m_j')}\langle j||rC^{(1)}||j'\rangle \sum_{q=-1}^{1}\begin{pmatrix} j & 1 & j' \\ -m_j & q & m_j' \end{pmatrix}{c_i}^{(q)}\boldsymbol{\epsilon_i}\end{aligned} \tag{C.3}$$

where $C_q^{(1)}$ is the $q$-component of the Racah tensor, related to the normalized spherical wavefunctions, and where $\langle j||rC^{(1)}||j'\rangle$ is the reduced matrix element. ${c_i}^{(q)}$ are the normalized spherical basis vectors. They are given as follows:

$$\begin{aligned}c^{(1)} &= -\frac{1}{\sqrt{2}}(1, -i, 0) \\ c^{(0)} &= (0, 0, 1) \\ c^{(-1)} &= \frac{1}{\sqrt{2}}(1, i, 0)\end{aligned} \tag{C.4}$$

The Einstein A coefficient for the two levels is given by

$$\begin{aligned}\bar{A}_{12} =& \frac{4c\alpha k_{12}^3}{3} \sum_{q=-1}^{1} |\langle j, m_j | r C_q^{(1)} | j', m_j' \rangle|^2 \\ =& \frac{4c\alpha k_{12}^3}{3} |\langle j || r C^{(1)} || j' \rangle|^2 \sum_{q=-1}^{1} \begin{pmatrix} j & 1 & j' \\ -m_j & q & m_j' \end{pmatrix}^2\end{aligned} \tag{C.5}$$

where $\alpha$ is the fine structure constant and $k_{12} = \frac{2\pi}{\lambda_{12}}$ is the wavenumber of the transition.

However, the Einstein A coefficient in literature is normally given as the decay to all of the sublevels, given as

$$A_{12} = \sum_{m=-j}^{j} \bar{A}_{12} = \frac{4c\alpha k_{12}^3}{3(2j'+1)} |\langle j || r C^{(1)} || j' \rangle|^2 \tag{C.6}$$

These decay rates are the same for all of the upper states. This results in

$$\Omega_0 = \frac{e|E|}{\hbar\sqrt{c\alpha}} \sqrt{\frac{3A_{12}}{4k_{12}^3}} \sigma \tag{C.7}$$

where

$$\sigma = \sqrt{2j'+1} (-1)^{j'+j+j_> - m_j'} \left| \sum_{q=-1}^{1} \begin{pmatrix} j & 1 & j' \\ -m_j & q & m_j' \end{pmatrix} c_i^{(q)} \boldsymbol{\epsilon_i}^{(q)} \right| \tag{C.8}$$

Without the polarization terms, $\sigma$ is equivalent to the Clebsch-Gordon coefficients.

## C.2 Quadrupole transitions

For quadrupole transitions between lower state $|j, m_j\rangle$ and upper state $|j', m_j'\rangle$, the vacuum Rabi frequency is given by

$$\Omega_0 = \left| \frac{eEk_{12}}{2\hbar} \langle j, m_j | \hat{r}_i \hat{r}_j | j', m_j' \rangle \boldsymbol{\epsilon_i} n_j \right| \tag{C.9}$$

where $n$ is the propagation direction of the light and where

$$\begin{aligned}\langle j, m_j | \hat{r}_i \hat{r}_j | j', m_j' \rangle \boldsymbol{\epsilon_i} n_j =& \sum_{q=-2}^{2} \langle j, m_j | r^2 C_q^{(2)} | j', m_j' \rangle c_{ij}^{(q)} \boldsymbol{\epsilon_i} n_j \\ =& \langle j || r^2 C^{(2)} || j' \rangle \sum_{q=-2}^{2} \begin{pmatrix} j & 2 & j' \\ -m_j & q & m_j' \end{pmatrix} c_{ij}^{(q)} \boldsymbol{\epsilon_i} n_j\end{aligned} \tag{C.10}$$

where $\langle j || r^2 C^{(2)} || j' \rangle$ is the reduced matrix element [70]. $c_{ij}^{(q)}$ are second-rank tensors given by

$$c_{ij}^{(q)} = \frac{10}{3} (-1)^q \sum_{m_1, m_2 = -1}^{1} \begin{pmatrix} 1 & 1 & 2 \\ m_1 & m_2 & -q \end{pmatrix} c_i^{(m1)} c_j^{(m2)} \tag{C.11}$$

The Einstein A coefficient for the two levels is given by

$$\begin{aligned}\bar{A}_{12} =& \frac{c\alpha k_{12}^5}{15} \sum_{q=-2}^{2} |\langle j, m_j | r^2 C_q^{(2)} | j', m_j' \rangle|^2 \\ =& \frac{c\alpha k_{12}^5}{15} |\langle j || r^2 C^{(2)} || j' \rangle|^2 \sum_{q=-2}^{2} \begin{pmatrix} j & 2 & j' \\ -m_j & q & m_j' \end{pmatrix}^2\end{aligned} \tag{C.12}$$

However, the Einstein A coefficient in literature is normally given as the decay to all of the sublevels, given as

$$A_{12} = \sum_{m=-j}^{j} \bar{A}_{12} = \frac{c\alpha k_{12}^5}{15(2j'+1)} |\langle j||r^2 C^{(2)}||j'\rangle|^2 \tag{C.13}$$

This gives

$$\Omega_0 = \frac{e|E|}{\hbar\sqrt{c\alpha}} \sqrt{\frac{15A_{12}}{4k_{12}^3}} \sigma \tag{C.14}$$

where

$$\sigma = \sqrt{2j'+1} \left| \sum_{q=-2}^{2} \begin{pmatrix} j & 2 & j' \\ -m_j & q & m_j' \end{pmatrix} {c_{ij}}^{(q)} {\epsilon_i}^{(q)} n_j \right| \tag{C.15}$$

For a polarization as defined in the introduction, the geometry-dependent component $g^{(q)} = {c_{ij}}^{(q)} \epsilon_i n_j$ can be written as the following for the $^2S_{1/2} \rightarrow {}^2D_{5/2}$ transition in $^{40}Ca^+$ [74]:

$$\begin{aligned} g^{(0)} &= \frac{1}{2} |\cos\gamma \sin(2\phi)| \\ g^{(\pm 1)} &= \frac{1}{\sqrt{6}} |\cos\gamma \cos(2\phi) + i \sin\gamma \cos\phi| \\ g^{(\pm 2)} &= \frac{1}{\sqrt{6}} \left| \frac{1}{2} \cos\gamma \sin(2\phi) + i \sin\gamma \sin\phi \right| \end{aligned} \tag{C.16}$$

This yields geometry and polarization dependent coupling strengths on the different $\Delta m_j$ transitions, as shown in Figure C.1. This figure shows only the geometry component. To get the full transition-dependence, one also needs to multiply by the Clebsch-Gordan coefficients.

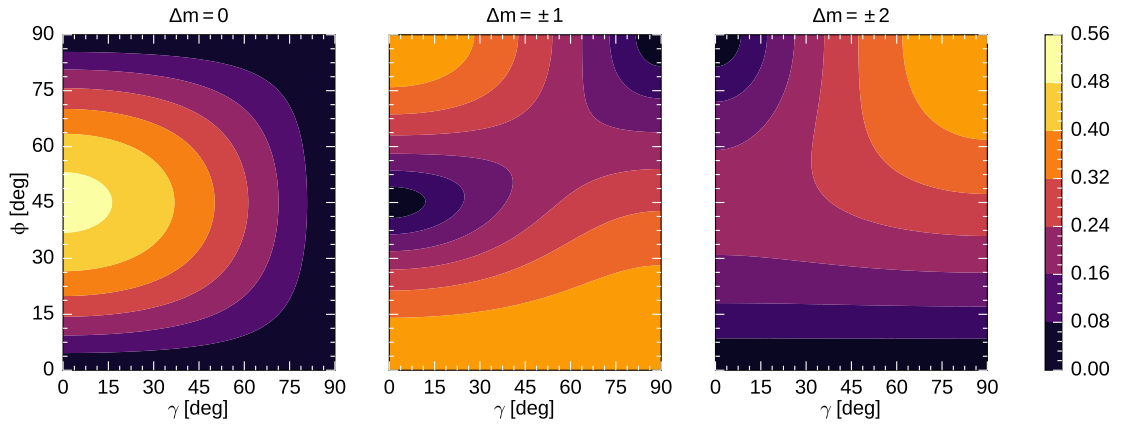


Figure C.1: Geometry-dependent relative coupling strengths on the $^2S_{1/2} \rightarrow {}^2D_{5/2}$ transition.

## C.3 Two ions

When we have two ions in the trap, the Rabi frequency is given by [80]

$$\begin{aligned}\Omega_{n_+,n_-,s_+,s_-} &= \langle n_+, n_- | \Pi_\alpha e^{i\eta^\alpha(\hat{a}_\alpha + \hat{a}_\alpha^\dagger)} | n_+ + s+, n_- + s_- \rangle \\ &= \Omega_0 \Pi_\alpha e^{-\frac{\eta_i^{\alpha 2}}{2}} \eta_i^{\alpha|s_\alpha|} \sqrt{\frac{n_{\alpha<}!}{n_{\alpha>}!}} L_{n_{\alpha<}}^{|s_\alpha|}(\eta^2)\end{aligned} \tag{C.17}$$

The product over the modes means that the motional state of one mode affects the Rabi frequency of the any other mode (and of the carrier). Thus, if there is heating on the in-phase mode and no heating on the out-of-phase mode, the sideband (on-resonance) height of the cold out-of-phase mode will be influenced by the hot in-phase mode by

$$\begin{aligned}\rho_{bsb} &= \sum_0^{n_+} \sum_0^{n_-} P_{n_+} P_{n_-} \sin\left(\Omega_{n_+,n_-,0,1} t\right) \\ \rho_{rsb} &= \sum_0^{n_+} \sum_1^{n_-} P_{n_+} P_{n_-} \sin\left(\Omega_{n_+,n_-,0,-1} t\right)\end{aligned} \tag{C.18}$$

where $P_{n_\alpha}$ is the population distribution of each mode (taken here to be thermal).

Because the sum over $n_+$ does not change motional quantum number, it is the same on both the red and blue sideband Thus, the ratio between the red and the blue sidebands does not change and still gives a measure of the mode temperature. It does cause the sideband height to decrease. Figure C.2 shows the decrease of the out-of-phase blue sideband with an increase of $\bar{n}_+$.

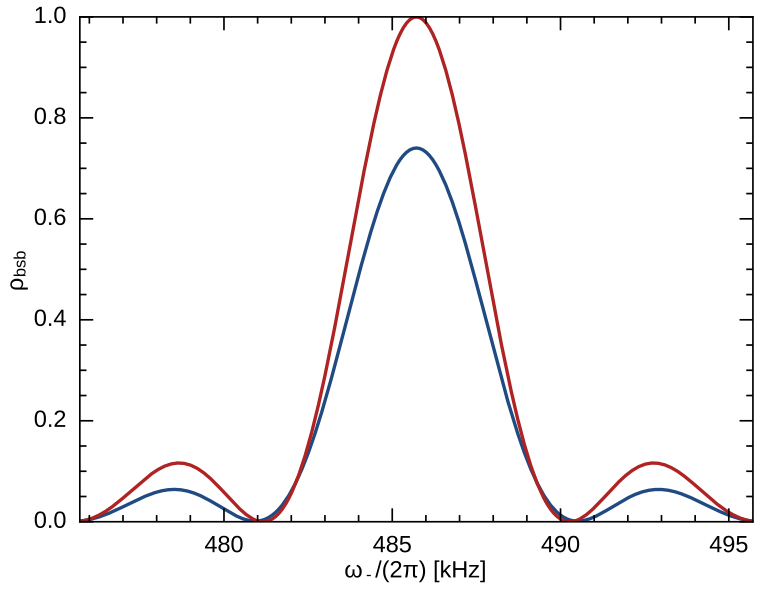


Figure C.2: Theoretical comparison of blue sidebands with $\bar{n}_- = 0$ and $\bar{n}_+ = 0$ and $\bar{n}_+ = 23$, both with $\eta_= = 0.126$ and $\eta_+ = 0.100$.

# Appendix D

# Schematics

The following pages contain schematics of the electronics discussed in Chapter 9.

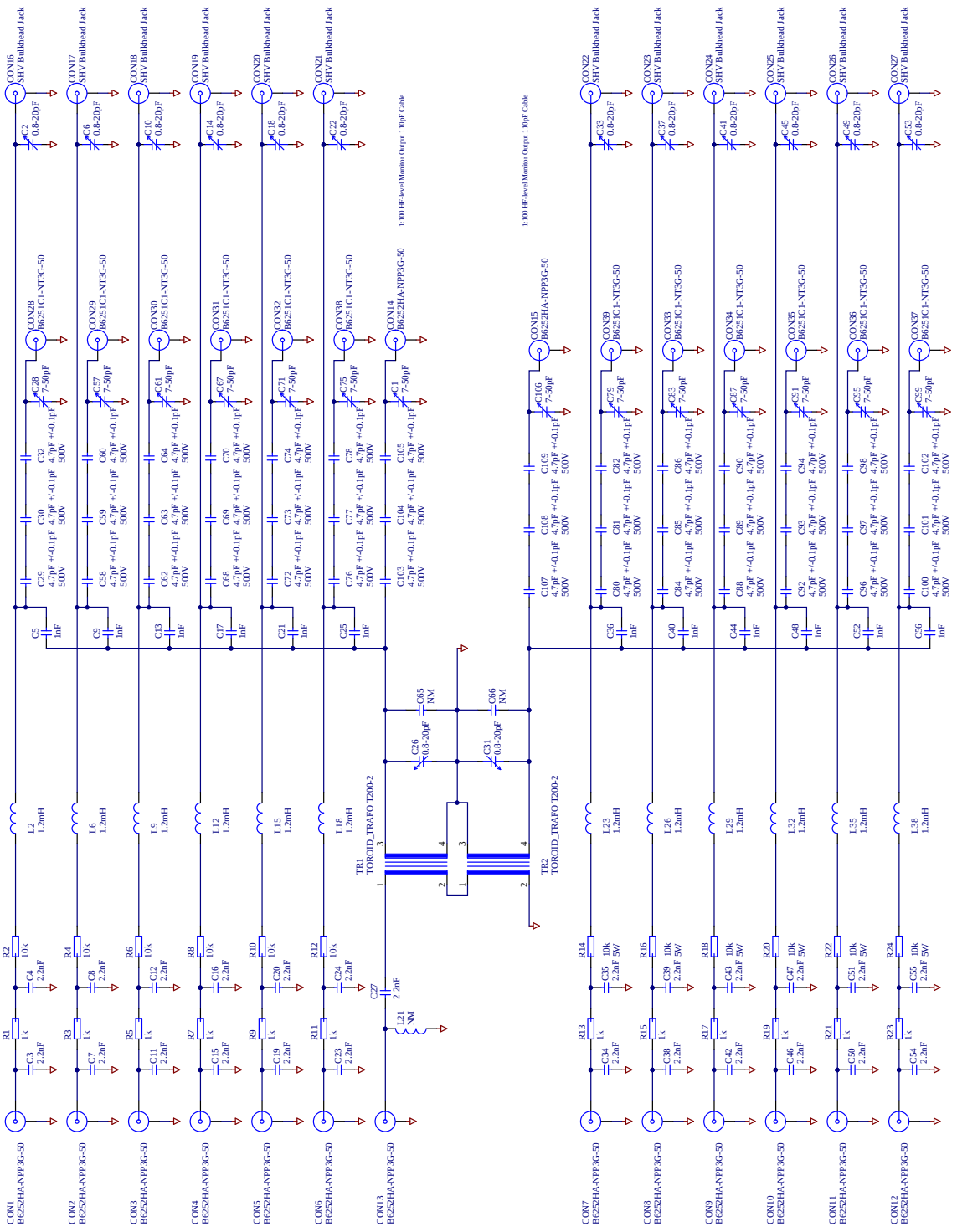

Figure D.1: Schematic of the RF/DC mixer. Designed by Martin Stougaard.

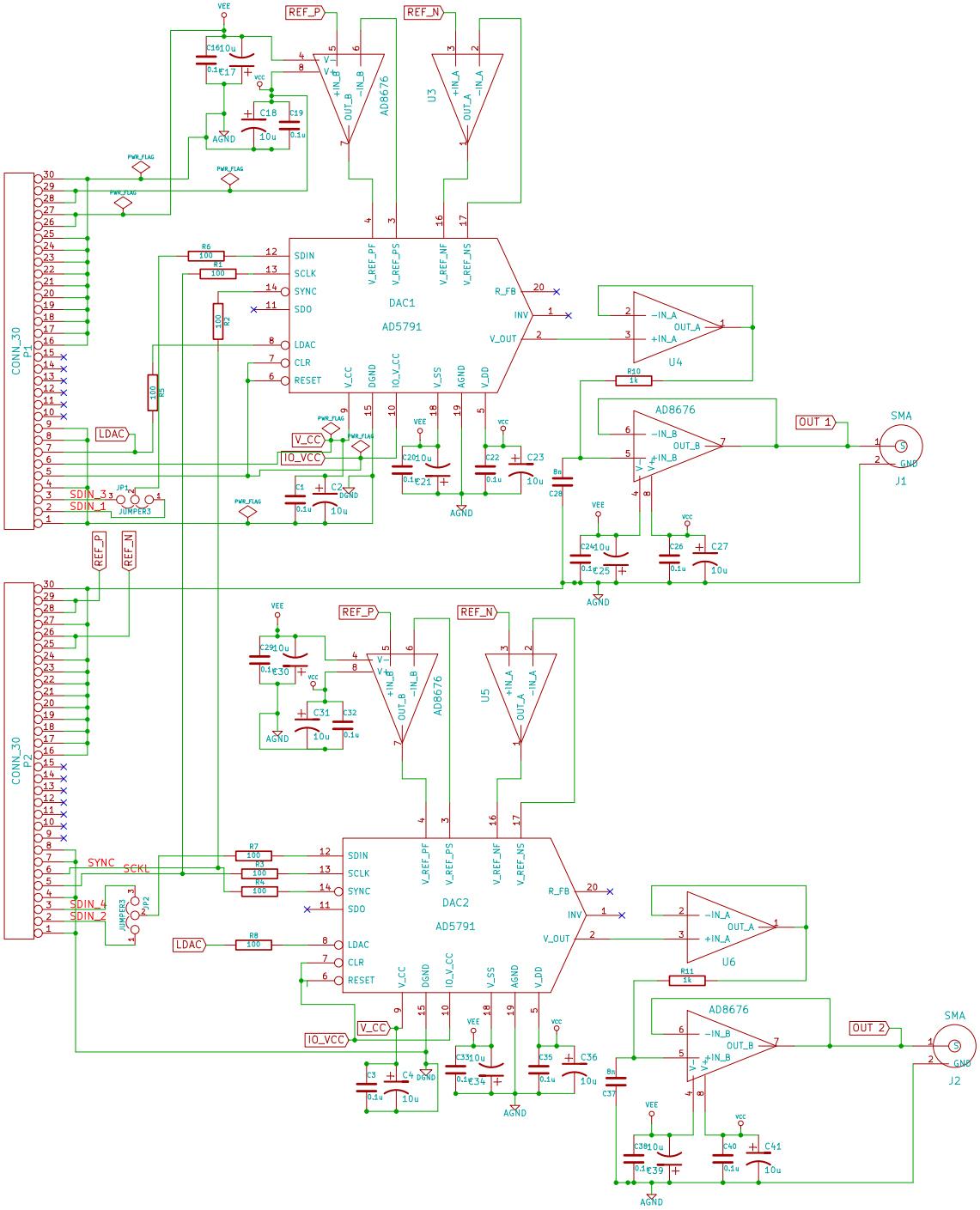


Figure D.2: Schematic of the etherDAC 1.0 DAC board.

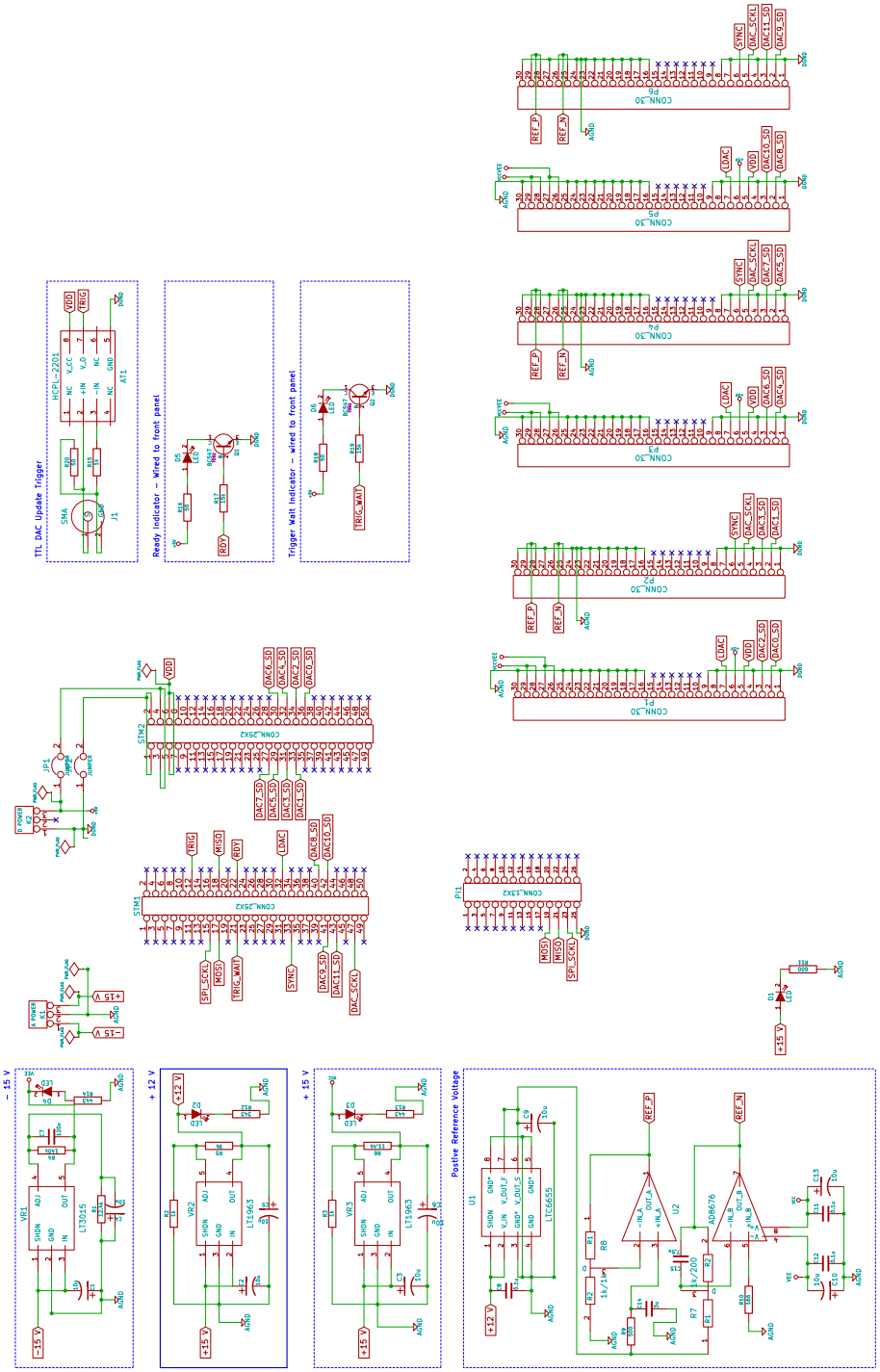

Figure D.3: Schematic of the etherDAC 1.0 main board.

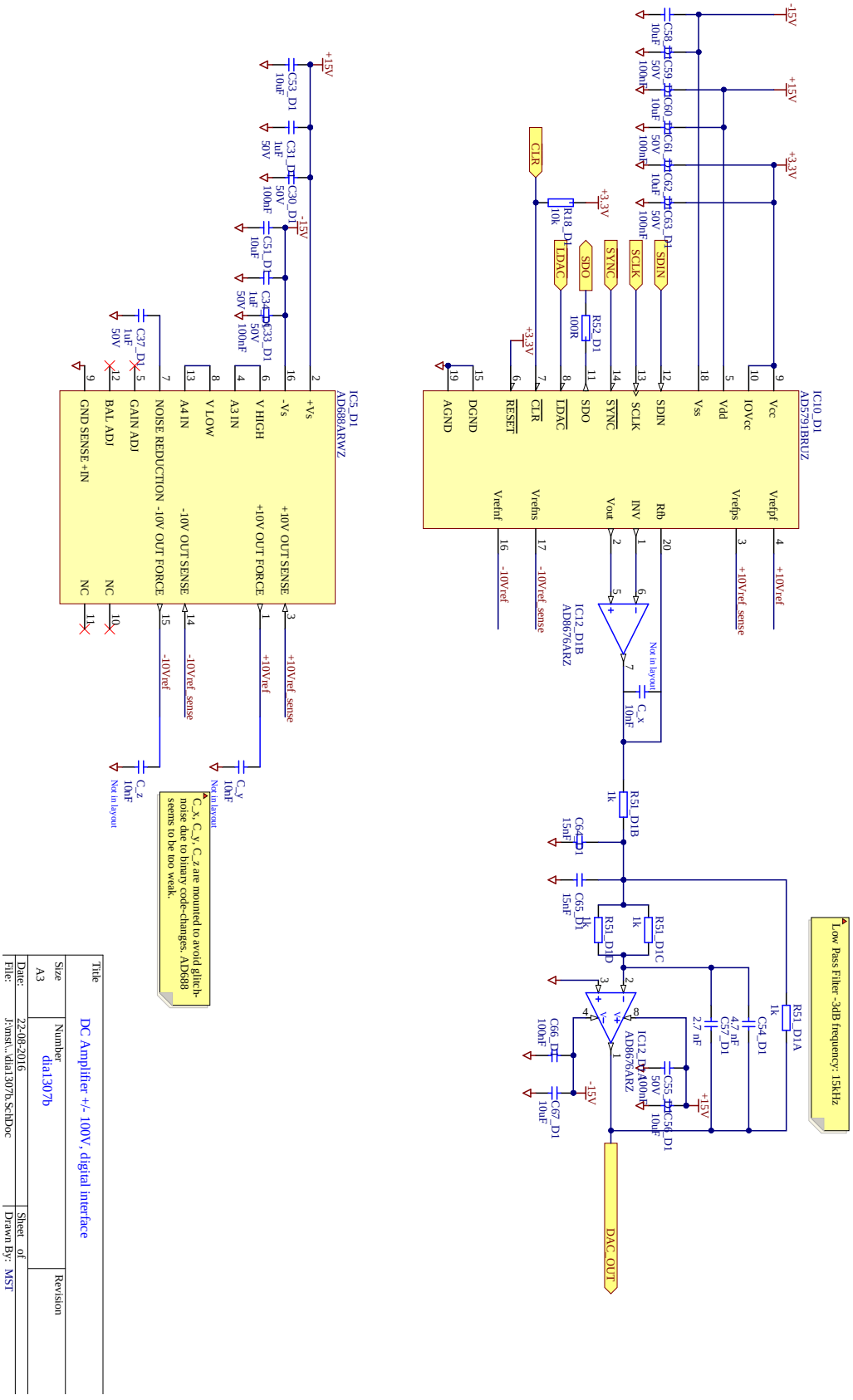


Figure D.4: Schematic of the etherDAC 2.1 DAC. Designed by Martin Stougaard.

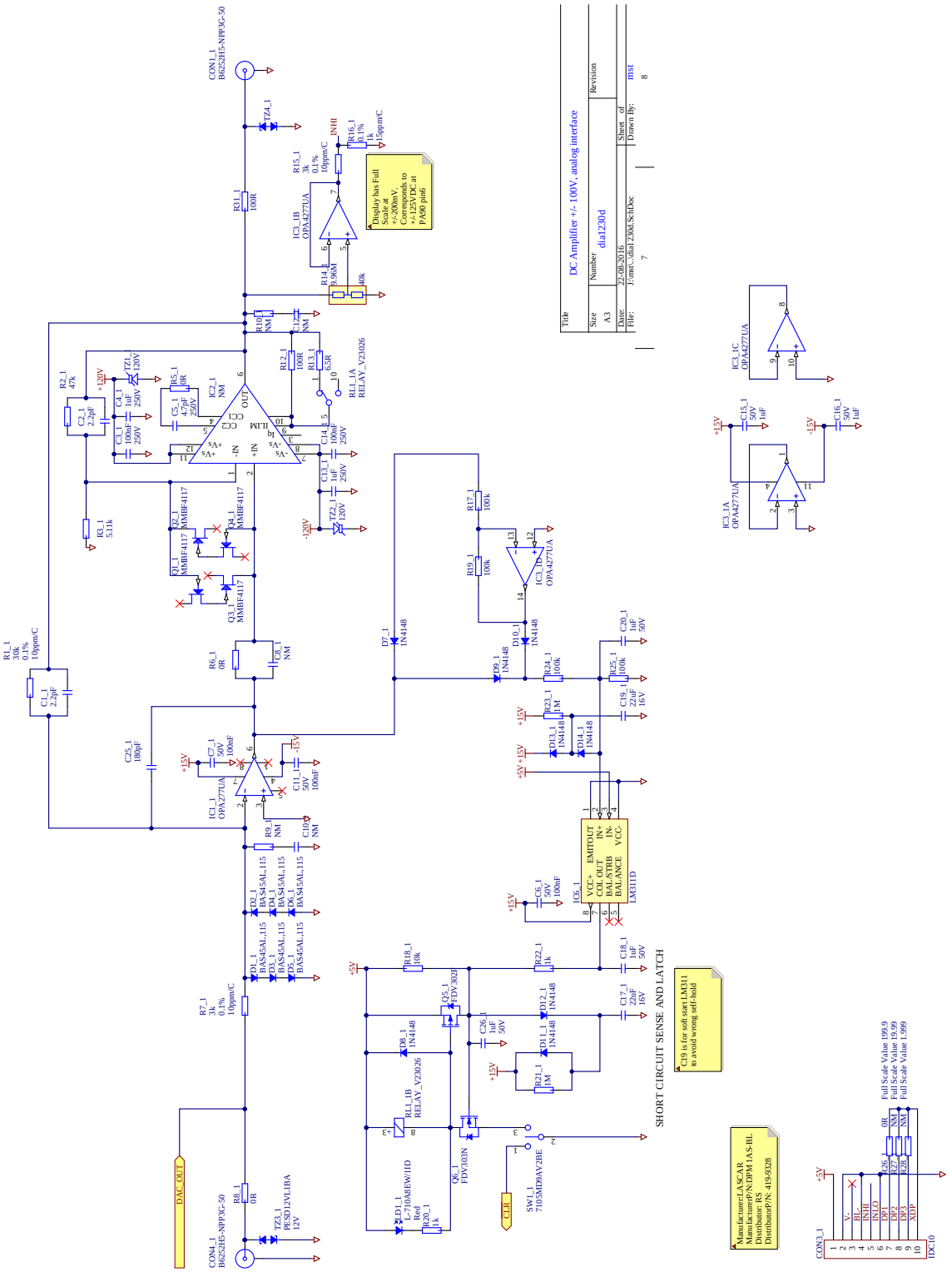


Figure D.5: Schematic of the etherDAC 2.1 amplifier. Designed by Martin Stougaard.

# Bibliography


[1] E. Schrödinger. Are there quantum jumps? Part II*. *Br. J. Philos. Sci.*, III(11), 233 (1952). URL http://dx.doi.org/10.1093/bjps/III.11.233.

[2] W. Paul. Electromagnetic Traps for Charged and Neutral Particles (Nobel Lecture). *Angew. Chem. Int. Ed. Engl.*, 29(7), 739 (1990). URL http://dx.doi.org/10.1002/anie.199007391.

[3] Hans G. Dehmelt - Biographical. URL https://www.nobelprize.org/nobel_prizes/physics/laureates/1989/dehmelt-bio.html.

[4] The Nobel Prize in Physics 1989. URL http://www.nobelprize.org/nobel_prizes/physics/laureates/1989/.

[5] T. W. Hänsch and A. L. Schawlow. Cooling of gases by laser radiation. *Optics Communications*, 13(1), 68 (1975). URL http://dx.doi.org/10.1016/0030-4018(75)90159-5.

[6] W. Neuhauser, M. Hohenstatt, P. E. Toschek, and H. Dehmelt. Localized visible $Ba^+$ mono-ion oscillator. *Phys. Rev. A*, 22(3), 1137 (1980). URL http://dx.doi.org/10.1103/PhysRevA.22.1137.

[7] W. M. Itano, J. C. Bergquist, and D. J. Wineland. Early observations of macroscopic quantum jumps in single atoms. *International Journal of Mass Spectrometry*, 377, 403 (2015). URL http://dx.doi.org/10.1016/j.ijms.2014.07.005.

[8] W. Nagourney, J. Sandberg, and H. Dehmelt. Shelved optical electron amplifier: Observation of quantum jumps. *Phys. Rev. Lett.*, 56(26), 2797 (1986). URL http://dx.doi.org/10.1103/PhysRevLett.56.2797.

[9] J. C. Bergquist, R. G. Hulet, W. M. Itano, and D. J. Wineland. Observation of Quantum Jumps in a Single Atom. *Phys. Rev. Lett.*, 57(14), 1699 (1986). URL http://dx.doi.org/10.1103/PhysRevLett.57.1699.

[10] T. Sauter, W. Neuhauser, R. Blatt, and P. E. Toschek. Observation of Quantum Jumps. *Phys. Rev. Lett.*, 57(14), 1696 (1986). URL http://dx.doi.org/10.1103/PhysRevLett.57.1696.

[11] The Nobel Prize in Physics 2012. URL https://www.nobelprize.org/nobel_prizes/physics/laureates/2012/.

[12] N. Tamura. Shonisaurus popularis (2007). URL https://commons.wikimedia.org/wiki/File:Shonisaurus_BW_2.jpg.

[13] H. Dehmelt. Proposed $10^{14}\delta\nu/\nu$ laser fluorescence spectroscopy on Tl+ mono-ion oscillator II (spontaneous quantum jumps). *Bull. Am. Phys. Soc.*, 20, 637 (1975).

[14] H. G. Dehmelt. Monoion oscillator as potential ultimate laser frequency standard. *IEEE Transactions on Instrumentation and Measurement*, IM-31(2), 83 (1982). URL http://dx.doi.org/10.1109/TIM.1982.6312526.

[15] S. A. Diddams, T. Udem, J. C. Bergquist, E. A. Curtis, R. E. Drullinger, L. Hollberg, W. M. Itano, W. D. Lee, C. W. Oates, K. R. Vogel, and D. J. Wineland. An Optical Clock Based on a Single Trapped $^{199}Hg^+$ Ion. *Science*, 293(5531), 825 (2001). URL http://dx.doi.org/10.1126/science.1061171.

[16] C. W. Chou, D. B. Hume, J. C. J. Koelemeij, D. J. Wineland, and T. Rosenband. Frequency Comparison of Two High-Accuracy $Al^+$ Optical Clocks. *Phys. Rev. Lett.*, 104(7), 070802 (2010). URL http://dx.doi.org/10.1103/PhysRevLett.104.070802.

[17] N. Huntemann, C. Sanner, B. Lipphardt, C. Tamm, and E. Peik. Single-Ion Atomic Clock with $3 \times 10^{-18}$ Systematic Uncertainty. *Phys. Rev. Lett.*, 116(6), 063001 (2016). URL http://dx.doi.org/10.1103/PhysRevLett.116.063001.

[18] F. Diedrich, J. C. Bergquist, W. M. Itano, and D. J. Wineland. Laser Cooling to the Zero-Point Energy of Motion. *Phys. Rev. Lett.*, 62(4), 403 (1989). URL http://dx.doi.org/10.1103/PhysRevLett.62.403.

[19] J.-S. Chen, S. M. Brewer, C. W. Chou, D. J. Wineland, D. R. Leibrandt, and D. B. Hume. Sympathetic Ground State Cooling and Time-Dilation Shifts in an $^{27}Al^+$ Optical Clock. *Phys. Rev. Lett.*, 118(5), 053002 (2017). URL http://dx.doi.org/10.1103/PhysRevLett.118.053002.

[20] J. H. V. Nguyen, C. R. Viteri, E. G. Hohenstein, C. D. Sherrill, K. R. Brown, and B. Odom. Challenges of laser-cooling molecular ions. *New J. Phys.*, 13(6), 063023 (2011). URL http://dx.doi.org/10.1088/1367-2630/13/6/063023.

[21] D. J. Larson, J. C. Bergquist, J. J. Bollinger, W. M. Itano, and D. J. Wineland. Sympathetic cooling of trapped ions: A laser-cooled two-species nonneutral ion plasma. *Phys. Rev. Lett.*, 57(1), 70 (1986). URL http://dx.doi.org/10.1103/PhysRevLett.57.70.

[22] T. Baba and I. Waki. Cooling and Mass-Analysis of Molecules Using Laser-Cooled Atoms. *Jpn. J. Appl. Phys.*, 35(9A), L1134 (1996). URL http://dx.doi.org/10.1143/JJAP.35.L1134.

[23] K. Mølhave and M. Drewsen. Formation of translationally cold $MgH^+$ and $MgD^+$ molecules in an ion trap. *Phys. Rev. A*, 62(1), 011401 (2000). URL http://dx.doi.org/10.1103/PhysRevA.62.011401.

[24] J. Shen, A. Borodin, M. Hansen, and S. Schiller. Observation of a rotational transition of trapped and sympathetically cooled molecular ions. *Phys. Rev. A*, 85(3), 032519 (2012). URL http://dx.doi.org/10.1103/PhysRevA.85.032519.

[25] J. Biesheuvel, J.-P. Karr, L. Hilico, K. S. E. Eikema, W. Ubachs, and J. C. J. Koelemeij. Probing QED and fundamental constants through laser spectroscopy of vibrational transitions in $HD^+$. *Nature Communications*, 7, ncomms10385 (2016). URL http://dx.doi.org/10.1038/ncomms10385.

[26] S. Schiller and V. Korobov. Tests of time independence of the electron and nuclear masses with ultracold molecules. *Phys. Rev. A*, 71(3), 032505 (2005). URL http://dx.doi.org/10.1103/PhysRevA.71.032505.

[27] E. R. Meyer, J. L. Bohn, and M. P. Deskevich. Candidate molecular ions for an electron electric dipole moment experiment. *Phys. Rev. A*, 73(6), 062108 (2006). URL http://dx.doi.org/10.1103/PhysRevA.73.062108.

[28] S. Willitsch. Coulomb-crystallised molecular ions in traps: Methods, applications, prospects. *International Reviews in Physical Chemistry*, 31(2), 175 (2012). URL http://dx.doi.org/10.1080/0144235X.2012.667221.

[29] S. Willitsch, M. T. Bell, A. D. Gingell, and T. P. Softley. Chemical applications of laser- and sympathetically-cooled ions in ion traps. *Phys. Chem. Chem. Phys.*, 10(48), 7200 (2008). URL http://dx.doi.org/10.1039/B813408C.

[30] D. Gerlich and M. Smith. Laboratory astrochemistry: Studying molecules under inter- and circumstellar conditions. *Phys. Scr.*, 73(1), C25 (2006). URL http://dx.doi.org/10.1088/0031-8949/73/1/N05.

[31] S. Canuto, M. A. Castro, and K. Sinha. Theoretical determination of the spectroscopic constants of $CaH^+$. *Phys. Rev. A*, 48(3), 2461 (1993). URL http://dx.doi.org/10.1103/PhysRevA.48.2461.

[32] D. I. Schuster, L. S. Bishop, I. L. Chuang, D. DeMille, and R. J. Schoelkopf. Cavity QED in a molecular ion trap. *Phys. Rev. A*, 83(1), 012311 (2011). URL http://dx.doi.org/10.1103/PhysRevA.83.012311.

[33] J. Mur-Petit, J. J. García-Ripoll, J. Pérez-Ríos, J. Campos-Martínez, M. I. Hernández, and S. Willitsch. Temperature-independent quantum logic for molecular spectroscopy. *Phys. Rev. A*, 85(2), 022308 (2012). URL http://dx.doi.org/10.1103/PhysRevA.85.022308.

[34] M. Shi, P. F. Herskind, M. Drewsen, and I. L. Chuang. Microwave quantum logic spectroscopy and control of molecular ions. *New J. Phys.*, 15(11), 113019 (2013). URL http://dx.doi.org/10.1088/1367-2630/15/11/113019.

[35] J. Mur-Petit, J. Pérez-Ríos, J. Campos-Martínez, M. I. Hernández, S. Willitsch, and J. J. García-Ripoll. Toward a Molecular Ion Qubit. In *Architecture and Design of Molecule Logic Gates and Atom Circuits*, Advances in Atom and Single Molecule Machines, pp. 267–277. Springer, Berlin, Heidelberg (2013). URL http://dx.doi.org/10.1007/978-3-642-33137-4_20.

[36] J.-P. Karr, S. Patra, J. C. J. Koelemeij, J. Heinrich, N. Sillitoe, Albane Douillet, and L. Hilico. Hydrogen molecular ions: New schemes for metrology and fundamental physics tests. *J. Phys.: Conf. Ser.*, 723(1), 012048 (2016). URL http://dx.doi.org/10.1088/1742-6596/723/1/012048.

[37] K. Højbjerre, A. K. Hansen, P. S. Skyt, P. F. Staanum, and M. Drewsen. Rotational state resolved photodissociation spectroscopy of translationally and vibrationally cold MgH+ ions: Toward rotational cooling of molecular ions. *New J. Phys.*, 11(5), 055026 (2009). URL http://dx.doi.org/10.1088/1367-2630/11/5/055026.

[38] K. Højbjerre, D. Offenberg, C. Z. Bisgaard, H. Stapelfeldt, P. F. Staanum, A. Mortensen, and M. Drewsen. Consecutive photodissociation of a single complex molecular ion. *Phys. Rev. A*, 77(3), 030702 (2008). URL http://dx.doi.org/10.1103/PhysRevA.77.030702.

[39] K. A. E. Meyer, L. L. Pollum, L. S. Petralia, A. Tauschinsky, C. J. Rennick, T. P. Softley, and B. R. Heazlewood. Ejection of Coulomb Crystals from a Linear Paul Ion Trap for Ion–Molecule Reaction Studies. *J. Phys. Chem. A*, 119(50), 12449 (2015). URL http://dx.doi.org/10.1021/acs.jpca.5b07919.

[40] P. F. Staanum, K. Højbjerre, P. S. Skyt, A. K. Hansen, and M. Drewsen. Rotational laser cooling of vibrationally and translationally cold molecular ions. *Nat. Phys.*, 6(4), 271 (2010). URL http://dx.doi.org/10.1038/nphys1604.

[41] W. G. Rellergert, S. T. Sullivan, S. J. Schowalter, S. Kotochigova, K. Chen, and E. R. Hudson. Evidence for sympathetic vibrational cooling of translationally cold molecules. *Nature*, 495(7442), 490 (2013). URL http://dx.doi.org/10.1038/nature11937.

[42] C.-Y. Lien, C. M. Seck, Y.-W. Lin, J. H. V. Nguyen, D. A. Tabor, and B. C. Odom. Broadband optical cooling of molecular rotors from room temperature to the ground state. *Nature Communications*, 5, ncomms5783 (2014). URL http://dx.doi.org/10.1038/ncomms5783.

[43] A. K. Hansen, O. O. Versolato, Ł. Kłosowski, S. B. Kristensen, A. Gingell, M. Schwarz, A. Windberger, J. Ullrich, J. R. C. López-Urrutia, and M. Drewsen. Efficient rotational cooling of Coulomb-crystallized molecular ions by a helium buffer gas. *Nature*, 508(7494), 76 (2014). URL http://dx.doi.org/10.1038/nature12996.

[44] G. Poulsen. Sideband Cooling of Atomic and Molecular Ions. Phd thesis, Aarhus University, Aarhus, Denmark (2011).

[45] R. Rugango, J. E. Goeders, T. H. Dixon, J. M. Gray, N. B. Khanyile, G. Shu, R. J. Clark, and K. R. Brown. Sympathetic cooling of molecular ion motion to the ground state. *New J. Phys.*, 17(3), 035009 (2015). URL http://dx.doi.org/10.1088/1367-2630/17/3/035009.

[46] Y. Wan, F. Gebert, F. Wolf, and P. O. Schmidt. Efficient sympathetic motional-ground-state cooling of a molecular ion. *Phys. Rev. A*, 91(4), 043425 (2015). URL http://dx.doi.org/10.1103/PhysRevA.91.043425.

[47] C. W. Chou, C. Kurz, D. B. Hume, P. N. Plessow, D. R. Leibrandt, and D. Leibfried. Preparation and coherent manipulation of pure quantum states of a single molecular ion. *Nature*, 545(7653), 203 (2017). URL http://dx.doi.org/10.1038/nature22338.

[48] P. O. Schmidt, T. Rosenband, C. Langer, W. M. Itano, J. C. Bergquist, and D. J. Wineland. Spectroscopy Using Quantum Logic. *Science*, 309(5735), 749 (2005). URL http://dx.doi.org/10.1126/science.1114375.

[49] F. Wolf, Y. Wan, J. C. Heip, F. Gebert, C. Shi, and P. O. Schmidt. Non-destructive state detection for quantum logic spectroscopy of molecular ions. *Nature*, 530(7591), 457 (2016). URL http://dx.doi.org/10.1038/nature16513.

[50] I. S. Vogelius, L. B. Madsen, and M. Drewsen. Probabilistic state preparation of a single molecular ion by projection measurement. *J. Phys. B: At. Mol. Opt. Phys.*, 39(19), S1259 (2006). URL http://dx.doi.org/10.1088/0953-4075/39/19/S31.

[51] P. O. Schmidt, T. Rosenband, J. C. J. Koelemeij, D. B. Hume, W. M. Itano, J. C. Bergquist, and D. J. Wineland. Spectroscopy of atomic and molecular ions using quantum logic. In *Non-Neutral Plasma Physics VI*, volume 862, pp. 305–312 (2006). URL http://dx.doi.org/10.1063/1.2387937.

[52] G. Poulsen and M. Drewsen. Adiabatic cooling of a single trapped ion. *arXiv:1210.4309 [physics, physics:quant-ph]* (2012). URL http://arxiv.org/abs/1210.4309.

[53] R. Grimm, M. Weidemüller, and Y. B. Ovchinnikov. Optical Dipole Traps for Neutral Atoms. *Advances In Atomic, Molecular, and Optical Physics*, 42, 95 (2000). URL http://dx.doi.org/10.1016/S1049-250X(08)60186-X.

[54] S. Earnshaw. On the nature of the molecular forces which regulate the constitution of the luminiferous ether. *Trans. Camb. Phil. Soc.*, 7, 97 (1842).

[55] F. M. Penning. Die Glimmentladung bei niedrigem Druck zwischen koaxialen Zylindern in einem axialen Magnetfeld. *Physica*, 3(9), 873 (1936). URL http://dx.doi.org/10.1016/S0031-8914(36)80313-9.

[56] W. Paul and H. Steinwedel. Notizen: Ein neues Massenspektrometer ohne Magnetfeld. *Zeitschrift für Naturforschung A*, 8(7), 448 (1953). URL http://dx.doi.org/10.1515/zna-1953-0710.

[57] L. S. Brown and G. Gabrielse. Geonium theory: Physics of a single electron or ion in a Penning trap. *Rev. Mod. Phys.*, 58(1), 233 (1986). URL http://dx.doi.org/10.1103/RevModPhys.58.233.

[58] J. D. Prestage, G. J. Dick, and L. Maleki. New ion trap for frequency standard applications. *Journal of Applied Physics*, 66, 1013 (1989). URL http://dx.doi.org/10.1063/1.343486.

[59] R. J. Champeau, A. Crubellier, D. Marescaux, D. Pavolini, and J. Pinard. Photodetachment of trapped negative gold ions: I. Experimental methods and near-threshold cross sections. *J. Phys. B: At. Mol. Opt. Phys.*, 31(2), 249 (1998). URL http://dx.doi.org/10.1088/0953-4075/31/2/008.

[60] J. P. Schermann and F. G. Major. Characteristics of electron-free plasma confinement in an rf quadrupole field. *Appl. Phys.*, 16(3), 225 (1978). URL http://dx.doi.org/10.1007/BF00885116.

[61] D. J. Larson, C. J. Edge, R. E. Elmquist, N. B. Mansour, and R. Trainham. Physics with Negative Ions in Ion Traps. *Phys. Scr.*, 1988(T22), 183 (1988). URL http://dx.doi.org/10.1088/0031-8949/1988/T22/028.

[62] S. Trippel, J. Mikosch, R. Berhane, R. Otto, M. Weidemüller, and R. Wester. Photodetachment of Cold $OH^-$ in a Multipole Ion Trap. *Phys. Rev. Lett.*, 97(19), 193003 (2006). URL http://dx.doi.org/10.1103/PhysRevLett.97.193003.

[63] W. Walter, C. D. Gibson, N. J. Matyas, D. C. Crocker, A. Dungan, K. R. Matola, B. and J. Rohlén. Candidate for Laser Cooling of a Negative Ion: Observations of Bound-Bound Transitions in $La^-$. *Phys. Rev. Lett.*, 113(6), 063001 (2014). URL http://dx.doi.org/10.1103/PhysRevLett.113.063001.

[64] P. Yzombard, M. Hamamda, S. Gerber, M. Doser, and D. Comparat. Laser Cooling of Molecular Anions. *Phys. Rev. Lett.*, 114(21), 213001 (2015). URL http://dx.doi.org/10.1103/PhysRevLett.114.213001.

[65] M. G. Raizen, J. M. Gilligan, J. C. Bergquist, W. M. Itano, and D. J. Wineland. Ionic crystals in a linear Paul trap. *Phys. Rev. A*, 45(9), 6493 (1992). URL http://dx.doi.org/10.1103/PhysRevA.45.6493.

[66] M. Drewsen and A. Brøner. Harmonic linear Paul trap: Stability diagram and effective potentials. *Phys. Rev. A*, 62(4), 045401 (2000). URL http://dx.doi.org/10.1103/PhysRevA.62.045401.

[67] H. G. Dehmelt. Radiofrequency Spectroscopy of Stored Ions I: Storage. In D. R. Bates and I. Estermann, eds., *Advances in Atomic and Molecular Physics*, volume 3, pp. 53–72. Academic Press (1968). URL http://dx.doi.org/10.1016/S0065-2199(08)60170-0.

[68] H. H. Andersen. Cooling and manipulating ions in traps with integrated optical cavities. Phd thesis, Aarhus University (2015).

[69] G. Morigi and H. Walther. Two-species Coulomb chains for quantum information. *Eur. Phys. J. D*, 13(2), 261 (2001). URL http://dx.doi.org/10.1007/s100530170275.

[70] D. F. V. James. Quantum dynamics of cold trapped ions with application to quantum computation. *Appl. Phys. B.*, 66(2), 181 (1998). URL http://dx.doi.org/10.1007/s003400050373.

[71] J. B. Wübbena, S. Amairi, O. Mandel, and P. O. Schmidt. Sympathetic Cooling of Mixed Species Two-Ion Crystals for Precision Spectroscopy. *Physical Review A*, 85(4) (2012). URL http://dx.doi.org/10.1103/PhysRevA.85.043412.

[72] C. J. Foot. *Atomic Physics*. Oxford University Press, Oxford ; New York, 1 edition (2005).

[73] D. Leibfried, R. Blatt, C. Monroe, and D. Wineland. Quantum dynamics of single trapped ions. *Rev. Mod. Phys.*, 75(1), 281 (2003). URL http://dx.doi.org/10.1103/RevModPhys.75.281.

[74] C. Roos. Controlling the quantum state of trapped ions. Phd thesis, University of Innsbruck, Innsbruck, Austria (2000).

[75] R. Loudon. *The Quantum Theory of Light*. OUP Oxford (2000).

[76] M. O. Scully and M. S. Zubairy. *Quantum Optics*. Cambridge University Press (1997).

[77] K. E. Cahill and R. J. Glauber. Ordered Expansions in Boson Amplitude Operators. *Phys. Rev.*, 177(5), 1857 (1969). URL http://dx.doi.org/10.1103/PhysRev.177.1857.

[78] D. J. Wineland and W. M. Itano. Laser cooling of atoms. *Phys. Rev. A*, 20(4), 1521 (1979). URL http://dx.doi.org/10.1103/PhysRevA.20.1521.

[79] J. Alonso, F. M. Leupold, Z. U. Solèr, M. Fadel, M. Marinelli, B. C. Keitch, V. Negnevitsky, and J. P. Home. Generation of large coherent states by bang–bang control of a trapped-ion oscillator. *Nature Communications*, 7, 11243 (2016). URL http://dx.doi.org/10.1038/ncomms11243.

[80] D. J. Wineland, C. Monroe, W. M. Itano, B. E. King, and D. M. Meekhof. Experimental Issues in Coherent Quantum-State Manipulation of Trapped Atomic Ions. *Journal of Research of the National Institute of Standards and Technology*, 103(3), 259 (May-June 1998). URL http://tf.nist.gov/general/pdf/1275.pdf.

[81] S. Webster. Raman Sideband Cooling and Coherent Manipulation of Trapped Ions. Phd thesis, Oxford University (2005).

[82] J. P. Home. Entanglement of Two Trapped-Ion Spin Qubits. Phd thesis, Oxford University (2006). URL https://www2.physics.ox.ac.uk/sites/default/files/JHomethesis.pdf.

[83] D. J. Wineland, R. E. Drullinger, and F. L. Walls. Radiation-Pressure Cooling of Bound Resonant Absorbers. *Phys. Rev. Lett.*, 40(25), 1639 (1978). URL http://dx.doi.org/10.1103/PhysRevLett.40.1639.

[84] W. Neuhauser, M. Hohenstatt, P. Toschek, and H. Dehmelt. Optical-Sideband Cooling of Visible Atom Cloud Confined in Parabolic Well. *Phys. Rev. Lett.*, 41(4), 233 (1978). URL http://dx.doi.org/10.1103/PhysRevLett.41.233.

[85] S. Stenholm. The semiclassical theory of laser cooling. *Rev. Mod. Phys.*, 58(3), 699 (1986). URL http://dx.doi.org/10.1103/RevModPhys.58.699.

[86] J. Javanainen and S. Stenholm. Broad band resonant light pressure. *Appl. Phys.*, 21(1), 35 (1980). URL http://dx.doi.org/10.1007/BF00886481.

[87] W. M. Itano and D. J. Wineland. Laser cooling of ions stored in harmonic and Penning traps. *Phys. Rev. A*, 25(1), 35 (1982). URL http://dx.doi.org/10.1103/PhysRevA.25.35.

[88] J. I. Cirac, L. J. Garay, R. Blatt, A. S. Parkins, and P. Zoller. Laser cooling of trapped ions: The influence of micromotion. *Phys. Rev. A*, 49(1), 421 (1994). URL http://dx.doi.org/10.1103/PhysRevA.49.421.

[89] D. J. Berkeland, J. D. Miller, J. C. Bergquist, W. M. Itano, and D. J. Wineland. Minimization of ion micromotion in a Paul trap. *Journal of Applied Physics*, 83(10), 5025 (1998). URL http://dx.doi.org/10.1063/1.367318.

[90] D. Wineland and H. Dehmelt. Proposed $10^{14}\delta\nu/\nu$ laser fluorescence spectroscopy on Tl+ mono-ion oscillator III (sideband cooling). *Bull. Am. Phys. Soc.*, 20, 637 (1975).

[91] H. Sawamura, K. Kanda, R. Yamazaki, K. Toyoda, and S. Urabe. Optimum parameters for sideband cooling of a $^{40}Ca^{+}$ ion. *Appl. Phys. B*, 93(2-3), 381 (2008). URL http://dx.doi.org/10.1007/s00340-008-3162-8.

[92] D. J. Wineland, W. M. Itano, J. C. Bergquist, and R. G. Hulet. Laser-cooling limits and single-ion spectroscopy. *Phys. Rev. A*, 36(5), 2220 (1987). URL http://dx.doi.org/10.1103/PhysRevA.36.2220.

[93] M. Brownnutt, M. Kumph, P. Rabl, and R. Blatt. Ion-trap measurements of electric-field noise near surfaces. *Rev. Mod. Phys.*, 87(4), 1419 (2015). URL http://dx.doi.org/10.1103/RevModPhys.87.1419.

[94] Q. A. Turchette, Kielpinski, B. E. King, D. Leibfried, D. M. Meekhof, C. J. Myatt, M. A. Rowe, C. A. Sackett, C. S. Wood, W. M. Itano, C. Monroe, and D. J. Wineland. Heating of trapped ions from the quantum ground state. *Phys. Rev. A*, 61(6), 063418 (2000). URL http://dx.doi.org/10.1103/PhysRevA.61.063418.

[95] T. A. Savard, K. M. O'Hara, and J. E. Thomas. Laser-noise-induced heating in far-off resonance optical traps. *Phys. Rev. A*, 56(2), R1095 (1997). URL http://dx.doi.org/10.1103/PhysRevA.56.R1095.

[96] C. Henkel and M. Wilkens. Heating of trapped atoms near thermal surfaces. *EPL*, 47(4), 414 (1999). URL http://dx.doi.org/10.1209/epl/i1999-00404-8.

[97] D. Kielpinski, B. E. King, C. J. Myatt, C. A. Sackett, Q. A. Turchette, W. M. Itano, C. Monroe, D. J. Wineland, and W. H. Zurek. Sympathetic cooling of trapped ions for quantum logic. *Phys. Rev. A*, 61(3), 032310 (2000). URL http://dx.doi.org/10.1103/PhysRevA.61.032310.

[98] M. Hettrich, T. Ruster, H. Kaufmann, C. F. Roos, C. T. Schmiegelow, F. Schmidt-Kaler, and U. G. Poschinger. Measurement of Dipole Matrix Elements with a Single Trapped Ion. *Phys. Rev. Lett.*, 115(14), 143003 (2015). URL http://dx.doi.org/10.1103/PhysRevLett.115.143003.

[99] M. Ramm, T. Pruttivarasin, M. Kokish, I. Talukdar, and H. Häffner. Precision measurement method for branching fractions of excited $P_{1/2}$ states applied to $^{40}Ca^{+}$. *Phys. Rev. Lett.*, 111(2), 023004 (2013). URL http://dx.doi.org/10.1103/PhysRevLett.111.023004.

[100] D. J. Berkeland and M. G. Boshier. Destabilization of dark states and optical spectroscopy in Zeeman-degenerate atomic systems. *Phys. Rev. A*, 65(3), 033413 (2002). URL http://dx.doi.org/10.1103/PhysRevA.65.033413.

[101] R. Hughes, D. James, J. Gomez, M. Gulley, M. Holzscheiter, P. Kwiat, S. Lamoreaux, C. Peterson, V. Sandberg, M. Schauer, C. Simmons, C. Thorburn, D. Tupa, P. Wang, and A. White. The Los Alamos Trapped Ion Quantum Computer Experiment. *Fortschr. Phys.*, 46(4-5), 329 (1998). URL http://dx.doi.org/10.1002/(SICI)1521-3978(199806)46:4/5<329::AID-PROP329>3.0.CO;2-X.

[102] P. Staanum. Quantum Optics with Trapped Calcium Ions. Phd thesis, Aarhus University, Aarhus, Denmark (2004).

[103] R. Gerritsma, G. Kirchmair, F. Zähringer, J. Benhelm, R. Blatt, and C. F. Roos. Precision measurement of the branching fractions of the $4p\ ^2P_{3/2}$ decay of Ca II. *Eur. Phys. J. D*, 50(1), 13 (2008). URL http://dx.doi.org/10.1140/epjd/e2008-00196-9.

[104] I. Marzoli, J. I. Cirac, R. Blatt, and P. Zoller. Laser cooling of trapped three-level ions: Designing two-level systems for sideband cooling. *Phys. Rev. A*, 49(4), 2771 (1994). URL http://dx.doi.org/10.1103/PhysRevA.49.2771.

[105] W. Balfour. Rotational Analysis of the $A^1\Sigma^+ \rightarrow X^1\Sigma^+$ and $B^1\Pi \rightarrow X^1\Sigma^+$ Systems of $^{24}MgH^+$, $^{25}MgH^+$, and $^{26}MgH^+$. *Can. J. Phys.*, 50, 1082 (1972).

[106] F. Jensen. *Personal Communication*. Department of Chemistry, Aarhus University.

[107] A. Bertelsen, S. Jørgensen, and M. Drewsen. The rotational temperature of polar molecular ions in Coulomb crystals. *J. Phys. B: At. Mol. Opt. Phys.*, 39(5), L83 (2006). URL http://dx.doi.org/10.1088/0953-4075/39/5/L02.

[108] A. K. Hansen. Cold Molecular Ions: Rotational State Preparation and Single Ion Reaction Experiments. Phd thesis, Aarhus University (2012).

[109] D. Gerlich. Ion-neutral collisions in a 22-pole trap at very low energies. *Phys. Scr.*, 1995(T59), 256 (1995). URL http://dx.doi.org/10.1088/0031-8949/1995/T59/035.

[110] B. Höltkemeier, P. Weckesser, H. López-Carrera, and M. Weidemüller. Buffer-Gas Cooling of a Single Ion in a Multipole Radio Frequency Trap Beyond the Critical Mass Ratio. *Phys. Rev. Lett.*, 116(23), 233003 (2016). URL http://dx.doi.org/10.1103/PhysRevLett.116.233003.

[111] T. Schneider, B. Roth, H. Duncker, I. Ernsting, and S. Schiller. All-optical preparation of molecular ions in the rovibrational ground state. *Nat. Phys.*, 6(4), 275 (2010). URL http://dx.doi.org/10.1038/nphys1605.

[112] I. S. Vogelius, L. B. Madsen, and M. Drewsen. Blackbody-Radiation-Assisted Laser Cooling of Molecular Ions. *Phys. Rev. Lett.*, 89(17), 173003 (2002). URL http://dx.doi.org/10.1103/PhysRevLett.89.173003.

[113] A. K. Hansen, M. A. Sørensen, P. F. Staanum, and M. Drewsen. Single-Ion Recycling Reactions. *Angew. Chem. Int. Ed.*, 51(32), 7960 (2012). URL http://dx.doi.org/10.1002/anie.201203550.

[114] D. Hayes, D. N. Matsukevich, P. Maunz, D. Hucul, Q. Quraishi, S. Olmschenk, W. Campbell, J. Mizrahi, C. Senko, and C. Monroe. Entanglement of Atomic Qubits Using an Optical Frequency Comb. *Phys. Rev. Lett.*, 104(14), 140501 (2010). URL http://dx.doi.org/10.1103/PhysRevLett.104.140501.

[115] S. Ding and D. N. Matsukevich. Quantum logic for the control and manipulation of molecular ions using a frequency comb. *New J. Phys.*, 14(2), 023028 (2012). URL http://dx.doi.org/10.1088/1367-2630/14/2/023028.

[116] R. E. Drullinger, D. J. Wineland, and J. C. Bergquist. High-resolution optical spectra of laser cooled ions. *Appl. Phys.*, 22(4), 365 (1980). URL http://dx.doi.org/10.1007/BF00901058.

[117] D. J. Wineland, J. C. Bergquist, W. M. Itano, J. J. Bollinger, and C. H. Manney. Atomic-Ion Coulomb Clusters in an Ion Trap. *Phys. Rev. Lett.*, 59(26), 2935 (1987). URL http://dx.doi.org/10.1103/PhysRevLett.59.2935.

[118] P. Bowe, L. Hornekær, C. Brodersen, M. Drewsen, J. S. Hangst, and J. P. Schiffer. Sympathetic Crystallization of Trapped Ions. *Phys. Rev. Lett.*, 82(10), 2071 (1999). URL http://dx.doi.org/10.1103/PhysRevLett.82.2071.

[119] H. Rohde, S. T. Gulde, C. F. Roos, P. A. Barton, D. Leibfried, J. Eschner, F. Schmidt-Kaler, and R. Blatt. Sympathetic ground-state cooling and coherent manipulation with two-ion crystals. *J. Opt. B: Quantum Semiclass. Opt.*, 3(1), S34 (2001). URL http://dx.doi.org/10.1088/1464-4266/3/1/357.

[120] M. D. Barrett, B. DeMarco, T. Schaetz, V. Meyer, D. Leibfried, J. Britton, J. Chiaverini, W. M. Itano, B. Jelenković, J. D. Jost, C. Langer, T. Rosenband, and D. J. Wineland. Sympathetic cooling of $^{9}Be^{+}$ and $^{24}Mg^{+}$ for quantum logic. *Phys. Rev. A*, 68(4), 042302 (2003). URL http://dx.doi.org/10.1103/PhysRevA.68.042302.

[121] A. Bertelsen, I. S. Vogelius, S. Jørgensen, R. Kosloff, and M. Drewsen. Photo-dissociation of Cold MgH+ ions. *Eur. Phys. J. D*, 31(2), 403 (2004). URL http://dx.doi.org/10.1140/epjd/e2004-00152-9.

[122] K. Højbjerre. Experiments with cold trapped molecular ions. Phd thesis, Aarhus University, Aarhus, Denmark (2009).

[123] Y. Wan, F. Gebert, J. B. Wübbena, N. Scharnhorst, S. Amairi, I. D. Leroux, B. Hemmerling, N. Lörch, K. Hammerer, and P. O. Schmidt. Precision spectroscopy by photon-recoil signal amplification. *Nature Communications*, 5, ncomms4096 (2014). URL http://dx.doi.org/10.1038/ncomms4096.

[124] N. B. Khanyile. Vibrational spectroscopy of sympathetically laser-cooled CaH+. Ph.D. thesis, Georgia Tech (2015). URL https://smartech.gatech.edu/handle/1853/55492.

[125] C. R. Clark, J. E. Goeders, Y. K. Dodia, C. R. Viteri, and K. R. Brown. Detection of single-ion spectra by Coulomb-crystal heating. *Phys. Rev. A*, 81(4), 043428 (2010). URL http://dx.doi.org/10.1103/PhysRevA.81.043428.

[126] Y. Guberman. Adiabatic Cooling of Ion Chains and Realizing the Frenkel-Kontorova Model with Ions. M.sc. thesis, The Hebrew University, Jerusalem (2014).

[127] N. Kjærgaard. Methods in Laser Cooling of Ions in Storage Rings and Traps. Phd thesis, Aarhus University, Aarhus, Denmark (2001).

[128] D. R. Denison. Operating Parameters of a Quadrupole in a Grounded Cylindrical Housing. *Journal of Vacuum Science and Technology*, 8(1), 266 (1971). URL http://dx.doi.org/10.1116/1.1316304.

[129] Toellner. Datasheet TOE 8840 to 8850. Technical report. URL http://www.toellner.de/html/img/pool/EN_8840_50.pdf.

[130] A. Mortensen. Aspects of Ion Coulomb Crystal based Quantum Memory for Light. Phd thesis, Aarhus University (2005).

[131] D. R. Lide. *CRC Handbook of Chemistry and Physics, 84th Edition*. CRC Press (2003).

[132] D. N. Madsen, S. Balslev, M. Drewsen, N. Kjærgaard, Z. Videsen, and J. W. Thomsen. Measurements on photo-ionization of $3s3p\ ^1P_1$ magnesium atoms. *J. Phys. B: At. Mol. Opt. Phys.*, 33(22), 4981 (2000). URL http://dx.doi.org/10.1088/0953-4075/33/22/302.

[133] N. Kjaergaard, L. Hornekaer, A. M. Thommesen, Z. Videsen, and M. Drewsen. Isotope selective loading of an ion trap using resonance-enhanced two-photon ionization. *Appl Phys B*, 71(2), 207 (2000). URL http://dx.doi.org/10.1007/s003400000296.

[134] A. Mortensen, J. J. T. Lindballe, I. S. Jensen, P. Staanum, D. Voigt, and M. Drewsen. Isotope shifts of the $4s^2\ ^1s_0 \rightarrow 4s5p\ ^1p_1$ transition and hyperfine splitting of the $4s5p\ ^1p_1$ state in calcium. *Phys. Rev. A*, 69(4), 042502 (2004). URL http://dx.doi.org/10.1103/PhysRevA.69.042502.

[135] S. Gulde, D. Rotter, P. Barton, F. Schmidt-Kaler, R. Blatt, and W. Hogervorst. Simple and efficient photo-ionization loading of ions for precision ion-trapping experiments. *Appl Phys B*, 73(8), 861 (2001). URL http://dx.doi.org/10.1007/s003400100749.

[136] D. M. Lucas, A. Ramos, J. P. Home, M. J. McDonnell, S. Nakayama, J.-P. Stacey, S. C. Webster, D. N. Stacey, and A. M. Steane. Isotope-selective photoionization for calcium ion trapping. *Phys. Rev. A*, 69(1), 012711 (2004). URL http://dx.doi.org/10.1103/PhysRevA.69.012711.

[137] U. Tanaka, I. Morita, and S. Urabe. Selective loading and laser cooling of rare calcium isotope 43Ca+. *Appl. Phys. B*, 89(2-3), 195 (2007). URL http://dx.doi.org/10.1007/s00340-007-2784-6.

[138] P. F. Herskind. Cavity Quantum Electrodynamics with Ion Coulomb Crystals. Phd thesis, Aarhus University (2008).

[139] J. B. Andersen. Konstruktion og optimering af mekanisk shutter. Bachelor thesis, Aarhus University, Aarhus, Denmark (2010).

[140] R. W. P. Drever, J. L. Hall, F. V. Kowalski, J. Hough, G. M. Ford, A. J. Munley, and H. Ward. Laser phase and frequency stabilization using an optical resonator. *Appl. Phys. B*, 31(2), 97 (1983). URL http://dx.doi.org/10.1007/BF00702605.

[141] Nobelprize.org. The Nobel Prize in Physics 2005. URL https://www.nobelprize.org/nobel_prizes/physics/laureates/2005/.

[142] T. W. Hänsch. Nobel Lecture: Passion for precision. *Rev. Mod. Phys.*, 78(4), 1297 (2006). URL http://dx.doi.org/10.1103/RevModPhys.78.1297.

[143] MenloSystems. FC1500-250-WG User Manual. Technical report.

[144] A. Kreuter, C. Becher, G. P. T. Lancaster, A. B. Mundt, C. Russo, H. Häffner, C. Roos, W. Hänsel, F. Schmidt-Kaler, R. Blatt, and M. S. Safronova. Experimental and theoretical study of the $3d^2D$–level lifetimes of $^{40}Ca^+$. *Phys. Rev. A*, 71(3), 032504 (2005). URL http://dx.doi.org/10.1103/PhysRevA.71.032504.

[145] T. Talvard, P. G. Westergaard, M. V. DePalatis, N. F. Mortensen, M. Drewsen, B. Gøth, and J. Hald. Enhancement of the performance of a fiber-based frequency comb by referencing to an acetylene-stabilized fiber laser. *Opt. Express, OE*, 25(3), 2259 (2017). URL http://dx.doi.org/10.1364/OE.25.002259.

[146] J. Hald, L. Nielsen, J. C. Petersen, P. Varming, and J. E. Pedersen. Fiber laser optical frequency standard at 1.54 µm. *Opt. Express, OE*, 19(3), 2052 (2011). URL http://dx.doi.org/10.1364/OE.19.002052.

[147] G. Venturini, I. Daniher, R. Crowther, and KOLANICH. Ahkab: An interactive circuit simulator (2015).

[148] LTspice. URL http://www.linear.com/designtools/software/.

[149] R. B. Blakestad, C. Ospelkaus, A. P. VanDevender, J. H. Wesenberg, M. J. Biercuk, D. Leibfried, and D. J. Wineland. Near-ground-state transport of trapped-ion qubits through a multidimensional array. *Phys. Rev. A*, 84(3), 032314 (2011). URL http://dx.doi.org/10.1103/PhysRevA.84.032314.

[150] L. de Clercq. Transport Quantum Logic Gates for Trapped Ions. Phd thesis, ETH Zurich (2015).

[151] C. K. Boggs, A. D. Doak, and F. L. Walls. Measurement of voltage noise in chemical batteries. In *Proceedings of the 1995 IEEE International Frequency Control Symposium (49th Annual Symposium)*, pp. 367–373 (1995). URL http://dx.doi.org/10.1109/FREQ.1995.483923.

[152] Pulse Programmer. URL https://sourceforge.net/projects/pulse-sequencer/.

[153] P. T. T. Pham. A general-purpose pulse sequencer for quantum computing. Thesis, Massachusetts Institute of Technology (2005). URL http://dspace.mit.edu/handle/1721.1/32106.

[154] P. Schindler. Frequency synthesis and pulse shaping for quantum information processing with trapped ions. Diploma thesis, University of Innsbruck (2008).

[155] P. Schindler, M. Harlander, L. Peterson, B. Hemmerling, and T. Holleis. Sequencer2: Sequencer2 python compiler for the PBox used in Innsbruck (2015). URL https://github.com/pschindler/sequencer2.

[156] P. Schindler. Vhdl-ad9910: Vhdl code for the Innsbruck ad9910 dds board (2015). URL https://github.com/pschindler/vhdl-ad9910.

[157] Welcome to the PBox documentation! — Python documentation. URL http://pboxdoc.readthedocs.io/en/latest/index.html.

[158] C. Monroe, D. M. Meekhof, B. E. King, S. R. Jefferts, W. M. Itano, D. J. Wineland, and P. Gould. Resolved-Sideband Raman Cooling of a Bound Atom to the 3D Zero-Point Energy. *Phys. Rev. Lett.*, 75(22), 4011 (1995). URL http://dx.doi.org/10.1103/PhysRevLett.75.4011.

[159] R. G. DeVoe and C. Kurtsiefer. Experimental study of anomalous heating and trap instabilities in a microscopic $^{137}$Ba ion trap. *Phys. Rev. A*, 65(6), 063407 (2002). URL http://dx.doi.org/10.1103/PhysRevA.65.063407.

[160] L. Deslauriers, S. Olmschenk, D. Stick, W. K. Hensinger, J. Sterk, and C. Monroe. Scaling and Suppression of Anomalous Heating in Ion Traps. *Phys. Rev. Lett.*, 97(10), 103007 (2006). URL http://dx.doi.org/10.1103/PhysRevLett.97.103007.

[161] P. Huang, X. Kong, N. Zhao, F. Shi, P. Wang, X. Rong, R.-B. Liu, and J. Du. Observation of an anomalous decoherence effect in a quantum bath at room temperature. *Nature Communications*, 2, ncomms1579 (2011). URL http://dx.doi.org/10.1038/ncomms1579.

[162] R. McConnell, C. Bruzewicz, J. Chiaverini, and J. Sage. Reduction of trapped ion anomalous heating by in situ surface plasma cleaning. *Physical Review A*, 92(2) (2015). URL http://dx.doi.org/10.1103/PhysRevA.92.020302.

[163] M. Harlander. Architecture for a scalable ion-trap quantum computer. Phd thesis, University of Innsbruck (2012). URL http://www.quantumoptics.at/images/publications/dissertation/MH_diss.pdf.

[164] N. Daniilidis, S. Narayanan, S. A. Möller, R. Clark, T. E. Lee, P. J. Leek, A. Wallraff, S. Schulz, F. Schmidt-Kaler, and H Häffner. Fabrication and heating rate study of microscopic surface electrode ion traps. *New J. Phys.*, 13(1), 013032 (2011). URL http://dx.doi.org/10.1088/1367-2630/13/1/013032.

[165] N. Daniilidis, S. Gerber, G. Bolloten, M. Ramm, A. Ransford, E. Ulin-Avila, I. Talukdar, and H. Häffner. Surface noise analysis using a single-ion sensor. *Phys. Rev. B*, 89(24), 245435 (2014). URL http://dx.doi.org/10.1103/PhysRevB.89.245435.

[166] D. T. C. Allcock, T. P. Harty, H. A. Janacek, N. M. Linke, C. J. Ballance, A. M. Steane, D. M. Lucas, R. L. J. Jr, S. D. Habermehl, M. G. Blain, D. Stick, and D. L. Moehring. Heating rate and electrode charging measurements in a scalable, microfabricated, surface-electrode ion trap. *Appl. Phys. B*, 107(4), 913 (2011). URL http://dx.doi.org/10.1007/s00340-011-4788-5.

[167] D. T. C. Allcock, L. Guidoni, T. P. Harty, C. J. Ballance, M. G. Blain, A. M. Steane, and D. M. Lucas. Reduction of heating rate in a microfabricated ion trap by pulsed-laser cleaning. *New J. Phys.*, 13(12), 123023 (2011). URL http://dx.doi.org/10.1088/1367-2630/13/12/123023.

[168] D. A. Hite, Y. Colombe, A. C. Wilson, K. R. Brown, U. Warring, R. Jördens, J. D. Jost, K. S. McKay, D. P. Pappas, D. Leibfried, and D. J. Wineland. 100-Fold Reduction of Electric-Field Noise in an Ion Trap Cleaned with *In Situ* Argon-Ion-Beam Bombardment. *Phys. Rev. Lett.*, 109(10), 103001 (2012). URL http://dx.doi.org/10.1103/PhysRevLett.109.103001.

[169] D. Hite, Y. Colombe, A. Wilson, D. Allcock, D. Leibfried, D. Wineland, and D. Pappas. Surface science for improved ion traps. *MRS Bulletin*, 38(10), 826 (2013). URL http://dx.doi.org/10.1557/mrs.2013.207.

[170] S. A. Schulz, U. Poschinger, F. Ziesel, and F. Schmidt-Kaler. Sideband cooling and coherent dynamics in a microchip multi-segmented ion trap. *New J. Phys.*, 10(4), 045007 (2008). URL http://dx.doi.org/10.1088/1367-2630/10/4/045007.

[171] U. G. Poschinger, G. Huber, F. Ziesel, M. Deiß, M. Hettrich, S. A. Schulz, K. Singer, G. Poulsen, M. Drewsen, R. J. Hendricks, and F. Schmidt-Kaler. Coherent manipulation of a 40Ca+ spin qubit in a micro ion trap. *J. Phys. B: At. Mol. Opt. Phys.*, 42(15), 154013 (2009). URL http://dx.doi.org/10.1088/0953-4075/42/15/154013.

[172] J. J. McLoughlin, A. H. Nizamani, J. D. Siverns, R. C. Sterling, M. D. Hughes, B. Lekitsch, B. Stein, S. Weidt, and W. K. Hensinger. Versatile ytterbium ion trap experiment for operation of scalable ion-trap chips with motional heating and transition-frequency measurements. *Phys. Rev. A*, 83(1), 013406 (2011). URL http://dx.doi.org/10.1103/PhysRevA.83.013406.

[173] S. Weidt, J. Randall, C. Webster, S. D. Standing, E. A. Rodriguez, E. Webb, A. B. Lekitsch, and K. Hensinger, W.˙ Ground-State Cooling of a Trapped Ion Using Long-Wavelength Radiation. *Phys. Rev. Lett.*, 115(1), 013002 (2015). URL http://dx.doi.org/10.1103/PhysRevLett.115.013002.

[174] J. Britton. Microfabrication techniques for trapped ion quantum information processing. Phd thesis, University of Colorado (2008). URL http://www.nist.gov/pml/div688/grp10/upload/Joe-Britton.pdf.

[175] G. Poulsen, Y. Miroshnychenko, and M. Drewsen. Efficient ground-state cooling of an ion in a large room-temperature linear Paul trap with a sub-Hertz heating rate. *Phys. Rev. A*, 86(5), 051402 (2012). URL http://dx.doi.org/10.1103/PhysRevA.86.051402.

[176] B. G. U. Englert, M. Mielenz, C. Sommer, J. Bayerl, M. Motsch, P. W. H. Pinkse, G. Rempe, and M. Zeppenfeld. Storage and Adiabatic Cooling of Polar Molecules in a Microstructured Trap. *Phys. Rev. Lett.*, 107(26), 263003 (2011). URL http://dx.doi.org/10.1103/PhysRevLett.107.263003.

[177] J. Chen, J. G. Story, J. J. Tollett, and R. G. Hulet. Adiabatic cooling of atoms by an intense standing wave. *Phys. Rev. Lett.*, 69(9), 1344 (1992). URL http://dx.doi.org/10.1103/PhysRevLett.69.1344.

[178] ATRAP Collaboration, G. Gabrielse, W. S. Kolthammer, R. McConnell, P. Richerme, R. Kalra, E. Novitski, D. Grzonka, W. Oelert, T. Sefzick, M. Zielinski, D. Fitzakerley, M. C. George, E. A. Hessels, C. H. Storry, M. Weel, A. Müllers, and J. Walz. Adiabatic Cooling of Antiprotons. *Phys. Rev. Lett.*, 106(7), 073002 (2011). URL http://dx.doi.org/10.1103/PhysRevLett.106.073002.

[179] M. Greiner, O. Mandel, T. Esslinger, T. W. Hänsch, and I. Bloch. Quantum phase transition from a superfluid to a Mott insulator in a gas of ultracold atoms. *Nature*, 415(6867), 39 (2002). URL http://dx.doi.org/10.1038/415039a.

[180] J. Schachenmayer, D. M. Weld, H. Miyake, G. A. Siviloglou, W. Ketterle, and A. J. Daley. Adiabatic cooling of bosons in lattices to magnetically ordered quantum states. *Phys. Rev. A*, 92(4), 041602 (2015). URL http://dx.doi.org/10.1103/PhysRevA.92.041602.

[181] J. C. Bergquist, F. Diedricht, W. M. Itano, and D. J. Wineland. Hg+ Single Ion Spectroscopy. In *Frequency Standards and Metrology*, pp. 287–292. Springer, Berlin, Heidelberg (1989). URL http://dx.doi.org/10.1007/978-3-642-74501-0_50.

[182] R. J. Glauber. Coherent and Incoherent States of the Radiation Field. *Phys. Rev.*, 131(6), 2766 (1963). URL http://dx.doi.org/10.1103/PhysRev.131.2766.

[183] G. Lachs. Theoretical Aspects of Mixtures of Thermal and Coherent Radiation. *Phys. Rev.*, 138(4B), B1012 (1965). URL http://dx.doi.org/10.1103/PhysRev.138.B1012.

[184] P. Filipowicz. Quantum revivals in the Jaynes-Cummings model. *J. Phys. A: Math. Gen.*, 19(18), 3785 (1986). URL http://dx.doi.org/10.1088/0305-4470/19/18/024.

[185] A. Karmakar and G. Gangopadhyay. Fermionic thermocoherent state: Efficiency of electron transport. *Phys. Rev. E*, 93(2), 022141 (2016). URL http://dx.doi.org/10.1103/PhysRevE.93.022141.

[186] R. Bowler, J. Gaebler, Y. Lin, T. R. Tan, D. Hanneke, J. D. Jost, J. P. Home, D. Leibfried, and D. J. Wineland. Coherent Diabatic Ion Transport and Separation in a Multizone Trap Array. *Phys. Rev. Lett.*, 109(8), 080502 (2012). URL http://dx.doi.org/10.1103/PhysRevLett.109.080502.

[187] A. Abdelrahman, O. Khosravani, M. Gessner, A. Buchleitner, H.-P. Breuer, D. Gorman, R. Masuda, T. Pruttivarasin, M. Ramm, P. Schindler, and H. Häffner. Local probe of single phonon dynamics in warm ion crystals. *Nature Communications*, 8, ncomms15712 (2017). URL http://dx.doi.org/10.1038/ncomms15712.

[188] E. Fasci, N. Coluccelli, M. Cassinerio, A. Gambetta, L. Hilico, L. Gianfrani, P. Laporta, A. Castrillo, and G. Galzerano. Narrow-linewidth quantum cascade laser at 86 µm. *Optics Letters*, 39(16), 4946 (2014). URL http://dx.doi.org/10.1364/OL.39.004946.

[189] M. G. Hansen, E. Magoulakis, Q.-F. Chen, I. Ernsting, and S. Schiller. Quantum cascade laser-based mid-IR frequency metrology system with ultra-narrow linewidth and $1 \times 10^{-13}$-level frequency instability. *Optics Letters*, 40(10), 2289 (2015). URL http://dx.doi.org/10.1364/OL.40.002289.

[190] B. Argence, B. Chanteau, O. Lopez, D. Nicolodi, M. Abgrall, C. Chardonnet, C. Daussy, B. Darquié, Y. Le Coq, and A. Amy-Klein. Quantum cascade laser frequency stabilization at the sub-Hz level. *Nat. Photon*, 9(7), 456 (2015). URL http://dx.doi.org/10.1038/nphoton.2015.93.

[191] R. Höppner, E. Roldán, and G. J. de Valcárcel. A semiclassical optics derivation of Einstein's rate equations. *American Journal of Physics*, 80(10), 882 (2012). URL http://dx.doi.org/10.1119/1.4740247.

[192] M. Lindberg and S. Stenholm. The master equation for laser cooling of trapped particles. *J. Phys. B: At. Mol. Phys.*, 17(16), 3375 (1984). URL http://dx.doi.org/10.1088/0022-3700/17/16/019.

[193] C. Zener. Non-Adiabatic Crossing of Energy Levels. *Proceedings of the Royal Society of London A: Mathematical, Physical and Engineering Sciences*, 137(833), 696 (1932). URL http://dx.doi.org/10.1098/rspa.1932.0165.

[194] A. Turrin. Pulse-shape dependence in population inversion with frequency chirping. *Optics Communications*, 23(2), 220 (1977). URL http://dx.doi.org/10.1016/0030-4018(77)90311-X.

[195] N. V. Vitanov, T. Halfmann, B. W. Shore, and K. Bergmann. Laser-Induced Population Transfer by Adiabatic Passage Techniques. *Annual Review of Physical Chemistry*, 52(1), 763 (2001). URL http://dx.doi.org/10.1146/annurev.physchem.52.1.763.

[196] S. Willitsch. Ion-atom hybrid systems. *arXiv:1401.1699 [physics]* (2014). URL http://arxiv.org/abs/1401.1699.

[197] Z. Meir, T. Sikorsky, R. Ben-shlomi, N. Akerman, Y. Dallal, and R. Ozeri. Dynamics of a Ground-State Cooled Ion Colliding with Ultracold Atoms. *Phys. Rev. Lett.*, 117(24), 243401 (2016). URL http://dx.doi.org/10.1103/PhysRevLett.117.243401.

[198] M. Berglund and M. E. Wieser. Isotopic compositions of the elements 2009 (IUPAC Technical Report). *Pure Appl. Chem., PAC*, 83(2), 397 (2011). URL http://dx.doi.org/10.1351/PAC-REP-10-06-02.

[199] J. Jin and D. Church. Precision lifetimes for the $Ca^+ 4p\ ^2P$ levels: Experiment challenges theory at the 1% level. *American Physical Society*, 70(21), 3213 (1993). URL http://dx.doi.org/10.1103/PhysRevLett.70.3213.

[200] M. Chwalla, J. Benhelm, K. Kim, G. Kirchmair, T. Monz, M. Riebe, P. Schindler, A. S. Villar, W. Hänsel, C. F. Roos, R. Blatt, M. Abgrall, G. Santarelli, G. D. Rovera, and P. Laurent. Absolute Frequency Measurement of the $^{40}Ca^+$ $4s\ ^2S_{1/2} - 3d\ ^2D_{5/2}$ Clock Transition. *Phys. Rev. Lett.*, 102(2), 023002 (2009). URL http://dx.doi.org/10.1103/PhysRevLett.102.023002.

[201] C. Shi, F. Gebert, C. Gorges, S. Kaufmann, W. Nörtershäuser, B. K. Sahoo, A. Surzhykov, V. A. Yerokhin, J. C. Berengut, F. Wolf, J. C. Heip, and P. O. Schmidt. Unexpectedly large difference of the electron density at the nucleus in the $4p\ ^2P_{1/2,3/2}$ fine-structure doublet of $Ca^+$. *Appl. Phys. B*, 123(1), 2 (2017). URL http://dx.doi.org/10.1007/s00340-016-6572-z.

[202] F. Gebert, Y. Wan, F. Wolf, C. N. Angstmann, J. C. Berengut, and P. O. Schmidt. Precision Isotope Shift Measurements in Calcium Ions Using Quantum Logic Detection Schemes. *Phys. Rev. Lett.*, 115(5), 053003 (2015). URL http://dx.doi.org/10.1103/PhysRevLett.115.053003.

[203] R. Yamazaki, H. Sawamura, K. Toyoda, and S. Urabe. Stimulated Raman spectroscopy and the determination of the D-fine-structure level separation in 40Ca+. *Phys. Rev. A*, 77(1), 012508 (2008). URL http://dx.doi.org/10.1103/PhysRevA.77.012508.

[204] W. Nörtershäuser, K. Blaum, K. Icker, P. Müller, A. Schmitt, K. Wendt, and B. Wiche. Isotope shifts and hyperfine structure in the transitions in Calcium II. *Eur. Phys. J. D*, 2(1), 33 (1998). URL http://dx.doi.org/10.1007/s100530050107.

[205] A.-M. Mårtensson-Pendrill, A. Ynnerman, H. Warston, L. Vermeeren, R. E. Silverans, A. Klein, R. Neugart, C. Schulz, P. Lievens, and The ISOLDE Collaboration. Isotope shifts and nuclear-charge radii in singly ionized $^{40-48}Ca$. *Phys. Rev. A*, 45(7), 4675 (1992). URL http://dx.doi.org/10.1103/PhysRevA.45.4675.

[206] B. E. King. Angular Momentum Coupling and Rabi Frequencies for Simple Atomic Transitions. *arXiv:0804.4528 [physics]* (2008). URL http://arxiv.org/abs/0804.4528.